A COUPLED HEAT, SALT AND WATER BALANCE MODEL OF EVAPORATION AND STRATIFICATION IN SALINE TERMINAL LAKES: AN APPLICATION TO THE DEAD SEA

by
ATUL MOHAN SALHOTRA
E. ERIC ADAMS
and
DONALD R.F. HARLEMAN

RALPH M. PARSONS LABORATORY
AQUATIC SCIENCE AND ENVIRONMENTAL ENGINEERING

Report Number 311

Prepared under the support of the

Water Resources and Environmental Engineering Program
National Science Foundation
and
Mediterranean-Dead Sea Co. Ltd.
Israel

April, 1986

MIT

DEPARTMENT
OF
CIVIL
ENGINEERING

SCHOOL OF ENGINEERING
MASSACHUSETTS INSTITUTE OF TECHNOLOGY
Cambridge, Massachusetts 02139

R86-17

OSP 91857
OSP 95003

A COUPLED HEAT, SALT AND WATER BALANCE MODEL OF EVAPORATION AND STRATIFICATION IN SALINE TERMINAL LAKES: AN APPLICATION TO THE DEAD SEA

by

Atul Mohan Salhotra
E. Eric Adams

and

Donald R.F. Harleman

RALPH M. PARSONS LABORATORY

AQUATIC SCIENCE AND ENVIRONMENTAL ENGINEERING

Report No. 311

Prepared under the support of the
Water Resources and Environmental Engineering Program
National Science Foundation
and
Mediterranean-Dead Sea Co. Ltd.
Israel

April 1986

Abstract

A time varying, one-dimensional, coupled heat, salt and water budget model is developed for a hypersaline water body in which the vertical stability depends on the opposing influences of temperature and salinity stratification. A mixed layer modelling approach is used in which entrainment from the hypolimnion into the epilimnion occurs as a result of mass, heat, salt and momentum fluxes at the water surface.

The effect of salinity on evaporation has been discussed in detail using evaporation pan data collected at the Dead Sea. An accurate method to account for this effect based on the dependence of saturation vapor pressure on salinity and ionic composition is suggested and shown to be superior to the commonly used approach based on the ratio of salt water to fresh water evaporation. Also, the negative feedback effect of temperature on salinity has been quantified.

A comparison of various formulae to compute atmospheric long wave radiation is presented. Using data collected at the Dead Sea these formulae have been calibrated to account for site specific conditions. The importance of using accurate cloud cover values is indicated.

The primary components of the mixing algorithm are wind stirring and penetrative convection. The relative magnitudes of each during different periods in a year are compared. On an annual level, the energy supplied by wind mixing is significantly larger than the penetrative convective mixing energy.

The model is calibrated and verified using vertical temperature and salinity data from the Dead Sea over a period of five years. The model has been used to predict the lake levels, annual evaporation and vertical stratification over a period of thirty years with the proposed Mediterranean Dead Sea Hydro Power Project in operation.

Acknowledgements

This report essentially constitutes the doctoral dissertation of Atul M. Salhotra.

We acknowledge the generous assistance of Professor Keith D. Stolzenbach who participated in many of the technical discussions.

The research was supported by the National Science Foundation, Grant No. CEE-8119384, under the cognizance of Dr. Arthur Ezra, Program Director, Water Resources and Environmental Engineering program and the Mediterranean-Dead Sea Co. Ltd., Mr. Uri Wurzburger, Managing Director. We acknowledge with sincere appreciation the assistance of many individuals in Israel who assisted in making available information and data for the Dead Sea. They include Dr. Avner A. Arzi, and Mr. Eitan Gratch of the Mediterranean-Dead Sea Co.; Dr. Gerald Stanhill, Agricultural Research Center; Dr. David Anati, Solmat Systems, Ltd.; and Dr. Ilana Steinhorn, Weizmann Institute of Science.

LIST OF CONTENTS

LIST OF FIGURES

6.2 Variation of α with density and meteorology (Ref 133).

6.3 Measured Water Surface Temperature and Evaporation for Pans 12, 16 and 19

6.4 Cycle Average Air Temperature and Relative Humidity, Plus Surface Water Temperature and Evaporation for Pans 12 and 19

6.5 Comparison of β-values, With Error Bars, for the Eight Pans and the Data Reported by Arons and Kientzler [1954] and Dickson et al. [1965]

6.6 The α-values, γ-values and the feedback effect for Pans 13 to 19 relative to Pan 12.

7.1 The Effect of Various Physical Processes on the Stability Index of the Lake

7.2 The Effect of Two Differrent Sequences of Mixing Processes on Lake Stratification

8.1 Iterpolated Dead Sea Elevations October 1979 to July 1984

8.2 Dead Sea Salt Content Normalized by Area at 400 mbsl Relative to Salt Content on 2 October 1979

9.1(a) Data and Model Results for the Period 12 December 1979 to 12 March 1980 with $C_w = 6$ and $C_c = .1$

9.1(b) Daily Input of Wind and Penetrative convective Mixing Energy for the Period 12 December 1979 to 12 March 1980 with $C_w = 6$ and $C_c = .1$.

9.1(c) Cumulative Wind and Penetrative Convective Mixing Energy for the Period 12 December 1979 to 12 March 1980 with $C_w = 6$ and $C_c = .1$.

9.1(d) Daily Variation of Richardson Number for the Period 12 December 1979 to 12 March 1980 with $C_w = 6$ and $C_c = .1$.

9.1(e) Daily Water Balance for the Period 12 December 1979 to 12 March 1980 with $C_w = 6$ and $C_c = .1$.

9.1(f) Data and Model Results for the Period 12 December 1979 to 12 March 1980 with $C_w = 3$ and $C_c = .1$.

9.1(g) Data and Model Results for the Period 12 December 1979 to 12 March 1980 with C_w = 6 and C_c = .1 and using cube Root Mean Cube Wind Speed Values.

9.1(h) Data and Model Results for the Period 12 December 1979 to 12 March 1980 with C_w = 3 and C_c = .1 and using Cube Root Mean Cube Wind Speed Values.

9.2(a) Data and Model Results for the Period 19 December 1980 to 24 May 1981 with C_w = 6 and C_c = .1.

9.2(b) Daily Input of Wind and Penetrative Convective Mixing Energy for the Period 19 December 1980 to 24 May 1981 with C_w = 6 and C_c = .1.

9.2(c) Cumulative Wind and Penetrative Convective Mixing Energy for the Period 19 December 1980 to 24 May 1981 with C_w = 6 and C_c = .1.

9.2(d) Daily Variation of Richardson numbers for the Period 19 December 1980 to 24 May 1981 with C_w = 6 and C_c = .1.

9.2(e) Daily Water Balance for the Period 19 December 1980 to 24 May 1981 with C_w = 6 and C_c = .1.

9.2(f) Data and Model Results for the Period 19 December 1980 to 24 May with C_w = 3 and C_c = .1.

9.2(g) Data and Model Results for the Period 19 December 1980 to 24 May 1981 with C_w = 3 and C_c = .1 and using Cube Root Mean Cube Wind Speed Values.

9.3(a) Data and Model Results for the Period 12 March 1980 to 26 May 1980 with C_w = 0 and C_c = 0.0

9.3(b) Data and Model Results for the Period 12 March 1980 to 26 May 1980 with C_w = 6 and C_c = 0.1

9.3(c) Daily Input of Wind and Penetrative Convective Mixing Energy for the Period 12 March 1980 to 26 May 1980 with C_w = 6 and C_c = .1.

9.3(d) Daily Variation of Richardson numbers for the Period 12 March 1980 to 26 May 1980 with C_w = 6 and C_c = .1.

9.3(e) Daily Water Balance for the Period 12 March 1980 to 26 May 1980 with C_w = 6 and C_c = .1.

9.3 (f) Data and Model Resutls for the Period 19 December 1980 to 24 May 1981 with C_w = 3 and C_c = 0.1

9.4(a) Data and Model Results for the Period 24 May 1981 to 20 July 1981 with C_w = 0.0 and C_c = 0.0

9.4(b) Data and Model Results for the Period 24 May 1981 to 20 July 1981 with C_w = 6 and C_c = .1.

9.4(c) Data and Model Results for the Period 24 May 1981 to 20 July 1981 with C_w = 3 and C_c = .1.

9.4(d) Daily Water Balance for the Period 24 May 1981 to 20 July 1981 with C_w = 6 and C_c = .1.

9.4(e) Daily Input of Wind and Penetrative Convective Mixing Energy for the Period 24 May 1981 to 20 July 1981 with C_w = 6 and C_c = .1.

9.4(f) Cumulative Wind and Penetrative Convective Mixing Energy for the Period 24 May 1981 to 20 July 1981 with C_w = 6 and C_c = .1.

9.4(g) Daily Variation of Richardson number for the Period 24 May 1981 to 20 July 1981 with C_w = 6 and C_c = .1.

9.5(a) Data and Model Results for the Period 21 September 1981 to 18 December 1981 with C_w = 6 and C_c = 0.0

9.5(b) Data and Model Results for the Period 21 September 1981 to 18 December 1981 with C_w = 6 and C_c = .1.

9.5(c) Data and Model Results for the Period 21 September 1981 to 18 December 1981 with C_w = 6 and C_c = .25

9.5(d) Daily Water Balance for the Period 21 September 1981 to 18 December 1981 with C_w = 6 and C_c = .1.

9.5(e) Daily Input of Wind and Penetrative Convective Energy for the Period 21 September 1981 to 18 December 1981 with C_w = 6 and C_c = .1.

9.5(f) Cumulative Wind and Penetrative Convective Mixing Energy for the Period 21 September 1981 to 18 December 1981 with C_w = 6 and C_c = .1.

9.5(g) Daily Variation of Richardson number for the Period 21 September 1981 to 18 December 1981 with C_w = 6 and C_c = .1.

9.6(a) Data and Model Results for the Period 3 October 1983 to 10 November 1983 with C_w = 6 and C_c = 0.0.

9.6(b) Data and Model Results for the Period 3 October 1983 to 10 November 1983 with C_w = 6 and C_c = .1.

9.6(c) Data and Model Results for the Period 3 October 1983 to 10 November 1983 with $C_w = 6$ and $C_c = 0.25$

9.6(d) Daily Water Balance for the Period 3 October 1983 to 10 November 1983 with $C_w = 6$ and $C_c = .1$.

9.6(e) Daily Input of Wind and Penetrative Convective Mixing Energy for the Period 3 October 1983 to 10 November 1983 with $C_w = 6$ and $C_c = .1$.

9.6(f) Cumulative Wind and Penetrative Convective Mixing Energy Data for the Period 3 October 1983 to 10 November 1983 with $C_w = 6$ and $C_c = .1$.

9.6(g) Daily Variation of Richardson number for the Period 3 October 1983 to 10 November 1983 with $C_w = 6$ and $C_c = .1$.

9.7(a) Data and Model Results for the Period 26 May 1980 to 6 October 1980 with $C_w = 0$ and $C_c = .1$.

9.7(b) Daily Reduction in Potential Energy due to Convective Overturns for the Period 26 May 1980 to 6 October 1980 with $C_w = 0$ and $C_c = .1$.

9.7(c) Data and Model Results for the Period 26 May 1980 to 6 October 1980 with $C_w = 0$ and $C_c = .1$.

9.7(d) Daily Input of Wind and Penetrative Convective Mixing Energy for the Period 26 May 1980 to 6 October 1980 with $C_w = 0$ and $C_c = .1$.

9.7(e) Cumulative Wind and Penetrative Convective Mixing Energy for the Period 26 May 1980 to 6 October 1980 with $C_w = 0$ and $C_c = .1$.

9.7(f) Daily Variation of Richardson numbers for the Period 26 May 1980 to 6 October 1980 with $C_w = 6$ and $C_c = .1$.

9.7(g) Daily Water Balance for the Period 26 May 1980 to 6 October 1980 with $C_w = 6$ and $C_c = .1$.

9.8(a) Data and Model Results for the Period 20 July 1981 to 21 September 1981 with $C_w = 6$ and $C_c = 0.0$

9.8(b) Daily Reduction in Potential Energy Due to Convective Overturns for the Period 20 July 1981 to 21 September 1981 with $C_w = 0$ and $C_c = 0.0$

9.8(c) Data and Model Results for the Period 20 July 1981 to 21 September 1981 with $C_w = 6$ and $C_c = .1$.

9.8(d) Daily Water Balance for the Period 20 July 1981 to 21 September 1981 with $C_w = 6$ and $C_c = .1$.

9.8(e) Daily Input of Wind and Penetrative Convective Mixing Energy for the Period 20 July 1981 to 21 September 1981 with $C_w = 6$ and $C_c = .1$.

9.9(a) Meteorological Variables for the Period 12 December 1979 to 21 September 1981

9.9(b) Daily Values of Jordan River Inflows for the Period 12 December 1979 to 21 September 1981

9.9(c) Daily Values of Pumpage by the Salt Works for the Period 12 December 1979 to 21 September 1981

9.9(d) Comparison of Data and Model Results for the Period 12 December 1979 to 21 September 1981 with $C_w = 6$ and $C_c = .1$ and Initial Conditions of 12 December 1979.

9.9(e) Comparison of Data and Model Results for 24 May 1981 with $C_w = 6$ and $C_c = .1$ and Initial Conditions of 12 December 1979.

9.9(f) Comparison of Data and Model Results for 20 July 1981 with $C_w = 6$ and $C_c = .1$ and Initial Conditions of 12 December 1979.

9.9(g) Comparison of Data and Model Results for 21 September 1981 with $C_w = 6$ and $C_c = .1$ and Initial Conditions of 12 December 1979.

9.9(h) Daily Variation of Surface Temperature (Data and Model Results for the Period 12 December 1979 to 21 September 1981 with $C_w = 6$ and $C_c = .1$.

9.9(i) Daily Variation of Surface Salinity (Data and Model Results for the Period 12 December 1979 to 21 September 1981 with $C_w = 6$ and $C_c = .1$.

9.9(j) Daily Variation of Mixed Layer Depth for the Period 12 December 1979 to 21 September 1981 with $C_w = 6$ and $C_c = .1$.

9.9(k) Daily Variation of Evaporation for the Period 12 December 1979 to 21 September 1981 with $C_w = 6$ and $C_c = .1$.

9.9(l) Daily Input of Wind Mixing Energy for the Period 12 December 1979 to 21 September 1981 with $C_w = 6$ and $C_c = .1$.

9.9(m) Cumulative Input of Wind Mixing Energy for the Period 12 December 1979 to 21 September 1981 with $C_w = 6$ and $C_c = .1$.

9.9(n) Daily Values of Penetrative Convective Mixing Energy for the Period 12 December 1979 to 21 September 1981 with $C_w = 6$ and $C_c = .1$.

9.9(o) Cumulative Penetrative convective Mixing Energy for the Period 12 December 1979 to 21 September 1981 with $C_w = 6$ and $C_c = .1$.

9.9(p) Daily Variation of Richardson Numbers for the Period 12 December 1979 to 21 September 1981 with $C_w = 6$ and $C_c = .1$.

9.9(q) Various Components of the Thermal Energy Balance for the Period 12 December 1979 to 21 September 1981

10.1 The Activity Coefficient of Water in the Dead Sea and Mediterranean Sea Water

10.2 Dead Sea Elevation and Surface Salinity with the Power Project in Operation

10.3 Annual Evaporation and Surface Temperatures with the Power Project in Operation

10.4 Variation of α with Water Surface Temperatures for the Dead Sea Meteorology (Also see Fig. 10.5)

10.5 Monthly Meteorology and α-Values for a Pan and Lake at Equilibrium

10.6 Temperature, Salinity and Density Profiles for Year 1 with the Power Project in Operation

10.7 Temperature, Salinity and Density Profiles for Year 2 with the Power Project in Operation

10.8 Temperature, Salinity and Density Profiles for Year 5 with the Power Project in Operation

10.9 Temperature, Salinity and Density Profiles for Year 10 with the Power Project in Operation

10.10 Temperature, Salinity and Density Profiles for Year 20 with the Power Project in Operation

10.11 Temperature, Salinity and Density Profiles for Year 30 with the Power Project in Operation

10.12(a) Temperature Isopleths for year 1 with the Power Project in Operation

10.12(b) Salinity Isopleths for year 1 with the Power Project in Operation

10.12(c) Density Isopleths for year 1 with the Power Project in Operation

10.13(a) Temperature Isopleths for year 2 with the Power Project in Operation

10.13(b) Salinity Isopleths for year 2 with the Power Project in Operation

10.13(c) Density Isopleths for year 2 with the Power Project in Operation

10.14(a) Temperature Isopleths for year 5 with the Power Project in Operation

10.14(b) Salinity Isopleths for year 5 with the Power Project in Operation

10.14(c) Density Isopleths for year 5 with the Power Project in Operation

10.15(a) Temperature Isopleths for year 10 with the Power Project in Operation

10.15(b) Salinity Isopleths for year 10 with the Power Project in Operation

10.15(c) Density Isopleths for year 10 with the Power Project in Operation

10.16(a) Temperature Isopleths for year 20 with the Power Project in Operation

10.16(b) Salinity Isopleths for year 20 with the Power Project in Operation

10.16(c) Density Isopleths for year 20 with the Power Project in Operation

10.17(a) Temperature Isopleths for year 30 with the Power Project in Operation

10.17(b) Salinity Isopleths for year 30 with the Power Project in Operation

10.17(c) Density Isopleths for year 30 with the Power Project in Operation

LIST OF TABLES

CHAPTER 1

INTRODUCTION

The general purpose of this research has been to develop a mathematical model to study the vertical stratification and surface exchange processes in a saline lake. A large number of models of varying degrees of complexities have been used to study these processes in fresh water lakes. However, very few if any detailed investigations have been undertaken to study these processes in saline lakes in which a number of factors complicate the analysis: (i) a greater range of both positive and negative stabilizing forces exist to oppose/supplement mixing due to wind and penetrative convection, (ii) properties such as heat capacity, density and saturation vapor pressure have strong dependence on time varying salinity and ionic composition, (iii) differing solubilities of dissolved salts can result in differential precipitation, and (iv) absence of sufficient field data for model calibration and verification. The succeeding chapters describe our approach to model the vertical stratification in a saline lake. Although the research objective has been to develop a model of general applicability, the model calibration, verification and application will concentrate on the Dead Sea for which sufficient data is available.

Since the historic overturn of the Dead Sea in 1979, various interesting changes in lake stratification, surface temperature and salinity have been observed. These are of significant interest to scientists and engineers. Whereas the efforts of the scientists are

directed towards explaning the inherent physics of the various processes affecting the Dead Sea, engineers are primarily concerned with the influence of these processes on the design, operation and maintenance of existing and proposed facilities on the Dead Sea including the proposed Mediterranean Dead Sea project, salt gradient solar ponds and the salt works. These aspects are further elaborated in Chapter 2.

The model basically consists of four coupled budgets - thermal energy, salt, water and mechanical energy. The latter includes the various mixing processes. As mentioned in Chapter 3, the model has been developed along the lines of the MIT Reservoir Stratification Model (Hurley et al., 1977) and MITSOL (Atkinson et al. 1983).

The following three chapters describe the Dead Sea meteorology and the important surface heat flux terms. Based on field data, a number of models of atmospheric long wave radiation have been calibrated to site specific conditions. A major part of the research effort has been devoted to understanding the effect of salinity on evaporation and the development of a physically correct analytical formation. The dependence of evaporation on meteorological variables, salinity and ionic composition has been analysed using data from evaporation pans located near the Dead Sea. The negative temperature feedback effect on evaporation has been quantified.

Chapter 7 discusses the potential energy and the mechanical energy budget. A mixing algorithm based on the parameterization of the turbulent kinetic energy equation is presented and simplified to include only two calibration coefficients, one of which is associated with wind mixing and the other with penetrative convection.

Chapter 8 discusses the salt and water budgets for the lake and indicates the importance of the salt works on the overall mass and salt balance of the Dead Sea. The coefficients in the mixing algorithm are calibrated and verified in Chapter 9 by analysing a number of Dead Sea profiles which evolve as a result of one of the two mixing processes. The calibrated values lie within the range of values suggested in the literature.

Finally in Chapter 10, the model is used to study the future evolution of the lake over a period of thirty years with the Mediterranean Dead Sea Power project in operation. Results indicate that the surface layers of the lake continue to dilute during the filling period. This results in a progressive increase in the annual rate of evaporation and hence a cooling of the lake surface. This negative temperature feedback effect in the lake is further discussed in this chapter. This is followed by a chapter that outlines the important conclusions of this research.

CHAPTER 2

THE DEAD SEA

2.1 Introduction

The Dead Sea occupies a depression in the 600 km long tectonic valley extending from the Gulf of Elat in the South to the Huleh depression in the north, (Fig. 2.1). Geologic evidence suggests that during the Plistocene epoch the valley formed a large lagoon connected at times to the ocean. This marine connection was disrupted by tectonic movements about two million years ago, following which the valley was occupied by a series of lakes. About 10,000 years ago, the valley and Dead Sea attained their present shape, but the level of the lake has continued to fluctuate. A detailed account of the physiography, stratigraphy and paleolimnology of the Dead Sea is presented by Neev and Emery (1967) and Steinhorn and Gat (1983).

2.2 Physical Description and Hydrology of the Dead Sea

The Dead Sea extends from latitude 31° N to 31° 45' N at a longitude of 35° 30' E. It is bounded to the East by the mountains of Moab and by the Judean Desert to the West. Historically, the Dead Sea could be divided into a Northern basin and a Southern basin, connected by the Lisan Straits with a sill level at 401 mbsl. The Northern basin covers an area of about 750 km^2 with a maximum depth of about 330 m and has a salinity of about 28%. Of all the hypersaline lakes in the world this is the deepest and probably the saltiest. The Southern basin is 2-3 m deep

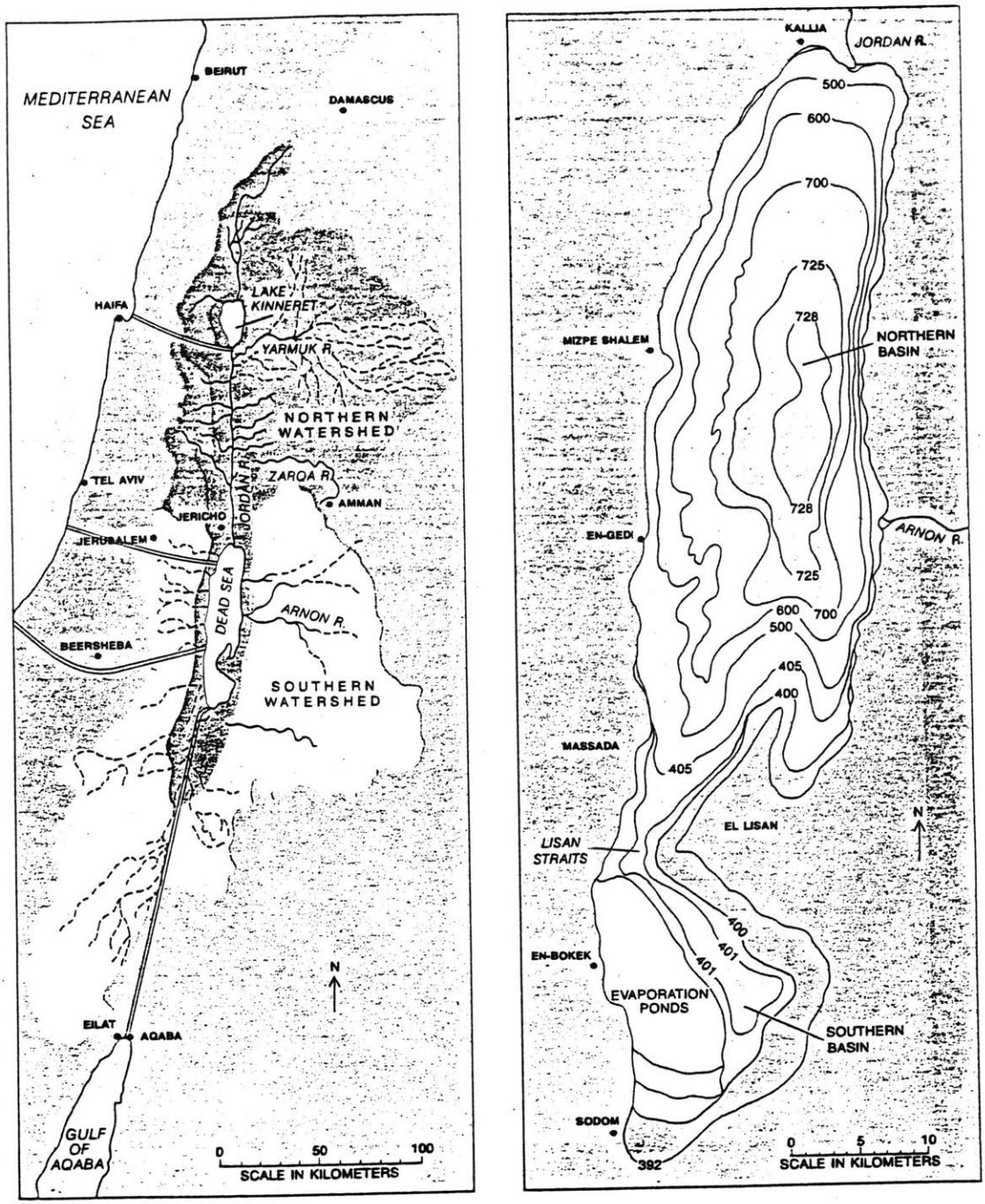

Fig. 2.1 Location Map of The Dead Sea

with a maximum surface area of about 250 km^2. Since 1966, the western half of the Southern basin has been diked off and transformed into evaporation ponds by the Dead Sea Works to extract potassium salts. In 1982, the Arab Potash Works contructed similar evaporation ponds on the eastern edge of the Southern basin. Details of these salt works are included in Chapter 8 and Appendix D.

It is important to note that the political border between Israel and Jordan passes north-south through the center of the lake. Absence of cordial and friendly political relations between the two countries has serious implications on the availability of hydrographic data for the Dead Sea as well as the implementation of any project involving the entire Dead Sea (United Nations (1982, 1983 and 1984)).

The Dead Sea is a terminal lake and hence its salinity and surface elevation fluctuates in response to changes in inflows and climatic conditions. The Jordan River at the northern shore of the lake accounts for 80%-90% of the lake inflow, the remainder is accounted for by the Arnon River, saline and fresh water--springs, seasonal wadis and groundwater seepage. These sources are distributed all around the shore. The lake is located in the "rain shadow" of the Judean mountains and receives an annual mean rainfall of only 50 to 75 millimeters. Since the beginning of this century, the lake level has dropped by about 10 m primarily due to human activities (Fig. 2.2) and has resulted in the segregation of the two basins.

In 1929, the Jordan River was dammed at two locations -- the outlet of the Sea of Galilee (Lake Kinneret) and at the junction of the Jordan and the Yarmak Rivers. The creation of these reservoirs increased the

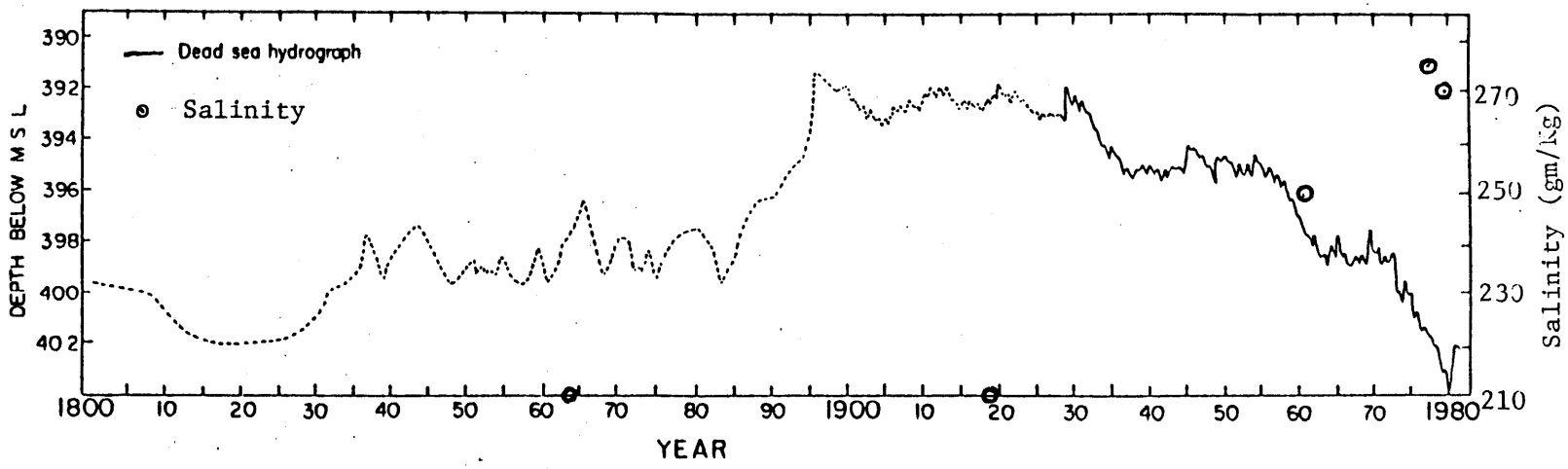

Fig. 2.2 Dead Sea Water Level and Salinity (1800-1980)

evaporative water loss from Jordan and decreased the inflows to the lake. This caused a drop of about 2.5 m in the Dead Sea Level. Subsequently, in early 1960's, fresh water flow was diverted from the Dead Sea Watershed into Israel's National Water Carrier system and also the Jordan Ghori Canal for intensive agricultural development. These diversions have further reduced inflows to the lake as a result of which the Dead Sea level has dropped to -402 mbsl and continues to drop at about 0.5-1.0 m per year.

Outflows from the lake consist of fresh water loss due to evaporation and the pumpage of saline water into the evaporation ponds of the two salt works. Net fresh water loss from the lake due to reduced inflows and evaporation has caused a significant increase in the salinity and density of the upper 40 m of the Dead Sea (Fig. 2.2). (Details of recent fluctuations in lake level, salinity and density are discussed in Chapter 8.) This resulted in a reduction of the vertical stability of the Dead Sea culminating in a complete overturn in early 1979. The halothermal stratification observed in the lake since then is discussed in Section 2.3.

The salinity and ionic composition of the Dead Sea is a result of the complex processes that have affected the origin and evolution of the lake, details of which are still in dispute. Table 2.1 is a comparison of the ionic composition of the present-day Dead Sea, the Great Salt Lake (of marine origin) and sea water. Compared with brines of marine origin, Dead Sea brine has a higher fraction of calcium, magnesium, potassium and bromine and a lower fraction of sodium, sulphate and carbonate. This unique conglomeration of ions has significant commercial implications in terms of the operation of the salt works (Section 2.4.2 and Appendix D).

Table 2.1
Percentage Ionic Composition for Dead Sea
Great Salt Lake and Sea Water (Refs. 44 and 123)

Sample	S(g/kg)	Mg	Ca	Na	K	HCO_3	SO_4	Br	Cl
Sea Water	34	3.69	1.18	30.62	1.11	0.41	7.69	0.19	55.1
D.S. July 1970	259	12.37	5.00	12.86	2.11	0.075	0.21	1.52	65.9
D.S. July 1960	251	12.33	5.00	12.77	2.17	0.076	0.21	1.51	65.8
D.S. March 1977	274	12.88	5.04	11.90	2.25	0.083	0.14	1.53	66.1
D.S. Feb. 1976	276	12.67	5.18	12.06	2.27	0.069	0.13	1.56	66.1
Evaporation Pond	285	16.88	6.56	3.30	2.98	0.081	0.06	1.96	68.1
Great Salt Lake		2.79	0.16	32.94	1.66		6.68		55.7

and also affects the rate of evaporative water loss.

2.3 Observed Vertical Stratification 1979-1984

The 300 m deep Dead Sea water column can be divided into an Upper Water Mass extending to a depth of about 40 m below the surface and a Lower Water Mass from 40 m below the surface to the bottom of the lake. In response to the various atmospheric forcing functions the Upper Water Mass undergoes seasonal variations in temperature, salinity and density exhibiting interesting stratification patterns. For the period October 1979 to June 1984 -- the period for which data was analysed during this study -- the surface temperature ranged from about 19°C to 35°C; the surface salinity from 24.0% to 27.9% and the surface density from 1200 kg/m^3 to 1235 kg/m^3. At 40 m below the surface the corresponding variations were 21.8°C to 24.9°C; 27.71% to 27.88% and 1233.5 kg/m^3 to 1235.5 kg/m^3. These variations occured primarily during the periods November/December 1982 and November to January 1983/84 when the lake overturned (Weizmann Institute of Technology, 1979-1984). A part of these variations could also result from measurement errors. Excluding the periods when the lake is approaching an overturn, the two water masses can thus be considered independent entities except for heat and salt diffusion at the interface. Since both the (molecular) diffusion coefficients and the gradients are small, the fluxes of salt and heat across the interface are virtually negligible.

To understand the various stratification patterns in a saline lake it is important to realize the opposing influences of salinity and temperature on the vertical stability of the water column. An increase

(decrease) in the salinity of the surface layers of the column due to evaporation (net inflows) adds negative (positive) buoyancy to the lake thus reducing (increasing) the stability of the water column. On the contrary, an increase (decrease) in temperature during summer (autumn) adds positive (negative) buoyancy and increases (decreases) the stability of the column. The total buoyancy of the lake is the sum of the thermal and saline buoyancies. These can be computed from measured temperature and salinity profiles using the following equations:

$$B_T = \int_{\text{Datum}}^{\text{Surface}} g\,\alpha_T\{T(z) - T_\infty\}\,dz \qquad (2.1)$$

$$B_S = -\int_{\text{Datum}}^{\text{Surface}} g\,\alpha_S\{S(z) - S_\infty\}\,dz \qquad (2.2)$$

$$B_{Tot} = B_T + B_S \qquad (2.3)$$

where, α_T and α_S = the change in density of the Dead Sea brine per unit change in temperature (T) and salinity (S), and T_∞ and S_∞ = reference temperature and salinity. For reasons discussed above, the datum is fixed at 440 mbsl, approximately 40 m below the lake surface. Using measured temperature and salinity profiles the buoyancy of the Dead Sea for a period of five years is shown in Fig. 2.3 and discussed below.

For the Dead Sea, the net heating period extends from March to September during which the thermal buoyancy of the water column is positive and increasing. Also, this period is characterized by net evaporation that increases the salinity of the surface layers -- a destabilizing influence. The saline buoyancy of the lake thus

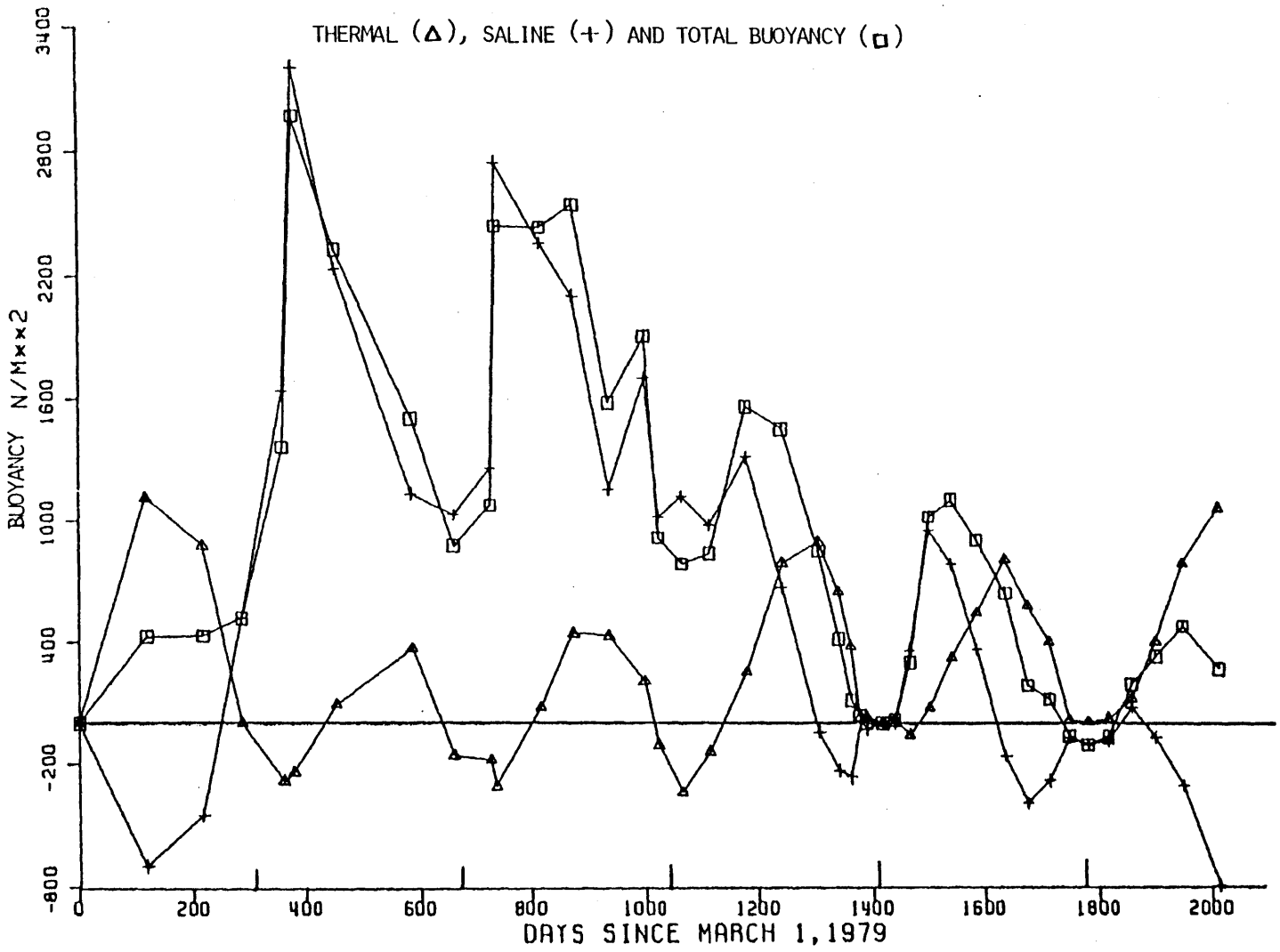

Fig. 2.3 Buoyancy of The Dead Sea Water Column (1979-84)

decreases. The absolute value of saline buoyancy and whether positive or negative depends on the fresh water inflows during the previous winter or more precisely the residual fresh water in the surface layers since the last overturn.

For example, the summer of 1979 -- following the historic overturn -- characterized by the absence of any residual fresh water from previous floods experienced a reverse halocline or an upside down solar lake effect. During such periods, the stabilizing influence of temperature dominates the destabilizing influence of the salinity, resulting in a stable water column.

The winter of 1979-1980 was unusually wet with fresh water inflows of the order of 1.5 m. These inflows, being fresh and exposed to similar meteorology as the saline Dead Sea water, would have been colder than the latter (see also Section 6.3.3). Thus, during the winter periods the positive buoyancy effect of salinity dominates the negative thermal buoyancy effect, resulting in a stable water column.

Throughout the summer of 1980, the water column indicates positive thermal and saline buoyancies. An inverse halocline is not observed due to the existence of residual fresh water from the previous wet winter. Overturn of the Dead Sea did not occur in 1980 since the 1980-1981 winter inflows arrived before the previous year's flood had sufficient time to evaporate entirely. This is consistent with the fact that during this period a net increase in the surface elevation was observed. The summer and fall of 1981 indicate a stratification pattern very similar to that of the previous year.

The dry winter of 1981-82 followed by the concentration effect of evaporation during the summer resulted in an inverse halocline in July 1982 -- for the first time since the 1979 overturn. The latter is held up by the stable thermocline. Fall cooling thus resulted in a weakening of the pycnocline and subsequent overturn in November-December 1982 ($B_{Tot} = 0$). This overturn was followed by a period of stable pycnocline during the summer of 1983 followed by another overturn in the fall of 1983 -- a direct consequence of a dry 1982-83 winter.

The above discussion highlights the unique and interesting stratification patterns of the Dead Sea that depend on nature's delicate balance between salinity and temperature. These four possible stratification patterns are summarized in Table 2.2, and can be observed in the time-depth plots of temperature and salinity (Figure 2.4) (Anati et. al. 1985).

The above analysis suggests the following stratification pattern for the Dead Sea. For those years when the fresh water inflow is less than or equal to the annual evaporation, an overturn would occur at the beginning of the following water year (overturn of 1983 fall). For the case when inflows exceed the annual evaporation, an overturn would be delayed until after the summer of the year, by which time the entire fresh water inflow would have evaporated.

2.4 Economic Implications of the Dead Sea Stratification Study

2.4.1 The Mediterranean Dead Sea Project

The proposed Mediterranean Dead Sea link project envisages conveying Mediterranean Sea water at a flow rate of about 50 m^3/s to the Dead Sea

Table 2.2

Stratification Patterns For The Dead Sea

Case No.	Thermocline	Halocline	Pycnocline	Occurence
1	stable	stable	very stable	summer after wet winter
2	stable	unstable	weakly stable/ unstable	summer after dry winter
3	unstable	stable	weakly stable/ unstable	during wet winters
4	unstable	unstable	unstable	late summer or fall following a dry winter after all the previous winter's floods have evaporated. Results in overturn.

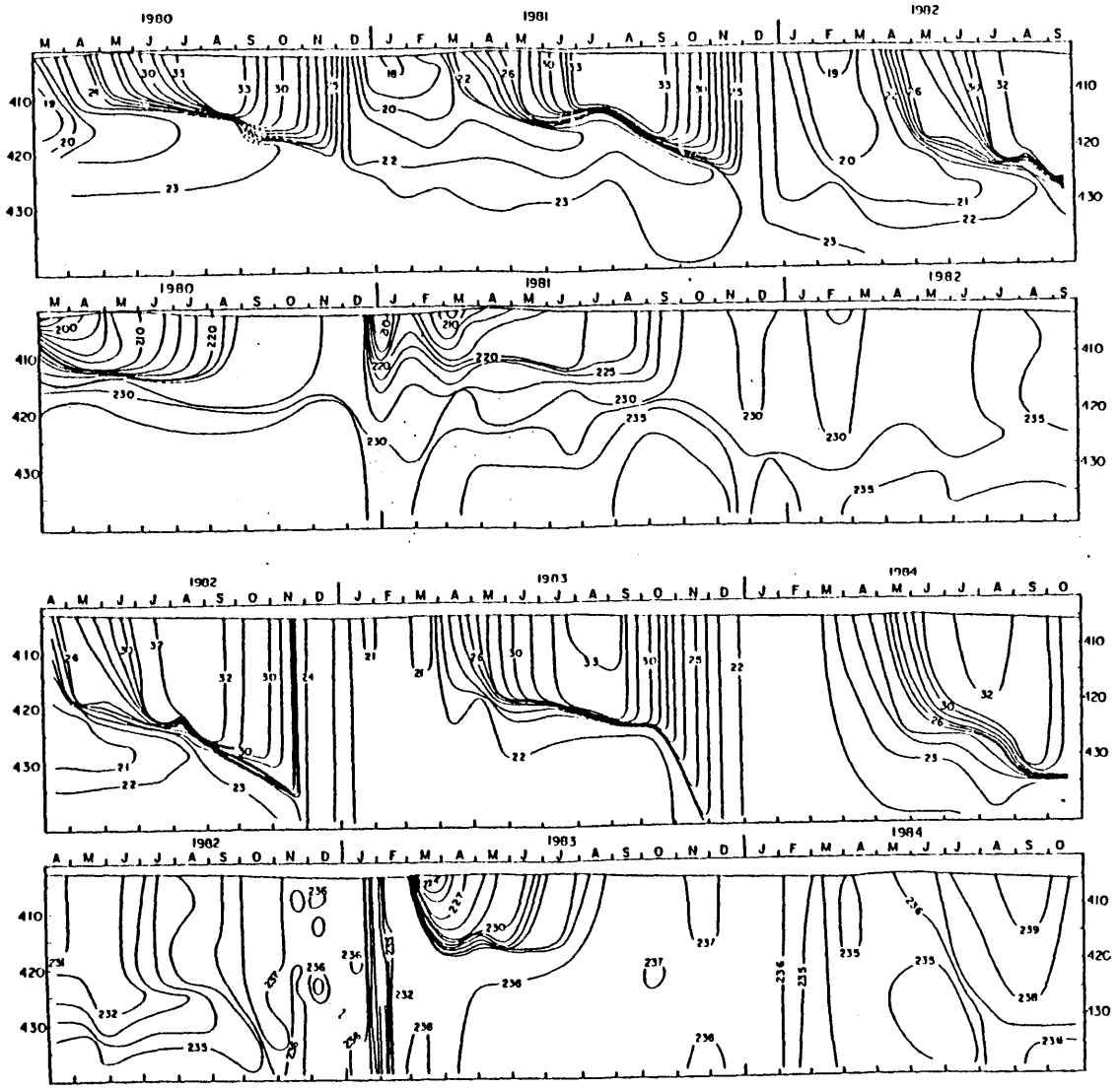

Fig. 2.4 Temperature and Sigma-20 Isopleths for The Dead Sea ()980-84) (Ref. ,6)

for the generation of hydropower using the 400 m head difference. An initial period of 20 years, with inflows from the Mediterranean Sea of about 53 m^3/s, would raise the Dead Sea level to -390 mbsl (historic level observed at the turn of the century). Thereafter the flow would be reduced to about 40 m^3/s to maintain an annual steady state level. Various schemes to convey the water have been examined. The most favorable one, shown in Fig. 2.5, involves a pumping station at the Qatif shore on the Mediterranean, to raise water to + 100 m elevation. At this level, water would flow in a 20 km long open channel followed by an 80 km long tunnel to two regulating reservoirs. Water from these would flow through a high pressure penstock to an underground four unit power station of 800 MW base load capacity. The hydropower plant would be operated primarily during peak hours to supply about 1850 MKWh/year during the filling period and 1450 MKWh/year during the steady state operation. Detailed discussion of the project are included in Mediterranean Dead Sea Co., Ltd. (1983).

The amount of water that can be diverted in steady state, the duration of the filling period and the lake elevations depend on the rate of evaporation from the Dead Sea water surface. Since the latter depends on the surface salinity and temperature both of which in turn depend on the vertical stratification, the study of physical processes in the Dead Sea has important engineering implications.

2.4.2 The Salt Works

The Dead Sea is an inexhaustible source of valuable chemicals. Commercially important minerals include potassium chloride, magnesium

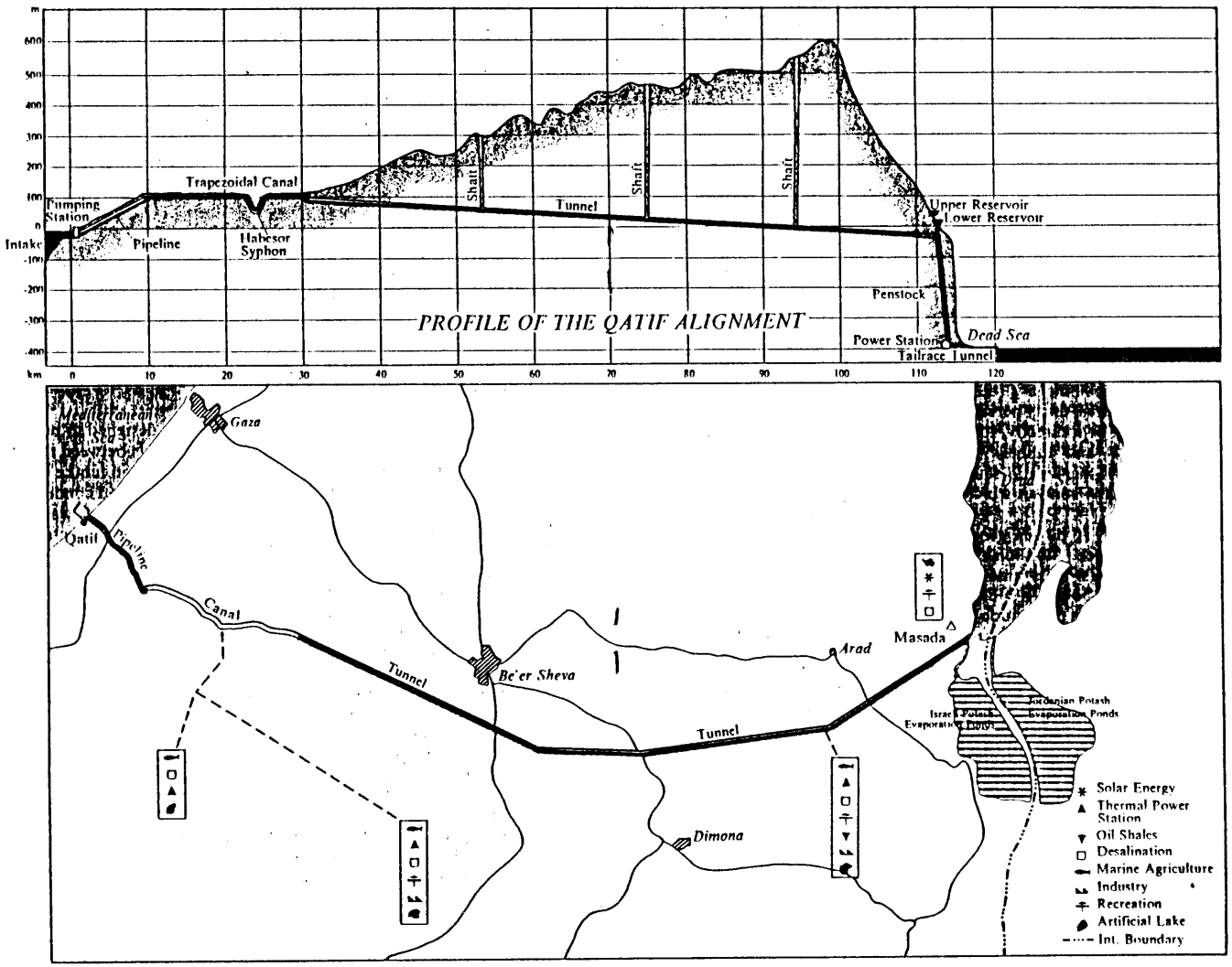

Fig. 2.5 Route Plan for The Mediterranean Dead Sea

chloride, bromine and sodium chloride. Currently the Dead Sea Works, Ltd., Be'er Sheva (Israel) and the Arab Potash Co., Ltd., Amman (Jordan) are both operating large solar-evaporation ponds in the Southern Basin of the Dead Sea to harvest these salts. Both the companies have plans to expand their operations. For further details refer to Khasawneh and Khoury (1983); Ballard and Brice (1984), Ashford and Boocock (1984), UN (1982-1984). The impact of the salt works on the salt and water balance of the Dead Sea is discussed in Chapter 8.

The successful operation of these salt works depends on the salinity and chemistry of the Dead Sea as well as the surface elevation. A rise in surface elevations can cause significant damage due to the flooding of the existing evaporation ponds. This can be avoided by the construction of dikes -- an expensive proposition. Similarly, a fall in the lake level would result in an increase in pumping costs. Operation of the hydropower project would affect both the lake elevation and its chemical composition and hence warrants a detailed modelling of the various hydrological and geochemical processes to asses the impact of the project on the operation of the salt works.

2.4.3 Salt Gradient Solar Ponds

In the last decade, significant solar pond activity has taken place in Israel. A 7500 m^2 pond with a power generating capacity of 150 KW was commissioned in 1979. Since then two new ponds with areas 50,000 m^2 and 250,000 m^2 have been constructed at the Northern end of the Dead Sea. These ponds supply thermal energy to a 2.5 MWe and a 5 MWe power plant. It has been proposed to install a series of floating solar ponds on the

surface of the Dead Sea to be operated in conjunction with the Mediterranean Dead Sea link project (Assaf, 1976).

The efficient operation of the existing and proposed floating solar ponds requires a knowledge of the mixing mechanisms in saline water bodies. In particular, knowledge gained in the parameterization of wind mixing in the Dead Sea would be useful for future studies related to solar ponds.

CHAPTER 3

MODELLING THE DEAD SEA

3.1 Introduction

The mathematical modelling of a physical phenomenon in the domain of environmental and water resource engineering involves a number of steps: (1) a precise definition of the objectives of the model being built and the engineering problem at hand, (2) a clear conceptual understanding of the various processes that need to be modelled and the interactions between them, (3) formulation of the governing equations including initial and boundary conditions, (4) specification of functional relationships and physical constants, (5) development of solution techniques, (6) calibration and verification of the model results with field data and, (7) the use of model for predictive purposes as a tool in the engineering decision making process.

The objective of modelling the heat, salt and water budgets as well as the mixing processes in the Dead Sea is two fold. First, to identify the dominant mixing mechanisms in the evolution of the Dead Sea stratification since the lake's historic overturn in early 1979. This has been discussed in Section 2.3. The second objective is to use this model to study the future evolution of lake stratification and the annual evaporative water loss with the power project in operation and its impact on the salt works. (See Section 2.4.1 and 2.4.2)

3.2 Conceptual Model For The Stratification Of A Saline Lake

An outline of the conceptual model for the evaporation and stratification in the Dead Sea is shown in Fig. 3.1. The model basically consists of four coupled budgets - the thermal energy, salt, mass and the mechanical energy budget. The latter includes the various mixing processes. These budgets are discussed in detail in subsequent chapters.

Fig. 3.1 shows the coupling and feedback links between the heat, salt water and the mechanical energy budgets. The heat balance affects the water surface temperature which affects evaporation and hence the water budget. The water budget in turn affects the concentration/ dilution of the lake and hence influences the salt budget. The surface temperature and salinity determine the surface density that affects the mixing processes and the vertical stratification. In turn, the vertical mixing determines the surface temperature and salinity.

For example, high rate of evaporation during late summer and fall causes the surface of the lake to cool and concentrate. This results in a top heavy water column that experiences significant penetrative convection. Thus, during late summer and early fall both penetrative convective mixing and wind mixing would be important. During early summer when the surface layers of the lake are warming and the rate of evaporation is low, the lake experiences very little convective activity (except for the diurnal effects). Hence wind mixing is the dominant mixing process. The importance of different mixing agents during different seasons of the year is further discussed in Chapter 7.

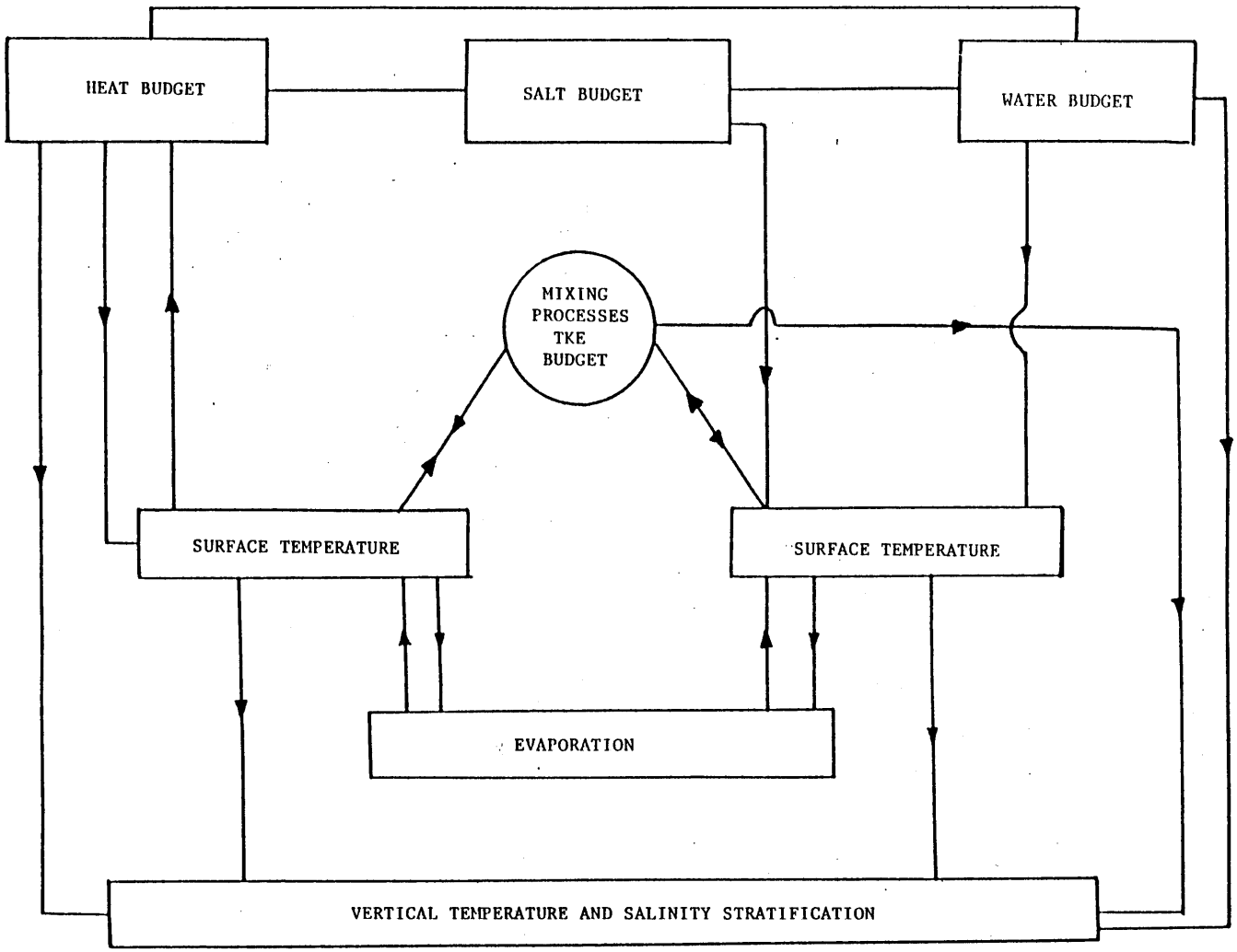

Fig. 3.1 Coupling of The Heat, Salt, Water and TKE Budgets for a Saline Lake

Fig. 3.1 also shows the feedback effect that exists between evaporation and surface temperature. An increase in evaporation during a time period, for example, due to high wind speed and/or low humidity, tends to decrease the water surface temperature and hence reduce evaporation in the subsequent period and vice-versa. (see also Section 6.3.5 and 10.4). Also, evaporation results in an increase in surface salinity that adversely affects the rate of evaporation. These negative feedbacks introduce a non-linearity in the lake's response to atmospheric forcing functions. Thus, a given increase in the wind speed does not increase the rate of evaporation by an equivalent amount. (Salhotra et. al. (1981)).

3.3 Mathematical Model

The model used to study the vertical stratification and the evaporative water loss from the Dead Sea requires the solution of water, salt and heat balance equations in conjunction with an appropriate mixing algorithm. Assuming the Dead Sea to be horizontally homogenous with inflows (I) and outflows (O) occurring at the surface only, the three balance equations can be written as:

$$\frac{dV}{dt} = I - O \tag{3.1}$$

$$\frac{\partial}{\partial t}(\rho C_p T) = \frac{1}{A}\frac{\partial}{\partial z}\left[A\, k_T \frac{\partial}{\partial z}(\rho C_p T)\right] - \frac{1}{A}\frac{\partial}{\partial z}(A\, \phi_{sn}) \tag{3.2}$$

$$\frac{\partial}{\partial t}(\rho S) = \frac{1}{A}\frac{\partial}{\partial z}\left[A\, k_S \frac{\partial}{\partial z}(\rho S)\right] \tag{3.3}$$

where, t = time (days), A = the area of the lake (m^2), V = the volume of the lake (m^3), ρ = the density of the lake (kg/m^3) that is a function of

lake temperature and salinity, k_T = the thermal diffusion coefficient (m^2/day), C_p = heat capacity of the brine (KCal/kg-°C), k_S = the salt diffusion coefficient (m^2/day), ϕ_{sn} = the net incoming short wave solar radiation (KCal/m^2-day), and z = the vertical distance (positive upwards). In eq. 3.3, S is expressed in weight units, i.e., weight of salt/weight of solution.

The initial conditions for the above equations are the observed water surface elevation, temperature and salinity profiles. Important characteristics of the observed profiles for the top 40 m of the lake since 1979 have been analyzed in Section 2.3 and are further discussed in Chapter 9.

In all, four boundary conditions are required. These are the heat and salt conditions at the bottom and surface of the lake. The bottom boundary conditions at 440 mbsl (see also Section 2.3) are:

$$z = 0, \qquad \rho C_p T = \text{constant} \tag{3.4}$$

$$z = 0, \qquad \rho S = \text{constant} \tag{3.5}$$

At the water surface, the boundary conditions reflect the exchange of heat and fresh water (evaporation and inflows) with the ambient. The conditions can be represented as:

$$z = z_s, \quad k_T \frac{\partial}{\partial z}(\rho C_p T) = \beta \phi_{sn} + (\phi_{ac} - \phi_{ar}) - \phi_b - (\phi_e + \phi_c) + \phi_i \tag{3.6}$$

$$z = z_s, \quad k_S \frac{\partial}{\partial z}(\rho S) = \left[\frac{\phi_e}{\rho_s L_s} - q_s\right] \rho S \tag{3.7}$$

where the subscript s refers to the lake surface, β = the fraction of the

net incoming short wave radiation absorbed in the top few millimeters of the lake, ϕ_{ac} = the atmospheric long wave radiation, ϕ_{ar} = reflected portion of atmospheric radiation, ϕ_b = the back (long wave) radiation from the lake surface, ϕ_c = the sensible heat-flux, ϕ_e = the evaporative heat flux, ϕ_i = the advective heat flux, L_s = the latent heat of vaporization of the surface water (KCal/kg-°C) and q_s = the fresh water inflow or rain at the surface (m/day). Note all the thermal energy flux terms are expressed in KCal/m^2/day and discussed in detail in Chapters 5 and 6.

In addition to the above set of differential equations, the model includes a mixing algorithm based on the parameterization of the turbulent kinetic energy budget. The sources of kinetic energy are wind stirring, penetrative convection and shear generation. The sinks include the leakage of turbulent energy into the hypolimnion by internal waves, storage in the mixed layer and viscous dissipation. The remaining energy, sum of sources less the sum of sinks is available for entraining heavier fluid from the hypolimnion into the upper mixed layer thereby increasing the potential energy of the lake. The mechanical energy budget is discussed in detail in Chapter 7.

The above set of equations coupled with the mixing algorithm are solved using an explicit finite difference scheme. This requires the discretization of the lake into horizontal layers (Stefan and Ford, 1975) and the use of a discrete time step. It should be borne in mind that this numerical scheme involves both truncation errors, due to neglect of higher order terms in the Taylor Series expansion, as well as round-off errors. Also, the scheme is not unconditionally stable and requires a

restriction on the relative size of spatial and temporal discretization. Details of these are not discussed here as they are available in most textbooks on numerical methods.

A flow diagram of the model is shown in Fig. 3.2. Appendix 1 contains a brief description of the various subroutines and their interactions. It should be emphasized that the model has been developed, very closely, along the lines of Massachusetts Institute of Technology Reservoir Stratification Model (Hurley-Octavio, et. al. 1977) and the Massachusetts Institute of Technology Solar Pond Program (Atkinson et.al. 1983).

An important addition to the model includes the effect of expansion and contraction of the water column due to heating and cooling. This enables the model to accurately compute the mass and salt budgets for the lake. The former is particularly important for bookkeeping the potential energy changes associated with covective mixing i.e. the removal of any density instabilities by mass and thermal energy conserving rearrangement. Even slight errors in the computation of mass can result in very large errors in potential energy and hence the mechanical energy budget.

3.4 Functional Relationships, Data Requirements and Model Parameters

Application of the above model requires a number of lake-specific functional relationships. These include relationships that depend on the physical-chemical properties of the lake water such as an equation of state, specific heat capacity, the effect of salinity and ionic composition on the evaporative heat flux, effective latent heat of vaporization for saline waters and heat and salt diffusion coefficients.

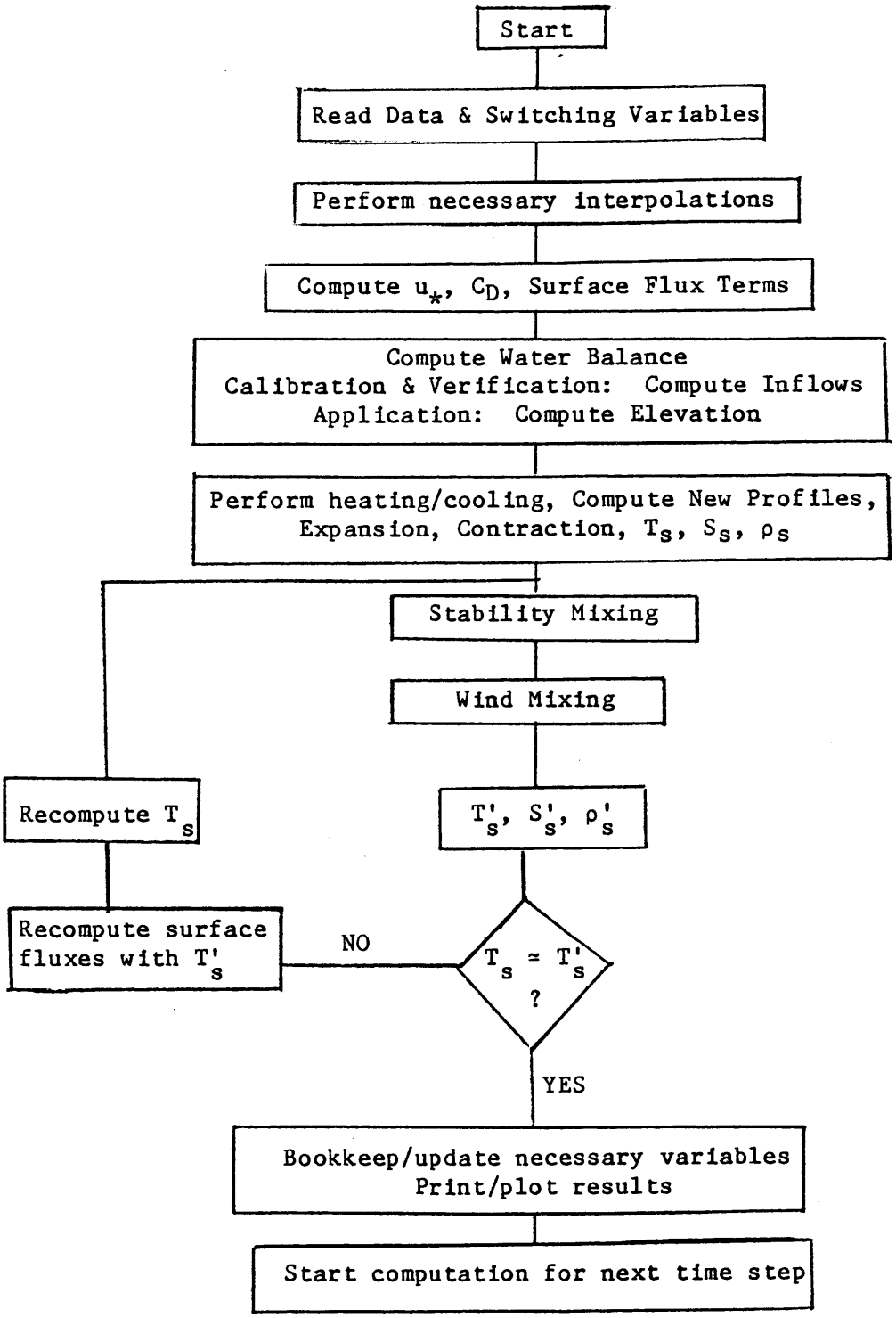

Fig. 3.2 Flow Diagram of The Dead Sea Computer Model

Of these the effect of salinity and ionic composition of brine on evaporation was studied in detail and is included in Chapter 6. Other functional relationships, including the lake depth-area relationship are included in Appendix B.

In addition to these relationships, meteorological data are required at each time step to calculate the surface heat flux terms. These data include measurements of wind speed, air temperature, relative humidity, cloud cover, solar short wave and atmospheric long wave radiation. These are discussed in detail in Chapter 4 and Chapter 5 respectively.

Finally, the model includes calibration coefficients associated with the mixing algorithm. These are discussed in Chapter 7. Data on lake elevations and pumpage of brine by the salt works are included in Chapter 8. Model calibration and verification is discussed in Chapter 9. Finally, the application of the model with the hydro-power project in operation is addressed in Chapter 10.

CHAPTER 4

THE DEAD SEA METEOROLOGY

4.1 Introduction

The air temperature, humidity and wind speed to a large extent determine evaporation as well as the magnitude of mixing processes. These are indeed the primary variables/inputs to the model. Accurate knowledge of these can also be used to compute the surface flux terms, i.e., the other atmospheric forcing variables. This chapter presents an analysis of the meteorological data that was made available by the Mediterranean Dead Sea Company (1983) and by Dr. Stanhill (1984).

A historical perspective of meteorological measurements at the Dead Sea has been reported by Stanhill (1980). Since 1984, The Israel Meterological service has operated eight standard climatological stations in the immediate vicinity, approximately at shore level, of the Dead Sea. These stations are operated in accordance with internationally recognized practice. The data analyzed in Sections 4.2, 4.3 and 4.4, from the station located at Kalia, at the north shore of the Dead Sea is one such station. In addition, a number of non-standard special stations have been established on the shores of the Dead Sea by various research organizations in Israel. An example of such a station is the one operated by Dr. Stanhill at Quidron, on the north western shore of the Dead Sea. This station was set up to primarily study the incident solar short wave and atmospheric long wave thermal energy fluxes of the Dead Sea (See also Chapter 5). Simultaneous measurements of meterological

variables including air temperature, humidity and wind speed at this station are also discussed in subsequent sections.

4.2 Air Temperature Measurements

Daily air temperature values are used in the model to compute vapor pressure gradient for the computation of evaporation (eq. 6.5) and to compute the atmospheric radiation (Section 5.3). The latter is one of the most important terms in the heat budget equation.

Air temperature data at six hourly intervals -- 08, 14, 20, and 02 hours -- were made available for the period from October 1979 to December 1982--a period of 39 months. Fig. 4.1 shows the daily averaged data for the period October 1979 to September 1980. The seasonal trend, with minimum temperatures in January and maximum in July-August, is clearly visible. The daily averaged temperatures ranged from 10°C to 37°C. The six hourly measured data shows a larger variation from 7°C to 40°C for the same period.

Table 4.1 shows the mean monthly values of air temperature as well as the range based on six hourly measurements (daily values for Stanhill's data). As expected there is little inter-year variability. Seasonal variability is again apparent. Also included in Table 4.1 is the monthly mean and range of air temperature values measured at Quidron. During the winter months, temperatures measured at Quidron are about 2°C to 4°C higher than those measured at Kalia for the same months in previous year. Also the annual mean air temperature is about 1.5°C higher than the annual mean values for the previous years. Since simultaneous measurements (July 1983 to June 1984) are not available for the Kalia station, it is not clear whether this difference represents

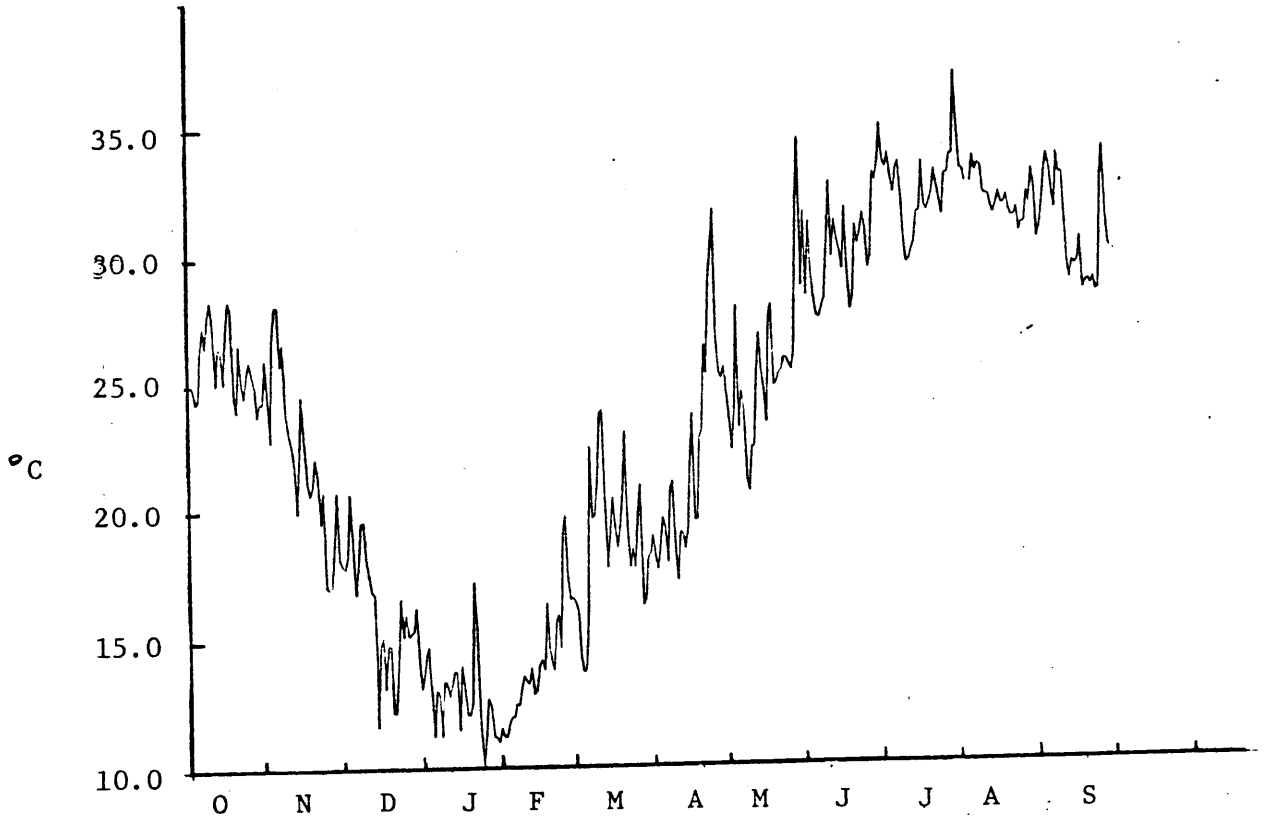

Fig. 4.1 Daily Air Temperature for the Dead Sea (1979-80)

TABLE 4.1 Range and monthly mean values of air temperature for the Dead Sea (1979-1984)

AIR TEMPERATURE °C

	1979		1980		1981		1982		1983*		1984*	
	Mean	Range	Mean	Range	Mean	Range	Mean	Range	Mean	Range	Mean	Range
JAN			13.08	5.0-22.5	12.51	5.5-23.0	15.35	2.8-24.7			17.55	15-20
FEB			14.81	7.0-24.5	14.68	7.2-26.0	14.73	5.8-25.0			19.58	18-23
MAR			17.91	7.0-34.5	18.95	8.4-31.0	17.37	8.0-29.7			19.42	15-23
APR			23.39	10.8-39.8	22.32	11.0-39.0	24.24	10.0-38.5			23.01	21-25
MAY			27.97	16.0-50.0	25.70	14.0-44.5	26.86	15.5-39.8			28.33	24-33
JUN			30.83	19.5-47.5	30.38	20.4-43.5	30.05	20.0-40.4			30.02	29-32
JUL			32.26	23.4-43.0	32.43	23.5-45.0	31.72	23.0-42.0	32.52	30-34		
AUG			32.18	23.8-41.0	31.96	24.0-39.0	32.42	25.5-42.0	32.63	31-35		
SEP			28.33	20.0-40.0	30.61	22.0-42.5	30.77	23.0-41.0	30.77	29-34		
OCT	25.82	17.5-37.5	25.76	17.5-37.8	27.67	17.5-40.0	27.37	19.0-36.5	27.12	24-30		
NOV	21.01	11.0-31.0	21.61	11.0-34.6	18.41	8.0-30.0	18.52	11.0-31.0	23.26	19-29		
DEC	15.13	8.0-23.7	15.66	7.8-29.0	16.67	7.4-27.0	14.40	9.0-23.0	18.53	16-21		
MEAN			23.65	5-50	23.52	6.45	23.65	3-42			25.23**	15-35

* Data from Dr. Stanhill's station at Quidron

** Mean for period July 1983 to June 1984

areal variability or inter-year temporal variability.

4.3 Relative Humidity Measurements

Daily relative humidity values are used in the model to compute vapor pressure gradient for the computation of evaporation (eq. 6.5). Also, some of the relationships that can be used to compute the atmospheric longwave radiation require vapor pressure of the air. This can be obtained from humidity and air temperature data.

Relative humidity measurements at six hourly intervals -- 08, 14, 20 and 02 hours -- were made available for the period from October 1979 to September 1980. Fig. 4.2 shows a plot of daily mean values for a one year period, October 1979 to September 1980. The seasonal trend with relatively high values during the wet, cold winter months and low values during the hot summer months is apparent. Daily mean values range mostly from 40% to 60% except during winter months when values reach as high as 85%. The variation based on six hourly measured values, shown in Table 4.2 is obviously much larger.

Table 4.2 includes the monthly mean values of relative humidity for the four years. Seasonal variability as well as some inter-year variations are apparent. For example, the wet winters of 1979/80 and 1980/81 show as much as 10% higher values than the dry 1982 winter. The relative humidity values for July 1983 to June 1984 were calculated using air temperature and vapor pressure (e_a) data reported by Stanhill (1984) using the following relation:

$$\phi = \frac{e_a}{e_{sat}(T_a)} \qquad (4.1)$$

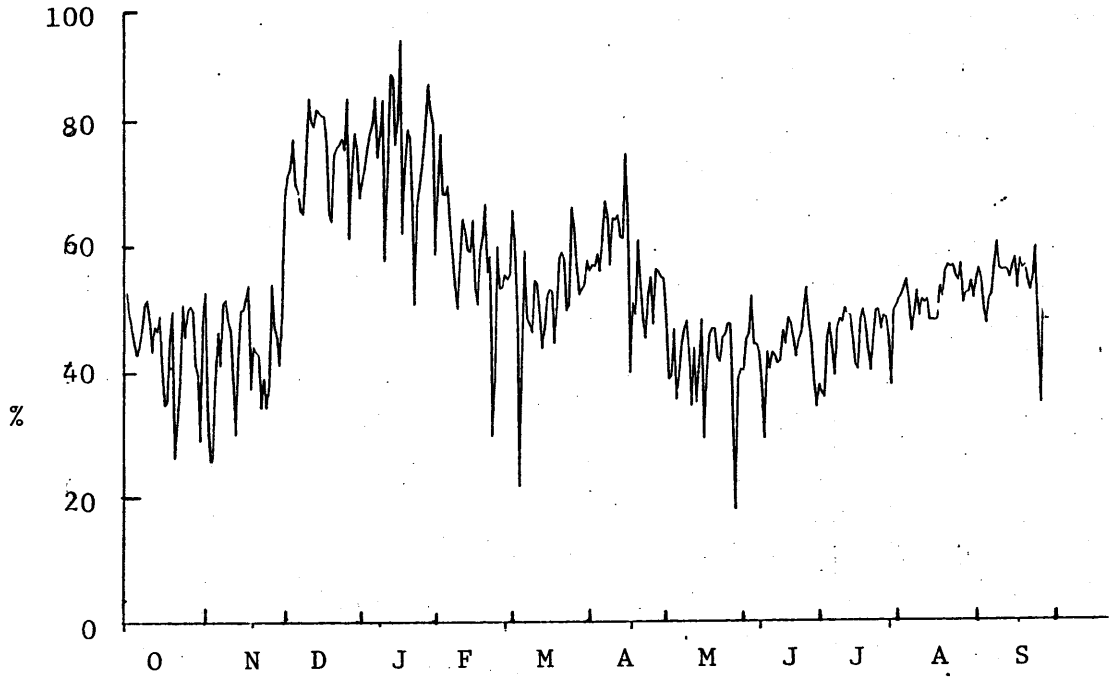

Fig. 4.2 Daily Relative Humidity for The Dead Sea (1979-80)

TABLE 4.2 Range and monthly mean values of relative humidity for the Dead Sea(1979-1984)

RELATIVE HUMIDITY %

	1979		1980		1981		1982		1983*		1984*	
	Mean	Range	Mean	Range	Mean	Range	Mean	Range	Mean	Range	Mean	Range
JAN			52.68	12-83	74.76	39-98	60.85	19-83			55.28	42-78
FEB			48.58	9-60	58.04	19-97	63.10	26-84			44.08	33-65
MAR			69.19	30-91	52.12	13-78	59.28	14-84			51.31	33-52
APR			54.37	23-90	57.17	24-92	50.48	17-78			42.58	34-52
MAY			43.49	5-75	41.64	6-76	56.19	34-78			35.39	15-46
JUN			40.63	5-66	43.30	14-67	53.54	29-78			37.57	27-47
JUL			43.86	17-66	45.52	17-68	47.10	21-75	39.30	32-45		
AUG			47.92	15-67	52.23	30-72	50.61	25-69	38.83	30-56		
SEP			49.21	9-67	53.64	13-76	53.25	23-75	41.80	33-47		
OCT	54.54	16-79	44.07	8-66	54.92	23-79	47.37	19-74	43.36	21-54		
NOV	58.84	25-86	42.46	16-64	56.95	21-85	55.77	22-80	55.96	27-75		
DEC	72.82	39-85	73.25	40-86	62.34	30-83	62.41	19-80	55.17	33-75		
MEAN			50.81	5-91	54.39	6-98	55.00	14-84		15-78	45.05**	

* Data from Dr. Stanhill's Station at Quidron

** Mean for period July 1983 to June 1984

where, $e_{sat(T_a)}$ was obtained using eq. (6.16). During the summer months, the monthly mean values of relative humidity for 1983/84 are about 10%-20% lower than for the previous year. Also, the annual mean relative humidity values for 1983/84 are lower than the annual means for the previous three years. As in the case of air temperature values, it is not clear whether this is due to areal or inter-year temporal variability.

4.4 Analysis of Wind Speed

4.4.1 Wind Speed Measurements

Daily wind speed values are used in the model to compute evaporation (eq. 6.5) and to determine kinetic energy available for entrainment due to wind mixing. The latter is proportional to the third power of wind speed and hence the effect of temporal averaging is important. This aspect is discussed in detail in Section 4.4.2.

Wind speed data from Kalia measured at 2-m height at hourly intervals was made available for the period November 1979 to December 1982. Daily as well as six hourly averaged data is shown in Fig. 4.3(a) and Fig. 4.3(b) respectively. On an annual level, no significant trend is apparent. For most days, the daily mean values range between 2 m/s and 4 m/s. Days with highest wind speeds occur in the winter when daily values reach as high as 7 m/s - 10 m/s. Also, the six hourly mean values show a much greater variability than the daily mean values.

Table 4.3 shows the monthly mean as well as the range of wind speed values for the four years. Data for the period July 1983 to June 1984, from Stanhill's station at Quidron, is measured at 3.3 m height. Assuming a value of z_o = .01 mm, (roughness height representative of

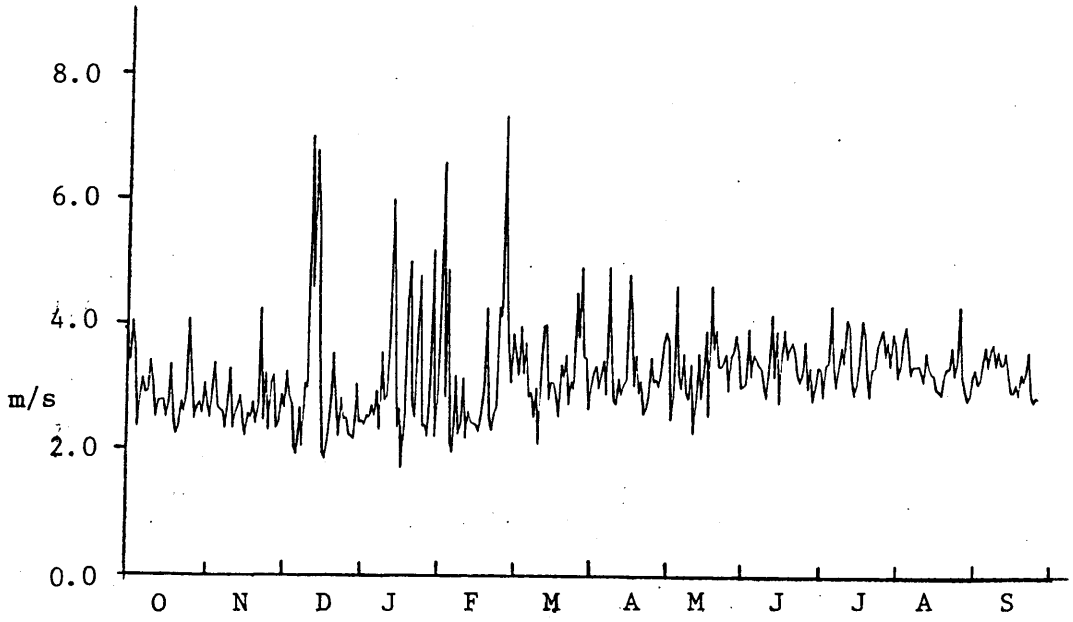

Fig. 4.3(a) Daily Wind Speed for The Dead Sea (1979-80)

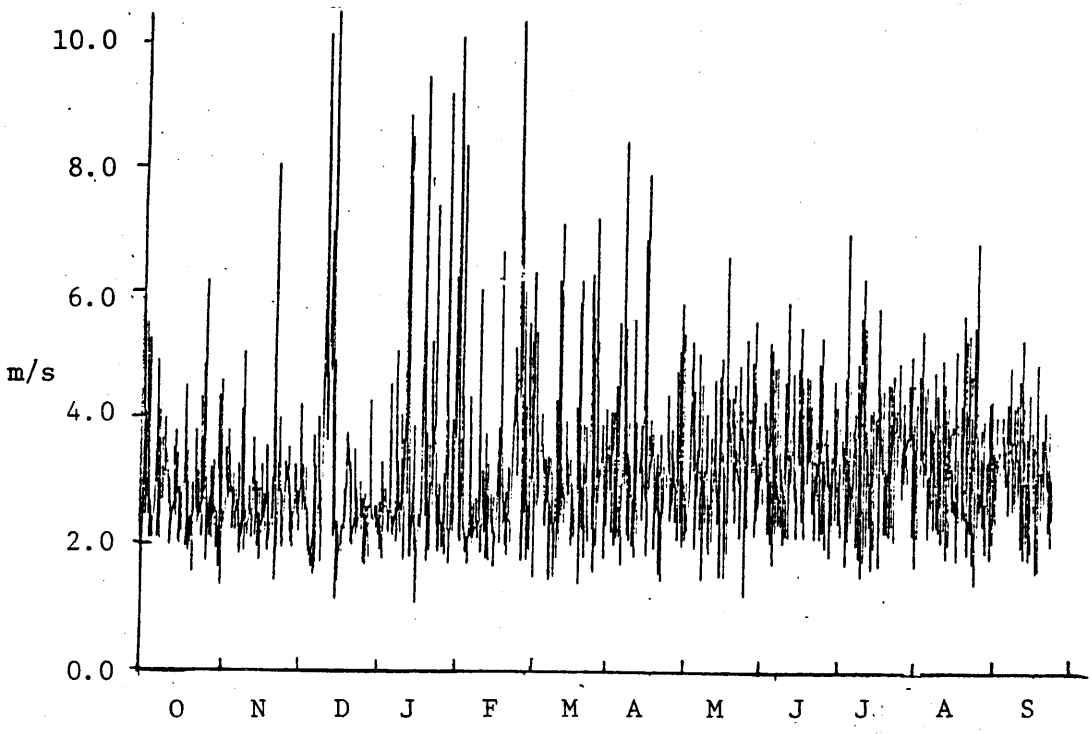

Fig. 4.3(b) Six Hourly Wind Speed for The Dead Sea (1979-80)

TABLE 4.3 Range and monthly mean values of wind speed for the Dead Sea (1979-1984)

WIND SPEED m/s

	1979		1980		1981		1982		1983*		1984*	
	Mean	Range	Mean	Range	Mean	Range	Mean	Range	Mean	Range	Mean	Range
JAN			2.92	1.27-9.35	3.30	1.05-10.12	2.90	1.43-8.33			2.88	1.6-6.1
FEB			2.83	1.25-7.70	3.14	1.63-10.28	2.91	1.40-9.58			2.90	1.8-5.0
MAR			3.12	1.67-7.93	3.26	1.37-7.22	2.96	1.45-5.15			2.99	1.4-4.6
APR			3.27	1.32-6.82	3.28	1.42-6.87	3.27	1.83-7.17			2.51	1.5-3.7
MAY			3.38	1.47-6.17	3.31	1.17-6.60	3.45	1.32-5.55			2.52	1.7-3.2
JUN			3.30	1.58-5.43	3.35	1.68-5.88	3.30	1.72-5.42			2.80	1.9-3.0
JUL			3.37	1.22-6.47	3.47	1.48-6.98	3.50	1.50-6.10	3.10	1.2-4.2		
AUG			3.19	1.50-5.32	3.27	1.60-6.60	3.28	1.63-6.03	2.81	2.6-3.9		
SEP			3.02	1.48-5.28	3.14	1.55-5.30	3.08	1.70-5.13	2.70	2.0-3.5		
OCT			2.89	1.33-5.53	2.75	1.77-4.58	2.72	1.92-5.03	2.80	2.0-4.3		
NOV	2.94	1.52-8.83	2.70	1.40-8.07	2.86	1.62-6.98	2.93	1.28-7.22	2.43	1.6-4.9		
DEC	3.48	1.48-10.93	2.97	1.10-10.52	2.67	1.52-7.17	2.75	1.12-9.35	2.53	1.7-5.1		
MEAN			3.08	1.1-10.5	3.15	1.1-10.3	3.09	1.1-9.6			2.75**	1.2-6.1**

* Data from Dr. Stanhill's Station at Quidron

** Mean for period July 1983 to June 1984

mud flats) these wind speed values have to be reduced by a factor of 0.96 to make them comparable to the 2-m measurement height for the data from Kalia (eq. 6.2). For z_o = 1 mm (roughness height representative for grass), the corresponding factor is 0.93. In general the wind speed values at Quidron are lower than those from Kalia, possibly due to shading effect of a nearby groove.

4.4.2 Kinetic Energy Input by Wind

The energy input due to wind is proportional to the cube of the wind speed (Section 7.3.2). Therefore, kinetic energy computed using different averaging periods can result in significantly different values. An equivalent mean wind speed for period N that accounts for this non-linear effect can be defined as:

$$W_{ei} = \left[\frac{1}{N} \sum_{j=1}^{N} (W_i^3)_j \right]^{1/3} \qquad (4.2)$$

where, i = averaging period, W_{ei} = the equivalent mean wind speed for period N based on the averaging period i and W_i = representative mean wind speed for period i. This representative wind speed is obtained either by direct measurements at intervals of i or by averaging values measured over periods of duration less than i.

Monthly equivalent mean wind speeds with i = 1, 6, 12 and 24 hours are shown in Tables 4.4(a) to 4.4(c) for the period November 1979 to December 1982. For example, W_{e1} is obtained by summation of the cubes of hourly wind speed values divided by (24 x K) where K is the number of days in the month and taking the cube root of this quantity. Similarly W_{e6} is obtained by the summation of the cubes of six hourly mean wind

TABLE 4.4(a) The effect of temporal averaging on the kinetic energy input by wind (1979-1984)

1979	$\bar{W}_{e1}$	$\bar{W}_{e6}$	$\bar{W}_{e12}$	$\bar{W}_{e24}$	r_1	r_6	r_{12}
NOV	3.85	3.69	3.60	3.52	1.31	1.15	1.07
DEC	4.85	4.56	4.40	4.09	1.67	1.39	1.25
1980							
JAN	4.05	3.89	3.75	3.57	1.46	1.29	1.16
FEB	3.67	3.40	3.32	3.22	1.48	1.18	1.10
MAR	3.81	3.60	3.52	3.32	1.51	1.27	1.19
APR	3.92	3.67	3.54	3.34	1.62	1.33	1.19
MAY	3.82	3.59	3.51	3.43	1.38	1.15	1.07
JUN	3.69	3.47	3.41	3.33	1.36	1.13	1.07
JUL	3.92	3.63	3.53	3.42	1.51	1.20	1.10
AUG	3.68	3.43	3.31	3.21	1.51	1.22	1.10
SEP	3.44	3.25	3.10	3.04	1.45	1.22	1.06
OCT	3.44	3.19	3.09	2.97	1.55	1.24	1.13
NOV	3.17	2.97	2.91	2.77	1.50	1.23	1.16
DEC	4.16	3.89	3.79	3.58	1.57	1.28	1.19
MEAN	3.73	3.50	3.40	3.58	1.49	1.23	1.13

TABLE 4.4(b) The effect of temporal averaging on the kinetic energy input by wind (1981)

1981	$\bar{W}_{e1}$	$\bar{W}_{e6}$	$\bar{W}_{e12}$	$\bar{W}_{e24}$	r_1	r_6	r_{12}
JAN	4.52	4.29	4.15	3.74	1.77	1.51	1.37
FEB	4.31	4.05	3.98	3.59	1.73	1.44	1.36
MAR	4.04	3.74	3.63	3.37	1.72	1.37	1.25
APR	4.00	3.74	3.61	3.39	1.64	1.34	1.21
MAY	3.87	3.61	3.49	3.40	1.47	1.20	1.08
JUN	3.81	3.59	3.53	3.39	1.42	1.19	1.13
JUL	3.97	3.75	3.66	3.51	1.45	1.22	1.13
AUG	3.77	3.54	3.42	3.31	1.48	1.22	1.10
SEP	3.48	3.31	3.23	3.17	1.32	1.14	1.06
OCT	3.07	2.89	2.85	2.77	1.36	1.14	1.09
NOV	3.54	3.27	3.23	2.99	1.66	1.31	1.26
DEC	3.19	3.03	2.86	2.80	1.48	1.27	1.07
MEAN	3.80	3.57	3.47	3.29	1.54	1.28	1.18

TABLE 4.4(c) The effect of temporal averaging on the kinetic energy input by wind (1982)

1982	$\bar{W}_1$	$\bar{W}_{e6}$	$\bar{W}_{e12}$	$\bar{W}_{e24}$	r_1	r_6	r_{12}
JAN	3.63	3.41	3.34	3.21	1.45	1.20	1.13
FEB	3.93	3.77	3.48	3.33	1.64	1.45	1.14
MAR	3.51	3.28	3.17	3.02	1.57	1.19	1.16
APR	3.74	3.55	3.46	3.34	1.40	1.20	1.11
MAY	3.93	3.72	3.65	3.48	1.44	1.22	1.15
JUN	3.64	3.48	3.40	3.31	1.33	1.16	1.08
JUL	4.00	3.81	3.75	3.54	1.44	1.25	1.19
AUG	3.72	3.54	3.48	3.32	1.41	1.21	1.15
SEP	3.44	3.26	3.20	3.11	1.35	1.15	1.09
OCT	2.98	2.84	2.80	2.74	1.29	1.11	1.07
NOV	3.54	3.31	3.19	3.08	1.52	1.24	1.11
DEC	3.34	3.19	3.01	2.88	1.56	1.36	1.14
MEAN	3.62	3.43	3.33	3.20	1.45	1.23	1.13

speed values divided by (4 x K) and then taking the cube root of this quantity.

Based on the above, $\bar{r}_i$, the monthly mean of the daily ratios of equivalent kinetic energy for averaging period i to the kinetic energy computed based on daily mean values, can be computed using:

$$\bar{r}_i = \frac{1}{K} \sum_{m=1}^{K} \left(\frac{W_{ei}^3}{W_{e24}^3} \right)_m \qquad (4.3)$$

Clearly, the larger the variation in the wind speed values (W_i) used in the computation of W_{ei}, the larger is $\bar{r}_i$. Thus, the winter months that exhibit a larger varitaion in wind speeds, Fig. 4.3(a) and Fig. 4.3(b), have a higher $\bar{r}_i$ value than the summer months with less variability in the wind speeds. Also, the smaller the averaging period, i, the larger the variation in W_i (compare Fig. 4.3(a) and Fig. 4.3(b)). From the above it follows that the equivalent wind speeds W_{e1}, W_{e6}, W_{e12}, and W_{e24} as well as $\bar{r}_1$, $\bar{r}_6$ and $\bar{r}_{12}$ should always be in a descending order of magnitude. This is clearly shown in Tables 4.4(a) to 4.4(c).

The inter- and intra-year variability in the $\bar{r}_i$ values is shown in Tables 4.4. In general, kinetic energies based on hourly wind speed values is approximately 50% higher than those based on daily mean wind speed values. Corresponding numbers for 6 and 12 hourly wind speed values are 20% and 15% respectively. Clearly the effect is not negligible.

With reference to the model results discussed in Chapter 9, using a daily time step and daily mean wind speeds, the effect of non-linearities

is accounted for by the calibration coefficient C_w. However, the effect of non-linearities on C_w is not proportional, i.e., a calibrated value of $C_w = 6$ for a model using W_{e24} would not be equivalent to a $C_w = 6/\bar{r}_1$ for a model that uses W_{e1}. Use of W_{e24} would result in a different "sequence of evolution" of the pycnocline than the one obtained using W_{e24}. It is worth mentioning that this effect of time interval used for averaging is inherent in any model/system with non-linear inputs. For example, lake circulation models in which wind shear stress is one of the surface boundary conditions would also involve similar "errors" due to temporal averaging.

CHAPTER 5

THE RADIATIVE HEAT FLUX AT THE WATER SURFACE

5.1 Introduction

Accurate knowledge of the energy flux terms at the surface of water bodies is required for many engineering analyses. These include the computation of evaporation from a water body using the energy budget method; hydrothermal modelling of lakes, reservoirs and cooling ponds; a variety of agricultural purposes and the analysis of numerous solar energy collection devices. In each of these cases the emphasis is on different aspects/terms of the surface heat flux budget. For modelling a vertically stratified water body, eq. 3.6 (repeated below for reference) has to be satisfied as the thermal condition at the air-water interface.

$$k_T \frac{\partial}{\partial z} (\rho C_p T) = \beta \phi_{sn} + (\phi_{ac} - \phi_{ar}) - \phi_b - (\phi_e + \phi_c) + \phi_i \qquad (3.6)$$

(for explanation of terms see eq. 3.6)

Of the various terms included in eq. 3.6, the atmospheric longwave radiation (wavelengths 4 to 50 μm) is generally the largest supplier of energy to the water body followed by the short wave component (wavelength < 4 μm). The magnitude of the back radiation term depends on the water surface temperature. For highly saline lakes such as the Dead Sea, that exhibit surface temperatures higher than fresh water

lakes subjected to identical meteorological forcing functions (see Section 6.3.3), the back radiation term may be larger than the atmospheric radiation term. These radiative flux terms are discussed in detail in the following sections. The only other important component (both for heat and water balance computations) in eq. 3.6 is the evaporative flux term. This is affected by the surface water temperature, salinity and meteorological variables and is discussed in detail in the following chapter. The remaining components -- advective and conductive terms -- are of relatively less significance.

5.2 Incident Short Wave Radiation, ϕ_{sc}

5.2.1 Clear Sky Short Wave Radiation, ϕ_s

The short wave radiation reaching the earth's surface also referred to as the global solar radiation, originates from the thermonuclear reactions that proceed deep within the sun at about 6000°K. The energy flux density of this outward radiation is 70×10^6 W/m^2 and diminishes outwards with the square of the distance from the sun to 1375 W/m^2 at the mean distance of the earth. The latter is also referred to as the extra-terrestrial solar radiation. This energy is emitted over a range of frequencies with the wavelength (λ) varying from 0.3 μm to several thousand μm. Of the total energy flux, 50% is concentrated in the infra-red range ($\lambda > 0.7$ μm), 40% in the visible range (0.4 $\mu m \leq \lambda \leq 0.7$ μm) and the remaining 10% in the ultra-violet range ($\lambda < 0.4$ μm). (Miller, 1981)

As the extra-terrestrial solar radiation passes through the earth's atmosphere, it is absorbed and scattered by the air molecules, water-vapor, dust, aerosols and other particles in the atmosphere.

This process of absorption and scattering is very complex and depends on the size, shape and density of the particles, the chemical nature of the aerosols and their effective refractive indicies. Consequently, the short-wave solar energy reaches the earth's surface after being attenuated by the atmosphere, partly as direct radiation and partly as diffuse radiation.

A commonly used instrument for the measurement of direct-beam solar radiation only is the pyrheliometer. The sum of direct and diffuse radiation that is of relevance in hydrothermal modelling, can be measured using the pyranometer with an accuracy of up to $\pm$ 3%.

In the absence of direct measurements, one of the many available empirical formulae or graphs could be used. Details of these are given by Wunderlich (1972) and Hamon et. al. (1954). However, most of these are site-specific to the extent that they contain empirical coefficients calibrated with data from a particular or a set of sites. Further, these yield clear sky radiation values that have to be corrected to account for the attenuating effect of clouds.

5.2.2 The Effect of Clouds on Short Wave Radiation

Various empirical formulae have been proposed relating solar radiation under cloudy skies to that under clear skies. These relations are of the form:

$$\phi_{sc} = f(C)\ \phi_s \qquad (5.1)$$

where f(C), [$f(C) \leq 1.0$], is a function of the cloud cover C expressed in tenths of sky covered. The function f(C) typically accounts for only

the areal extent or the duration of cloud cover. Other important factors such as the type, areal variability, thickness, altitude and the characteristics of the water droplets and ice particles that constitute the cloud are not included. The cummulative effect of all these factors is accounted for by one or more calibration coefficients in the formulation of f(C).

As mentioned above, the characteristics of the clouds included in relations of the form shown in eq. 5.1 is either the extent (C) or the duration of clouds. The former is expressed as the percentage of the total sky covered by clouds and relies on visual observation of the sky a few times a day. At best this results in a subjective estimate.

The measure of duration of clouds is expressed as the ratio of observed hours of sunshine duration n on a cloudy day to the maximum possible sunshine hours N on a clear day. Unlike the previous measure of cloudiness, this measure is less subjective but does not account for the areal variability of the clouds. The relation between the cloud cover and percent sunshine, obtained from observed values of cloud cover and sunshine in several locations in Tennessee and Alabama is (TVA 1972):

$$\frac{n}{N} = 1 - C^{5/3} \qquad (5.2)$$

Note the value of C and n/N both lie between 0 and 1.

Depending upon the form of the function f(C), the empirical (regression type) relations to calculate ϕ_{sc} can be grouped into two

categories. The first assumes a linear variation of ϕ_{sc} with cloud cover and second a non-linear polynomial type relationship. A comprehensive list of these formulae is included in Paily, et al. (1974).

One of the most popular relationships for f(C) developed by TVA (1972) is of the form:

$$f(C) = (1 - kC^2) \tag{5.3}$$

where k is a site specific calibration coefficient. Wunderlich (1972) has recommended a value of k = 0.65, resulting in a maximum reduction of 35% for an overcast sky in comparison to clear sky short wave radiation. To the extent that k is a site specific coefficient and that at best an approximate value of C is available, the cloud correction is very approximate. Thus, whenever possible, site specific (historic) measured values of short wave radiation are to be preferred with due recognition of the fact that significant variability may occur in future due to variations in the clouds.

5.2.3 Reflection, Absorption and Penetration of Short Wave Radiation in Water

The short wave solar radiation reaching the surface of water is partly reflected, a fraction is absorbed at the surface and the remaining portion is transmitted into the water body. The percent reflected depends on the wavelength, the angle of incidence and hence season and latitude of the water body. A detailed study conducted at Lake Hefner (Anderson, 1954) yielded monthly mean values shown in Table 5.1. On an annual average, only about 6% of the incoming short wave radiation is reflected. Since this is small, errors in the

reflectivity of water are not likely to have a considerable influence on the overall heat budget.

Table 5.1 Percentage of Incoming Solar Radiation Reflected at the Water Surface (Ref. 3)

Month	J	F	M	A	M	J	J	A	S	O	N	D
% reflected	9	7	7	6	6	6	6	6	7	7	9	10

A fraction (β) of the incoming solar radiation is absorbed in the top few millimeters of the water body. For natural water bodies the value of β is about 0.5. The penetration of radiation energy into the water body can be represented as (Dake and Harleman, 1969):

$$\phi(z) = \phi_s (1-r)(1-\beta)e^{-\eta z} \qquad (5.4)$$

where z = the depth below the water surface (m), r = fraction of incoming solar radiation reflect at the surface and η = the extinction coefficient (l^{-1}) that depends on the clarity of water. Recent interest in solar ponds has resulted in more sophisticated models for solar energy penetration in water (Cengel et. al. 1984 and Hull 1980).

5.2.4 Solar Radiation Measurements at The Dead Sea

Mean monthly values of short wave radiation for the Dead Sea are available from a number of different sources. These are compared in Table 5.2. Column 1 lists the data for 1981 measured at Ein Bokek and made available by the Mediterranean Dead Sea Company (1982). Column 2

Table 5.2

Mean Monthly Values of Short Wave Radiation For The Dead Sea
(Kcal/m^2-day)

Month	Ein Bokok (1)	Sedom (2) 31° 02N	Neumann (3)	Assaf (4)	Quidron (5)	Net Clear Sky (6) 31°N	Clear Sky (7) 31°N
Jan.	276	269	280	291	248	282	405
Feb.	292	344	339	365	368	322	485
Mar.	379	436	448	469	358	411	585
Apr.	430	538	601	601	485	525	675
May	540	620	636	652	581	625	730
June	617	651	770	691	638	695	740
July	557	654	734	674	640	713	725
Aug.	551	616	670	625	588	674	665
Sept.	565	529	610	553	507	589	575
Oct.	473	418	419	446	400	479	510
Nov.	316	291	307	330	284	373	420
Dec.	255	248	254	280	245	298	370
Mean	430	468	508	494	445	461	573
%	100	107	115	113	104	105	130

lists historically averaged data for Sedom used by Stanhill (1983) in his estimation of evaporation from the Dead Sea based on an energy budget. Columns 3 and 4 list historically averaged data reported by Neuman (1958) and Assaf (1980) respectively. Finally, Column 5 lists the monthly mean values computed from daily measured values (Stanhill, 1984) at Quidron for the period July 1983 to June 1984. On an annual average these values differ by a maxiumum of 15%. For numerical simulation, values reported in Column 2 and 5 were linearly interpolated to yield daily short wave radiation values. In order to effect good agreement between the observed and modelled heat budgets of the lake, a correction factor ranging from 5% to 15% (in one case 40%) was applied to these values. This is most likely due to inter-year variability in the attenuation of short wave radiation by the atmosphere or errors in the estimation of other terms in the heat budget. (See also Section 5.2.2 and Chapter 9.)

Column 6 and Column 7 list the clear sky global radiation values computed using empirical relationship developed by Thackston (1974) and Hammon et. al. (1954) respectively. It is to be noted that the values computed using Thackston's relation, column 6 are for net short wave radiation i.e. on an annual average they need to be increased by about 6% to yield values comparable to other entries in Table 5.2. Also, these values are derived for clear sky conditions and do not account for the attenuating effect of the clouds.

5.2.5 Penetration of Short Wave Radiation in the Dead Sea

The penetration of short wave radiation in the Dead Sea has been measured by Anati (1982-1984) on a number of occasions using a silicon

SOLAREX detector. Table 5.3(a) shows the solar radiation measured at various depths during May 1980 to June 1984. (These values have been obtained from solar energy penetration curves presented by Anati (1982-1984). Table 5.3(b) indicates the fraction of the solar energy at the surface reaching various depths. Column 12 and 13 indicate the mean and standard deviation of these measurements. About 15% of the incoming solar energy is absorbed in the top 0.1 m of the lake; about 45% in the top 0.5 m and a little over 60% in the top 1 m. About 14% of the surface radiation penetrates beyond 3 m. No temporal or seasonal variation is apparent from the data in spite of the occasional blooms of red halophylic bacteria or surface whitening observed during summer months due to salt precipitation. Using linear regression, a two parameter relationship, eq. 5.4, can be used to describe these measurements. The values of β and η and the corresponding R^2 value for the linear regression are also included in Table 5.3(b). A mean value of $\beta = .18$ and the extinction coefficient $\eta = .64$, with standard deviations of 0.04 and 0.05 respectively, fit the data well.

5.3 Atmospheric Long Wave Radiation, ϕ_{ac}

5.3.1 Radiation Under Clear Sky, ϕ_a

The passage of solar short wave radiation through the earth's atmosphere heats up the molecules and particles that constitute the atmosphere. These in turn radiate part of the absorbed energy. The temperature of the particles is much lower than that of the sun, therefore the energy is emitted at much longer wave lengths (4 μm-50 μm). This energy source is referred to as the atmospheric long wave radiation.

Table 5.3(a) Measurement of solar radiation penetration in the Dead Sea (Ref. 5)

($Kcal/m^2$-day)

z	1	2	3	4	5	6	7	8	9	10	11
0.0	700	650	750	675	825	625	420	550	700	862	820
0.1	675	525	600	600	730	450	360	430	625	715	705
0.5	385	340	375	362	525	275	225	290	400	470	450
1.0	275	200	260	250	350	200	175	200	240	320	330
1.5	200	-	-	200	275	160	130	125	205	240	270
2.0	-	-	-	-	225	130	100	100	185	190	210
2.5	-	-	-	-	-	100	90	80	120	140	160
3.0	-	-	-	-	-	80	70	55	100	-	130

1. May 27, 1980
2. Aug. 4-7, 1980
3. June 6, 1980
4. Oct. 29, 1981
5. July 20, 1982
6. Oct. 10, 1982
7. Oct. 18, 1982
8. Feb. 21, 1984
9. Apr. 2, 1984
10. May 16, 1984
11. June 12, 1984

Table 5.3(b) Analysis of solar radiation penetration in the Dead Sea

z	1	2	3	4	5	6	7	8	9	10	11	12	13
0.0	1.00	1.00	1.00	1.00	1.00	1.00	1.00	1.00	1.00	1.00	1.00	1.00	0.00
0.1	0.96	0.81	0.80	0.89	0.88	0.72	0.86	0.78	0.89	0.83	0.86	0.84	0.06
0.5	0.55	0.52	0.50	0.54	0.64	0.44	0.54	0.53	0.57	0.55	0.55	0.54	0.05
1.0	0.39	0.31	0.35	0.37	0.42	0.32	0.42	0.36	0.34	0.37	0.40	0.37	0.04
1.5	0.29	-	-	0.30	0.33	0.26	0.31	0.23	0.29	0.28	0.33	0.29	0.03
2.0	-	-	-	-	0.27	0.21	0.24	0.18	0.26	0.22	0.26	0.23	0.03
2.5	-	-	-	-	-	0.16	0.21	0.15	0.17	0.16	0.20	0.18	0.02
3.0	-	-	-	-	-	0.13	0.17	0.10	0.14	-	0.16	0.14	0.02
β	-	-	-	-	-	.267	.170	.179	.154	.138	.158	.173	-
η	-	-	-	-	-	.621	.573	.728	.636	.705	.584	.628	-
r^2(%)						94	96	98	96	98	97	97	

Column 1 to 11 See Table 5.3(a)

12 Mean of Columns 1-11
13 Standard Deviation

	β	η
Mean	.177	.04
Std. Dev.	.639	.05

Atmospheric long wave radiation depends on the absorption and radiation characteristics of various components of the atmosphere. Variations in the concentration of gases, aerosols, water vapor, temperature and cloud cover -- both the extent and type -- affect the intensity of the flux reaching the earth's surface. Due to random as well as seasonal variations in some or all of these factors, the radiative flux reaching the earth's surface is inherently difficult to predict accurately. The problem is further exacerbated by the lack of sufficient quantitative data on these factors. Typically the radiative characteristics of all these factors are lumped together in the clear sky emissivity (ε_a) given by

$$\varepsilon_a = \frac{\phi_a}{\sigma T_a^4} \qquad (5.5)$$

where, σ = Stefan-Boltzmann constant [1.171×10^{-6} KCal $m^{-2} {}^\circ K^{-4}$ day^{-1}], T_a = the air temperature expressed in degrees Kelvin and ϕ_a = the clear sky atmospheric radiation (KCal/m^2-day).

Numerous formulae have been proposed for computing the clear sky emissivity based on commonly measured meterological variables. These are essentially empirical formulae calibrated for a specific location and atmospheric conditions and therefore may not be of universal applicability. A brief review is included in Section 5.3.2.

5.3.2 Review of Formulae For Computing Clear Sky Atmospheric Radiation

Angstrom (1918, 1936) and Brunt (1932) related the atmospheric radiation to screen-level values of the vapor pressure e (mb) and air

temperature T_a(°A) only. Angstrom's equation takes the form:

$$\phi_a = (\alpha - \beta\ 10^{-\gamma e})\ \sigma T_a^4 \qquad (5.6)$$

and Brunt's relationship is

$$\phi_a = (a + b\sqrt{e})\ \sigma T_a^4 \qquad (5.7)$$

where, β, γ, a and b are site-specific calibration constants. Implicit in the above formulations is the assumption that the clear sky emissivity is a function of vapor pressure (e) only. Further, the effect of air temperature on the emissivity is indirectly accounted for by the dependence of vapor pressure on air temperature.

Brunt computed the values of a and b to be 0.52 and 0.065 based on mean monthly values of radiation measured by Dines and Dines (1927) at Benson, England. Since then, this relationship has been calibrated by numerous investigators using different sets of data. Some of their results are presented in Table 5.4. The wide variation in the coefficients indicates their site specificity and hence precludes the possibility of recommending any set of parameters as being of universal applicability.

Swinbank (1963) re-evaluated the subject in an effort to develop a universally applicable formula to avoid the site-specific nature of the earlier formulations. He hypothesized that the incoming radiation is a function of the air temperature alone. Based on the analysis of data collected at a number of different sites located both on land and ocean, he obtained the following linear regression equation with a correlation coefficient of 0.985:

Table 5.4

Values of Calibration Coefficients in Brunt's Formula

Reference	Location	Latitude	Altitude, m	a	b	Correlation	Period
Brunt (1932)	Benson (England)	52°W	6	0.52	0.065	0.97	monthly
Yamamoto (1950)	Various data sets			0.51	0.066		
Anderson (1954)	Lake Hefner	36°W	369	0.68	0.036	0.92	monthly
Goss & Brooks (1956)	California	38°N	14	0.66	0.039	0.89	monthly
DeCoster & Schuepp (1957)	Zaire	48°N	321	0.645	0.648		daily

* from Brutsaert (1980). In the text these are referred to as Brunt 1 to 5 respectively.

$$\log \phi_{ac} = -13.638 + 6.148 \log_{10} T_a \qquad (5.8)$$

with a standard deviation of 0.4 for the factor 6.148, which he rounded off to 6, yielding

$$\phi_{ac} = 5.31 \times 10^{-14} T_a^{6} \qquad (5.9)$$

Similar analysis using the Benson (Dines and Dines (1927)) observations yielded a coefficient of 5.21 instead of 5.31 in eq. 5.8 with a correlation coefficient of 0.984. From eq. 5.9 the emissivity of the atmosphere can be computed as

$$\varepsilon = 0.936 \times 10^{-5} T_a^{2} \qquad (5.10)$$

Although Swinbank derived eq. 5.9 from purely empirical correlation, a few later investigators(Deacon (1970), Gates (1965) and Brutsaert (1975)) have attempted to justify the formula based on semi-physical considerations.

Idso and Jackson (1969) rejected Swinbank's formulation on the grounds that at low temperatures it yielded radiation values less than the theoretical minimum radiation. Starting with a Brunt type relationship they related vapor pressure with air temperature on the assumption that the actual vapor pressure varies with temperature in a manner similar to saturation vapor pressure. Their formulation takes the form:

$$\phi_{ac} = \left[1-c \exp\{-d(273-T_a)^2\}\right] \sigma T_a^{4} \qquad (5.11)$$

where, c and d are calibration constants. Based on a statistical analysis of data from a number of climatically different stations they

computed the value of coefficients c and d to be 0.261 and 7.77×10^{-4}. These values yielded a correlation of 0.992 between the measured and computed values of ϕ_a. Since their data covered a very wide range of air temperature and climatic conditions, they claimed universal applicability for their formulae.

Brutsaert (1975) presented a formula based on the integration of Schwarzschild's transfer equation (Goody 1964) for standard atmospheric conditions. His analysis yields:

$$\phi_{ac} = 1.24 \, (e/T_a)^{1/7} \, \sigma \, T_a^{\,4} \tag{5.12}$$

which was approximated as

$$\phi_{ac} = 0.553 \, e^{1/7} \, \sigma \, T_a^{\,4} \tag{5.13}$$

The coefficients in the above formulation are based on typical profiles of humidity, air temperature and pressure; however, it was indicated that the coefficients are insensitive to the assumed conditions. Mermier and Seguin (1976) present comparison of Brunt's and Brutsaert's type formulae with daily measured data collected at their experimental station in France. Their data indicate reasonably good agreement with Brutsaert's formulation.

Aase and Idso (1978) have compared the formulae of Idso and Jackson [1969] and Brutsaert (1975) with mean daily long wave radiation data collected over a wide range of air temperature values (26.9°C to -30.3°C). They conclude that both equations perform well for temperatures above 0°C, below which the comparisons are not very satisfactory. Thus, for sub-zero temperatures both equations need to

be modified. However, no new relationship was presented.

Recently Satterlund (1979) used two sets of measurements, those of Aase and Idso (1978) and the cold weather measurements (from Alaska, USA) of Stoll and Hardy (1955) to compare the performance of Idso Jackson's and Brutsaert's formulae. Based on his analysis, he suggests the following:

$$\phi_{ac} = 1.08 \left[1-\exp\left(-e^{T_a/2016}\right)\right] \sigma T_a^4 \qquad (5.14)$$

Another approach suggested in literature, though not widely used is to directly compute the net long wave radiation. This is based on relationships of the type, Anderson (1952):

$$\phi_b - \phi_a = (0.26 - .0049e)\, \varepsilon\sigma T_a^4 \qquad (5.15)$$

It is important to note that all the above studies used clear sky radiation data to calibrate their relationships. The added complexity due to the occurence of clouds has thus been conveniently avoided.

5.3.3 The Effect of Clouds on Atmospheric Radiation

Longwave radiation increases when water vapor condenses into droplets. The effective atmospheric emissivity (ε_c) that includes the effect of clouds may be expressed as

$$\varepsilon_c = \varepsilon_a(1 + kC^2) \qquad (5.16)$$

where, k is an empirical constant and C = cloud cover ($C \leq 1$). The factor kC^2 empirically accounts for the effect of clouds in increasing the radiation. The value of k depends on the nature and height of clouds with recommended values ranging from 0.04 for cirrus to 0.25 for

nimbostratus clouds (Sellers, 1965). An average value of k = 0.17 has been suggested by Wunderlich (1972).

An alternate method to account for the effect of clouds was used by Penman (1948). In this method the multiplier $(1 + kC^2)$ in eq. 5.16 is replaced by $(a + b\ n/N)$ where the coefficients a and b are selected such that the multiplier approaches unity as n/N tends towards 1.0.

Recently, Kimbal and Idso (1982) have presented a model that accounts for the effect of clouds on long wave radiation in a manner quite different from eq. 5.16. The increase in radiation due to ith cloud layer ϕ_{aci} is given by

$$\phi_{aci} = C_s\ A_i\ \varepsilon_i\ f_i\ \sigma\ T_{ci}^4 \tag{5.17}$$

where, C_s = the long-wave transmittance of the atmosphere, ε_i = the emittance of the ith cloud layer, T_{ci} = the temperature in degree Kelvin of the ith cloud, A_i = fraction of the sky covered by the ith cloud layer and f_i = fraction of the black body radiation emitted in the long wave radiation band. The total radiation is given by the sum of the clear sky radiation, ϕ_a, and the sum of radiation emitted by the clouds, i.e.,

$$\phi_{ac} = \phi_a + \sum_{i=1}^{N} \phi_{aci} \tag{5.18}$$

where N = the number of cloud layers. Although this method is conceptually superior to eq. 5.16 to account for the effect of clouds, it requires detailed data about the cloud characteristics which is rarely available.

5.3.4 Analysis of Data Collected at the Dead Sea

The data analysed in this section consist of mean daily values of air temperature, vapor pressure and long wave radiation measured at Quidron by Dr. Stanhill of the Institute of Soil and Water, Agricultural Research Organization, Bet Dagan, Israel at the north west shore of the Dead Sea at an elevation of about -400 mbsl. These daily mean values were obtained by averaging observations made every minute. The data covers a period of 1 year from July 83 to June 84 during which there are 21 days with missing data, with the largest consecutive period of 8 days. Linear interpolation was used to obtain data for these days. Also, no cloud cover values for this period were recorded.

The mean monthly values of air temperature, vapor pressure and radiation are shown in Table 5.5. Maximum atmospheric radiation occurs during July and August, which are also the months with the highest air temperature. Using the daily mean air temperature and vapor pressure, the clear sky radiation was computed using the various methods discussed above. A plot of measured versus computed radiation is shown in Figure 5.1. It is clear that all the nine relationships underestimate the atmospheric radiation, though Idso-Jackson's, Swinbank's and Satterlund's formulae perform better than the rest. This underestimation is due to the assumption of zero cloud cover and the fact that the coefficients in the above relationships are not specific to the Dead Sea climate.

Figure 5.1 also shows the best fit line between the measured and computed values for each of the nine cases. The slope and intercept

Table 5.5

Mean Monthly Values of Air Temperature, Vapor Pressure, Atmospheric Radiation At Quidron and Cloud Cover*

Month	T_a °C	e (mb)	ϕ_a (kcal/m^2-day)	Cloud Cover*
JUL	32.5	19.0	8727	.07
AUG	32.6	19.1	8469	.04
SEP	30.8	19.0	8553	.09
OCT	27.1	15.0	8056	.29
NOV	23.3	15.0	7745	.43
DEC	18.5	11.6	7048	.50
JAN	17.6	11.3	7079	.50
FEB	19.6	9.7	6682	.46
MAR	19.4	12.2	7501	.44
APR	23.0	12.0	7614	.30
MAY	28.3	13.2	8060	.28
JUN	30.0	15.7	7946	.06
Mean	24.35	14.4	7788	0.30

* as reported by Newmann (1958)

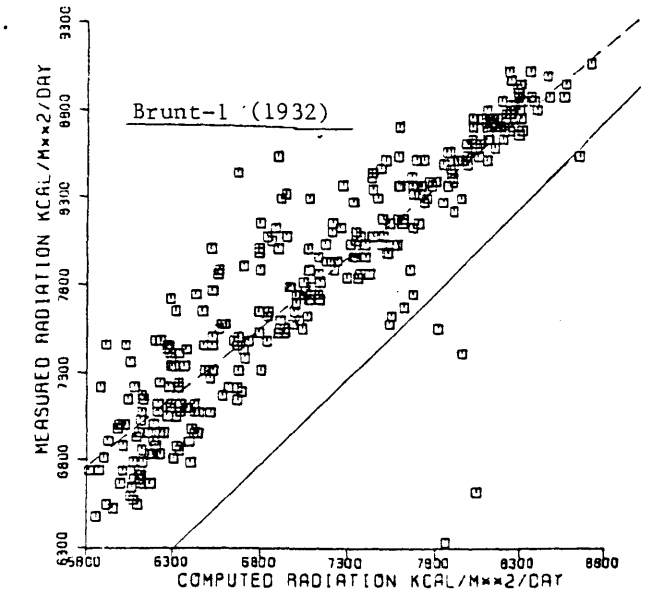

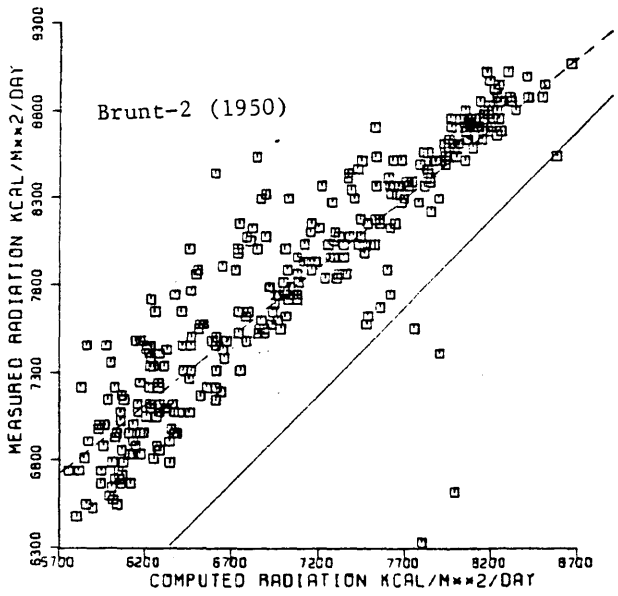

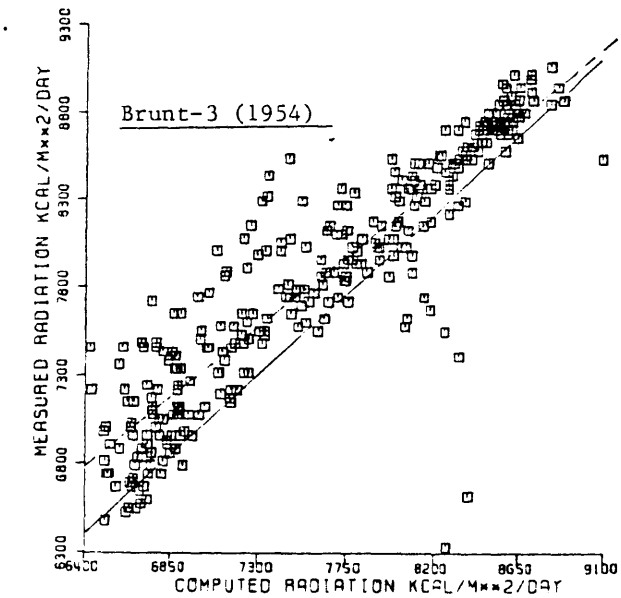

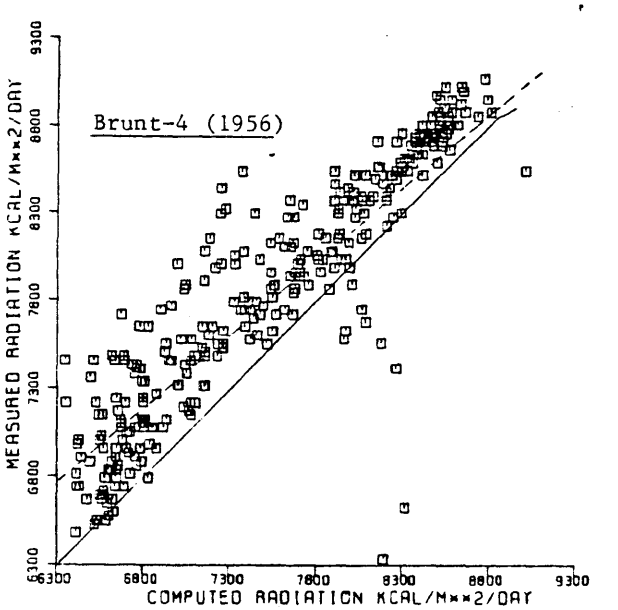

(Fig. 5.1 Continued.....)

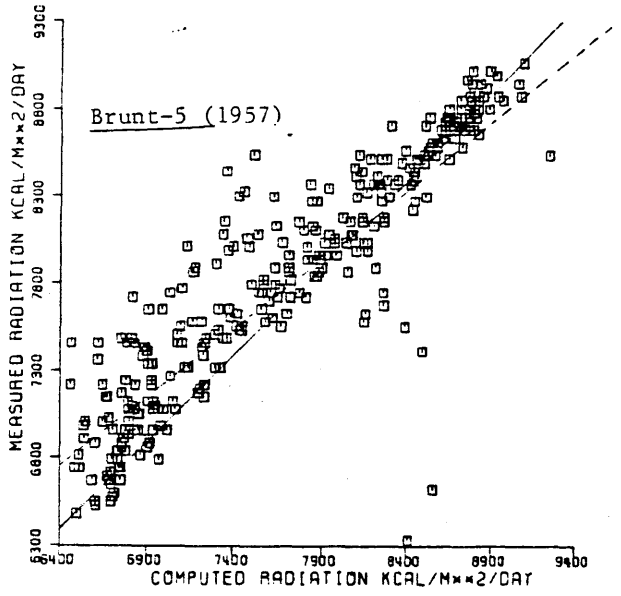

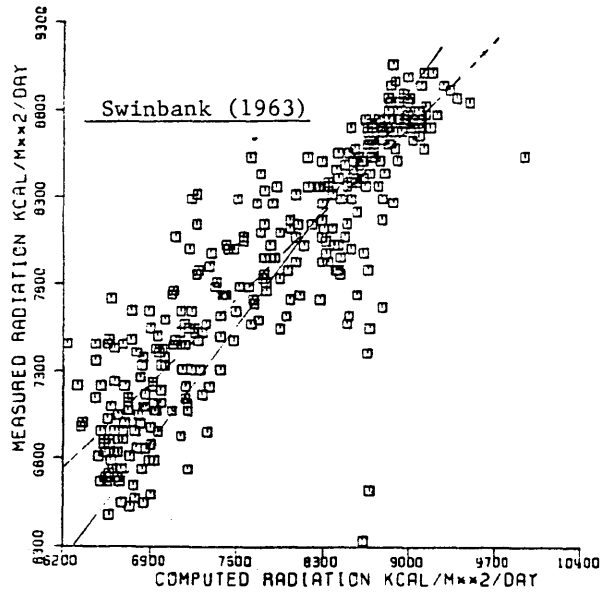

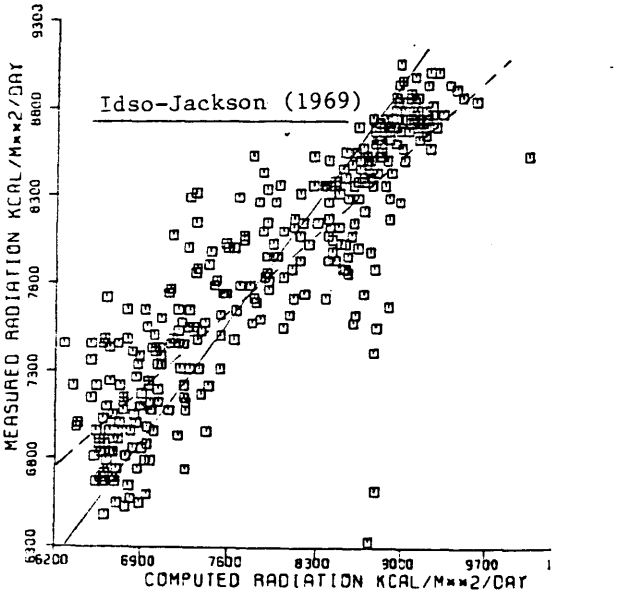

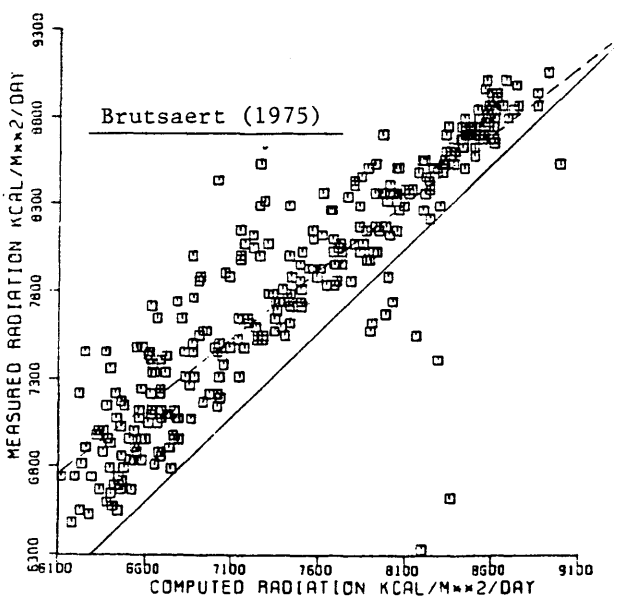

(Fig. 5.1 Continued.....)

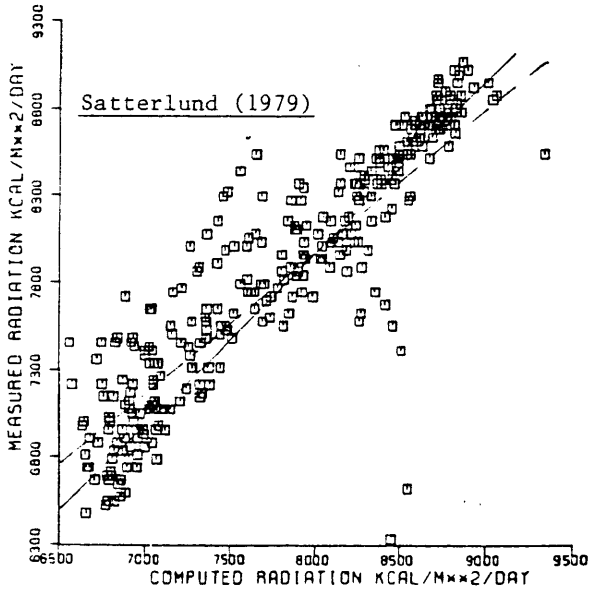

Fig. 5.1 Measured and Computed Atmospheric Radiation assuming no Cloud Cover

as well as the correlation coefficients are tabulated in Table 5.6. A 1:1 relationship between the data and computed values would result in zero intercept (a = 0) with a slope of unity (b = 1). Clearly none of the relationships satisfy these conditions even approximately.

These preliminary results suggested the necessity of including the cloud cover in computing the atmospheric radiative flux. The above analysis was thus repeated using daily values of cloud cover interpolated from the mean monthly cloud cover values reported by Neumann (1958), also included in Table 5.5. To our knowledge this is the only data on cloud cover available for the Dead Sea.

Figure 5.2 shows the plot of measured versus computed radiative flux for the nine relationships with the effect of clouds included as shown in eq. 5.16. In general these results indicate significant improvement over those shown in Figure 5.1, although some of the methods still underestimate the radiative flux. The result of the linear regression are tabulated in Table 5.7. Brunt 3, Brunt 4, Brunt 5 and Satterlund's results indicate a slope close to unity and an intercept of approximately zero.

5.3.5 Calibration of Atmospheric Radiation Formulae For The Dead Sea

The formulae selected for calibration are the ones due to Brunt (eq. 5.7), Swinbank (eq. 5.8), Idso and Jackson (eq. 5.11) and Brutsaert (eq. 5.12). For the first of these, clear sky emissivity depends only on screen level vapor pressure; for the second and third it depends only on air temperature, while for the fourth it depends on both vapor pressure and air temperature. The analysis was carried out by computing the daily clear sky emissivity ε_a using eq. 5.5 and

Table 5.6

Results of Linear Regression Between Measured and Computed Atmospheric Radiation Assuming Zero Cloud Cover Correction

Formula	Intercept	Slope	r^2 Correlation Coefficient %
Swinbank	2532	0.681	77
Idso Jackson	2655	0.659	77
Brutsaert	1830	0.805	82
Brunt 1	2176	0.794	82
Brunt 2	2222	0.794	82
Brunt 3	1149	0.880	82
Brunt 4	1264	0.874	82
Brunt 5	1524	0.820	82
Satterland	1120	0.865	81

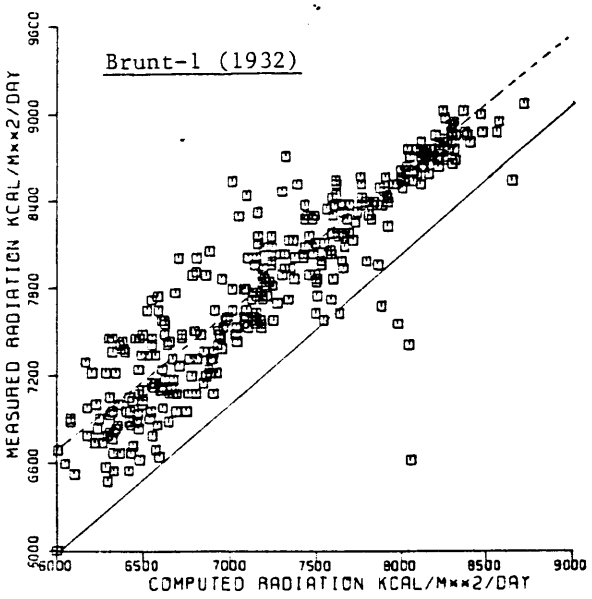

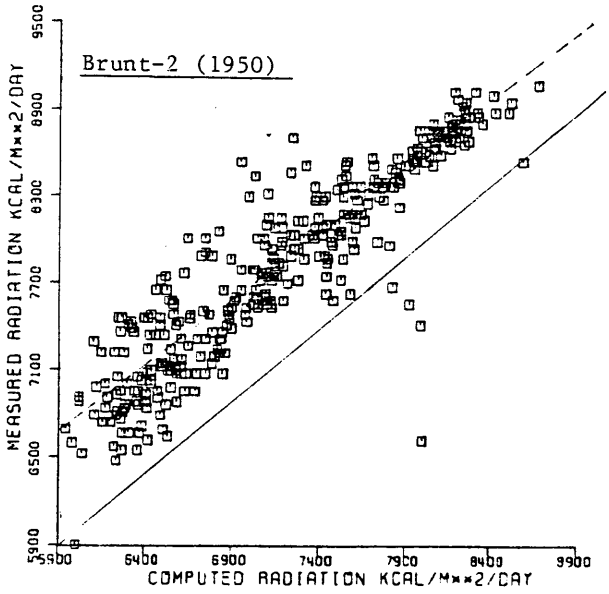

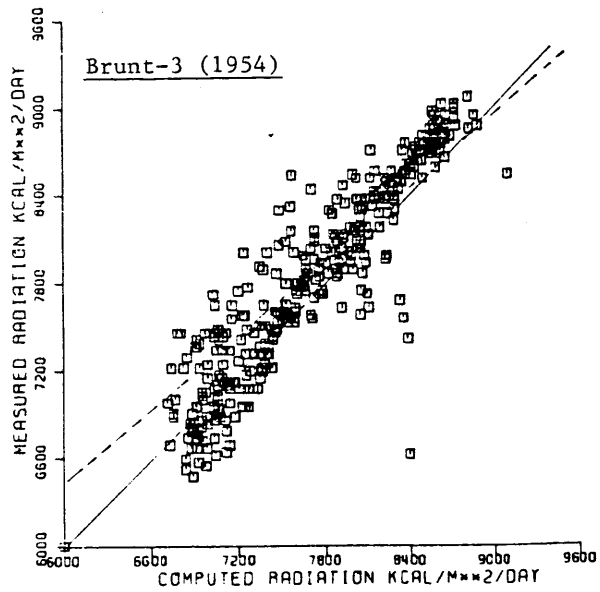

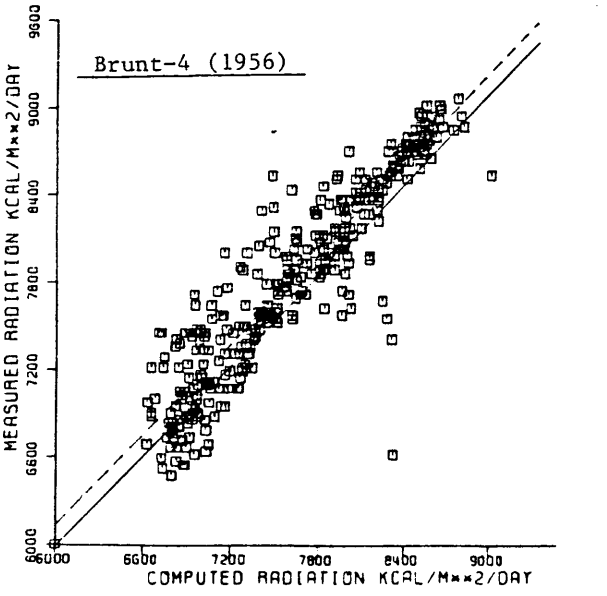

(Fig. 5.2 Continued.....)

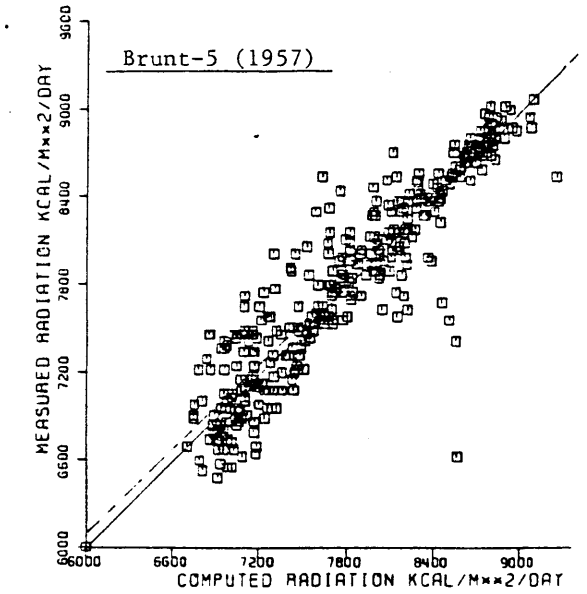

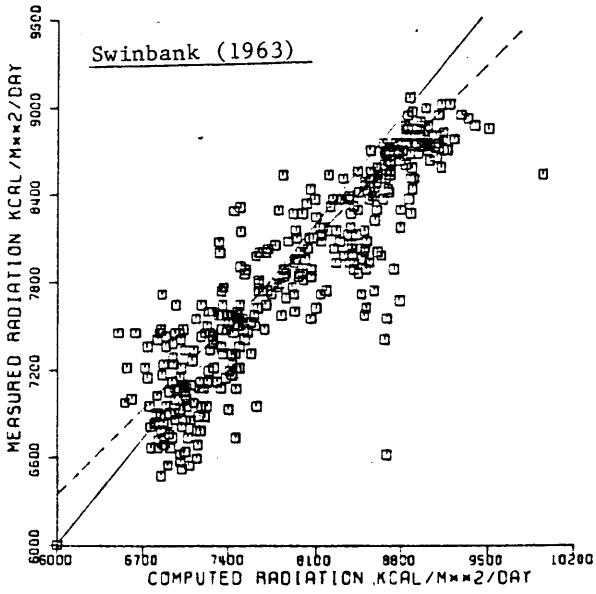

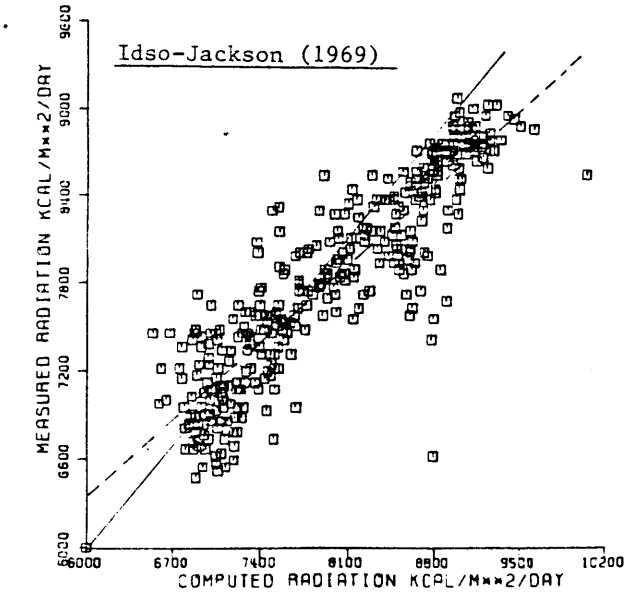

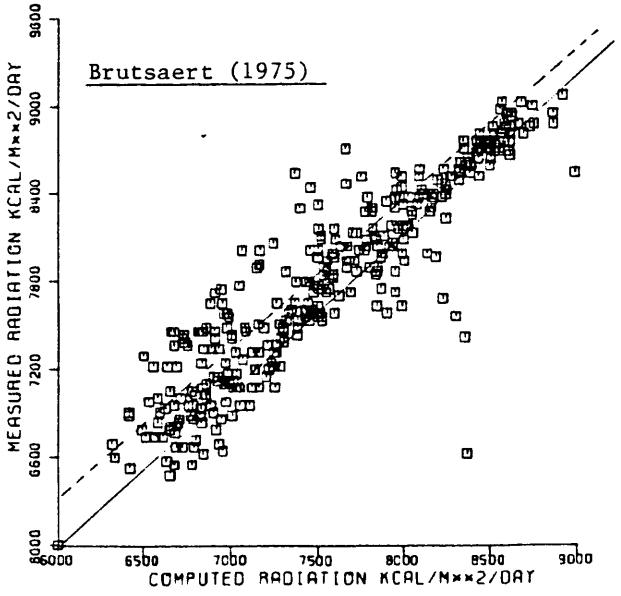

(Fig. 5.2 Continued.....)

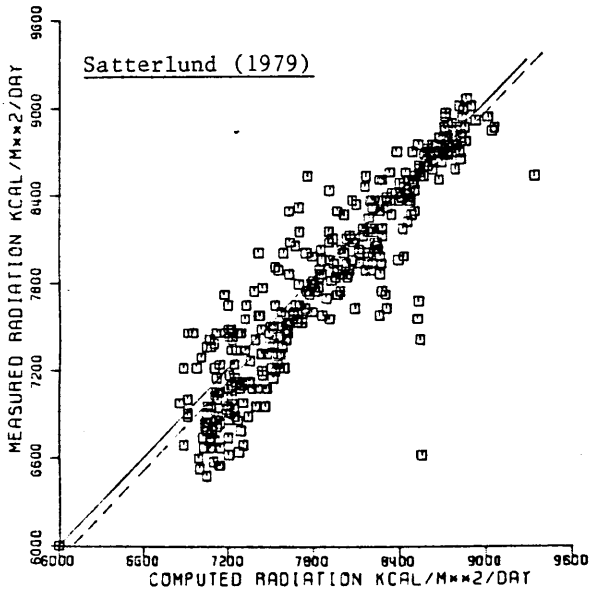

Fig. 5.2 Measured and Computed Atmospheric Radiation with Daily Interpolated Cloud Cover.

Table 5.7

Results of Linear Regression Between Measured and Computed Atmospheric Radiation With Cloud Cover Correction

Formula	a	b	c
Swinbank	1717	.77	79
Idso Jackson	1880	.75	79
Brutsaert	812	.92	84
Brunt 1	1280	.90	84
Brunt 2	1342	.90	84
Brunt 3	-172*	1.04	84
Brunt 4	-6*	1.02	84
Brunt 5	367	.95	84
Satterland	-222*	1.02	84

* Statistically, not different from 0

eq. 5.16 with k=.17, based on half the (even number days) measured data and then regressing linearized expressions for emissivity with the daily mean values of air temperature and/or vapor pressure to estimate the calibration coefficients.

Linear regression using Brunt's equation took the form

$$\varepsilon_a = a + b\ x \tag{5.19}$$

where $x = \sqrt{e}$. The best fit values of a and b obtained are 0.666 and 0.043, which are in the range reported by previous investigators (refer Table 5.4).

For calibrating the Swinbank type formula, two regressions were performed. The first took the form

$$\log \varepsilon_a = \log a + b \log x \tag{5.20}$$

where $x = T_a$ and yielded the relationship

$$\varepsilon_a = 6.76 \times 10^{-3}\ T_a^{.844} \tag{5.21}$$

A second attempt was made to fit Swinbank's expression by specifying a quadratic temperature dependence for emissivity

$$\varepsilon_a = a + b\ x \tag{5.22}$$

where $x = T_a^2$. The best fit values for a and b are 0.48 and 3.9×10^{-6} respectively.

Following similar procedures, the results obtained for Idso-Jackson and Brutsaert's relationship are as follows

$$\varepsilon_a = 1 - .20 \exp\left[-2.5 \times 10^{-4}\ (273 - T_a)^2\right] \tag{5.23}$$

and

$$\varepsilon_a = 1.12\ (e/T_a)^{.10} \tag{5.24}$$

A last regression was conducted using both temperature and vapor pressure values using the form

$$\log \varepsilon = a \log x + b \log y + c \tag{5.25}$$

where $x = T_a$ and $y = e$. This yielded the composite relationship

$$\varepsilon_a = 1.15\ T_a^{-.11}\ e^{.10} \tag{5.26}$$

The coefficients in eqs. 5.19 to 5.26 represent the site specific coefficients for the Dead Sea based on this set of mean daily data and Neumann's linearly interpolated cloud cover values. The performance of these site specific formulae as compared with the measured longwave atmospheric radiation is discussed below.

5.3.6 Verification of Calibrated Formulae

Daily atmospheric radiation was computed using the above calibrated values of clear sky emissivity for the other half of the data (odd numbered days) using:

$$\phi_{ac} = \varepsilon_a\ (1 + k\ C^2)\ \sigma\ T_a^4 \tag{5.27}$$

where ϕ_{ac} = computed radiation [KCal/m^2-day] and ε_a is obtained using eq. 5.19 to eq. 5.26. Figure 5.3 compares the measured and computed daily radiation. These results are significantly better than those presented in Figure 5.2. Table 5.8 shows the coefficients for linear regression between the computed and measured data. In all cases, the slope is approximately unity and the intercept close to zero. This suggests the superiority of using site-specific calibrated

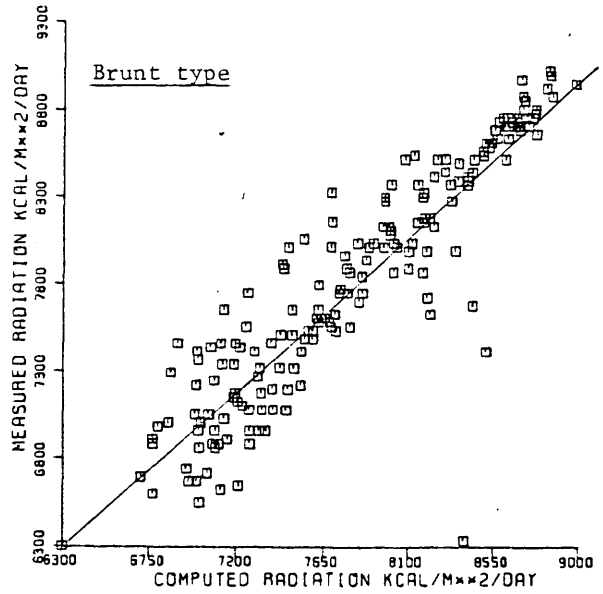

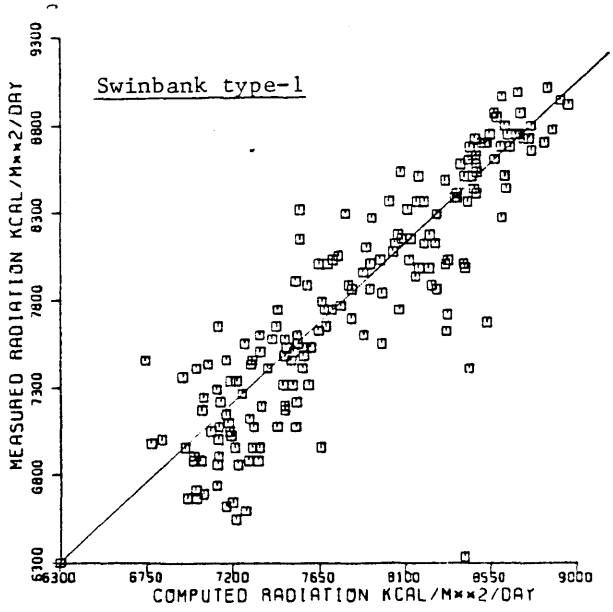

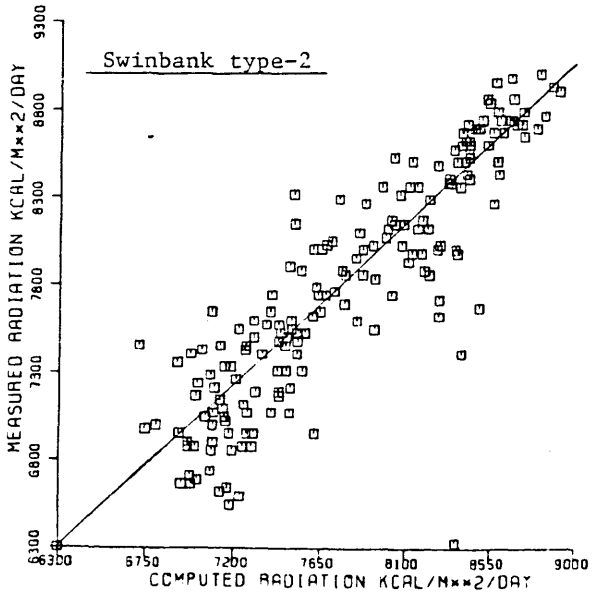

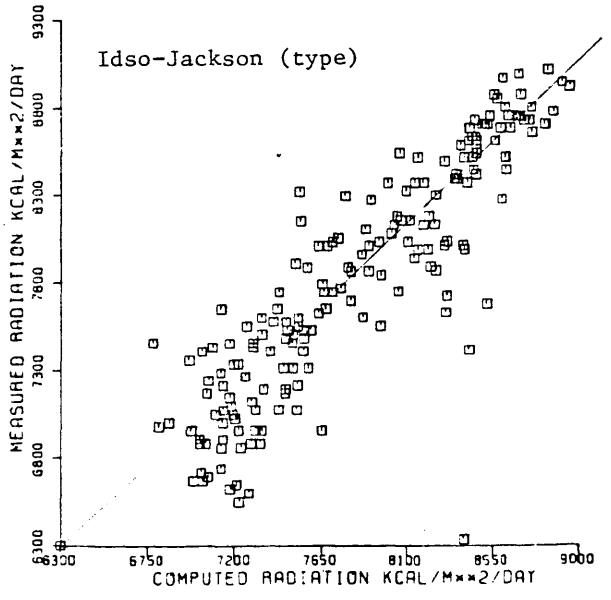

(Fig. 5.3 Continued.....)

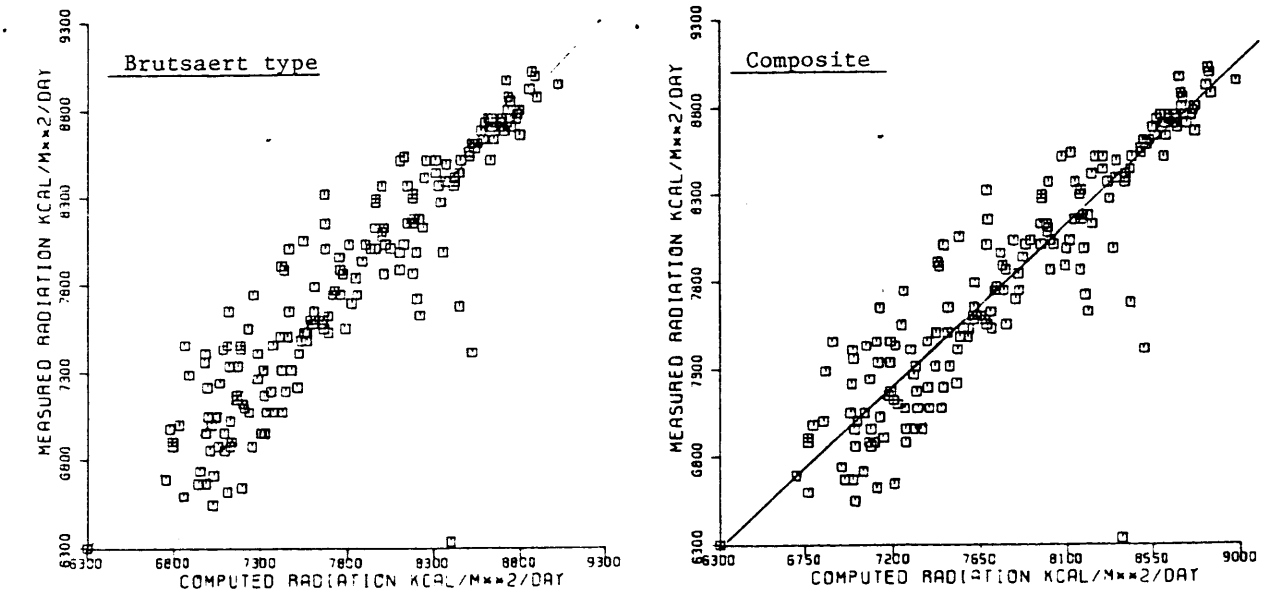

Fig. 5.3 Measured and Computed Atmospheric Radiation using Calibrated Formulae with Cloud Cover Correction.

Table 5.8

Results of Linear Regression Between Measured and Computed Atmospheric Radiation Using Calibrated Formulae and Cloud Correction*

Formula	Intercept**	Slope	Correlation Coefficient
Swinbank 1	16.3	0.999	78
Swinbank 2	39.5	0.991	78
Idso Jackson	-87.5	1.008	88
Bretsaert	95.4	0.988	82
Brunt	187.0	0.976	82
Composite	81.5	0.990	82

* Computed radiation for even numbered days only.

**None of the intercept values were statistically different from zero

coefficients for computing long wave atmospheric radiation as compared with using coefficients reported in literature. Table 5.8 also shows that for this set of data, the best fit values of coefficient explain only 78% - 82% of the variability observed in the radiation measurements. This is to be contrasted with the 98% correlation coefficients obtained in most studies discussed in Section 5.3.2 above. The discrepancy is due to the absence of concurrent site-specific data on cloud cover. As mentioned before, this complexity was absent in most studies referenced above that dealt with clear sky measurements only.

5.3.7 Summary of the Data Analysis On Long Wave Radiation

The above analysis of the long wave radiation data collected at Quidron at the North Western shore of the Dead Sea has yielded a number of important conclusions. A comparison of nine commonly used long wave radiation formulae presented above indicates the site-specific nature of the coefficients contained in these formulae. Further, the importance of using cloud cover in calculating atmospheric radiation is shown. It is recommended that as far as possible measurements of long wave radiation data should be supplemented with measurements of cloud cover as well as air temperature and humidity. Finally, Section 5.3.5 presents a set of formulae (calibrated using this set of data) that can be used for computing the clear sky emissivity for the Dead Sea and hence long wave atmospheric radiation. These site-specific relationships form an important component of hydrothermal modelling of the Dead Sea.

5.3.8 Reflection of Atmospheric Radiation at the Water Surface

Since water is practically opaque to long-wave radiation, the latter is absorbed almost entirely at the surface. The reflectivity for longwave radiation is thus very small. For the case of natural water bodies the reflected longwave radiation is about 3% of the incoming radiation, i.e.

$$\phi_{ar} = 0.03\ \phi_{ac} \tag{5.28}$$

To the Dead Sea, the reflected long wave radiation may be slightly higher during periods when the lake experiences a whitening of the surface due to salt precipitation. However, the exact duration and areal extent of this process needs to be determined before any correction can be applied to the reflectivity of water.

5.4 Back Radiation

For a body exposed to radiation, the following balance must hold

$$a + r + t_r = 1 \tag{5.29}$$

where a = the fraction of radiation absorbed, r = the fraction reflected and t_r = the fraction transmitted through the body. Since water is opaque to long wave radiation, $t_r = 0$ and as mentioned above r = 0.03. This yields a value of a = 0.97. Since the emissivity of a body is equal to its absorptivity, for any given wavelength, the emissivity of water is equal to 0.97. Thus, for the computation of back radiation from a water body, there is general agreement in the

literature to treat water surface as a grey body with an emissivity ε_w = 0.97. Hence, back radiation may be computed using the following

$$\phi_b = \varepsilon_w \sigma T_s^4 \qquad (5.30)$$

CHAPTER 6

EVAPORATION FROM THE DEAD SEA

6.1 Introduction

The rate of evaporation from a water surface is a function of local meteorological conditions and the temperature and salinity of the water surface. The effect of meteorological variables on the rate of evaporation from fresh water bodies has been studied by a number of researchers and is discussed briefly in Section 6.2. It is also known that evaporation from saline water is less than that from fresh water; however, few comprehensive studies of evaporation from saline water bodies have been reported in literature. This effect is important for water balance computations and other engineering studies related to terminal lakes, evaporation ponds used to dispose of saline industrial effluents, salt production ponds and the emerging technology of salt gradient solar ponds. For the case of hypersaline Dead Sea, the economic implications of accurately computing the rate of evaporation have been discussed in Section 2.4.

The primary emphasis of this chapter is to develop a scientifically sound methodology to account for the effect of salinity on evaporation. While the focus is on general application that can be used to estimate evaporation from any saline water body, specific numerical and statistical analysis is based on pan evaporation and meteorological data collected at the Dead Sea Works in Israel.

6.2 A Review of Evaporation From Fresh Water Bodies

The effect of meteorological variables on evaporation has been well summarized by Harbeck et. al. (1958), Sturrock (1978) and Brutsaert (1982). Historically, significant knowledge was gained from detailed and well documented studies conducted at Lake Hefner (1950-57), Lake Mead (1952-53) and Salton Lake, California (1961-62 and 1967-69). As a result of these studies, Dalton type formulae for estimating evaporation from natural lakes have gained considerable popularity. These are of the form:

$$E = f(W_z) \{e_{sat}(T_s) - \phi\, e_{sat}(T_a)\} \qquad (6.1)$$

where E = the evaporation rate, $f(W_z)$ = empirical wind speed function based on wind speed measured z-m above the water surface; $e_{sat}(T_s)$ and $e_{sat}(T_a)$ are saturation vapor pressure at water surface temperature (T_s) and air temperature (T_a) respectively and ϕ is the relative humidity of air.

The wind speed function $f(W_z)$, accounts for the effect of wind on evaporation and typically includes a calibration coefficient to account for the cummulative effect of all other variables that affect the evaporation process and not included directly in eq. 6.1. These include physical features of the lake such as fetch, size and shape; atmospheric stability, the effect of waves,the measurement height and location for wind speed, air temperature and the relative humidity.

Table 6.1 lists some of the wind speed functions that have been proposed. In each case an independent estimate of evaporation was obtained based on either water or energy budget method with

Table 6.1

A Few Wind Speed Functions Reported In Literature

$$E = f(W_z)(e_{sat}(T_s) - e(T_z))^*$$

	Location of Instruments	$f(W_z)^*$
Lake Hefner (Ref. 57)	Raft Station	.00236 W_2
Lake Mead (Ref. 57)	Boulder Basin barge, 8 m level,	.00208 W_8
	Las Vegas, Nevada	.00167 W_2
Salton Sea (Ref. 62)	Sandy Beach, 8 m level	.00156 W_8
(1961-62 Study)	Yuma, Arizona	.00136 W_2
Salton Sea (Ref. 62)	Land Stations	.00191 W_2
(1967-69 Study)	Test base station (land)	.00182 W_2
	Raft Stations	.00245 W_2
	All Stations	.00214 W_2
Lake Nasser (Ref. 97)	Lake Measurements, 2 m height	.0022 W_2

* E in/day
W_z mi/hr
e_{sat}, e mb

simultaneous measurements of the meteorology. $f(W_z)$ was then computed using eq. 6.1. Thus, $f(W_z)$ also includes the effect of all measurement and instrument errors and the influence of spatial and temporal averaging of the data. For the Salton Sea, a comparison of $f(W_z)$ computed using land based and water-based data is also included in Table 6.1.

In the absence of a calibrated site specific wind speed function, the values tabulated in Table 6.1 may be used. Of these the Lake Hefner value has been most frequently used.

At this point it is worth mentioning the feedback effect inherent in the overall energy balance of surface water bodies. This has been discussed briefly in Section 3.2. As a result of this, errors in computing evaporation—for example due to a systematic bias in the wind speed function, $f(W_z)$—tend to be reduced when energy budget calculations are performed sequentially in time.

Eq. 6.1 generally requires the meteorological data to be measured at 2 m height. In cases where measurements are available at elevations other than 2 m above the water surface, data can be reduced to the standard 2 m height using the following relationship that assumes a logarithmic boundary layer profile (Adams et. al. 1981):

$$\frac{W_2}{W_{z_1}} = \frac{\ln W_2/z_0}{\ln z_1/z_0} \qquad (6.2)$$

where z_1 = the height at which wind speed is measured and z_o = the roughness height. A similar relation can be used for the atmospheric vapor pressure.

6.3 Evaporation from Saline Water Bodies

6.3.1 Computation of Evaporation from Saline Water

Evaporation from a saline water surface is less than that from a fresh water surface because (i) dissolved salts interfere with the motion of water molecules and (ii) the average number of water molecules in contact with air is reduced since part of the surface is occupied by salt molecules (Turk, 1970). Hence, the saturation vapor pressure above a saline surface, $e'_{sat}(T_s, S_s)$, decreases with surface salinity, S_s, expressed here in units of parts per thousand by weight ($^{o}/_{oo}$). This results in reduced evaporation which can be expressed:

$$E_{sal} = f(W_z) \left\{e'_{sat}(T_s,S_s) - \phi\, e_{sat}(T_a)\right\} \qquad (6.3)$$

where E_{sal} = evaporation rate from the saline water body. For a given water body the function $f(W_z)$ is essentially the same in Eq. 6.1 and Eq. 6.3.

The relationship between saturation vapor pressure and salinity depends on the particular salt in solution. Typically, saline lakes contain unique mixtures of two or more salts depending upon the geological characteristics of the catchment and the ionic composition of inflows. Moreover, the relative composition of a given lake may vary with time due to changes in inflow composition or, for highly concentrated waterbodies, differential precipitation of salts. Unfortunately, there is limited information regarding evaporation from such mixtures. As an approximation, it may be assumed that

$$e'_{sat}(T_s) = \beta(S_s)e_{sat}(T_s) \qquad (6.4)$$

so that eq. 6.3 can be written as:

$$E_{sal} = f(W_z)\{\beta(S_s)\, e_{sat}(T_s) - \phi\, e_{sat}(T_a)\} \qquad (6.5)$$

where $\beta(S_s)$ $(0 < \beta \leq 1)$ is the activity coefficient of the surface water of salinity S and represents the ratio of vapor pressure over salt water to the vapor pressure over fresh water at the same temperature.

The relation between salinity and the activity coefficient of water in solution of five different salts at 20°C is shown in Fig. 6.1. This figure is based on data from the International Critical Tables (National Research Council, 1928). From Figure 6.1, $\beta(S)$ clearly is also a function of the ionic composition. Over limited ranges, the activity coefficient has been expressed as a linear function of salinity,

$$\beta(S) = 1 - \delta S \qquad (6.6)$$

where δ, too, is a function of the ionic composition of the saline solution (Sverdrup et al., 1942).

Thermal energy budgets for a fresh water body and a similar saline water body exposed to identical meteorological forcings would result in an inverse relationship between fresh water surface temperature and evaporation rate. The lower vapor pressure over saline water permits less energy to escape as latent heat, thus causing an increase in temperature within the saline body, an increase in sensible heat loss and back radiation to the atmosphere. This increase in temperature also enhances the rate of evaporation from the saline water body

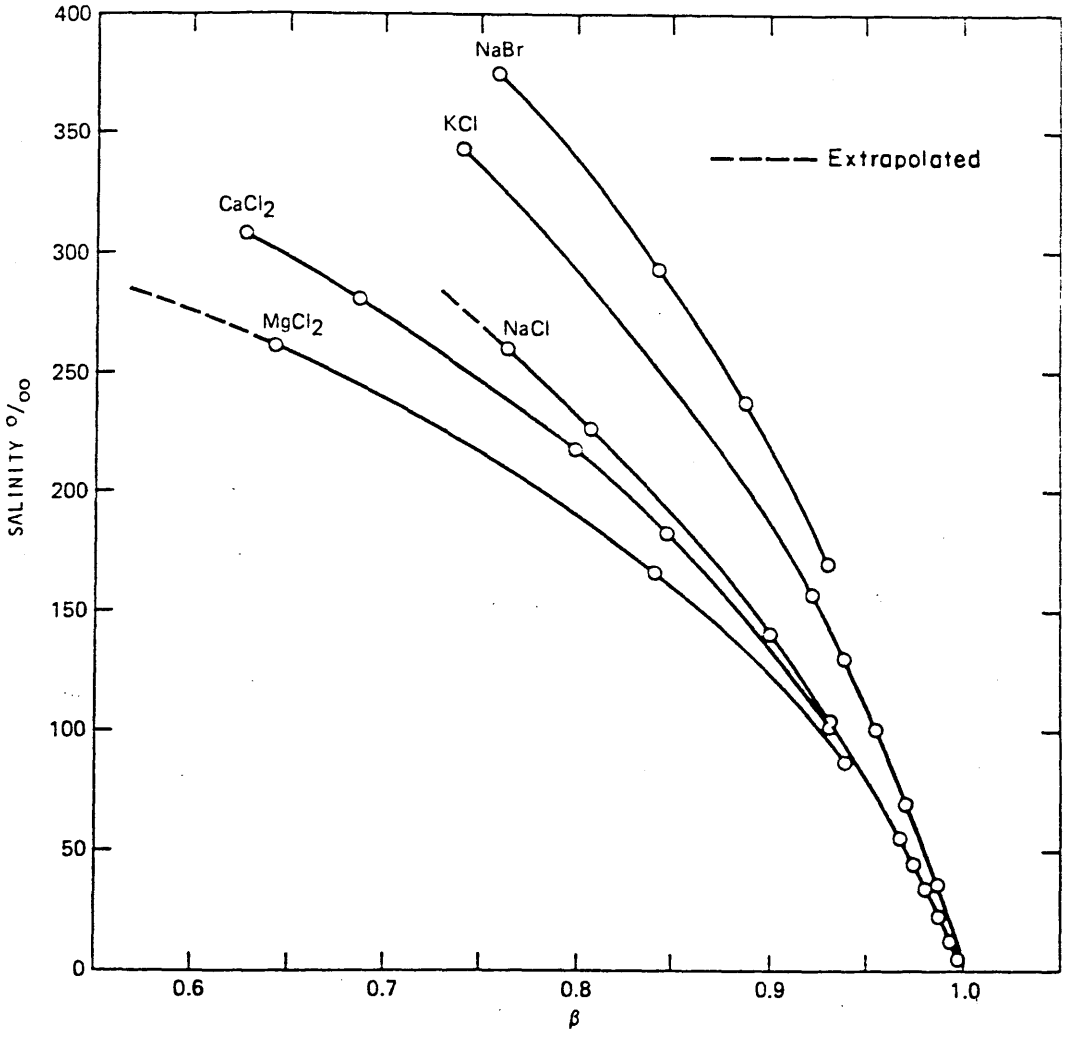

Fig. 6.1 Relation Between Salinity and Activity Coefficient for Water at 20°C for Solutions of Different Ionic Compositions.

partially compensating the reduction in evaporation due to salinity. This negative temperature feedback effect is further discussed in the subsequent sections.

The evaporation rates presented in Chapter 9 and Chapter 10 are based on eq. 6.5 and a coupled energy, salt, water and mechanical energy budget that simultaneously computes water temperature, salinity and evaporation. In such a model, the negative feedback effect due to temperature is directly included. This is further discussed in Chapter 10.

The above approach of accounting for the effect of evaporation can be contrasted with the following two approaches where the salt water evaporation is expressed as:

$$E_{sal} = \alpha\, f(W_z)\, \{e_{sat}(T_f) - \phi\, e_{sat}(T_a)\} \tag{6.7}$$

$$E_{sal} = \gamma\, f(W_z)\, \{e_{sat}(T_s) - \phi\, e_{sat}(T_a)\} \tag{6.8}$$

where, T_f = the surface temperature of a fresh water body. Note α accounts for both the salinity and the negative temperature feedback effect on evaporation and is the ratio of salt water to fresh water evaporation (assuming similar water bodies and meteorological conditions) i.e.

$$\alpha = \frac{E_{sal}}{E_{fresh}} \tag{6.9}$$

In the second approach, γ accounts for only the salinity effect. The feedback effect is directly accounted for by computing the saturation

vapor pressure at the temperature of the saline water body. ($e_{sat}(T_s)$ in eq. 6.8).

By equating eq. 6.5 to eq. 6.7 and to eq. 6.8, respectively,

$$\alpha = \frac{\beta(S_s)\, e_{sat}(T_s) - \phi\, e_{sat}(T_a)}{e_{sat}(T_f) - \phi\, e_{sat}(T_a)} \tag{6.10}$$

and,

$$\gamma = \frac{\beta(S_s)\, e_{sat}(T_s) - \phi\, e_{sat}(T_a)}{e_{sat}(T_s) - \phi\, e_{sat}(T_a)} \tag{6.11}$$

from which it is clear that both α and γ depend not only on the surface salinity and ionic composition, but also on the meteorological variables T_a and ϕ, both of which may exhibit considerable temporal variation. The correct use of the α or γ approach would thus require the specification of an α or γ as a function of salinity and meteorology, clearly a cumbersome task. This is in sharp contrast to the recommended β approach. Since β is a thermodynamic quantity it is a function of the salinity and the ionic composition only.

Comparing eq. 6.10 and eq. 6.11, since $T_s > T_a$ and hence $e_{sat}(T_s) > e_{sat}(T_a)$, $\gamma < \alpha < 1.0$.

6.3.2 The Use of Pans to Study Evaporation

Pans provide a common method to estimate evaporation from large water bodies which are not amenable to direct experimental measurement. Since the evaporation rate from pans is generally greater than that from large bodies, this technique requires correction using a

pan coefficient (Kohler, 1954; Nimmo, 1964, Brutsaert, 1982). Pans may also be used to identify the influence of salinity or other perturbations such as the addition of dye (Block et al., 1951) or waste heat (Nystrom, 1982) by performing experiments in otherwise identical ponds.

A few evaporation pan experiments using saline water have been reported in the literature. Bonython (1956 and 1966) has presented results of evaporation measurements from two thermally insulated pans over a period of two consecutive summers. One pan contained water and the other brine of density varying from 1.07 g/cm^3 to 1.245 g/cm^3. Turk (1970) conducted a similar experiment over a period of one month using eight pans installed within a small enclosed evaporation pond. The solution densities ranged from 1 g/cm^3 to 1.333 g/cm^3 and were maintained constant by adding fresh water to compensate for water lost due to evaporation. Janson (1959) measured evaporation from pans containing four different salt solutions ranging in salinity from 30 $^{o}/_{oo}$ to 260 $^{o}/_{oo}$. Similar studies were conducted at the Dead Sea from November 1966 to July 1967 using six different concentrations of Dead Sea brine (Tahal, 1982). Results from the studies shown in Fig. 6.2 clearly indicate the dependence of α on meteorology and salinity. In each of the above studies results have been presented as the ratio of salt water evaporation to freshwater evaporation (i.e., α in eq. 6.7 and eq. 6.9) as a function of the salinity or the density of the solution.

6.3.3 Analysis of Evaporation Pan Data Collected at the Dead Sea

The experimental set-up consisted of eight cylindrical evaporation pans located at Sedom at the southern end of the Dead Sea. The pans were

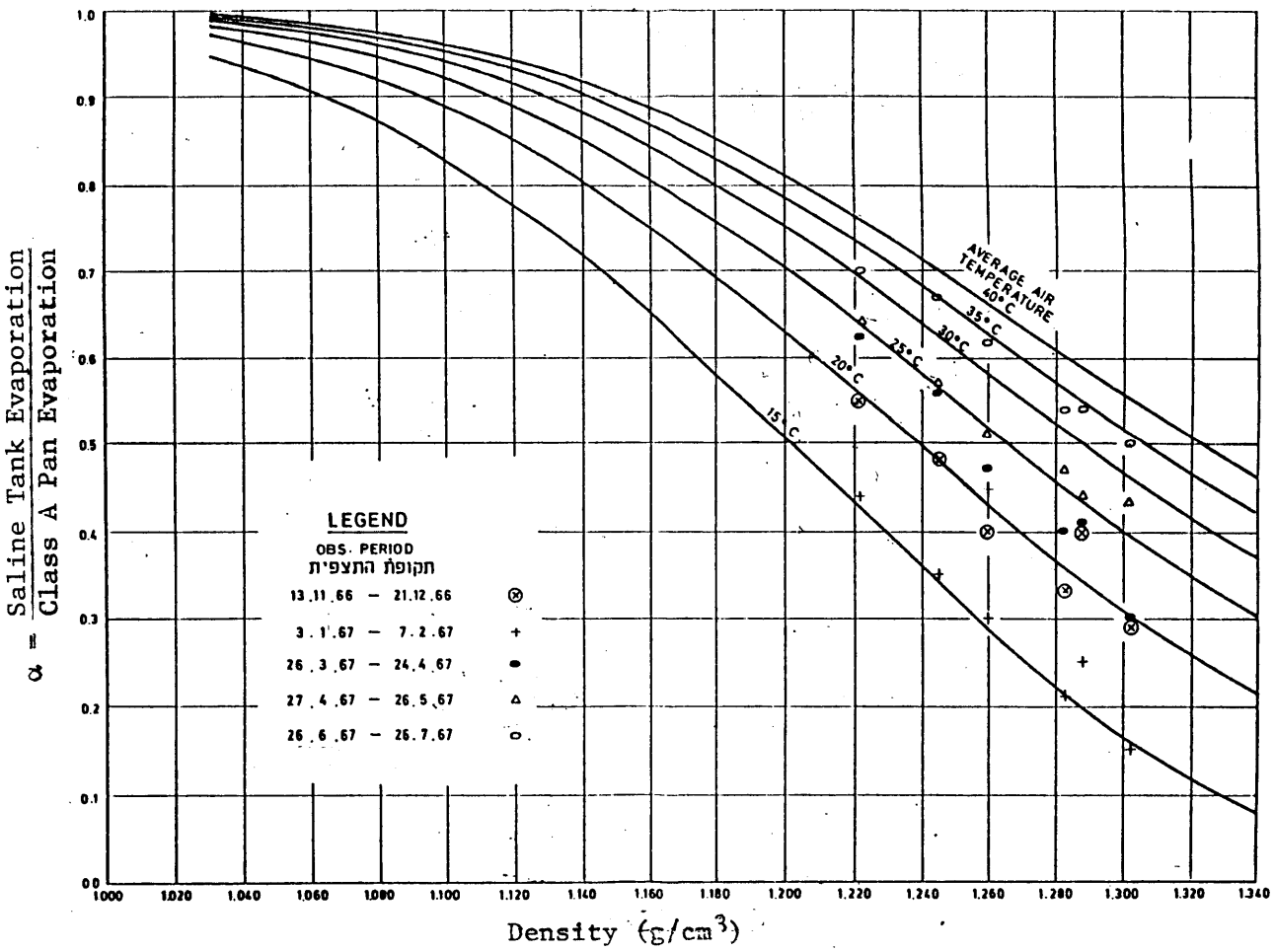

Fig. 6.2 Variation of α Values with Density and Meteorology (Ref. 133)

sunk in the ground and were three meters in diameter, about one meter deep and typically filled to a depth of about 0.95 m with mixtures of Mediterranean and Dead Sea waters in different proportions (see Table 6.2). Each pan was provided with thermometers to measure the temperature at the water surface and at various depths within the pans. Air temperature and relative humidity were also measured at the site. Since the eight pans were identical in shape and size and exposed to the same meteorological conditions, they can be used to study the effect of differences in salinity and chemical composition on the rate of evaporation.

At intervals ranging from three days to several weeks, fresh make-up water was added to each pan to compensate for the evaporative water loss and to maintain a constant chemical composition. Maximum make-up water added at any time was 5 mm. Since evaporation was higher in summer months, the frequency of make-up water addition and measurement of pan evaporation was higher in summer than in winter. Before and after adding make-up water, water surface elevations were measured and chemical assays were taken for each pan. At each addition of make-up water, the contents of the pans were vigorously mixed for two to three hours to re-dissolve any precipitated salts. This data was collected by the personnel of the Dead Sea Works, under the sponsorship of the Mediterranean Dead Sea Company.

Data for the period 28 November 1982 to 1 January 1984 were available and comprised 36 cycles. A cycle consists of the interval between two make-up water additions. For each cycle, mean air temperature, humidity, water-surface temperature, temperature at 10 cm

depth, duration of the cycle, make-up water added and net evaporation were recorded. Also densities and detailed chemical analysis for each cycle were reported. Table 6.2 shows the physico-chemical characteristics of the eight pans, Table 6.3 summarizes net evaporation, and Table 6.4 summarizes meteorological data and water surface temperatures for each cycle. The accuracy of the net evaporation rates is estimated to be .03 mm/d while that of the water temperature is .2°C.

Of the above 36 cycles, evaporation for the first four cycles (Nov. 28, 1982 to Feb. 23, 1983) is underestimated due to the occurrence of rain for which no measurements were made. Furthermore, meteorological data for 13 cycles (23 and 25-36) were missing. These were for the periods from July 31, 1983 to August 4, 1983 and August 17, 1983 to January 1, 1984. In addition, evaporation and surface temperature data for Pan 12 were missing for Cycle 25. Saturated vapor pressure for the remaining 23 cycles with complete data were calculated.

Table 6.2 lists the range and mean values of density in each pan for the 23 cycles for which complete data were available. Also included is the ionic composition for Cycle 9 which is typical of other cycles. Pans 12 - 14 contained concentrated Mediterranean Sea water. The salinity in Pan 12 (~50 $^{o}/_{oo}$) reflected the expected concentration due to evaporation of water conveyed from the Eastern Mediterranean to the Dead Sea as part of the proposed Mediterranean - Dead Sea project. Pans 13 and 14 were concentrated by additional factors of about 4 and 4.6 respectively. The relative composition in Pans 12 - 14 is approximately constant and similar to that of seawater.

TABLE 6.2

Salinity and Ionic Composition of the Eight Pans

Pan	Relative Composition by volume (weight)		Salinity Range [2] [3]	Density Range [3]	Composition [4] ($^0/_{00}$)					
					--	-	++	++	+	+
	Med. Sea	Dead Sea			So_4	Cl	Mg	Ca	Na	K
12	100 (100)	0 (0)	48-60	1.034-1.040	3.2	33.4	2.6	0.6	17.2	0.8
13	100 (100)	0 (0)	182-215	1.146-1.160	11.8	118.7	8.0	1.8	65.1	2.6
14	100 (100)	0 (0)	221-245	1.177-1.194	13.5	136.9	9.1	0.7	75.5	3.0
15	41 (36.9)	59 (63.1)	188-209	1.151-1.168	1.1	134.9	23.8	10.6	28.1	4.5
16	25.5 (22.4)	74.5 (77.6)	220-242	1.182-1.205	0.6	160.2	29.9	12.8	29.7	5.4
17	10.3 (8.8)	89.7 (91.2)	232-272	1.210-1.235	0.4	180.7	33.9	14.6	32.8	6.1
18	0 (0)	100 (100)	186-210	1.150-1.170	0.4	134.8	25.5	11.4	23.2	4.8
19	0 (0)	100 (100)	260-278	1.225-1.240	0.4	183.6	36.3	15.2	29.1	6.6

[1] Data have been collected and compositions analyzed by personnel of the Dead Sea Works, under sponsorship of the Mediterranean Dead Sea Company.

[2] Sum of six major ions in right hand columns. For pans with Dead Sea water, the salinity may be underestimated due to absence of measurements of Br^- (4-5 $^0/_{00}$) in Dead Sea.

[3] Range represents cycle to cycle variability.

[4] Values shown are for cycle 9.

Pans 15 - 17 contained mixtures of Dead Sea and Mediterranean Sea waters in volumetric ratios of 59/41, 74.5/25.5, and 89.7/10.3, respectively. Pan 18 contained diluted Dead Sea water, and Pan 19 contained undiluted Dead Sea water. The salinity of the Dead Sea water is about 276 $^{o}/_{oo}$ with a composition of about 68% chloride ions, 14% magnesium ions, and 11% sodium ions. Compared with the composition of Mediterranean Sea water, Dead Sea brines are richer in magnesium and chloride ions and deficient in sodium ions. At high concentrations, the reduction in saturation vapor pressure due to $MgCl_2$ is significantly more than that due to NaCl (Figure 6.1). Hence, among solutions with equal salinities, the ones with higher $MgCl_2$ concentration will exhibit lower evaporation. Thus pans can be arranged in order of expected increasing evaporation rate: Pan 19, 17, 16, 14, 15, 18, 13 and 12. This conclusion is confirmed by the weighted mean evaporation rates in Table 6.3

The inverse relationship between water surface temperature and evaporation rate was previously discussed in Section 6.3.1. This conclusion is confirmed by comparing data in Tables 6.3 and 6.4. The effect is also shown in Figure 6.3 which presents mean cycle water temperature and evaporation rate for several typical cycles for Pans 12, 16 and 19. For each cycle, Pan 19 with the lowest evaporation rate has the highest water temperature, Pan 12 with the highest evaporation rate has the lowest temperature, while Pan 16 with an intermediate evaporation rate has an intermediate water temperature. Cycle-average surface evaporation for Pans 12 (Mediterranean Sea) and 19 (Dead Sea) are shown in Figure 6.4 along with corresponding meteorological data. The weighted (by individual cycle duration) mean surface temperature for Pan 19 is

Table 6.3 Mean rate of evaporation (mm/day) for eight pans and thirty-six cycles 28 November 1982 to 1 January 1984

Cycle	Dates (da/mo/yr)	Pan 12 Med	Pan 13 Med	Pan 14 Med	Pan 15 59% Med 41% DS	Pan 16 74.5% Med 25.5% DS	Pan 17 89.7% Med 10.3% DS	Pan 18 DS	Pan 19 DS
1	28/11/82-16/12/82	2.81	2.43	2.08	2.16	1.87	1.63	2.29	1.48
2	16/12/82-4/1/83	3.31	2.88	2.49	2.67	2.32	2.00	2.70	1.88
3	5/1/83-7/2/83	2.38	2.20	1.58	1.70	1.39	1.18	1.75	1.07
4	9/2/83-23/2/83	2.88	2.45	2.22	2.29	2.02	1.77	2.33	1.72
5	24/2/83-9/3/83	4.10	3.45	3.13	3.25	2.91	2.56	3.31	2.47
6	10/3/83-23/3/83	4.65	3.80	3.27	3.42	3.12	2.68	3.57	2.60
7	27/3/83-3/4/83	7.37	6.20	6.13	6.26	5.49	4.89	6.14	4.79
8	6/4/83-14/4/83	6.22	5.61	5.23	5.55	4.89	4.54	5.27	4.29
9	14/4/83-19/4/83	8.87	8.21	7.68	7.65	7.06	6.63	7.91	6.55
10	22/4/83-29/4/83	8.27	7.68	7.23	7.25	6.62	5.89	7.20	5.67
11	29/4/83-11/5/83	8.00	7.29	6.92	7.17	6.52	6.12	7.14	5.87
12	11/5/83-19/5/83	10.34	9.40	8.69	8.92	8.48	7.60	9.71	7.55
13	19/5/83-26/5/83	9.68	9.36	9.27	9.36	8.39	8.14	9.46	7.84
14	26/5/83-2/6/83	9.53	8.72	8.96	9.04	9.25	7.95	9.33	7.79
15	2/6/83-8/6/83	12.32	11.21	10.65	10.64	10.11	9.27	10.77	9.23
16	8/6/83-17/6/83	11.19	10.19	9.61	9.84	9.02	8.54	9.68	8.04
17	17/6/83-22/6/83	11.42	10.54	10.04	10.56	9.72	9.10	10.44	8.72
18	23/6/83-27/6/83	14.51	13.47	12.15	12.61	11.89	11.18	12.53	10.57
19	29/6/83-5/7/83	11.60	10.51	9.83	10.13	9.61	8.96	10.05	8.57

(Table 6.3 .....

Table 6.3 Continued

20	10/7/83-14/7/83	12.17	12.87	12.84	12.37	10.52	12.08	11.49	11.23
21	17/7/83-21/7/83	13.72	12.08	11.53	11.32	10.93	10.68	11.65	9.33
22	24/7/83-27/7/83	15.99	14.04	12.81	13.36	13.03	12.22	13.59	12.01
23	31/7/83-4/8/83	12.44	11.44	10.98	11.18	10.71	10.16	11.32	9.62
24	9/8/83-14/8/83	11.14	9.54	9.02	9.46	8.80	8.26	9.40	7.61
25	17/8/83-22/8/83		8.87	8.64	8.74	8.21	6.99	8.95	7.29
26	31/8/83-6/9/83	10.40	9.85	9.00	9.80	8.48	8.24	9.60	7.70
27	11/9/83-15/9/83	9.30	8.16	8.03	7.83	7.50	7.10	8.16	6.32
28	19/9/83-25/9/83	9.38	8.27	7.71	8.21	7.79	6.69	8.15	6.42
29	26/9/83-4/10/83	7.79	7.02	6.61	6.93	6.12	5.87	6.94	5.73
30	6/10/83-13/10/83	7.44	6.94	6.51	6.93	6.50	5.31	6.95	5.29
31	17/10/83-26/10/83	5.51	4.69	4.68	4.70	4.55	3.76	4.74	3.69
32	27/10/83-6/11/83	5.85	5.21	4.78	4.87	4.46	3.98	4.95	3.83
33	6/11/83-17/11/83	5.17	4.39	4.13	4.21	3.80	3.39	4.16	3.22
34	17/11/83-1/12/83	3.60	3.06	2.85	3.00	2.78	2.31	2.98	2.20
35	1/12/83-21/12/83	2.85	2.33	2.13	2.21	1.95	1.64	2.22	1.42
36	21/12/83-1/1/84	2.09	1.58	1.38	1.49	1.14	0.96	1.43	0.71
Aver. Evap. (mm/day)		6.16	5.57	5.18	5.33	4.89	4.44	5.37	4.20

Table 6.4 Measured Water Surface Temperature and Meteorological Variables

NO.	AIR TEMP	HUMD %	PAN 12	PAN 13	PAN 14	PAN 15	PAN 16	PAN 17	PAN18	PAN19
1	18.9	58.0	14.3	15.2	15.8	15.4	16.0	16.2	15.6	16.7
2	17.0	59.9	13.8	14.5	15.2	15.1	15.5	16.0	15.0	16.4
3	15.6	61.6	12.3	13.2	13.7	13.6	14.1	14.6	13.7	14.9
4	17.6	60.0	13.0	14.0	14.5	14.3	14.8	15.3	14.4	15.4
5	18.5	54.0	15.0	16.3	16.9	16.5	17.2	17.9	16.7	18.3
6	19.0	47.5	17.5	18.3	18.7	18.6	20.0	19.7	18.9	20.2
7	25.4	44.8	21.4	22.6	23.5	23.0	23.7	24.4	23.0	24.6
8	25.0	46.3	21.2	22.5	23.2	22.9	23.7	24.5	23.1	24.8
9	24.4	39.0	19.8	21.7	22.2	21.8	22.7	23.5	22.0	23.8
10	25.9	50.3	22.3	23.9	24.6	24.3	25.0	25.7	24.2	26.1
11	29.5	39.9	24.6	25.9	26.7	26.4	27.3	28.4	26.5	28.4
12	30.2	39.1	24.5	25.7	26.4	26.2	26.8	27.7	26.2	27.8
13	31.1	41.5	26.4	28.3	28.7	28.2	29.1	30.0	28.2	30.4
14	32.1	40.5	26.2	27.8	28.4	28.2	30.0	29.8	28.4	30.1
15	31.4	44.2	25.9	27.1	27.8	27.7	28.6	29.2	28.0	29.8
16	31.0	42.9	26.5	28.0	28.0	28.5	29.1	30.4	28.9	30.2
17	32.4	41.4	28.6	30.0	30.6	30.9	31.2	31.9	30.6	32.3
18	30.7	51.0	28.0	29.9	30.7	30.3	31.0	32.4	30.3	32.7
19	31.9	41.8	27.6	29.7	30.4	30.2	30.6	32.9	29.9	32.3
20	34.0	39.7	28.5	30.3	30.7	31.1	31.2	33.0	30.3	32.7
21	34.9	29.1	28.9	30.5	31.2	32.2	30.9	33.6	30.9	33.2
22	33.9	41.1	28.4	30.5	31.1	30.8	31.3	33.1	30.8	33.6
24	31.8	48.1	28.1	29.6	30.0	30.3	30.7	32.3	29.9	32.4
29	N.A.	N.A.	23.1	24.4	24.2	24.3	24.6	27.4	25.4	27.4
31	N.A.	N.A.	23.6	25.2	25.5	25.6	26.1	27.2	25.5	27.3
32	N.A.	N.A.	22.2	23.6	23.9	24.5	24.1	25.6	23.9	25.8
33	N.A.	N.A.	20.2	21.6	22.0	22.0	22.5	23.5	21.9	23.7
34	N.A.	N.A.	19.2	20.5	20.8	20.9	21.2	22.4	20.7	22.4
35	N.A.	N.A.	16.0	17.1	17.4	17.6	17.9	18.7	17.4	18.6
36	N.A.	N.A.	13.5	14.5	14.8	14.5	15.8	15.8	14.4	15.2
MEAN	23.3	50.6	19.3	20.5	21.1	20.9	21.6	22.3	21.0	22.5

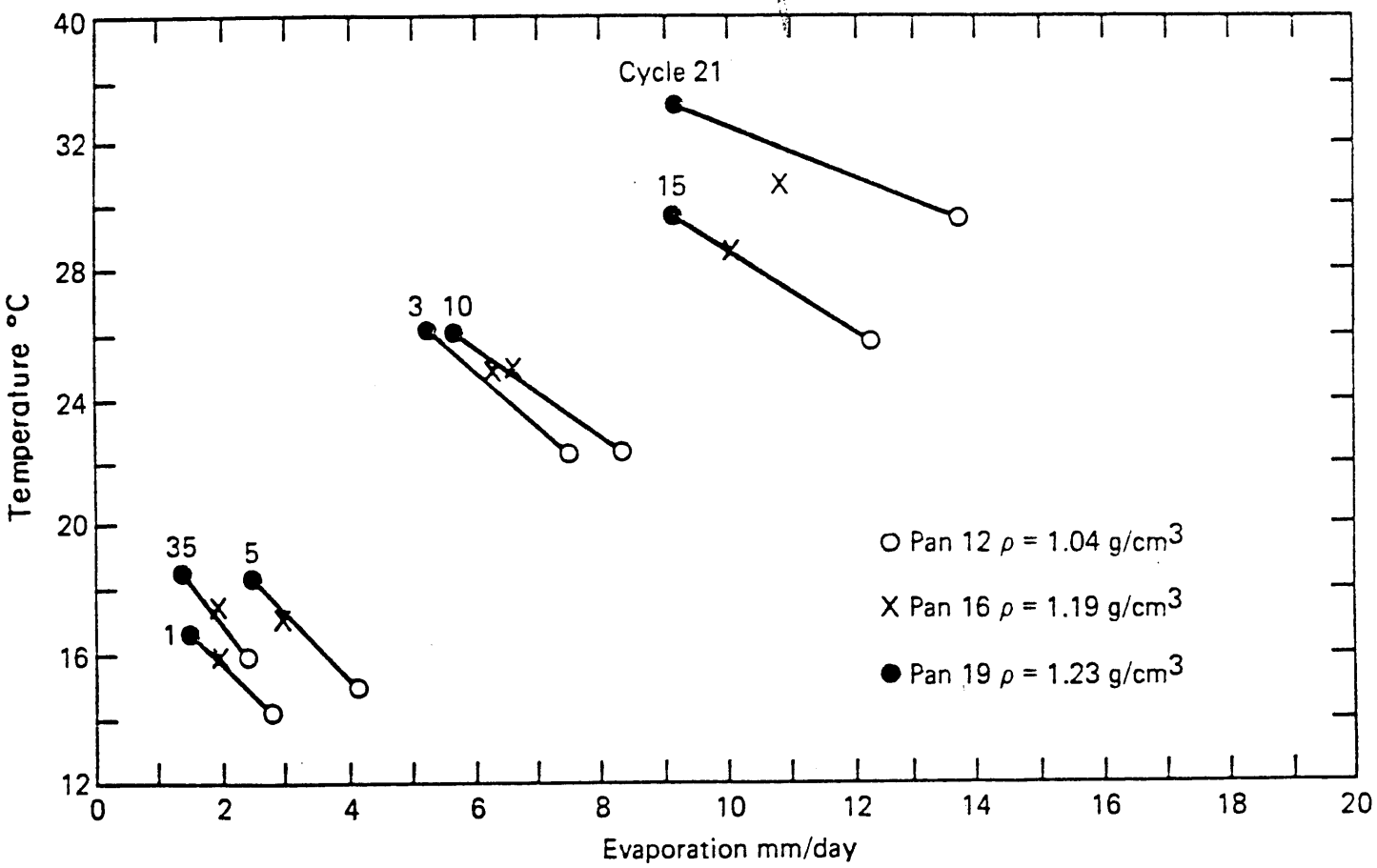

Fig. 6.3 Measured Water Surface Temperature and Evaporation for Pans 12, 16 and 19.

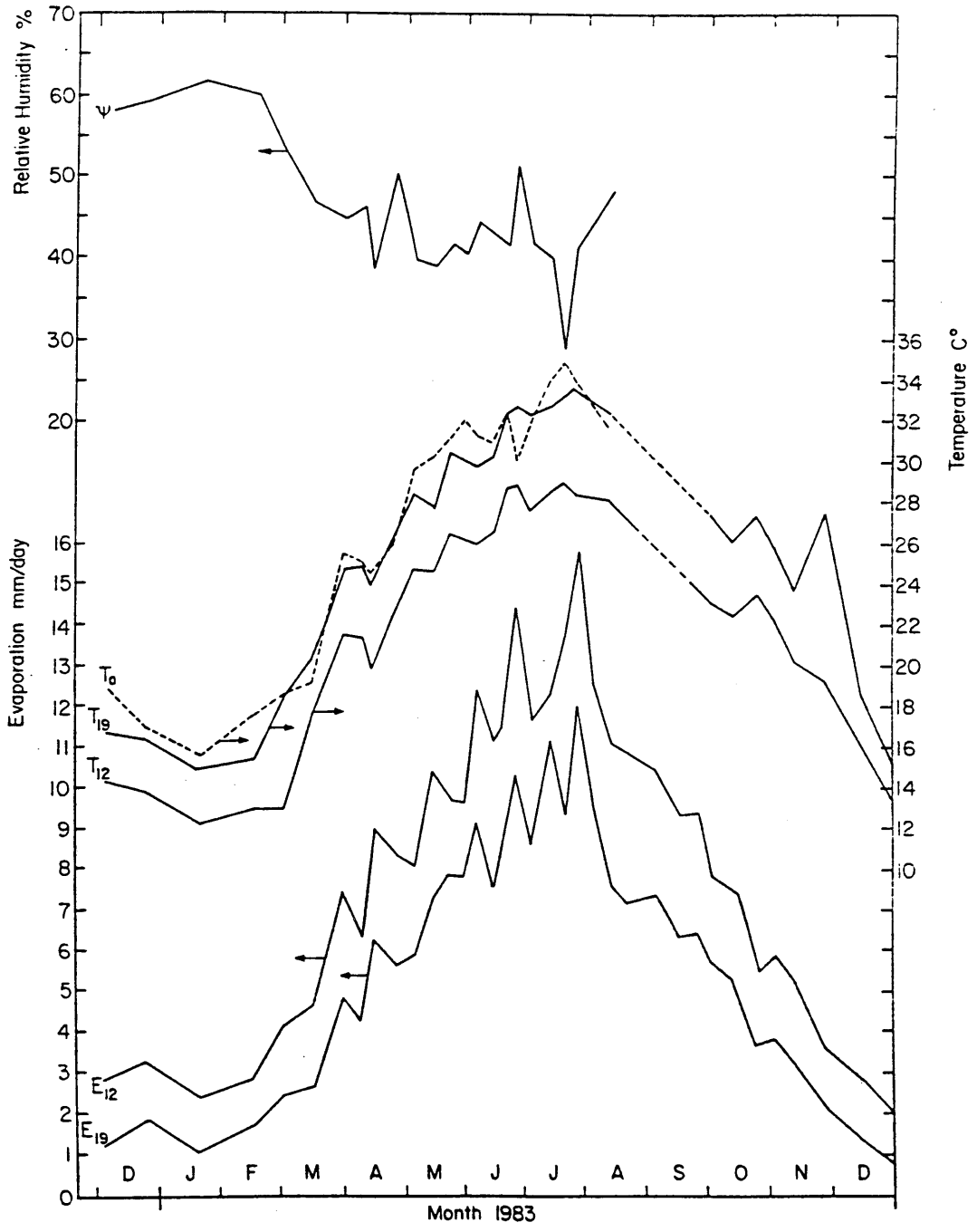

Fig. 6.4 Cycle Average Air Temperature and Relative Humidity plus Water Surface Temperature and Evaporation for Pan 12 and 19

22.5°C compared with 19.3°C for Pan 12. A maximum temperature difference between pans of greater than 5°C occured during July. The daily mean evaporation from Pan 12 was 6.16 mm/day compared with 4.20 mm/day for Pan 19.

6.3.4 Computation of Saturation Vapor Pressure For the Dead Sea Brines

Data from the 23 cycles with complete meteorological measurements were used to determine the effect of salinity, temperature and ionic composition on saturation vapor pressure. From eq. 6.3 evaporation rate in pan j is

$$E_j = f(W_z)\{e'_{sat}(T_j,S_j) - \phi\, e_{sat}(T_a)\} \tag{6.12}$$

Dividing eq. 6.12 by eq. 6.1, assuming identical $f(W_z)$ for the eight pans, and simplifying,

$$e'_{sat}(T_j,S_j) = \frac{E_j}{E_{fresh}}\,[e_{sat}(T_f) - \phi\, e_{sat}(T_a)] + \phi\, e_{sat}(T_a) \tag{6.13}$$

where T_f = the surface temperature for a fresh water pan. $e'_{sat}(T_j,S_j)$ can thus be determined from measurements of E_j, E_{fresh}, T_f, T_a and ϕ.

Unfortunately, none of the evaporation pans contained fresh water; therefore data from the least saline pan (Pan 12) were used in eq. 6.13.

Thus, E_{fresh} and $e_{sat}(T_f)$ in eq. 6.13 are replaced by E_{12} and $e'_{sat}(T_{12},S_{12})$, respectively, yielding

$$e'_{sat}(T_j,S_j) = \frac{E_j}{E_{12}} [e'_{sat}(T_{12},S_{12}) - \phi\, e_{sat}(T_a)] + \phi\, e_{sat}(T_a) \qquad (6.14)$$

where subscript j stands for Pan 13 to 19 and $e'_{sat}(T_{12},S_{12})$ is given by

$$e'_{sat}(T_{12},S_{12}) = \beta(S_{12})\, e_{sat}(T_{12}) \qquad (6.15)$$

The saturation pressure for fresh water at temperature T is computed by the Magnus-Tetens formula (TVA, 1972):

$$e_{sat}(T) = 6.093 \times 10^{(7.5T\ /(237+T))} \qquad (6.16)$$

where T is in °C and e_{sat} is in mbar. The value of $\beta(S_{12})$ in eq. 6.15 was obtained from data reported by Arons and Kientzler (1954) on saturation vapor pressure for sea water of salinity equal to that of concentrated Mediterranean Sea water in Pan 12. This value ranged from .969 to .971 due to slight cycle to cycle variation in the salinity of Pan 12.

Table 6.5 presents saturation vapor pressures computed from eq. 6.14 for the eight pans and the 23 cycles based on meteorological conditions and surface water temperatures of Table 6.4. Table 6.6 lists values of $\beta(S_j)$, i.e. the saturation vapor pressure for each pan divided by the saturation vapor pressure for fresh water computed at the same temperature from eq. 6.16. In addition to values of β for each cycle, the time weighted mean and the standard deviations are presented.

Table 6.5 Computed Values of Saturation Vapor Pressure (mbars) for the Eight Pans

CYCLE	PAN 12	PAN 13	PAN 14	PAN 15	PAN 16	PAN 17	PAN 18	PAN 19
1	15.83	15.40	15.01	15.09	14.76	14.50	15.24	14.33
2	15.33	14.85	14.41	14.61	14.22	13.86	14.65	13.72
3	13.89	13.66	12.88	13.04	12.65	12.38	13.10	12.24
4	14.53	14.16	13.96	14.02	13.79	13.58	14.06	13.54
5	16.56	15.76	15.36	15.51	15.09	14.66	15.58	14.55
6	19.43	17.79	16.76	17.05	16.47	15.61	17.35	15.47
7	24.75	23.12	23.03	23.21	22.13	21.30	23.04	21.17
8	24.43	23.48	22.87	23.39	22.35	21.79	22.94	21.41
9	22.36	21.58	20.95	20.92	20.22	19.72	21.22	19.62
10	26.10	25.43	24.93	24.95	24.24	23.42	24.89	23.18
11	29.98	28.78	28.15	28.57	27.48	26.79	28.52	26.38
12	29.88	28.68	27.79	28.09	27.53	26.41	29.09	26.35
13	33.45	32.98	32.83	32.98	31.50	31.12	33.13	30.66
14	33.05	31.88	32.23	32.34	32.65	30.78	32.75	30.55
15	32.48	31.38	30.84	30.83	30.30	29.47	30.96	29.43
16	33.63	32.35	31.60	31.90	30.85	30.24	31.70	29.58
17	37.98	36.61	35.82	36.62	35.31	34.35	36.44	33.76
18	36.60	35.59	34.30	34.75	34.05	33.36	34.68	32.77
19	35.80	34.29	33.35	33.76	33.04	32.15	33.65	31.60
20	37.82	38.78	38.75	38.10	35.56	37.67	36.89	36.54
21	38.65	35.97	35.07	34.73	34.08	33.68	35.26	31.48
22	37.55	35.62	34.41	34.95	34.62	33.82	35.17	33.61
24	36.92	34.86	34.19	34.77	33.92	33.22	34.69	32.38

Table 6.6 Computed Values of β for the Eight Pans (eq. 6.4)

CYCLE	PAN 12	PAN 13	PAN 14	PAN 15	PAN 16	PAN 17	PAN 18	PAN 19
1	0.97	0.89	0.84	0.86	0.81	0.79	0.86	0.75
2	0.97	0.90	0.84	0.85	0.81	0.76	0.86	0.74
3	0.97	0.90	0.82	0.84	0.79	0.75	0.84	0.72
4	0.97	0.89	0.85	0.86	0.82	0.78	0.86	0.77
5	0.97	0.85	0.80	0.83	0.77	0.72	0.82	0.69
6	0.97	0.85	0.78	0.80	0.70	0.68	0.80	0.65
7	0.97	0.84	0.80	0.83	0.76	0.70	0.82	0.68
8	0.97	0.86	0.80	0.84	0.76	0.71	0.81	0.68
9	0.97	0.83	0.78	0.80	0.73	0.68	0.80	0.67
10	0.97	0.86	0.81	0.82	0.77	0.71	0.82	0.69
11	0.97	0.86	0.80	0.83	0.76	0.69	0.82	0.68
12	0.97	0.87	0.81	0.83	0.78	0.71	0.86	0.71
13	0.97	0.86	0.83	0.86	0.78	0.73	0.87	0.71
14	0.97	0.85	0.83	0.85	0.77	0.73	0.85	0.72
15	0.97	0.88	0.83	0.83	0.77	0.73	0.82	0.70
16	0.97	0.86	0.84	0.82	0.77	0.70	0.80	0.69
17	0.97	0.86	0.82	0.82	0.78	0.73	0.83	0.70
18	0.97	0.84	0.78	0.81	0.76	0.69	0.80	0.66
19	0.97	0.82	0.77	0.79	0.75	0.64	0.80	0.65
20	0.97	0.90	0.88	0.84	0.78	0.75	0.85	0.74
21	0.97	0.82	0.77	0.72	0.76	0.65	0.79	0.62
22	0.97	0.82	0.76	0.79	0.76	0.67	0.79	0.65
24	0.97	0.84	0.81	0.81	0.77	0.69	0.82	0.67
MEAN	0.97	0.87	0.82	0.83	0.78	0.73	0.83	0.71
STD.DEV.	0.00	0.03	0.02	0.03	0.03	0.04	0.02	0.03

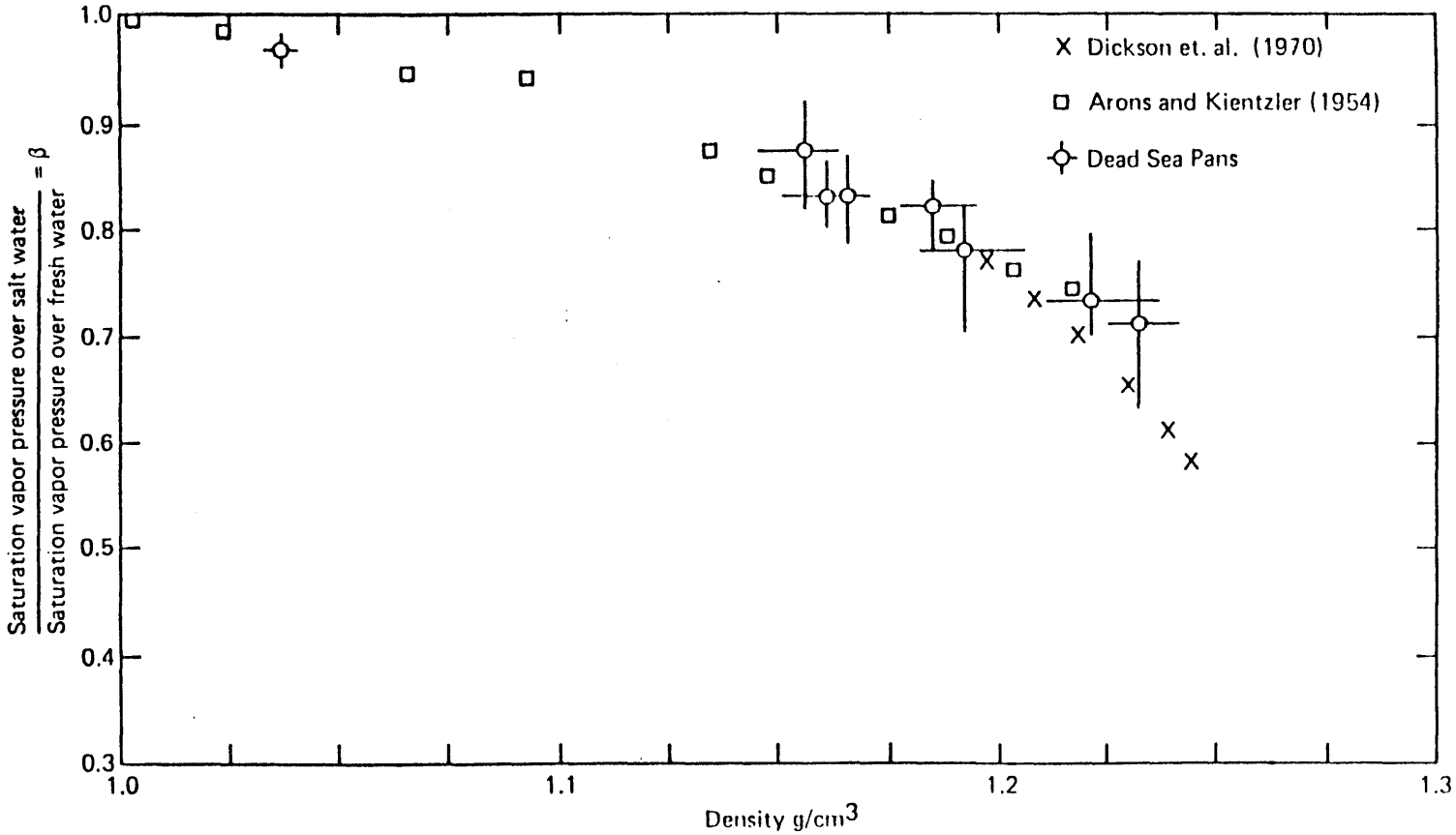

Fig. 6.5 Comparison of β-values with Error Bars for the Eight Pans and the Data Reported by Arons and Kientzler (1954) and Dickson et. al. (1954).

As expected, the maximum reduction in saturation vapor pressure is for Pan 19 (β = .71) which contained Dead Sea water. Pans 13 and 18 had approximately equal densities but Pan 18 had a higher proportion of magnesium ions which reduced the saturation vapor pressure for Pan 18 (β = .83) more than that for Pan 13 (β = .87). Similar results were found for Pans 14 and 16. Figure 6.5 shows a comparison of β for the Dead Sea pans and those computed from data recorded by Dickson et al. (1965) and Arons and Kientzler (1954) for concentrated sea water. For the Dead Sea data the means and the (cycle to cycle) variations in the densities and the computed β values are also shown. For density greater than 1.2 g/cm^3 (S $\simeq$ 265 $^0/_{00}$) the data from Dickson et al. (1965) show a lower value of β than the Dead Sea. This may be due to differential precipitation of salts (primarily NaCl) at high salinities that results in a higher $MgCl_2$ concentration. Unfortunately, information on this aspect is not presented in their paper.

Based on values of β reported in Table 6.6 and the total salinity for each cycle, eq. 6.6 can be used to compute δ for each water type. The mean value of δ for the Dead Sea water (Pan 19) is 1.13×10^{-3}, while that for concentrated sea water (Pan 14) is 0.81×10^{-3}. By contrast, the value for slightly concentrated Mediterranean Sea water (Pan 12) is 0.54×10^{-3} based on the mean value of β = 0.97. This value is consistent with the value ($.537 \times 10^{-3}$) reported by Sverdrup et al. (1942) for sea water. A comparison of δ for the Dead Sea and the Mediterranean seawaters shows the strong dependence of δ on salinity and the ionic composition of the solution. (However, values of δ computed for each cycle showed no apparent dependence on temperature.)

6.3.5 The Negative Temperature Feedback Effect on Evaporation

The inverse relationship between water surface temperature and evaporation and the negative temperature feedback effect on evaporation has been mentioned above. The γ approach is used here to quantitatively demonstrate this effect. Taking the ratio of evaporation of pan j to pan 12 the following expression results:

$$\frac{E_j}{E_{12}} = \left[\frac{\gamma_j}{\gamma_{12}} \right] \left[\frac{e_{sat}(T_j) - \phi\, e_{sat}(T_a)}{e_{sat}(T_{12}) - \phi\, e_{sat}(T_a)} \right] \qquad (6.17)$$

In the above equation, the first term on the right represents the relative salinity effect for pan j while the second term represents the feedback effect. The value of γ and the feed back effect for the eight pans can be computed using eq. 6.11 and known meteorology and water surface temperatures presented in Table 6.4.

The three relative terms of eq. 6.17 are tabulated in Tables 6.7, Table 6.8 and Table 6.9. The mean values for each of the pans are plotted in Fig 6.6 that effectively demonstrates the importance of the feedback effect in the computation of evaporation. For example, (relative to pan 12) the salinity effect for pan 19 would tend to depress the mean evaporation to about 39% of the evaporation from pan 12 (Table 6.8) while the feedback effect increases the rate of evaporation by 65% (Table 6.9). This results in an observed evaporation of 63% from pan 19 (relative to pan 12). This effect is further discussed in Chapter 10 with reference to the expected rate of evaporation from the Dead Sea with the power project in operation.

Table 6.7 Relative Evaporation from the Eight Pans.

CYCLE	PAN 12	PAN 13	PAN 14	PAN 15	PAN 16	PAN 17	PAN 18	PAN 19
1	1.00	0.86	0.74	0.77	0.66	0.58	0.81	0.53
2	1.00	0.87	0.75	0.81	0.70	0.61	0.82	0.57
3	1.00	0.92	0.66	0.71	0.58	0.49	0.74	0.45
4	1.00	0.85	0.77	0.80	0.70	0.62	0.81	0.60
5	1.00	0.84	0.76	0.79	0.71	0.62	0.81	0.60
6	1.00	0.82	0.70	0.74	0.67	0.58	0.77	0.56
7	1.00	0.84	0.83	0.85	0.74	0.66	0.83	0.65
8	1.00	0.90	0.84	0.89	0.79	0.73	0.85	0.69
9	1.00	0.93	0.87	0.86	0.80	0.75	0.89	0.74
10	1.00	0.93	0.87	0.88	0.80	0.71	0.87	0.69
11	1.00	0.91	0.87	0.90	0.82	0.76	0.89	0.73
12	1.00	0.91	0.84	0.86	0.82	0.74	0.94	0.73
13	1.00	0.97	0.96	0.97	0.87	0.84	0.98	0.81
14	1.00	0.91	0.94	0.95	0.97	0.83	0.98	0.82
15	1.00	0.91	0.86	0.86	0.82	0.75	0.87	0.75
16	1.00	0.91	0.86	0.88	0.81	0.76	0.87	0.72
17	1.00	0.92	0.88	0.92	0.85	0.80	0.91	0.76
18	1.00	0.93	0.84	0.87	0.82	0.77	0.86	0.73
19	1.00	0.91	0.85	0.87	0.83	0.77	0.87	0.74
20	1.00	1.06	1.06	1.02	0.86	0.99	0.94	0.92
21	1.00	0.88	0.84	0.83	0.80	0.78	0.85	0.68
22	1.00	0.88	0.80	0.84	0.81	0.76	0.85	0.75
24	1.00	0.86	0.81	0.85	0.79	0.74	0.84	0.68
MEAN	1.00	0.89	0.79	0.82	0.74	0.66	0.83	0.63

Table 6.8 Computed Values of γ for Pans 13 to 19 Relative to γ for Pan 12 (eq. 6.17)

CYCLE	PAN 12	PAN 13	PAN 14	PAN 15	PAN 16	PAN 17	PAN 18	PAN 19
1	1.00	0.68	0.51	0.58	0.44	0.37	0.58	0.30
2	1.00	0.74	0.55	0.61	0.49	0.38	0.63	0.34
3	1.00	0.74	0.47	0.52	0.38	0.29	0.52	0.25
4	1.00	0.63	0.50	0.55	0.43	0.34	0.54	0.32
5	1.00	0.66	0.55	0.60	0.49	0.38	0.60	0.35
6	1.00	0.74	0.60	0.64	0.50	0.44	0.64	0.40
7	1.00	0.71	0.63	0.69	0.55	0.45	0.67	0.43
8	1.00	0.75	0.64	0.71	0.56	0.48	0.65	0.44
9	1.00	0.74	0.65	0.68	0.57	0.49	0.69	0.47
10	1.00	0.73	0.63	0.65	0.54	0.44	0.66	0.41
11	1.00	0.78	0.67	0.72	0.59	0.50	0.71	0.48
12	1.00	0.78	0.67	0.70	0.62	0.50	0.76	0.50
13	1.00	0.77	0.73	0.78	0.63	0.56	0.79	0.51
14	1.00	0.74	0.71	0.74	0.62	0.54	0.74	0.51
15	1.00	0.77	0.66	0.67	0.57	0.49	0.66	0.45
16	1.00	0.75	0.71	0.69	0.59	0.49	0.65	0.47
17	1.00	0.79	0.70	0.72	0.64	0.56	0.73	0.51
18	1.00	0.72	0.59	0.64	0.56	0.45	0.64	0.41
19	1.00	0.71	0.61	0.65	0.59	0.44	0.66	0.44
20	1.00	0.85	0.81	0.75	0.63	0.60	0.76	0.58
21	1.00	0.76	0.68	0.61	0.66	0.51	0.70	0.46
22	1.00	0.68	0.58	0.62	0.58	0.45	0.63	0.42
24	1.00	0.70	0.63	0.64	0.56	0.44	0.66	0.40
MEAN	1.00	0.73	0.59	0.63	0.51	0.42	0.63	0.39

Table 6.9 Feedback Effect for Pans 13 to 19 Relative to the Feedback Effect for Pan 12 (eq. 6.17)

CYCLE	PAN 12	PAN 13	PAN 14	PAN 15	PAN 16	PAN 17	PAN 18	PAN 19
1	1.00	1.27	1.46	1.33	1.52	1.58	1.39	1.75
2	1.00	1.18	1.36	1.33	1.44	1.58	1.31	1.69
3	1.00	1.26	1.41	1.38	1.53	1.68	1.41	1.78
4	1.00	1.35	1.53	1.46	1.64	1.83	1.49	1.87
5	1.00	1.27	1.40	1.31	1.46	1.62	1.35	1.72
6	1.00	1.11	1.16	1.15	1.35	1.31	1.19	1.38
7	1.00	1.18	1.32	1.24	1.35	1.46	1.24	1.50
8	1.00	1.20	1.31	1.26	1.39	1.53	1.29	1.58
9	1.00	1.26	1.33	1.27	1.40	1.53	1.30	1.57
10	1.00	1.27	1.40	1.34	1.47	1.60	1.32	1.68
11	1.00	1.17	1.28	1.24	1.37	1.54	1.26	1.54
12	1.00	1.16	1.26	1.23	1.32	1.46	1.23	1.47
13	1.00	1.26	1.32	1.24	1.38	1.51	1.24	1.58
14	1.00	1.23	1.32	1.29	1.58	1.54	1.32	1.59
15	1.00	1.19	1.30	1.28	1.44	1.54	1.34	1.65
16	1.00	1.21	1.21	1.28	1.37	1.57	1.34	1.54
17	1.00	1.17	1.25	1.29	1.33	1.43	1.25	1.49
18	1.00	1.29	1.42	1.35	1.47	1.71	1.35	1.76
19	1.00	1.28	1.38	1.35	1.41	1.76	1.31	1.67
20	1.00	1.24	1.30	1.35	1.37	1.64	1.24	1.59
21	1.00	1.16	1.24	1.35	1.21	1.52	1.21	1.47
22	1.00	1.29	1.38	1.34	1.41	1.70	1.34	1.79
24	1.00	1.22	1.29	1.33	1.40	1.67	1.27	1.69
MEAN	1.00	1.23	1.35	1.31	1.45	1.59	1.33	1.65

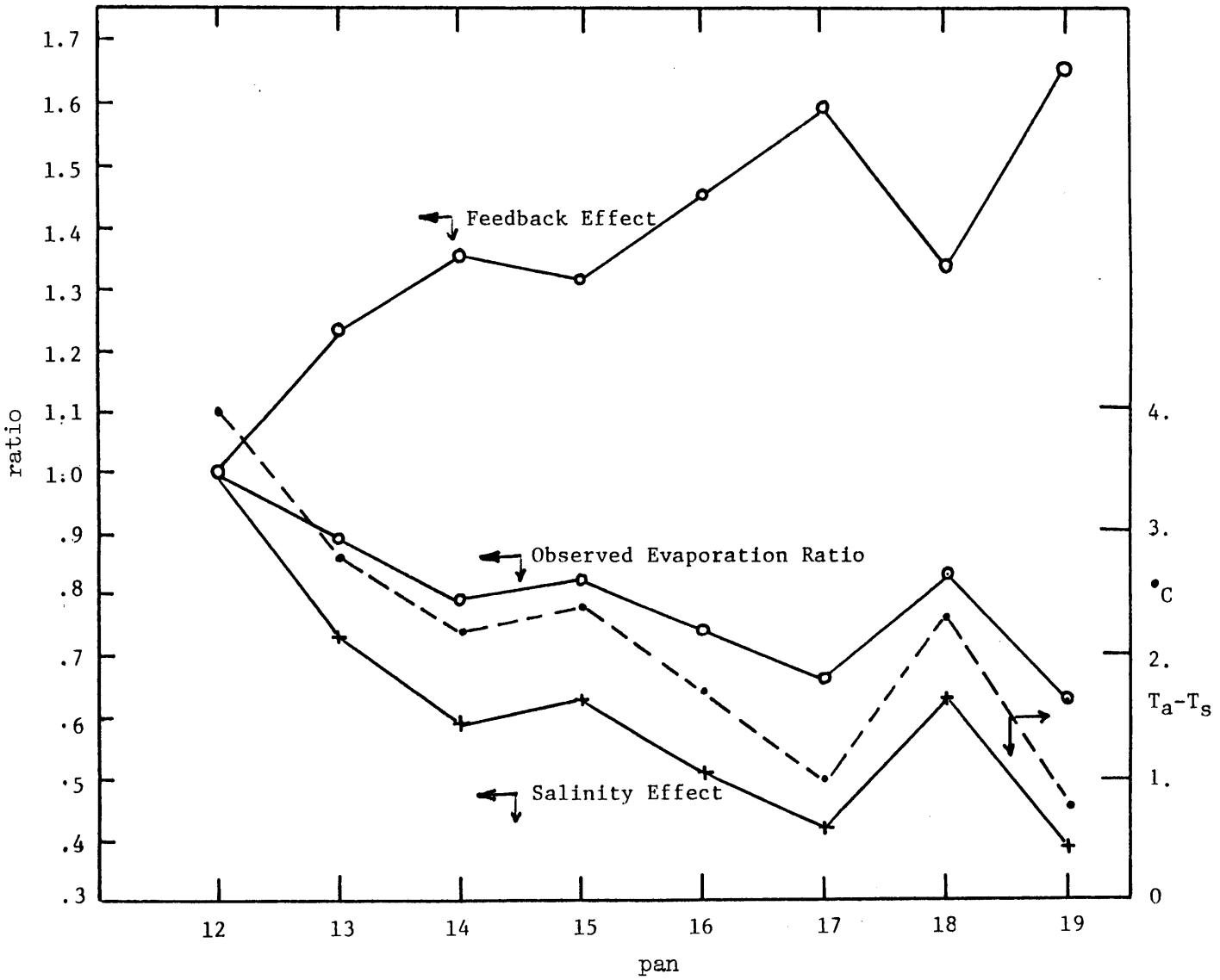

Fig. 6.6 The α-values, γ values and the feedback effect for Pans 13 to 19 relative to Pan 12

6.3.6 Computation of β Based on Compostion

The activity of water in a solution of known chemical composition can be approximated using a composite reduction factor obtained by summing the weighted reduction in saturation vapor pressure due to each of the constituent salts. Thus, for a solution of total concentration χ containing N salts of partial concentration χ_i

$$\beta(\chi) = \frac{1}{\chi} \sum_{i=1}^{N} \chi_i \beta_i(\chi) \tag{6.18}$$

where $\beta(\chi)$ is the activity coefficient of water in a solution of total concentration χ and $\beta_i(\chi)$ is the activity coefficient of water in a solution of single salt i at a total concentration of χ. Robinson and Stokes (1945) have represented χ by the ionic strength (I) defined as:

$$I = \frac{1}{2} \sum_{i=1}^{k} m_i Z_i^2 \tag{6.19}$$

where m_i = molal concentration of ion i and Z_i = charge on the ion (1 for a monovalent ion and 2 for a divalent ion), and k is the number of ions. Harbeck (1955) expressed χ in terms of salinity (S) and computed the vapor pressure reduction for sea water and various natural brines. Robinson and Bower (1965) suggested the use of ionic concentration (I_c) defined as:

$$I_c = \frac{1}{2} \sum_{i=1}^{k} m_i Z_i \tag{6.20}$$

However, based on their analysis of a water-sodium chloride-barium chloride system they rejected this method in favor of that based on ionic strength. A fourth possible weighting would use molality (m) as a

measure of concentration.

Using the above four measures of concentration, $\beta(\chi)$ was computed from data in Fig. 6.1 for Cycle 9 and Pans 18 and 19, based on the following chemical composition expressed in partial salinity (parts per thousand by weight):

Pan	NaCl	$MgCl_2$	$CaCl_2$	KCl	NaBr	Total
18	56.6	101.2	32.1	9.3	4.6	203.8
19	71.4	144.0	42.2	12.7	5.7	276.0

The computed values of β are shown in Table 6.10. It is clear that all four methods yield values of β approximately equal to the value obtained from the analysis of the evaporation pan data. This suggests that simple analytical procedures can be used to compute the reduction in saturation vapor pressure due to the presence of salts.

6.4 Direct Measurement of Saturated Vapor Pressure

6.4.1 Previous Studies

As discussed above, knowledge of saturation vapor pressure allows a direct assessment of evaporation using eq. 6.3. For simple aqueous solutions with one or two inorganic salts, data on saturation vapor pressure are available in standard handbooks of physics and chemistry (National Research Council, 1928; Weast, 1981). Fabuss et. al. (1965) have presented details of their experimental set-up to measure the saturation vapor pressure of aqueous solutions (and mixtures) of KCl, NaCl, Na_2SO_4 and $MgSO_4$. Their results show that for a given molality, the value of β (Eq. 6.4) does not vary significantly with temperature.

TABLE 6.10

Computed values of β using different measures of concentration

Pan	$\beta(S)$	$\beta(I)$	$\beta(I_c)$	$\beta(m)$	observed β (cycle 9)
18	0.81	0.79	0.80	0.80	0.80
19	0.66	0.68	0.67	0.65	0.67

Saline water bodies found in nature typically have complex chemical compositions. For such saline solutions, little data on saturation vapor pressure has been published. Arons and Kientzler (1954) reported saturation vapor pressure measurements for concentrated sea water ranging from about 9 $^{o}/_{oo}$ to 290 $^{o}/_{oo}$ for temperature ranging from freezing to 25°C and tied these to measurements by Higashi et. al. (1931) for the temperature range of 25 to 175°C. Values of β (eq. 6.4) computed using their measurements do not exhibit a temperature dependence. Based on controlled laboratory experiments, Dickson et. al. (1965) reported saturation vapor pressure values for Great Salt Lake brines in the salinity range of 247 $^{o}/_{oo}$ to 292 $^{o}/_{oo}$ and temperature range of -10 to 40°C. A small but systematic dependence of β on temperature was observed with maximum values occurring at temperatures between 15 and 20°C. Values at 40°C ranged from 4% (at 247 $^{o}/_{oo}$) to 7% (at 292 $^{o}/_{oo}$) less than maximum.

6.4.2 Direct Measurements of Saturation Vapor Pressure For the Dead Sea Brines

Marcus (1984) has reported saturation vapor pressure measurements for seven different mixtures of Dead Sea and Mediterranean Sea brines with Dead Sea water composition in the mixture ranging from 38.8% to 87.2% by weight and for temperatures from 15°C to 35°C. Based on his measurements, the activity coefficient of water (eq. 6.4) in each of the seven mixtures is shown in Table 6.11(a). Comparison between β values for samples 2, 3, and 4 suggests an error in measurements for sample 3. In each case, the minimum values of β occurs at 35°C. Apart from this no consistent systematic temperature dependence for the seven samples is

Table 6.11 (a) Computation of β based on Direct measurements of saturation vapor pressure Marcus (1984)

Sample	W*	Temperature °C 15	20	25	30	35	Mean	St. Dev.
1	38.8	0.88	0.88	0.89	0.89	0.88	0.88	.01
2	50.0	0.85	0.87	0.87	0.86	0.85	0.86	.01
3	53.3	0.90	0.91	0.90	0.88	0.87	0.89	.02
4	64.7	0.86	0.87	0.86	0.85	0.84	0.86	.01
5	73.1	0.85	0.84	0.83	0.80	0.78	0.82	.03
6	82.7	0.81	0.80	0.79	0.78	0.78	0.79	.01
7	87.2	0.76	0.76	0.76	0.76	0.76	0.76	.00
8**	91.2	0.72	0.72	0.73	0.74	0.73	0.73	.00

* Weight % of Dead Sea Water in Mixture

** 8 Based on extrapolation of SVP values using samples 6 and 7.

observed. The value of β for sample 8 has been obtained by linearly extrapolating the saturation vapor pressure for sample 6 and 7 and dividing by the saturation vapor pressure of fresh water at the appropriate temperature (eq. 6.16). Note the relative proportion of Dead Sea water in sample 8 is the same as that for pan 17.

Based on his analysis, Marcus (1984) recommends the use of the following relationship to compute the saturation vapor pressure for mixtures of Dead Sea and Mediterranean Sea water:

$$e'_{sat}(T,S) = (5.3 + .0526\ T + .0274\ T^2) - (-.029 + .0033T + 1.16 \times 10^{-5} T^2)w \qquad (6.21)$$

where, w = the fraction by weight of Dead Sea brine in the mixture. Using this relationship the activity coefficient for water in the 8 samples are tabulated in Table 6.11(b) along with the percentage errors relative to measured values tabulated in Table 6.11(a). For values of w less than 50% and greater than about 85% the regression relationship overestimates β. For values of w between 50% and 85% the regression relationship underestimates the value of β. Also, for values of w greater than about 87% the regression equation is no longer valid since the computed value of β for sample 8 exceeds the measured value of β for sample 7.

Table 6.12 shows a comparison of β-values for evaporation pans 15, 16 and 17 based on our analysis (Table 6.6) and the results reported by Marcus (1984). Since direct vapor pressure measurements were not available for the exact mixtures in pans, the regression relationship

Table 6.11 (b) Computation of β based on the regression relationship for saturation vapor pressure Marcus (1984).

Sample	W*	15	20	25	30	35	Mean	Std. Dev.	** % error
1	38.8	0.89	0.90	0.90	0.89	0.87	0.89	0.01	0.8
2	50.0	0.87	0.87	0.87	0.87	0.85	0.86	0.01	0.3
3	53.3	0.86	0.86	0.86	0.86	0.84	0.86	0.01	-4.0
4	64.7	0.84	0.83	0.83	0.83	0.81	0.83	0.01	-3.0
5	73.1	0.83	0.81	0.81	0.81	0.79	0.81	0.01	-1.5
6	82.7	0.81	0.79	0.79	0.78	0.77	0.79	0.01	-0.4
7	87.2	0.80	0.78	0.77	0.77	0.76	0.78	0.01	-2.6
8	91.2	0.79	0.77	0.77	0.76	0.75	0.77	0.01	1.5

Table 6.12 Comparison of β values for pans 15, 16 and 17 based on evaporation pan data (β_{pan}) and regression equation (β_r) (eq. 6.21).

	Pan 15		Pan 16		Pan 17	
Cycle	β_{pan}	β_r	β_{pan}	β_r	β_{pan}	β_r
1	0.86	0.84	0.81	0.81	0.79	0.78
2	0.85	0.84	0.81	0.81	0.76	0.79
3	0.84	0.85	0.79	0.82	0.75	0.80
4	0.86	0.85	0.82	0.82	0.78	0.79
5	0.83	0.84	0.77	0.81	0.72	0.78
6	0.80	0.84	0.70	0.80	0.68	0.77
7	0.83	0.84	0.76	0.80	0.70	0.77
8	0.84	0.84	0.76	0.80	0.71	0.77
9	0.80	0.84	0.73	0.80	0.68	0.77
10	0.82	0.84	0.77	0.80	0.71	0.77
11	0.83	0.84	0.76	0.80	0.69	0.78
12	0.83	0.84	0.78	0.80	0.71	0.76
13	0.86	0.83	0.78	0.80	0.73	0.76
14	0.85	0.83	0.77	0.79	0.73	0.76
15	0.83	0.83	0.77	0.80	0.73	0.76
16	0.82	0.83	0.77	0.80	0.70	0.76
17	0.82	0.83	0.78	0.79	0.73	0.75
18	0.81	0.83	0.76	0.79	0.69	0.75
19	0.79	0.83	0.75	0.79	0.64	0.75
20	0.84	0.83	0.78	0.79	0.75	0.75

Table 6.12 Cont.

	Pan 15		Pan 16		Pan 17	
Cycle	β_{pan}	β_r	β_{pan}	β_r	β_{pan}	β_r
21	0.72	0.82	0.76	0.79	0.65	0.75
22	0.79	0.83	0.76	0.79	0.67	0.75
23	0.81	0.83	0.77	0.79	0.69	0.75
Mean	0.83	0.84	0.78	0.80	0.73	0.77
Std. Dev.	0.03	0.01	0.03	0.01	0.04	0.02
% Dif. Means	1.2		2.6		5.5	

(eq. 6.21) has been used. For each of the three pans, the mean β-values based on the regression equation is higher than the values based on the analysis of evaporation pan data. For pan 15, with 63.1% Dead Sea brines, the % variation in the two means is 1.2% and for pan 16 with 77.6% Dead Sea brines, the corresponding variation is 2.6%. Clearly, as mentioned above, eq. 6.21 is not valid for pan 19 with 91.2% Dead Sea water. It is interesting to note however that the mean β value for pan 19 based on evaporation pan analysis (0.71) compares well with the β values obtained in Table 6.11(a) based on an extrapolation of the measured saturation vapor pressure values (β=.73).

It is worth noting that the field experiments and the controlled laboratory experiments were conducted at two different periods and by two different organizations. It is not clear whether the Mediterranean and the Dead Sea samples used in the two experiments had identical ionic composition. Thus, the observed small differences in the β values based on the two experiments could result from differences in chemical composition and total salinity of the Dead Sea samples. Controlled laboratory experiments if carefully conducted would yield more accurate results than field experiments.

6.5 Conclusions Based On Analysis of Evaporation Pan Data

The dependence of evaporation on meterological variables, salinity and chemical composition has been analysed using data from evaporation pans located near the Dead Sea. The commonly used approach to account for the salinity effects based on ratios of salt water to fresh water evaporation rates (α-approach; eq. 6.7) is hard to use accurately because

α is a function of salinity, ionic composition and the meteorological variables. A more accurate method is the β-approach (Eq. 6.5) which is based on the effect of salinity on saturation vapor pressure. Further, the importance of the negative temperatures feedback effect on evaporation has been discussed and quantified in Section 6.3.5.

The activity of water in a solution, β can be computed indirectly by field experiments as described herein or measured directly in a controlled laboratory experiment. For solutions involving more than one salt, several approaches of computing β based on a weighted average of the dependence for single solutions, show good agreement with relationships based on measured data. Comparison of the average decrease in evaporation for the diluted Dead Sea brine (β = .83; Pan 18) with that for concentrated seawater of the same salinity (β = .87; Pan 13) illustrates the dependence of evaporation on chemical composition.

Finally, the measurement of saturation vapor pressure of mixtures of Dead Sea and Mediterranean Sea water under controlled laboratory conditions has provided additional confidence in our analysis of the Dead Sea evaporation pan data as well as on the computation of the effect of salinity on evaporation.

6.6 Historical Estimates of Annual Evaporation From The Dead Sea

The classical study of evaporation from the Dead Sea is due to Neumann (1958). Using an energy balance approach he computed an annual evaporation rate of 1.47 m from the Northern Basin and 1.80 m from the Southern basin with an area weighted average of 1.55 m for the entire Dead Sea. The difference was attributed primarily to increased insolation in the Southern basin. A later study also based on the energy

budget approach, conducted by Assaf (1980) using historic data, yielded an annual evaporation rate of 1.80 m. It is interesting to note that the evaporative heat flux computed by both Neumann (1958) and Assaf (1980) agree very well -- 141 W/m^2 and 144 W/m^2 respectively. The difference in the evaporative mass flux arises because Neumann divides the heat flux by the density of brine (1.18 g/cc) whereas Assaf uses the density of fresh water which is correct.

Recently Stanhill (1983) has estimated evaporation using a combination of historic long-term meteorological data and recent measurements of the Dead Sea temperature profiles to be 1.38 m. This is close to a preliminary estimate of 1.37 m for the water year 1980 estimated by Salhotra et. al. (1984) as part of the current study. Calder and Neil (1984) used an approach similar to Penman (1948 and 1961) and estimated the rate to be 1.56 m. Finally, Tahal (1982) using a water balance approach for the year 1970/71 estimate the annual evaporation to be 1.60 m. These various estimates are tabulated in Table 6.13.

Table 6.13

Various estimates of annual Evaporation from the Dead Sea

Source	
Neumann (1958)	1.55 m
Assaf (1980)	1.80 m
Tahal (1982)	1.60 m*
Stanhill (1982)	1.38 m
Calder and Neal (1984)	1.56 m
Salhotra et. al. (1984) (also see Chapter 9 and 10)	1.37 m**

* For 1970-1971

** Water year 1980-1981

CHAPTER 7

THE TURBULENT KINETIC ENERGY BUDGET AND MIXING PROCESSES

7.1 Introduction

This chapter discusses the various components of the turbulent kinetic energy budget in the context of stratified lakes. These include wind stirring, penetrative convection and shear generation at the interface as the sources of turbulent kinetic energy and the sinks include the increase in potential energy associated with entrainment, leakage of energy by means of internal waves into the hypolimnion and dissipation of energy due to viscous friction.

These processes have been studied by a number of researchers using different techniques. These include a variety of experimental studies such as grid mixing and wind tunnel experiments (Turner (1968), Kato and Philips (1969), Wu (1973), Kantha and Long (1980) and Atkinson (1984), elaborate field studies (Turner (1969), Farmer (1975) and Halpern (1974), as well as numerical and analytical model studies (Imberger (1981), Bloss and Harleman (1979), Denman (1973) and Niiler (1975)). The ultimate objective of all these studies, has been to develop the ability to estimate the magnitude of mixing energy available for entrainment in a variety of field situations.

A popular numerical modelling approach has been to use an integral entrainment model based on the parameterization of the turbulent kinetic energy equation. This method is further discussed in Section 7.3. Typically the final mixing algorithm contains a number of calibration

coefficients whose value is estimated based on simplified laboratory experiments or site specific field studies.

An alternate approach that has also been suggested in the literature is to compute the net energy available for mixing based on an analysis of the stability index/potential energy budget for the water body. The merits of this method are discussed in Section 7.2.

7.2 The Stability Index Approach to Mixing Processes

7.2.1 Definition of Stability Index

Schmidt (1915, 1928) defined the stability of a lake as the amount of work required to mix the entire body of water to a uniform density without addition or subtraction of heat or mass. The Stability Index (SI) can thus be expressed as the potential energy of a fully mixed lake less the potential energy of the stratified lake possessing the same amounts of ass, salt, and heat, i.e.:

$$SI = Mg\,\bar{z} - \int_{\text{datum}}^{\text{surface}} \rho(z)\,A(z)\,gz\,dz \qquad (7.1)$$

where M = the mass of the lake and $\bar{z}$ = the center of mass of the fully mixed lake. The above can be expressed as:

$$SI = \int_{\text{datum}}^{\text{surface}} g(\bar{\rho} - \rho(z))(z - \bar{z})\;A(z)\,dz \qquad (7.2)$$

where,

$$\bar{z} = \frac{\int \rho(z)\,A(z)z\,dz}{\int \rho(z)\,A(z)\,dz} \qquad (7.3)$$

and

$$\bar{\rho} = \frac{\int \rho(z)\, A(z)\, dz}{\int A(z)\, dz} \tag{7.4}$$

Note that the limits of integration in eq. 7.3 and 7.4 are the same as is eq. 7.2. In the case of most field studies, $\rho(z)$ is measured at a few discrete locations in which case the above integrals are evaluated by suitably discretizing the lake into a number of horizontal layers and adding the contribution of each layer to the stability index.

7.2.2 The Stability Index Budget

The various physical processes that affect the vertical stratification within a lake can be classified as either increasing or decreasing the stability index of the lake. For example, mixing processes by entraining heavier fluid from the hypolimnion into the epilimnion, decrease the stability index of the lake. Similarly, warming of a lake during the summer increases the stability of the lake. The reverse is true during the fall and winter cooling periods. Fig. 7.1 qualitatively shows the effect of various physical processes on the stability of the Dead Sea.

The above ideas can be mathematically expressed in terms of a stability index budget for a lake expressed as:

$$SI_{t+\Delta t} = SI_t + \Delta SI_h + \Delta SI_i - \Delta SI_{mix} \tag{7.5}$$

where SI_t and $SI_{t+\Delta t}$ = the stability index of the lake at time t and $t + \Delta t$, ΔSI_h and ΔSI_i = the changes in stability index due to heating/cooling and due to inflow/outflows respectively. Finally ΔSI_{mix} = the reduction in stability index due to the mixing processes.

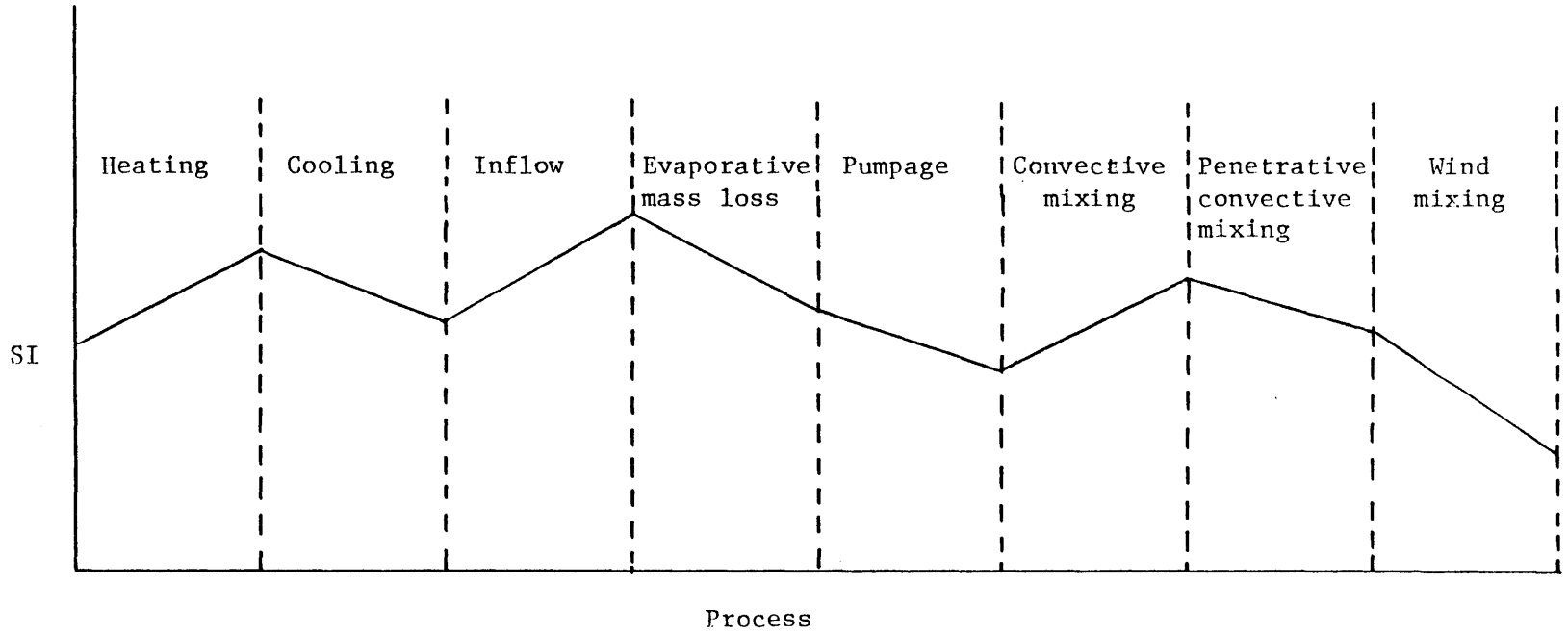

Fig. 7.1 The Effect of Various Physical Processes on the Stability Index of a Lake

This method of computing the mixing energy (ΔSI_{mix}), although intuitively very appealing, often cannot be used directly since it is very sensitive to the sequence in which the physical processes occur. This is illustrated by the following simple example.

Consider a deep fresh water lake that is fully mixed at time t_o, subjected to two different sequences of physical processes. In the first case, the lake experiences a period of intense wind mixing followed by a period of warming. Clearly, the wind would have no effect on the fully mixed profile. Subsequent warming would then result in some thermal stratification. This sequence is shown in Fig. 7.2(a).

Fig. 7.2(b) shows the evolution of profiles with the fully mixed lake first subjected to a period of warming followed by intense wind mixing, both proceses of the same magnitude as in the first case. Warming would lead to thermal stratification which would be completely or partially destroyed by the intense wind activity. The magnitude of mixing energy computed in the two cases by using eq. 7.5 would be quite different since the final profiles in the two cases are very different although the initial profile and the magnitudes of physical forcing functions are identical.

Similar more complex examples can be devised for halothermal lakes. This realization explains the ambiguous results obtained by the previous application of this method to the Dead Sea. (Ref. 109). For this reason the method is suitable only for cases where the exact sequence of processes is known or else the profiles are measured at very small intervals during which a single dominant process can be identified. Unfortunately, the Dead Sea data does not satisfy this criteria. Therefore mixing energies cannot be computed directly from the data.

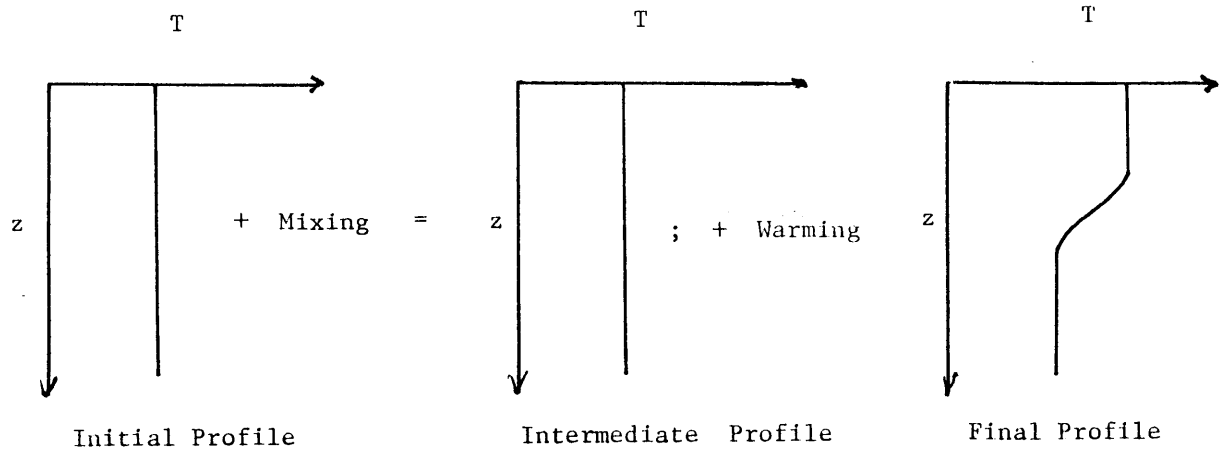

Fig. 7.2(a)

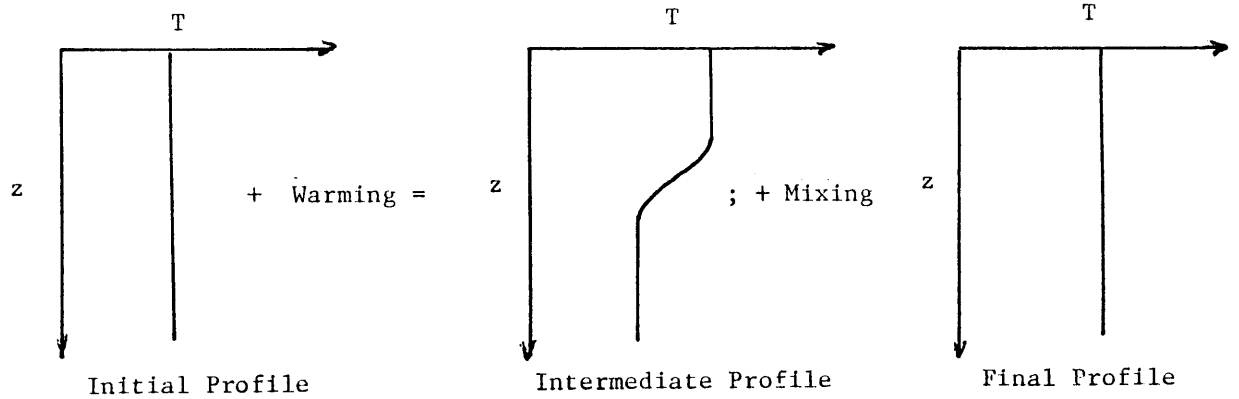

Fig. 7.2 (b)

Fig. 7.2 The Effect of Two Different Sequences of Physical Processes on Lake Stratification.

7.3 Integral Entrainment Model

7.3.1 The Turbulent Kinetic Energy Equation

Integral or mixed layer models typically use a mixing algorithm based on the parameterization of the turbulent kinetic energy (TKE) equation. For the horizontally homogeneous case this can be expressed as (Kraus 1972):

$$\frac{\partial \bar{q}}{\partial t} = -\frac{\partial}{\partial z}\left[\overline{w'\left(q + \frac{p'}{\rho}\right)}\right] - \overline{u'w'}\frac{\partial \bar{u}}{\partial z} - \frac{\overline{g\rho'w'}}{\rho_o} - \varepsilon \qquad (7.6)$$

where q = turbulent kinetic energy per unit mass, u' and w' = turbulent velocity fluctuations, p' = turbulent pressure fluctuations, $\bar{u}$ = the velocity scale associated with the mean motion of the epilimnion (see also Section 7.3.3), and ε = energy loss due to viscous dissipation.

The first term in eq. 7.6 is the storage term that accounts for the temporal change in TKE within the water body. The second represents the redistribution of kinetic energy in the vertical direction by turbulence itself. It includes the source of TKE due to wind stirring and pressure fluctuations due to wave action at the surface. The third term is a source of TKE representing the action of Reynolds stress on the mean flow (shear generation term). The remaining two terms represent the loss of TKE due to its conversion to potential energy in the process of entrainment and dissipation due to viscous effects.

Eq. 7.6 can be expressed in an integral form by considering the mechanical energy budget for the hypolimnion (see Appendix C):

$$\frac{d(PE)}{dt} = \Lambda_K + \Lambda_S - \Lambda_T - \Lambda_L - \Lambda_D \qquad (7.7)$$

where Λ_K = the TKE flux generated at the surface due to wind stirring and penetrative convection, Λ_S = the production of TKE by shear at interface, Λ_T = the temporal rate of increase of TKE in the epilimnion, Λ_L = the leakage of energy by radiation of internal waves and Λ_D = the rate of energy dissipation within the epilimnion due to viscous effects. The balance of these terms results in an increase in potential energy due to entrainment and can be expressed as:

$$\frac{d(PE)}{dt} = \frac{1}{2} \Delta\rho \; gh \frac{dh}{dt} \qquad (7.8)$$

where $\Delta\rho$ = the density step across which entrainment occurs, dh = the thickness of the hypolimnion entrained into the epilimnion of thickness h.

7.3.2 Wind Stirring, Penetrative Convection and Visious Dissipation (Λ_K, Λ_D)

One of the problems in the parameterization of the above terms is the identification of an appropriate velocity scale. Two different approaches have been suggested. Zeman and Tennekes (1977) added energies to define a velocity (σ') as:

$$\sigma' = (w_*^2 + c_1' u_{*,w}^2)^{1/2} \qquad (7.9)$$

where c_1' = some calibration constant, w_* = the velocity due to the motion associated with gravitational instabilities or the buoyancy velocity and can be expressed (Deardorff (1970)):

$$w_* = \left[\frac{\alpha_T g \phi h}{2 \rho_o C_p \rho} + \frac{\beta_S g E h S}{2 \rho_o} \right]^{1/3} \qquad (7.10)$$

where E = net evaporation (m/day), h = upper mixed layer depth (m), ϕ = net heat loss ($\frac{KCal}{m^2\text{-sec}}$) and α and β are parameters in the equation of state (Appendix B).

In eq. 7.10, the first term is associated with instabilities caused by surface cooling due to a net flux, ϕ. The second term is associated with instabilities caused by net evaporation. Note $w_* = 0$ if there is no instability, e.g., during periods of net warming and net dilution of the surface. Conversely, w_* is maximum during periods of net cooling and net evaporation.

The other velocity scale, $u_{*,w}$, in eq. 7.9 is the friction velocity at the water surface due to wind. This is computed assuming continuity of shear stress at the air-water interface i.e.,

$$\tau_w = \rho_s u_{*,w}^2 = \tau_a = \rho_a C_z (W_z - u_s)^2 \qquad (7.11)$$

where τ_w and τ_a = the shear stress at the air-water interface, C_z = a drag coefficient and u_s = surface drift velocity. Assuming $u_s \ll W_z$, $u_{*,w}$ can be expressed as:

$$u_{*,w} = \sqrt{\frac{\rho_a}{\rho_s} C_z W_z^2} \qquad (7.12)$$

The drag coefficient C_z depends on the roughness of the surface, kinematic viscosity of the air, the windspeed and atmospheric stability. Based on the analysis of numerous independent studies, Wu (1973) has proposed the following relationship:

$$\frac{1}{C_z} = \frac{1}{\kappa} \ln \frac{gz}{\sqrt{.011 C_z W_z^2}} \tag{7.13}$$

An alternate definition for σ (eq. 7.9) suggested by Kraus and Turner (1967) and followed by Sherman et. al. (1978) is based on adding the powers, i.e.

$$\sigma_1 = (w_*^3 + C_1 u_{*,w}^3)^{1/3} \tag{7.14}$$

where C_1 = some calibration coefficient associated with wind stirring. Note that eq. 7.14 implies a superposition of the power input by wind and penetrative convection.

Having defined the velocity scale, eq. 7.14, the term Λ_K in eq. 7.7 can be expressed as:

$$\Lambda_K = \rho_s \sigma_1^3 \tag{7.15}$$

and represents the flux of turbulent kinetic energy imposed at the water surface.

Following Zemen and Tennekes (1977) argument that the energy loss due to viscous dissipation is proportional to the kinetic energy flux at the surface, Λ_D can be expressed as:

$$\Lambda_D = \rho_s C_k \sigma_1^3 \tag{7.16}$$

where the coefficient C_k is less than 1.

Combining eq. 7.15 and eq. 7.16, the net energy at the interface available for entrainment due to wind stirring and penetrative convection (Λ^*) can be expressed as:

$$\Lambda^* = \Lambda_K - \Lambda_D = (1-C_k)\,\rho_s \sigma^3 \tag{7.17}$$

or

$$\Lambda^* = \rho_s\,(C_c\, w_*^3 + C_w\, u_{*,w}^3) \tag{7.18}$$

or

$$\Lambda^* = \rho_s\, \sigma^3 \tag{7.19}$$

where,

$$\sigma^3 = (C_c\, w_*^3 + C_w\, u_{*,w}^3) \tag{7.20}$$

where $C_c = 1-C_k$ and $C_w = (1-C_k)C_1$.

The two terms in eq. 7.18 represent the energy due to penetrative convection and wind stirring that is available at the interface.

The coefficient C_c represents the efficiency of convective mixing and its value is expected to be less than unity. Conceptually, instability or gravitational mixing releases potential energy (by driving heavier mass downwards) a fraction of which, C_c, is converted into useful kinetic energy that is available for entrainment.

The value of C_w, the parameter associated with wind mixing can however be greater than unity for it represents the product of two factors one of which is larger than unity and the other, $(1-C_k)$ is less than unity. This is further explained below.

The flux of kinetic energy due to wind per unit surface area at the water surface can be expressed as:

$$\frac{\Delta KE_w}{\Delta t} = C_w u_{*,w}^2\, u_s = m\rho_w\, u_{*,w}^3 \tag{7.21}$$

where m = the ratio of surface drift velocity to the friction velocity i.e.

$$m = \frac{u_s}{u_{*,w}} \tag{7.22}$$

Bloss and Harleman (1979) used a value of m equal to unity. Based on Wu's (1973) results, a value of m = 16 can be computed. Madsen (1977) suggests u_s to be an order of magnitude larger than $u_{*,w}$. The coefficient C_w in eq. 7.18 is thus:

$$C_w = m\ (1-C_k) \tag{7.23}$$

whose value may exceed unity. C_w thus includes two factors, one of which (m>1) represents the uncertainty in the estimation of an approximate wind velocity and the other ($1-C_k < 1$) the efficiency of wind mixing.

7.3.3 Shear Generation A_S

The parameterization of the shear generation term is based on an energy argument similar to penetrative convection. Consider the entrainment of hypolimnetic quiescent fluid of thickness Δh over an interval of time Δt, into the epilimnion that has a mean horizontal velocity scale given by $\bar{u}$. Conservation of mass and momentum would indicate a reduction of velocity in the epilimnion by the fraction $h/(h+\Delta h)$. The resultant decrease in kinetic energy will be proportional to $\rho\bar{u}^2 \frac{dh}{dt}$. A fraction of this kinetic energy is converted to potential energy due to entrainment, that has been parameterized as:

$$\Lambda_S = \rho_s C_s \bar{u}^2 \frac{dh}{dt} \tag{7.24}$$

where, C_s = the efficiency of entrainment and is expected to be less than unity for known values of $\bar{u}$.

A number of different estimates of $\bar{u}$ have been proposed. Possible velocity scales for $\bar{u}$ are $nu_{*,w}$, $n'u_s$ ($n \geq 1; n_1 \leq 1$). Csanady (1979) has suggested a value of n = 3.5 that is based on the development of a surface shear layer following the sudden application of windstress. Imberger (1979) derives the following expressions for $\bar{u}$ by equating the change of momentum $\rho_s \frac{d}{dt}(h\bar{u})$ to the applied wind stress $\rho_s u^2_{*,w}$

$$\bar{u} = \frac{u^2_{*,w}}{h} t \tag{7.25}$$

where t is expressed as

$$t = \frac{0.5L}{\left(\frac{\Delta\rho}{\rho} gh\right)^{1/2}} \tag{7.26}$$

and represents one half the time for the wave to travel the length (L) of the lake. Substituting eq. 7.26 in eq. 7.25,

$$\bar{u} = \frac{u^2_{*,w} L}{2h \left(\frac{\Delta\rho}{\rho} gh\right)^{1/2}} \tag{7.27}$$

Clearly the above estimate of $\bar{u}$ is very sensitive to the length scale (L).

A comparison of energy source due to wind stirring with energy generation due to shear, using Csandy's estimate for $\bar{u}$ indicates (Appendix C) the latter to be important only for low Richardson numbers.

7.3.4 Leakage Λ_L and Temporal Storage (Λ_T)

Internal waves are generated at the interface (bottom of the mixed layer depth) due to turbulence caused by wind stirring, shear generation and penetrative convection. These waves radiate energy away from the interface and hence reduce the energy available for entrainment. The energy carried away depends on the wave amplitude, length scale of the interface perturbations and stratification in the hypolimnion. A part of this energy radiated away into the hypolimnion can result in localized mixing. This mixing has been modelled by using an enhanced value of diffusion coefficient in the hypolimnion (Imberger (1981), Aldama and Bowen (1985)).

Although there is some evidence to suggest that internal waves could substantially reduce entrainment rates (Linden, 1975), sufficient information is not available for a better quantitative assessment of this term. A few suggested parameterizations are discussed below. Following an energy cascade argument, Λ_L, eq. 7.7 can be parameterized as, Linden (1975), Zemen and Tennekes (1977):

$$\Lambda_L = \rho_s C_d a^2 N^3 h \tag{7.28}$$

where a is a characteristic amplitude of the internal waves and

$$N = \left(\frac{g}{\rho_o} \frac{\partial \rho}{\partial z} \right)^{1/2} \tag{7.29}$$

The amplitude, a, can be estimated by equating the kinetic energy of an eddy impinging on the interface with the potential energy associated with maximum displacement of the interface. For the case of linear stratification underlying the upper mixed layer the amplitude can be expressed as:

$$a = \frac{\sigma}{N} \tag{7.30}$$

For a two layer system with a density jump $\Delta\rho$ at the interface,

$$a = \frac{\rho_s \sigma^2}{g\Delta\rho} \tag{7.31}$$

Sherman et. al. (1978) used an interpolation between these two extremes and expressed a as:

$$a = \frac{\sigma}{N}\left(1 + \frac{\Delta\rho g}{\rho\sigma N}\right)^{-1} \tag{7.32}$$

Note that for the case of a negligible density jump, eq. 7.32 reduces to eq. 7.30.

Finally, Kantha (1977) expressed a as:

$$a = \frac{1}{N^2}\left[\left(g\,\frac{\Delta\rho}{\rho}\right)^2 + N^2\,\sigma^2\right]^{1/2} \tag{7.33}$$

This expression approaches the same limit as eq. 7.32 for the cases where $\Delta\rho$ or N approach zero.

Finally the storage term Λ_T (Zilitinkinch (1975)) can be assumed proportional to the rate of growth of the thickness of the upper mixed

layer i.e.

$$\Lambda_T = C_t \sigma^2 \frac{dh}{dt} \tag{7.34}$$

where C_t is an empirical parameter.

Substituting eqs. 7.8, 7.19, 7.24, 7.28 and 7.34 in eq. 7.7 the following entrainment algorithm results

$$\frac{u_e}{\sigma} = \left[\frac{1 - C_d R_s}{C_t + .5R_i - C_s \bar{u}^2/\sigma^2}\right] \tag{7.35}$$

where

$$u_e = dh/dt \tag{7.36}$$

$$R_i = \frac{\Delta\rho}{\rho} \frac{gh}{\sigma^2} \tag{7.37}$$

$$R_s = \frac{a^2 N^3 h}{\sigma^3} \tag{7.38}$$

Multiplying eq. 7.35 by $.5R_i$, the following can be derived

$$\frac{\Delta PE}{\Delta KE} = .5R_i \frac{1 - C_d R_s}{C_t + .5R_i - C_s u^2/\sigma^2} \tag{7.39}$$

The algorithm presented in eq. 7.35 and 7.39 contains five empirical coefficients C_d, C_s, C_t, C_w and C_c. Table 7.1 lists the values of some of these parameters based on previous studies. The observed variation in these parameter values suggest an uncertainty in their value and the need to calibrate for each specific situation.

Table 7.1

Coefficient values for Parameters in the Mixing Algorithm (eq. 7.32) suggested in the literature (Ref. 118)

Author	η	C_k	C_t	C_s	a	C_d
Zeman & Tennekes (1977)	2.2	0.5	3.6	$0.5R_s$	$\frac{q}{N}$ $\frac{q^2}{g\alpha\Delta T}$	0.024
Niiler(1975)	1.3	1.0	0	1	0	0
Mahrt & Lenschow (1976)	0	0.2	0	1	0	0
Kraus & Turner (1967)	1.4	1	0	0	0	0
Linden (1975)	1	$C_{K^\circ}(s/h)^{9/2}$ s-stroke C_{K°=constant for particular experiment	0	0	1 cm fixed	0.01
Alexander & Kim (1976)	1	exponential	0	0	0	0
Imberger et al (1977)	$\frac{1.1(1+h/5)}{(1+h/20)}$	$\frac{1.0}{(1+h/5)^3}$	0	0	0	0
Best fit	1.8	0.38	2.25	0.3	$\frac{q}{N+g\alpha\Delta T/q}$	0.04

Note: $C_w = \eta^3 C_k$, $q = \sigma$, $\alpha\Delta T = \frac{\Delta\rho}{\rho}$, $R_s = \frac{Nh}{\sigma}$

7.4 The Dead Sea Mixing Algorithm

The mixing algorithm used for the Dead Sea is based on a simplification of the above general algorithm. Since C_t is of the order of unity and the values of Richardson number for the Dead Sea are much larger than unity (see Chapter 9) C_t can easily be dropped from eq. 7.35.

Further, as shown in Appendix C the shear term is important only at low Richardson number values, a condition that is in general not satisfied by the Dead Sea stratification. This allows the shear term to be dropped from eq. 7.35. Finally, the density profiles shown in Chapter 9 indicate a strong pycnocline that would prevent the propagation of internal waves into the hypolimnion. For such a case, using eq. 7.31, it can be shown that R_s (eq. 7.38) is much less than unity. Thus, leakage term can be neglected in eq. 7.35 that now reduces to

$$\frac{u_e}{\sigma} = \frac{2}{R_i} \tag{7.40}$$

the well known inverse Richardson number algorithm. Note that R_i is defined using σ as the velocity scale. Similarly, eq. 7.39 can be expressed as

$$\frac{\Delta PE}{\Delta KE} = 1 \tag{7.41}$$

where ΔKE is expressed as in eq. 7.18. Note the above algorithm contains only two calibration coefficients C_w and C_c associated with wind mixing and penetrative convection that can be calibrated by analyzing

periods when one of the two mixing mechanisms is predominant.

The results presented in Chapter 9 and Chapter 10 are based on a daily time step. Therefore, the model does not account for any diurnal convective or diurnal penetrative convective mixing. The velocity scale associated with night-time cooling and evaporation can also be computed using eq. 7.10, with h representing the diurnal mixed layer and ϕ the net heat loss at night. Compared with seasonal values, included in the model, the diurnal heat loss flux is larger than the seasonal flux but the diurnal pycnocline is smaller than the depth of the seasonal pycnocline. These two opposing effects could make the diurnal penetrative convective mixing small. However, detailed measurements of the mixed layer depth during the day and night need to be made before an accurate estimate of diurnal penetrative convective mixing is possible.

7.5 Suggested Values for C_w, and C_c based on field studies

The problem of estimating C_w and C_c has been addressed a number of times using model studies validated using field data in which C_w and/or C_c are the only calibration coefficients. Unfortunately, this method makes the value of C_w (C_c) model dependent and would thus lack universal applicability. The effect of model assumptions, temporal averaging of data (see also Section 4.4.2), neglect of any horizontal circulation, seiche effects, etc. all influence the value of C_w.

Kraus (1972) expressed the turbulent energy available for mixing per unit area as:

$$KE_w = k \tau W_{10} \tag{7.42}$$

Using eq. 7.18 with $w_* = 0$ and eq. 7.21, C_w can be expressed as:

$$C_w = k \left(\frac{\rho_s}{\rho_a C_z} \right)^{1/2} \tag{7.43}$$

or using typical values for the Dead Sea, $\rho_s = 1220$ kg/m^3. $\rho_a = 1.18$ kg/m^3 and $C_z = 1.3 \times 10^{-3}$ that is uncertain by about 20% Kraus (1972):

$$C_w = 885k \tag{7.44}$$

Denman and Miyake (1973) calibrated their model to a series of observations of the upper mixed layer of the ocean for a period of 12 days. Based on their simulation they suggest a value of k = .0012, corresponding to a value of $C_w = 1.1$. This value is close to k = .0015 ($C_w = 0.88$) suggested by the experiments of Kato and Phillips (1969). Further, Denman (1973) have shown that doubling the value of k increased the depth of the upper mixed layer by about 20%.

Halpren (1974) computed k directly based on ocean measurements before and after the passage of a storm of duration about 15 hours. He used the potential energy approach discussed in Section 7.2 and arrived at a value of k = .0039 or $C_w = 3.5$.

Turner (1969) used an approach similar to Halpren (1974) and suggested k = .01 or $C_w = 8.8$ based on two vertical salinity and temperature profiles in the open ocean.

Farmer (1975) analyzed his observation of the development of mixed layer due to penetrative convection in water beneath ice. Twelve

independent estimates of C_c based on the potential energy (stability index) approach, varied from .003 to .113 with an average value of .036. This value is about twice the C_c value of .015 found by Deardorff, Wills and Lilly (1969) in laboratory experiments.

There exists a number of factors that cause this large variation in the reported values of C_w and C_c. These include the neglect of mean flow, the interaction betwen the three mixing processes, as well as the effect of temporal averaging on the kinetic energy input of wind (see Section 4.4.2). These are a few of the many factors that make it difficult to evaluate universally applicable values for these coefficients.

CHAPTER 8

Water and Salt Budget for the Dead Sea

8.1 Introduction

In a saline lake, the vertical temperature, salinity and hence, density profiles, evolve in time as a result of the couplings between various components of the thermal energy, turbulent kinetic energy, water and salt budgets. Of these four budgets, the first two have been discussed in detail in Chapters 4 to 7. The remaining two water and salt budgets are discussed in this chapter.

Section 8.2 discusses the various components of the water budget. Data on lake elevations that forms an input to the model is presented. Section 8.3 discusses the salt budget for the Dead Sea. An important component of both these budgets is the extraction of Dead Sea brine by the salt works. Unfortunately, very little information is available on the operation of the salt works. The limited data that was made available for this study is analyzed in detail in Appendix D.

8.2 Dead Sea Elevations and Water Balance

8.2.1 Water Balance

The Dead Sea surface elevation fluctuates in response to fresh water inflows primarily from the Jordan River, evaporative mass loss and net extraction by the salt works. With the power project in operation, inflows from the Mediterranean Sea would be another important component. Assuming all these inflows and outflows occur at the surface, the water

balance may be expressed as:

$$A(z)z_{t+\Delta t} = A(z)z_t - EA_s - V_p + V_j + V_m \qquad (8.1)$$

where, $A(z)$ = the area of the lake as a function of lake elevation z, z_t and $z_{t+\Delta t}$ = the lake elevation at time t and $t+\Delta t$, E = the evaporative loss in the small time interval Δt, V_p = net extraction by the salt works, and V_j and V_m = inflows from the Jordan River and the Mediterranean Sea. In eq. 8.1, elevation and evaporation E are expressed in meters while inflows are in units of m^3. Note that $V_m = 0$ for model calibration and verification runs. The evaporative mass loss, E, is computed using the β-approach as discussed in Chapter 6.

Eq. 8.1 is used in different forms depending on whether the model is being used in the calibration/verification mode or the application mode. In the former case, the relationship is used to compute fresh water inflows (V_j) based on measured elevation values and estimates of pumpage (V_p) based on the salt budget as discussed in Section 8.3. Thus, in the model calibration mode, negative inflows would imply either errors in the other water budget terms or seepage from the lake. Estimated values of pumpage as well as fresh water inflows are presented in Chapter 9. Cummulative annual values of V_p/A_s and E are about 0.2 m and 1.5 m, respectively. Inflows from the Jordan River (V_j) vary from year to year.

When the model is used in a predictive mode, e.g. as discussed in Chapter 10 for the case with the power project inflows, eq. 8.1 is used to compute the future elevation ($z_{t+\Delta t}$). Evaporation is computed as before while pumpage by the salt works, fresh water inflows and the Mediterranean inflows are required inputs, (see also Chapter 10).

8.2.2 Dead Sea Elevations

Surface elevations of the Dead Sea are measured by a number of different organizations using different datums. This causes confusion and uncertainty about the correct elevations. Four sets of measurements were made available by the Mediterranean Dead Sea Company for this study. The first set consisted of elevations measured on the first of each month extending from October 1967 to November 1984. The other three sets consisted of measurements taken at about 10-day intervals for the periods 5/31/79 to 6/21/82; 9/29/82 to 5/21/83 and 1/30/84 to 9/24/84. The first and second set had a consistent bias of 0.08 m. For model calibration and verification, daily interpolated values using set 1 and set 2 (after correcting for the bias) were used.

Fig. 8.1 shows a plot of the Dead Sea elevations for the period October 1979 to July 1984 that were used for model calibration/ verification. It is clear that the winters of 1979/80 and 1980/81 were very wet with inflows of the order of 1.3 m and 0.8 m, respectively. The following three winters were dry. The summer time net evaporation is of the order of 1.0 m.

8.3 The Salt Budget

The integral salt balance for the Dead Sea can be expressed as:

$$St_{t_2} = St_{t_1} - St_p + St_{ppt} - St_m \qquad (8.2)$$

where, St_{t_1} and St_{t_2} = the salt content of the lake (see also eq. 8.4) at time t_1 and t_2, respectively, St_p = the salt extracted by the salt works, St_{ppt} = the salt that precipitates within the lake, and

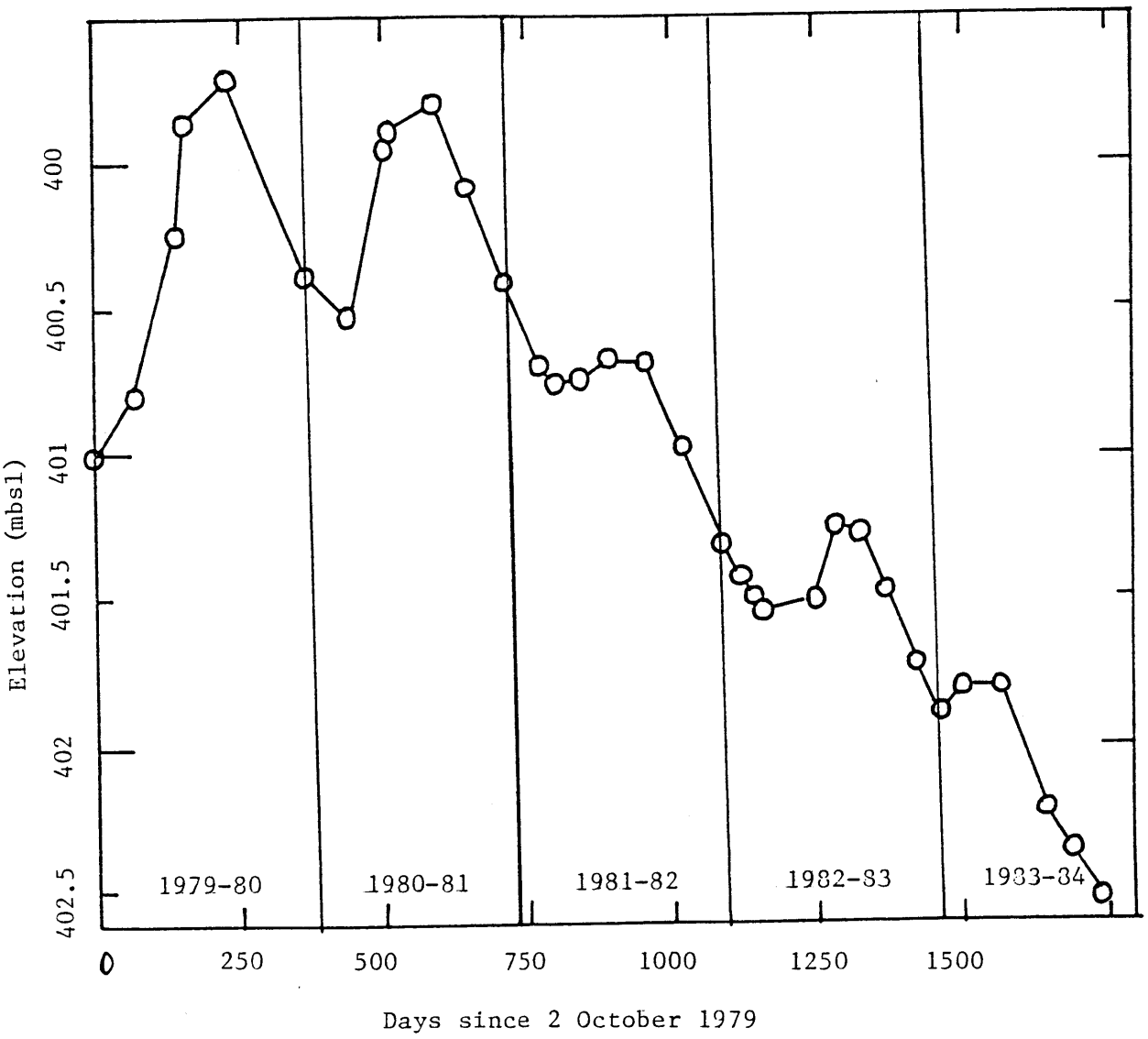

Fig. 8.1 Interpolated Dead Sea Elevations October 1979 to July 1984

St_m = salt inflow associated with the power project inflows from the Mediterranean Sea at a salinity of 50 $^{o}/_{oo}$. This reflects the expected concentration due to evaporation of water in the conveyance channel.

For the model calibration/verification phase, $St_m = 0$ and St_{ppt} is assumed negligible since no reliable estimates for this term are available. Eq. 8.2 can thus be used to compute St_p:

$$St_p = St_{t_2} - St_{t_1} \tag{8.3}$$

where St_{t_1} and St_{t_2} are computed based on the measured salinity and density profile at time t_1 and t_2 as:

$$St = \int_{\text{Datum}}^{\text{surface}} \rho(z)\, A(z)\, S(z)\, dz \tag{8.4}$$

where the datum is taken at 440 mbsl.

Using eq. 8.4, the salt content of the lake was computed for the period October 1979 to June 1984. Fig. 8.2 shows the salt content per unit area relative to the salt content for October 2, 1979. Overall the data indicates a gradual reduction in the salt content due to net extraction by the salt works. The impact of the salt works on the Dead Sea salt balance is apparent.

Over the period of about five years, total salt extracted from the top 40 m of the lake is about 50 kg/m^2 or 4 x 10^{11} kg. This compares well with a value of 3.5 x 10^{11} kg estimated in Appendix D based on limited data available from the salt works. A portion of this precipitates in the evaporation ponds and the remainder is returned to the Dead Sea in the form of return flow. The latter has a density of

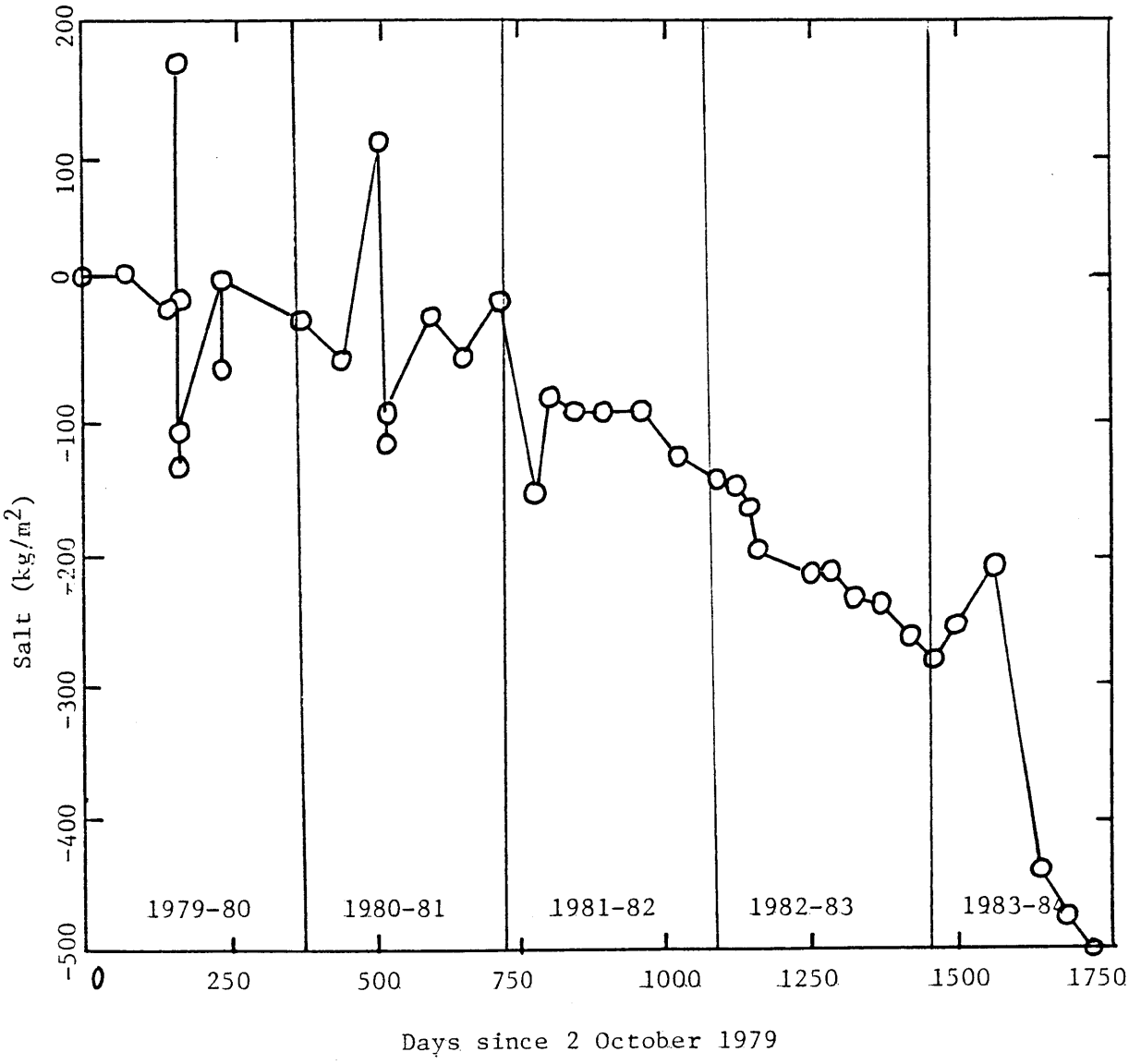

Fig. 8.2 Dead Sea Salt Content Normalised by Area at 400 mbsl Relative to Salt Content on 2 October 1979

1330 kg/m^3 and flows into the lower mass of the Dead Sea.

A few periods (Fig. 8.2) indicate an increase in salt content. This could be due to one or more of the following four factors: (i) errors in elevation, (ii) errors in the measurement of the salinity profiles, (iii) inflow of salt from surface runoff or saline springs and (iv) horizontal stratification of the lake. Unfortunately, no additional data is available to further comment on these aspects.

St_p in eq. 8.3 is the total quantity of salt extracted over a time period $t_2 - t_1$ (or the initial and final profile in the model calibration phase). However, it yields no information on the temporal variation of St_p that was obtained by assuming constant pumpage during each month, i.e.,

$$\sum_{i=t_1}^{t_2} h_p^i = k \sum_{i=t_1}^{t_2} h_{pd} \qquad (8.5)$$

$$\text{and} \quad \sum_{i=t_1}^{t_2} k\, h_{pd}^i\, \rho_s\, S_s = St_p \qquad (8.6)$$

where h_{pd}^i = the daily value of pumpage from the surface of the Dead Sea as obtained from Table D.3, assuming uniform pumpage during the month. The factor k is chosen such that the total amount of salt extracted over the time interval between the two profiles measured at t_1 and t_2 is St_p (eq. 8.6). For the period October 1979 to June 1984 k varied from 0.6 to 1.3 and represents the error/uncertainty in the data analyzed in Appendix D. Note that the value of k depends on the surface salinity and density and hence on the mixing algorithm. Therefore, k was estimated using an iterative procedure.

Chapter 9

MODEL CALIBRATION AND VERIFICATION

9.1 Introduction

The model described in the previous chapters and Appendix A, was calibrated and verified using the data collected by the Weizman Institute (Ref. 148) over the period October 1979 to July 1984. The model contains two calibration coefficients C_w and C_c associated with wind and penetrative convective mixing.

Owing to the non-unique and interacting characteristics of the mixing processes, only one of these parameters can be calibrated at a time. The calibration was performed by dividing the data into periods during which one of these mixing processes is dominant. For example, during periods of fresh water inflows and warming with the lake's stability increasing, wind mixing is the predominant mixing agent. This period can be used to calibrate C_w. Similarly, during the late summer and early winter periods characterized by net evaporation and cooling, the lake experiences significant convective activity. Data for this period can thus be used to determine C_c. However, since wind mixing is present throughout the year and some convective activity occurs even during the early summer periods, this method involves an iterative procedure to estimate C_w and C_c. The parameters thus selected were then verified by simulating the period June to September during which both mixing processes are significant.

In order to apply the model an initial and a final profile (for comparison) is necessary. The model was first calibrated over short

periods ranging from one to four months duration depending on the interval between successive profiles. These parameters were later verified by a continuous simulation over a period of about two years.

The effect of linearly averaging the wind speed (see also Section 4.4.2) on the calibrated value of C_w was also examined for two periods: December 1979 to March 1980 and December 1980 to May 1981. During these two periods, the wind speeds indicate maximum variability and the effect of non-linear averaging is maximum.

In order to calibrate and verify the model it is important that the model (computed) profile and the data (comparison profile) have the same salt, mass and thermal energy contents. The latter was achieved by applying a correction factor to the short wave radiation component over each period. This was of the order of 5% to 15% for most periods and is well within the range of various estimates of short wave radiation that have been suggested (Table 5.2) for the Dead Sea. Further, although the correction is applied only to the short wave radiation term, the magnitude of the correction represents the net error in the overall heat budget and includes, for example, error in the computation of atmospheric radiation due to lack of sufficient data on cloud cover. For simulations within the period October 79 to November 83 daily values of short wave radiation were obtained by a linear interpolation of historic values compiled by Stanhill (column 2, Table 5.2). These are referred to as the base case values. For the period July 1983 to July 1984, Stanhill's daily measured data from the station at Quidron has been used.

The monthly pumpage reported by the Dead Sea Potash works (see also Chapter 8 and Appendix D) was used to compute daily pumpage, assumed

uniform during the month. A correction factor was applied to these daily values, as explained in Section 8.3, so that the total salt extracted over each simulation period was equal to the difference in salt contents between the initial and final salinity profiles. This multiplicative factor varied from 0.6 to 1.3. For periods when the profiles indicated an increase in the salt content, e.g., March to May 1980, this factor is negative implying a net input of salt.

Inflows from the Jordan River were computed based on daily values of lake elevation, computed evaporation and pumpage. Daily lake elevations were computed by linearly interpolating lake elevations measured at a frequency of a week to ten days (see also Section 8.2). The daily inflows, computed in this fashion, are discussed in greater detail for each calibration and verification run. Ocasionally, model computations indicate negative inflows which are a direct consequence of errors in elevation either due to linear interpolation or actual measurement error.

For each period studied, a number of sensititivies to C_w and C_c were performed. The best values were selected based on a consideration of the following three criteria. First, a visual graphical comparison between the model predictions and measured data was made to determine any major deviations in surface temperature, salinity and the mixed layer depth.

Second, the root mean error as well as the maximum errors in temperature, salinity and density profiles were evaluated. These errors were based on a comparison between linearly interpolated data at 5 m intervals and the computed values at each grid point (1 m interval). Note lack of sufficient spatial resolution (hence the need for linear

interpolation) especially in the zone of the thermocline, halocline and the pycnocline, can cause large error values.

Further the stability index of the model results and data were compared. Over a period of time, the stability index changes as a result of a number of processes discussed in Section 7.2. Of these processes, changes in stability index due to mass inflows and outflows are much larger than the changes due to the mixing processes. Thus this method is not very useful where large changes in mass of the water column occur. Also, small errors in mass can result in large errors in the stability index. It is worth noting that for situations where mass balance can be accurately computed, minimization of errors in the stability index of the computed and measured data, is the best criteria for estimating C_w and C_c.

Finally, the reliability of the calibration coefficients can be no better than the quality of the data that is used for calibration. The model cannot yield more information than is contained in the data set. Keeping in view the insufficiency of the data both in terms of spatial and temporal resolution, the results of a number of sensitivities to C_w and C_c are presented.

9.2 Periods with Predominant Wind Mixing

Three sets of periods during which wind mixing is predominant have been identified. These include the following periods

12 Dec. 1979 - 12 March 1980	12 March - 26 May 1980	24 May - July 1981
19 Dec. 1980 - 24 May 1981	5 March - 24 May 1981	24 May - 25 July 1982
		16 May - 3 July 1984

Note that the above dates correspond to days on which profiles have been measured. Of these three sets, model results indicate maximum sensitivity to the calibration coefficient C_w during the fresh water inflow periods of December 1979 to March 1980 and December 1980 to May 1981. Therefore these periods were used to select our best estimate of C_w, as discussed below. (Also see Appendix E)

9.2.1 12 December 1979 - 12 March 1980

During this period, Fig. 9.1(a) indicates significant cooling as well as dilution. The December profile is very weakly stratified whereas the March profile has high stability due to fresh water inflows. Fig 9.1(a) shows the model results obtained with $C_w = 6$ and $C_c = 0.1$ (obtained by analysing profiles discussed in Section 9.3 and following an iterative procedure as mentioned above). The model results compare well with the measured profile. Table 9.1(a), Table 9.1(b) and Figs 9.1(b) to Fig 9.1(f) give additional details for this simulation.

Fig. 9.1(b) shows the daily input of wind and penetrative convective mixing energy. Clearly the penetrative convective mixing energy is small. During this period, the velocity scale associated with wind mixing $\bar{u}_{*,w}$ is about 1.5 times the velocity scale associated with penetrative convection $\bar{w}_*$. The figure also indicates the large variations in the wind mixing energy indicative of significant variations in the wind speed. Fig 9.1 (c) shows the cumulative energy over this period that amounts to 4270 Joule/m^2. This represents an equivalent reduction in the stability index due to wind mixing and is very small compared with the increase in stability due to fresh water inflows. The daily variation of Richardson number is shown in Fig. 9.1 (d), defined using the velocity scale σ (eq.

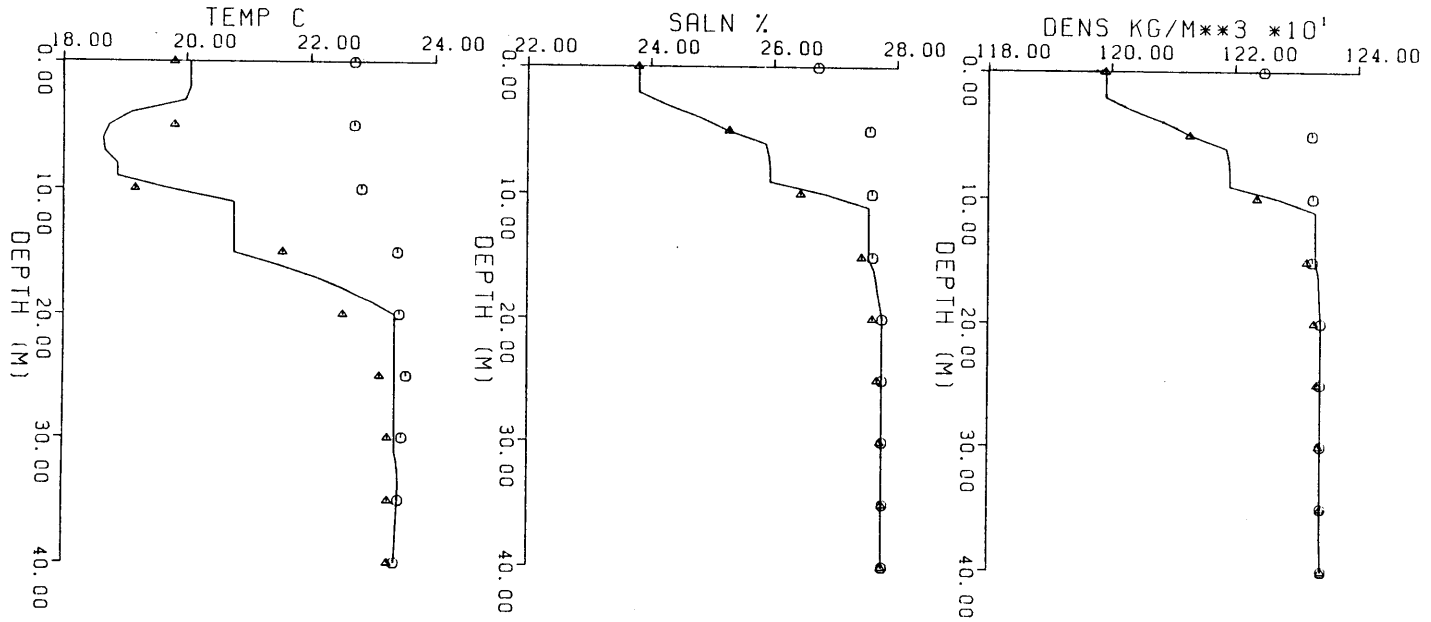

Fig. 9.1(a) Data and Model Results for the Period 12 December 1979 to 12 March 1980 with $C_w = 6$ and $C_c = .1$

o Initial Data
Δ Final Data
— Model Result

Table 9.1 (a)

Details of model run for the period 12 December 1979 - 12 March 1980

Calibration Coefficients				
C_w	3	6	3*	6*
C_c	0.1	0.1	0.1	0.1
Error Analysis Maximum Values				
Temperature °C	2.9	1.1	2.4	2.9
Salinity %	1.9	0.9	1.1	0.9
Density kg/m^2	17.9	7.8	9.4	8.4
Root Mean Square Values				
Temperature °C	1.1	0.5	0.7	1.1
Salinity %	0.7	0.3	0.4	0.3
Density kg/m^3	6.2	2.4	3.4	2.5
Mixing Parameters				
KE_w (J/m^2)	2140	4270	3513	7010
KE_c (J/m^2)	72	80	73	84
$\bar{u}_*$	.00323		.00378	.00377
$\bar{w}_*$	.00208	.00245	.00221	.00263
$\bar{R}_{i\sigma}$	3060	2920	1840	1540
Change in Stability Index	28850	28850	28850	28850
Error in Stability	-4222	-119	1634	4040

Change → Final - initial

Error → Data - model

* cube root mean cube wind speeds

Table 9.1 (b)

Water and Heat Balance for the period 12 December - 12 March 1980

Calibration Coefficients				
C_w	3	6	3*	6*
C_c	0.1	0.1	0.1	0.1
Water Balance				
Evaporation (mm)	155	172	165	186
Pumpage (mm)	54	54	54	54
Inflow (mm)	1168	1185	1178	1199
Net Inflow (mm)	959	959	959	959
Thermal Energy Balance				
Short Wave Radiation ($KCal/m^2/day$)	3240	3240	3240	3240
Atmospheric radiation (")	6030	6030	6030	6030
Back radiation (")	8030	8090	8060	8130
Evaporative Flux (")	1000	1120	1070	1210
Net Warming (")	-17	-276	-169	-477
Meteorology				
Air Temperature (°C)	14.2			
Humidity (%)	58			
Wind Speed (m/s)	3.08			

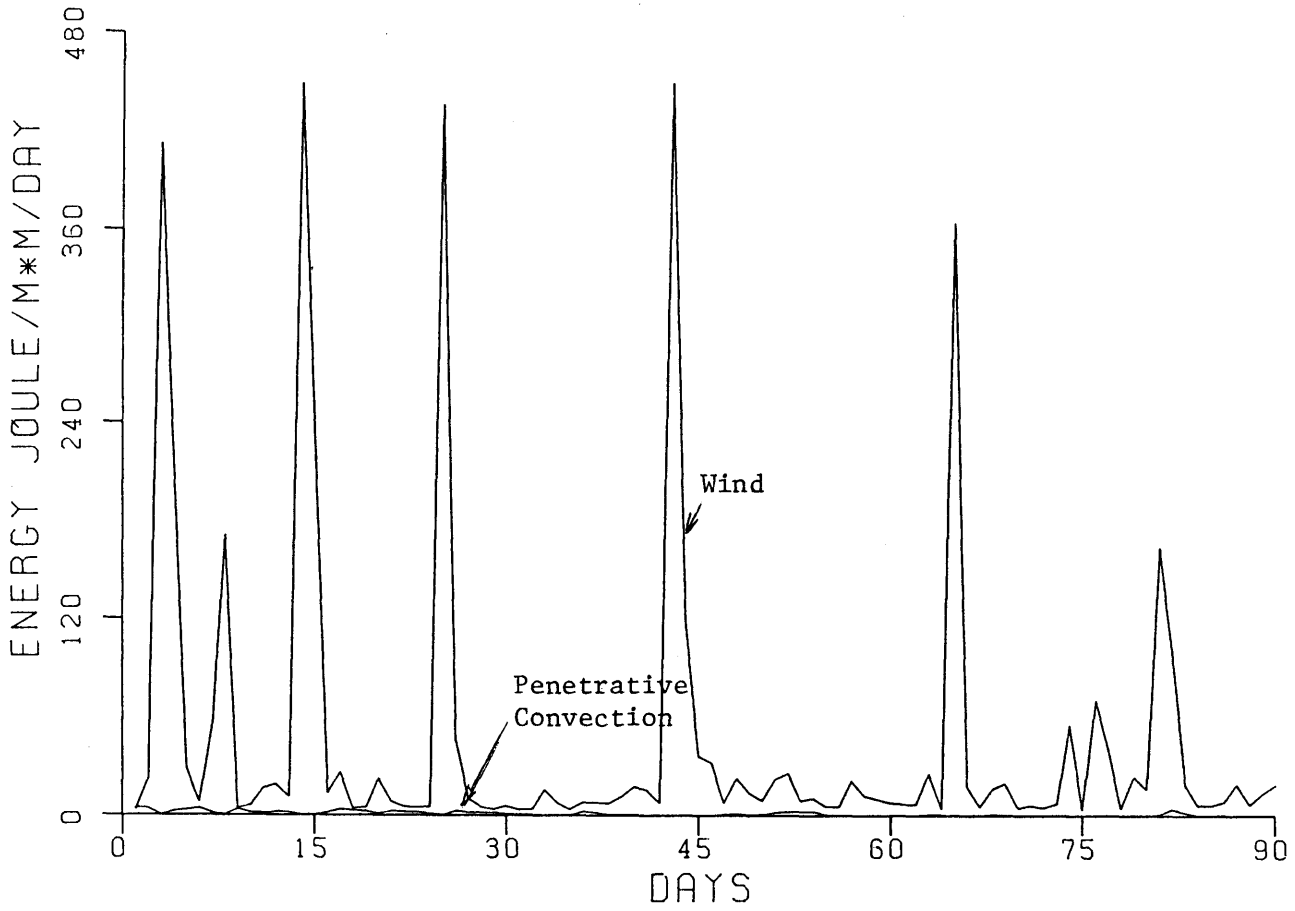

Fig. 9.1(b) Daily Input of Wind and Penetrative Convective Mixing Energy for the Period 12 December 1979 to 12 March 1980 with $C_w = 6$ and $C_c = .1$.

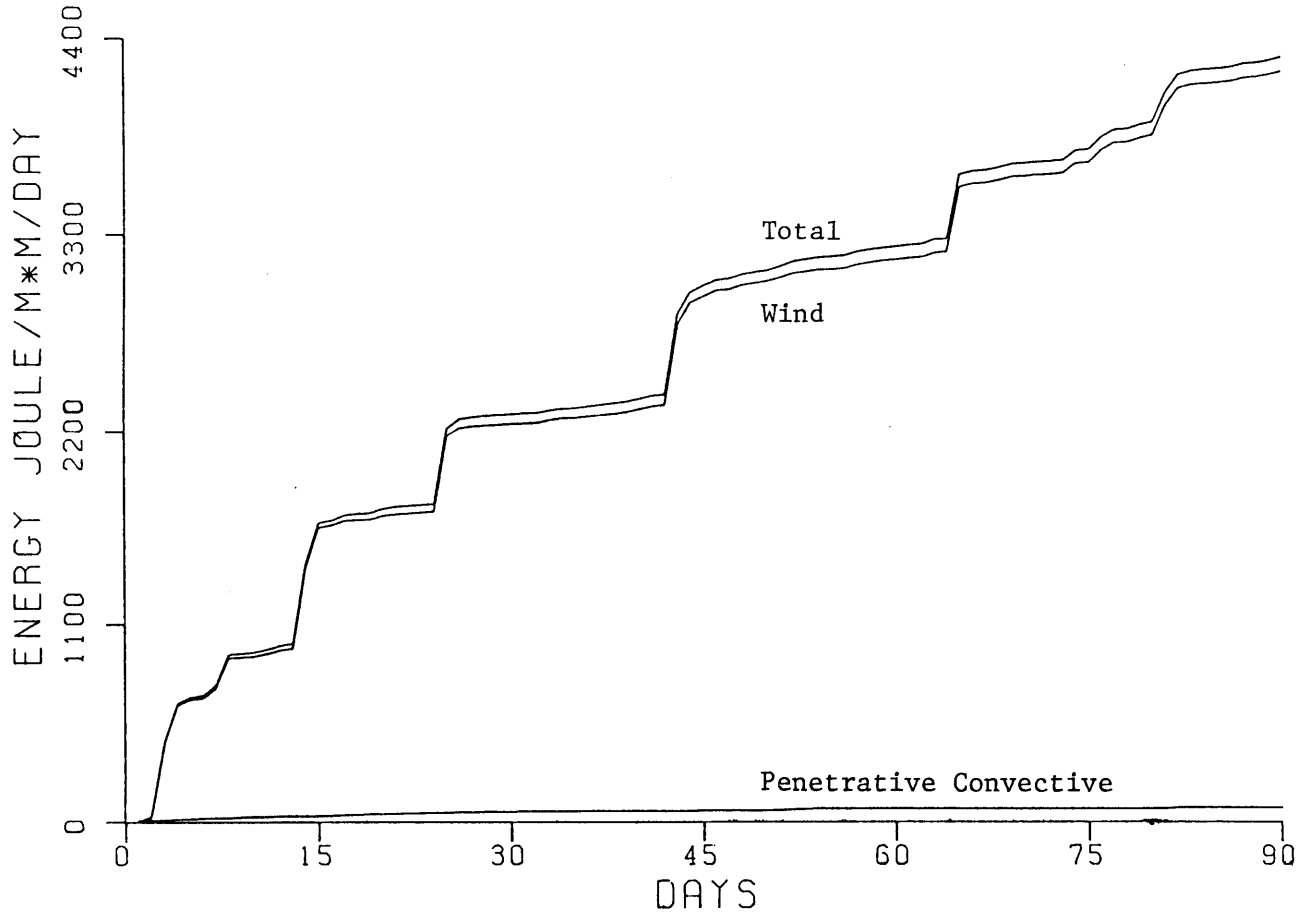

Fig. 9.1(c) Cumulative Wind and Penetrative Convective Mixing Energy for the Period 12 December1979 to 12 MArch 1980 with C_w = 6 and C_c = .1.

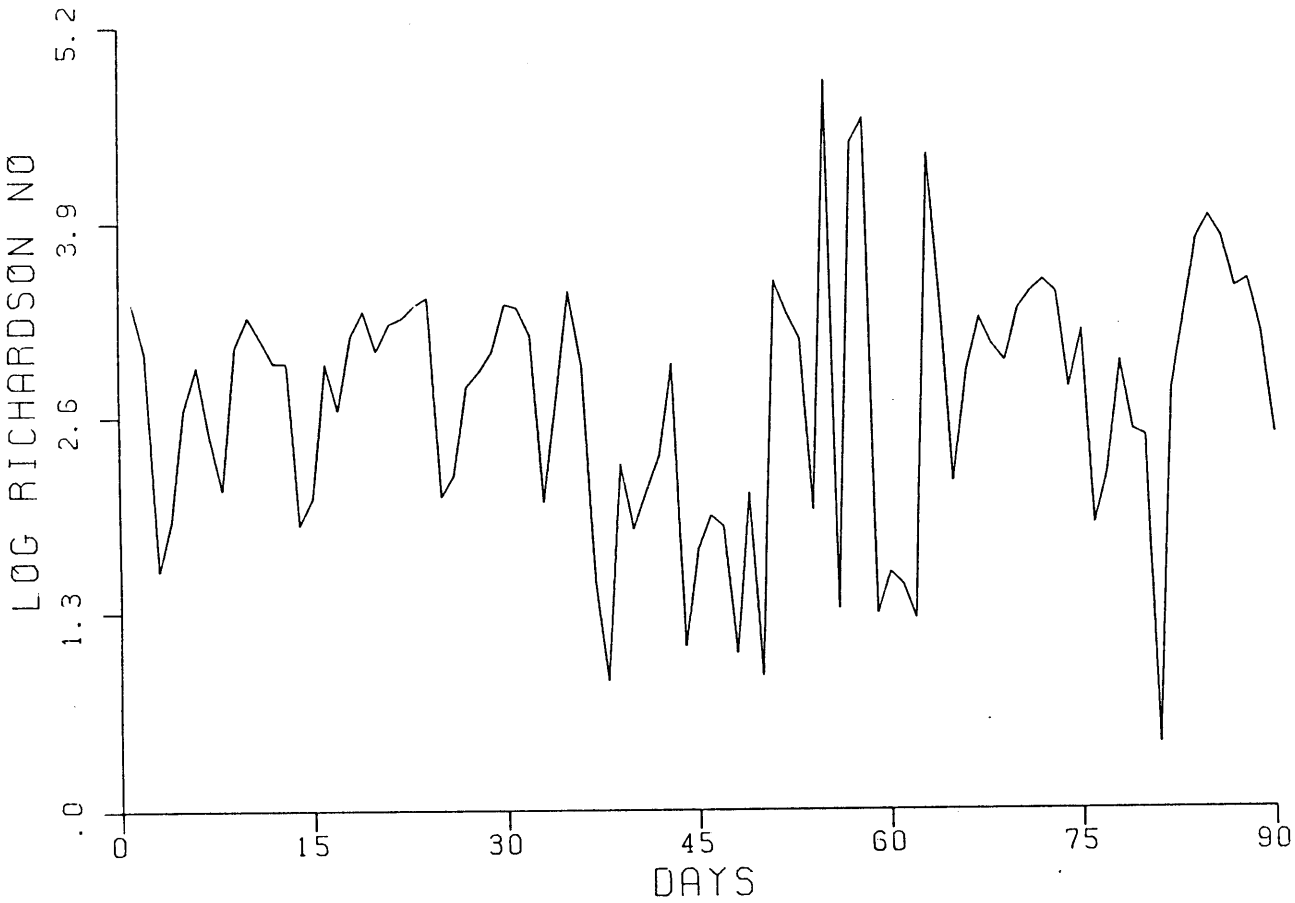

Fig. 9.1(d) Daily Variation of Richardson Number for the Period 12 December 1979 to 12 March 1980 with C_w = 6 and C_c = .1.

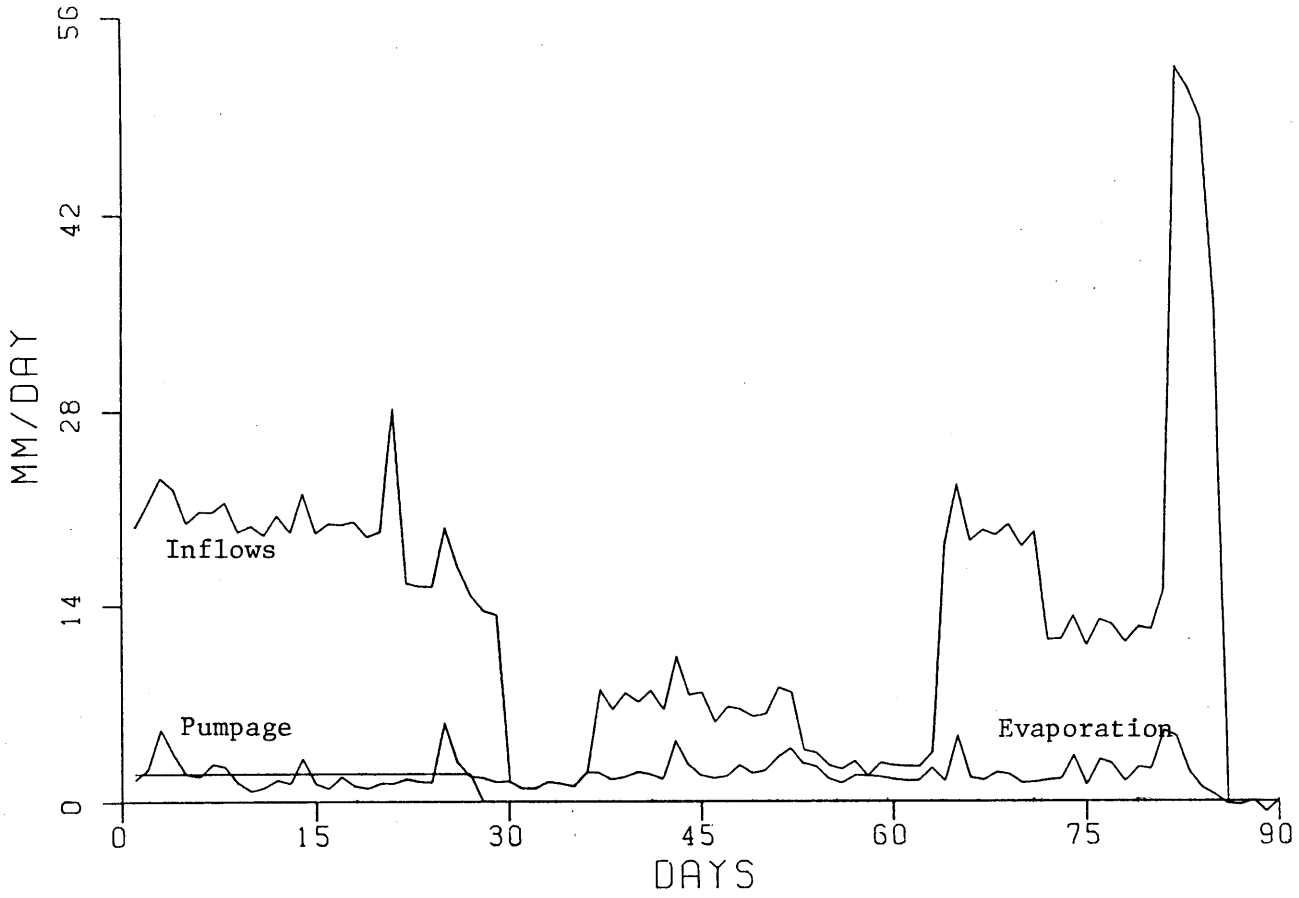

Fig. 9.1(e) Daily Water Balance for the Period 12 December 1979 to 12 March 1980 with C_w = 6 and C_c = .1.

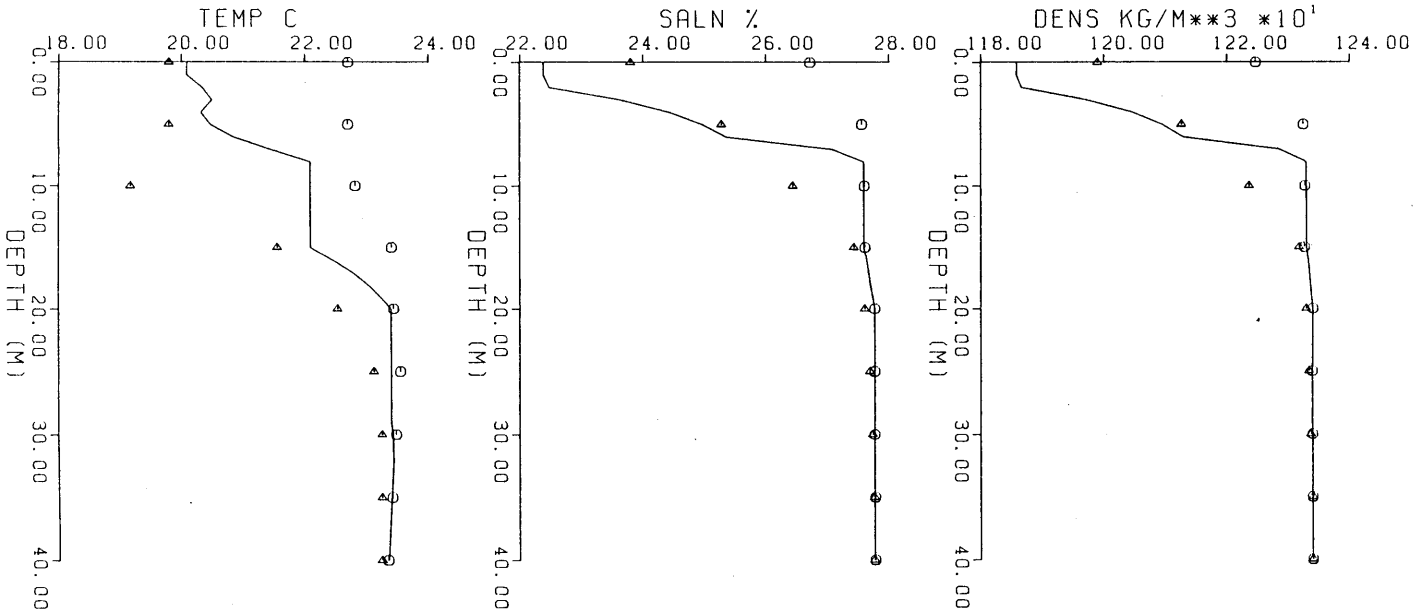

Fig. 9.1(f) Data and Model Results for the Period 12 December 1979 to 12 March 1980 with C_w = 3 and C_c = .1.

o Initial Data
Δ Final Data
— Model Result

7.37). The mean Richardson number for this period is about 3000.

Fig. 9.1 (e) shows the daily values of Jordan River inflows, evaporation and pumpage by the salt works. The cumulative value of inflows and evaporation is 1.2 m and 0.2 m, respectively as indicated in Table 9.1(b).

Fig. 9.1 (f) shows the model results for $C_w = 3$ and $C_c = 0.1$. Comparison of Fig. 9.1 (a) and Fig. 9.1 (f) indicates the sensitivity of the model results to wind mixing and that $C_w = 6$ is a better estimate for this coefficient. A corresponding range of variation in the value of C_w during the other periods of the year does not show a similar sensitivity.

The above results were obtained using linearly averaged daily wind speed values for computing evaporation as well as the value of $u_{*,w}$ used to compute the energy input due to wind. Fig. 9.1 (g) and Fig. 9.1 (h) show the results for a model simulation using daily cube root mean cube wind speed values based on hourly wind speed. (W_{el} in Eq. 4.2 with N = 24). Note that for the computation of evaporation daily mean wind speed values are still used. A value of $C_w = 6$ now indicates excess mixing while a value of $C_w = 3$ indicates a better fit with data. As indicated in Table 9.1 (a), the effect of nonlinear averaging is to increase the input of wind energy by about 60%.

Thus, the coefficient C_w accounts not only for the uncertainty in the estimation of u_s and the efficiency of wind mixing, as discussed in Section 7.3.2 but also for the above mentioned non-linear averaging effect. Note in this study, the final value of C_w is based on daily wind speed values that is consistent with other meteorological data.

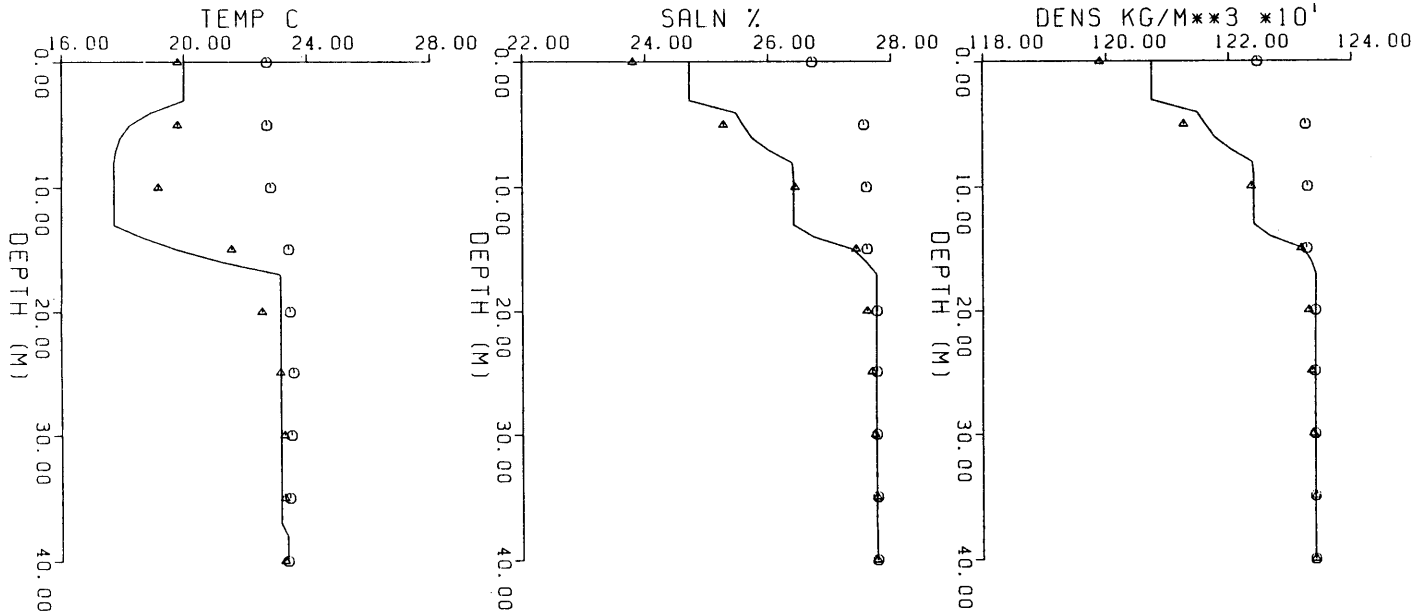

Fig. 9.1(g) Data and Model Results for the Period 12 December 1979 to 12 March 1980 with C_W = 6 and C_C = .1 and using Cube Root Mean Cube Wind Speed Values.

o Initial Data
Δ Final Data
— Model Result

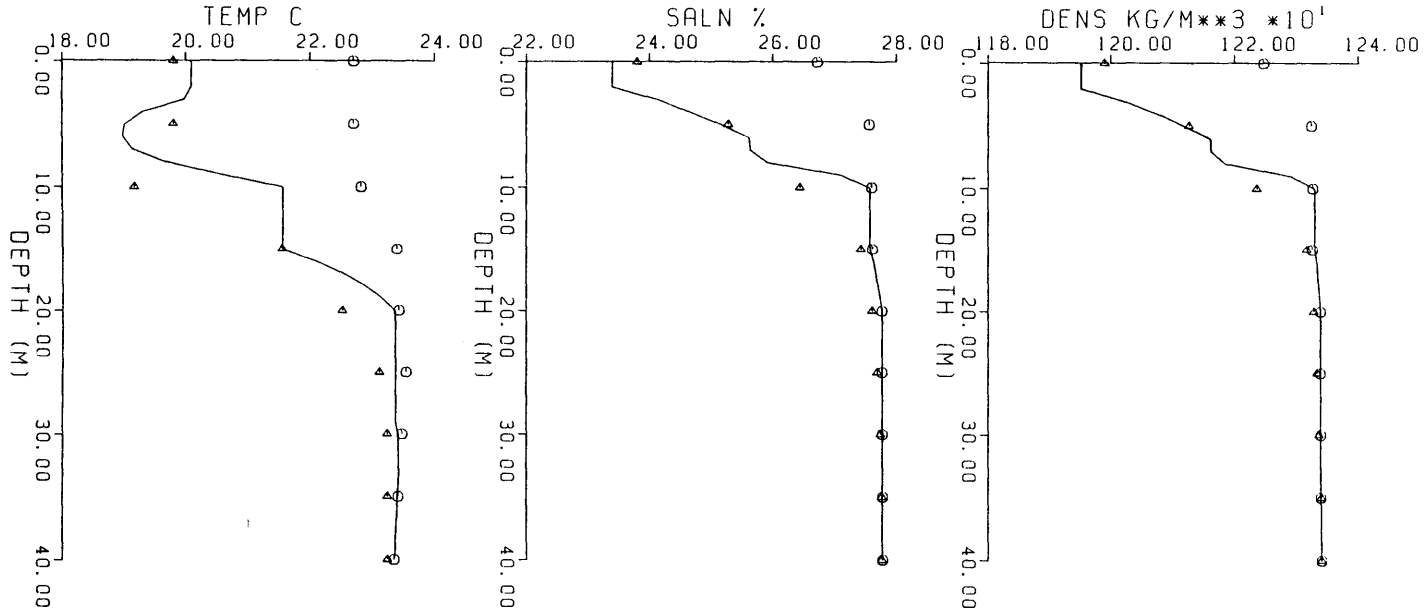

Fig. 9.1(h) Data and Model Results for the Period 12 December 1979 to 12 March 1980 with C_w = 3 and C_c = .1 and using Cube Root Mean Cube Wind Speed Values.

o Initial Data
Δ Final Data
— Model Result

9.2.2 19 December 1980 - 24 May 1981

Data for this period, Fig. 9.2(a), indicate significant warming and dilution due to fresh water inflows from the Jordan River. This results in a sharp increase in the stability of 20,400 Joule/m^2. In this respect this period is analagous to the period discussed in Section 9.2.1. Details of the simulations are included in Table 9.2(a) and Table 9.2(b).

Fig. 9.2 (a) also shows model results obtained with C_w = 6, and C_c = 0.1 with an increase of 15% in the base case short wave radiation values. Comparison with field data is good.

Fig. 9.2 (b) shows the daily values of wind and the penetrative convective component. The latter is clearly very small. Total input of kinetic energy due to wind, shown in Fig. 9.2(c), is about 5000 Joules/m^2. As for the previous period, the increase in stability index due to fresh water inflows dominates the decrease in stability due to wind mixing. The mean value of Richardson number for the period is about 700 (Fig. 9.2(d)). This large value justifies the assumptions (neglect of C_t and shear generation terms) made in the derivation of the mixing algorithm (Section 7.4).

Fig. 9.2 (e) shows the daily water balance for this period. Total inflows amount to about 1 m while the total evaporation is about 0.4 m, or at a rate of 2.7 mm/day. As shown in Fig. 9.2 (e), the evaporation rate increase towards the end of the period as the lake warms up with the onset of summer.

The sensitivity of model results to the parameter C_w are shown in Fig. 9.2 (f) that indicates insufficient mixing with C_w = 3. Also the error in the stability index is larger, Table 9.2 (a).

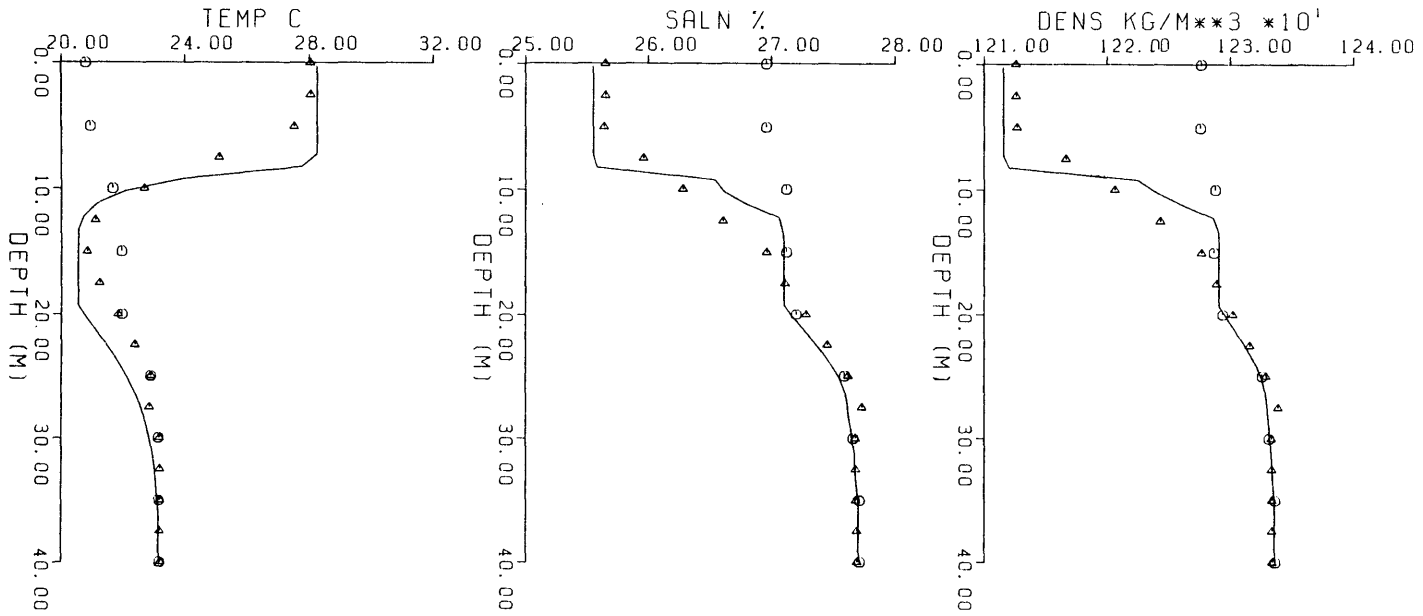

Fig. 9.2(a) Data and Model Results for the Period 19 December 1980 to 24 May 1981 with $C_w = 6$ and $C_c = .1$

o Initial Data
Δ Final Data
— Model Result

Table 9.2 (a)

Details of model run for the period 19 December 1980 - 24 May 1981

Calibration Coefficients			
C_w	3	6	3*
C_c	0.1	0.1	0.1
Error Analysis Maximum Values			
Temperature °C	1.6	3.1	2.7
Salinity %	1.0	0.5	0.5
Density kg/m^2	9.8	5.4	5.0
Root Mean Square Values			
Temperature °C	.6	.9	0.8
Salinity %	.5	.2	0.2
Density kg/m^3	4.4	2.0	1.9
Mixing Parameters			
KE_w (J/m^2)	2560	5200	4860
KE_c (J/m^2)	185	200	200
$\bar{u}_*$	.00333	.00332	.00397
$\bar{w}_*$	.00212	.00229	.00234
$\bar{R}_{i\sigma}$	1789	774	396
Change in Stability Index	20400	20400	20400
Error in Stability	-2579	-643	-702

Change → Final - initial

Error → Data - model

* cube root mean cube wind speeds

Table 9.2 (b)

Water and thermal budget for the period 19 December - 24 May 1981

Calibration Coefficients			
C_w	3	6	3*
C_c	0.1	0.1	0.1
Water Balance			
Evaporation (mm)	421	414	416
Pumpage (mm)	-124	-124	-124
Inflow (mm)	1019	1012	1014
Net Inflow (mm)	722	722	722
Thermal Energy Balance			
Short Wave Radiation ($KCal/m^2/day$)	4490	4490	4490
Atmospheric radiation (")	6400	6400	6400
Back radiation (")	8540	8540	8540
Evaporative Flux (")	1570	1570	1570
Net Warming (")	342	361	355
Meteorology			
Air Temperature (°C)	18.1		
Humidity (%)	59		
Wind Speed (m/s)	3.19		

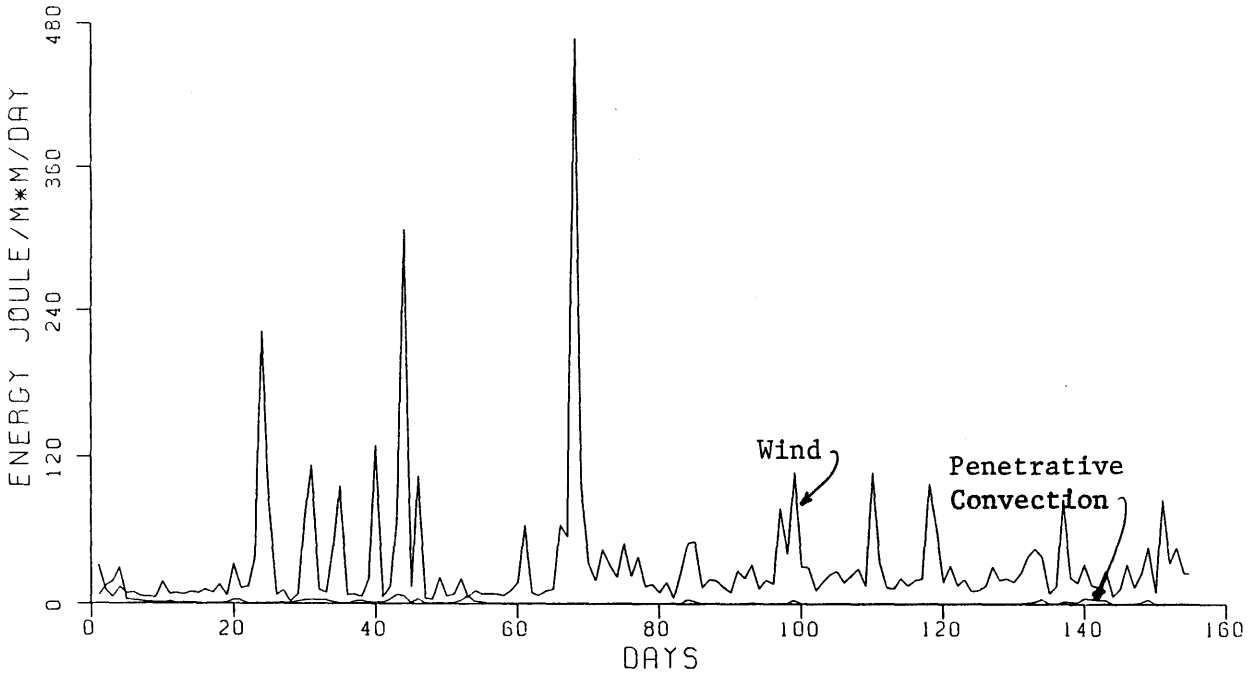

Fig. 9.2(b) Daily Input of Wind and Penetrative Convective Mixing Energy for the Period 19 December 1980 to 24 May 1981 with $C_w = 6$ and $C_c = .1$

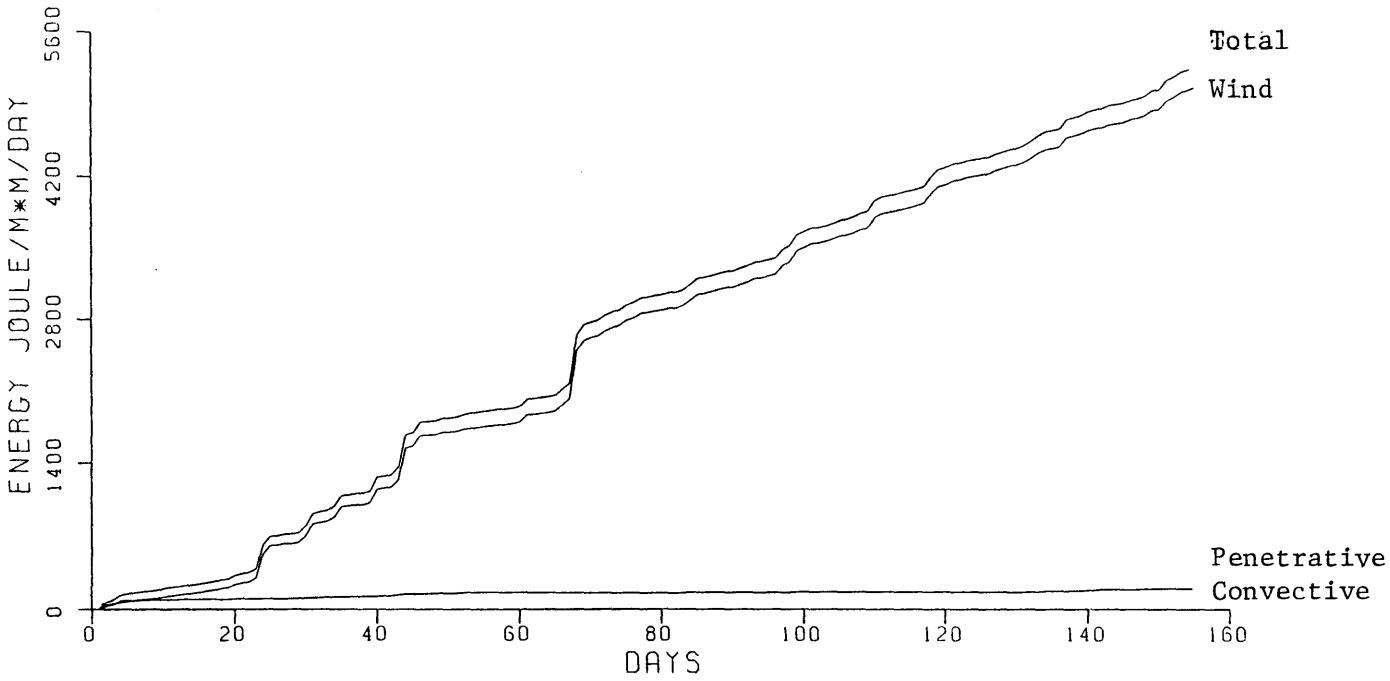

Fig. 9.2(c) Cumulative Wind and Penetrative Convective Mixing Energy for the Period 19 December 1980 to 24 May 1981 with $C_w = 6$ and $C_c = .1$.

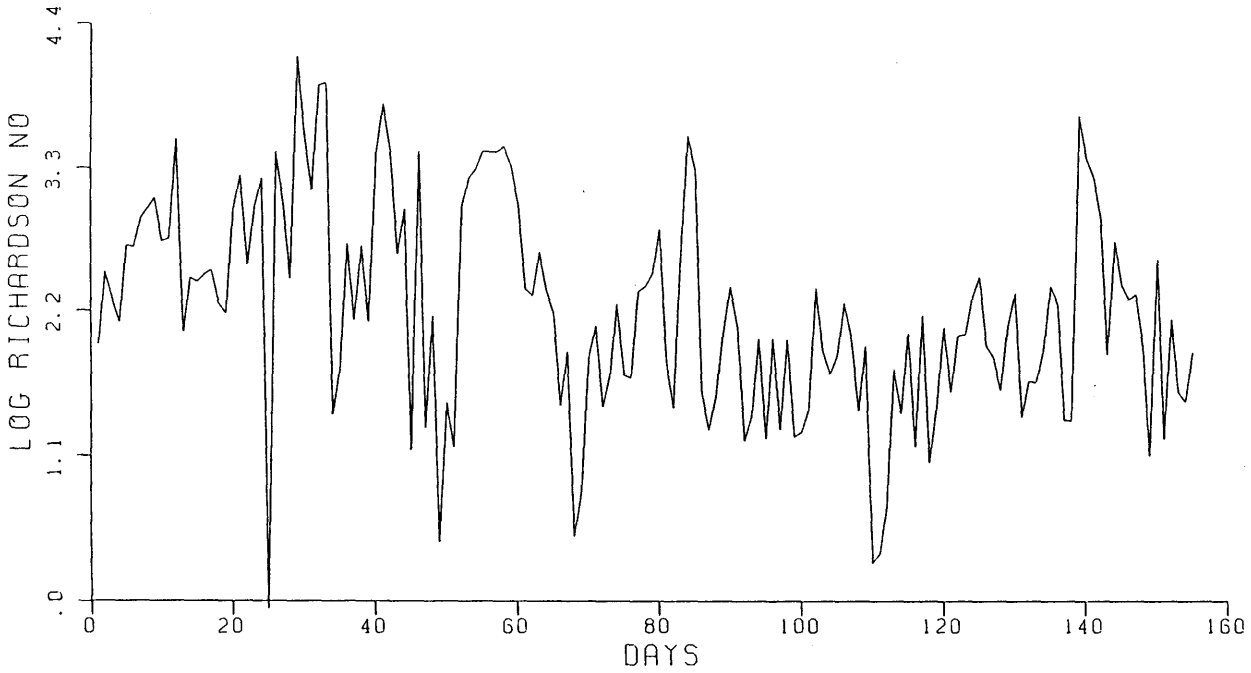

Fig. 9.2(d) Daily Variation of Richardson Numbers for the Period 19 December 1979 to 24 May 1980 with $C_w = 6$ and $C_c = .1$.

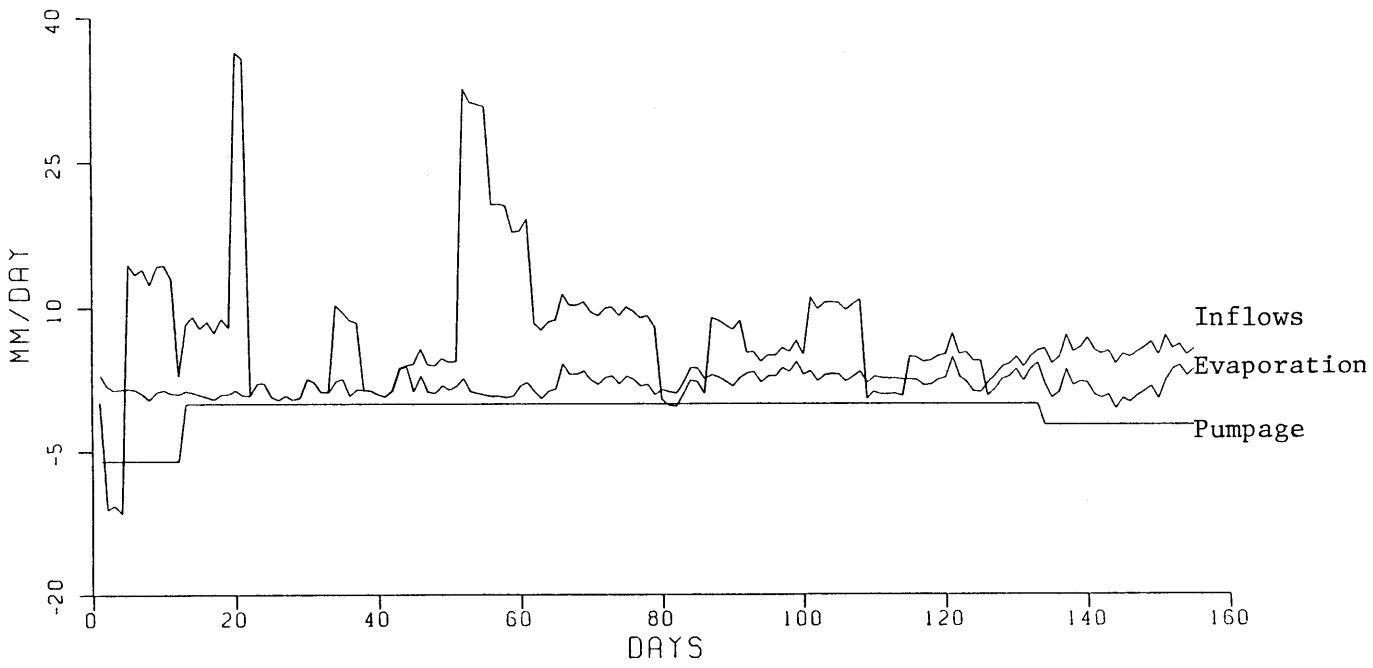

Fig. 9.2(e) Daily Water Balance for the Period 19 December 1980 to 24 May 1981 with $C_w = 6$ and $C_c = .1$.

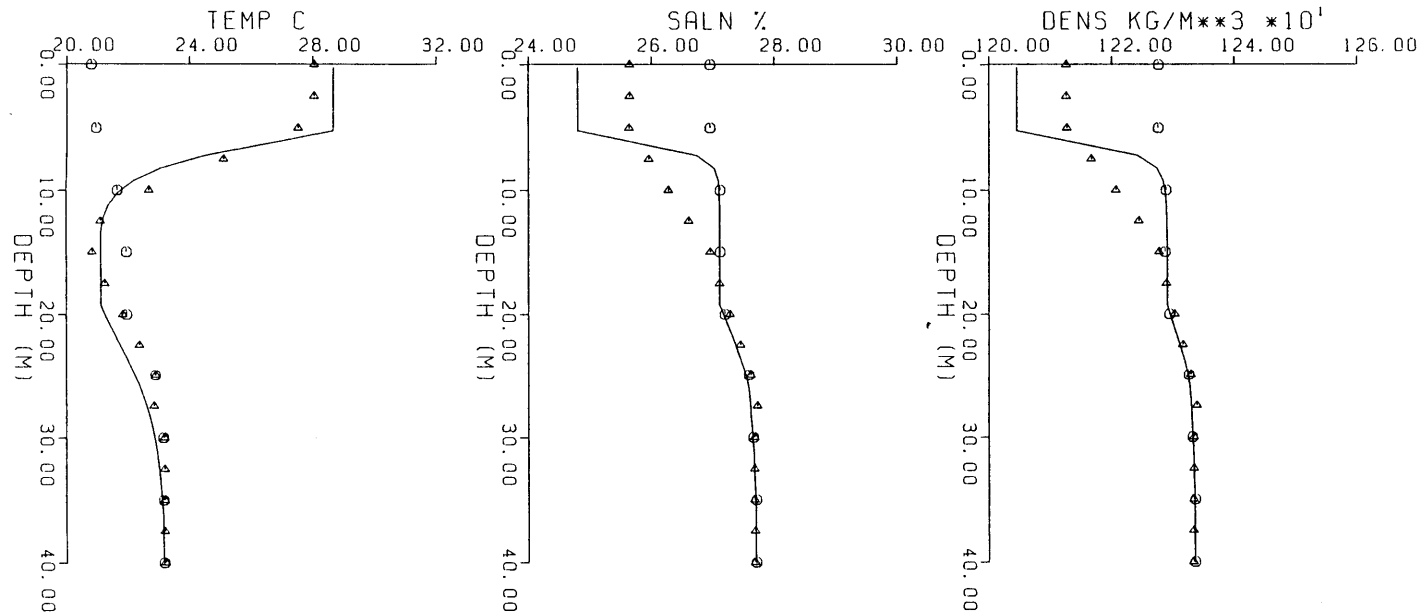

Fig. 9.2(f) Data and Model Results for the Period 19 December 1980 to 24 May 1981 with C_w = 3 and C_c = .1.

o Initial Data
Δ Final Data
— Model Result

Finally Fig. 9.2 (g) shows a model run using cube root mean cube wind speed values as defined in Section 4.4.3. Good agreement is obtained with a lower value of $C_w = 3$. Referring to Table 9.2 (a) and Table 9.2 (b), the non linear averaging effect results in an increase in wind energy input by a factor of about 1.9.

9.2.3 12 March - 26 May 1980

During this period, the elevation data indicates a net inflow of about 25 cms. This would imply a net dilution of the surface layers whereas the profile measurements indicate net concentration (see Fig 9.3 (a)). Also, the salt budget indicates an increase in salt content of about 22 kg/m^2. Clearly there is a discrepency in the data. Nevertheless, results for model runs with two different sets of mixing parameters with negative pumpage or a net input of salt, ($k = -3.0$ in eq. 8.3.) are presented here.

Fig 9.3 (a) compares the initial and the final profile with model results obtained using $C_w = C_c = 0.0$ and assuming no pumpage. The marked solar pond effect in the simulation results highlights the need to include wind mixing during this period. Fig. 9.3 (b) shows results obtained with $C_w = 6.0$ and $C_c = 0.1$. The surface salinities and the predicted mixed layer depth agrees well with data.

Fig. 9.3(c) shows the daily values of wind and penetrative convective mixing energy. The latter with a cummulative value of 80 $Joule/m^2$ is small compared with the cumulative value of 2060 $Joule/m^2$ for the wind mixing. The daily values of Richardson number based on the velocity scale σ are shown in Fig. 9.3(d). The mean Richardson number

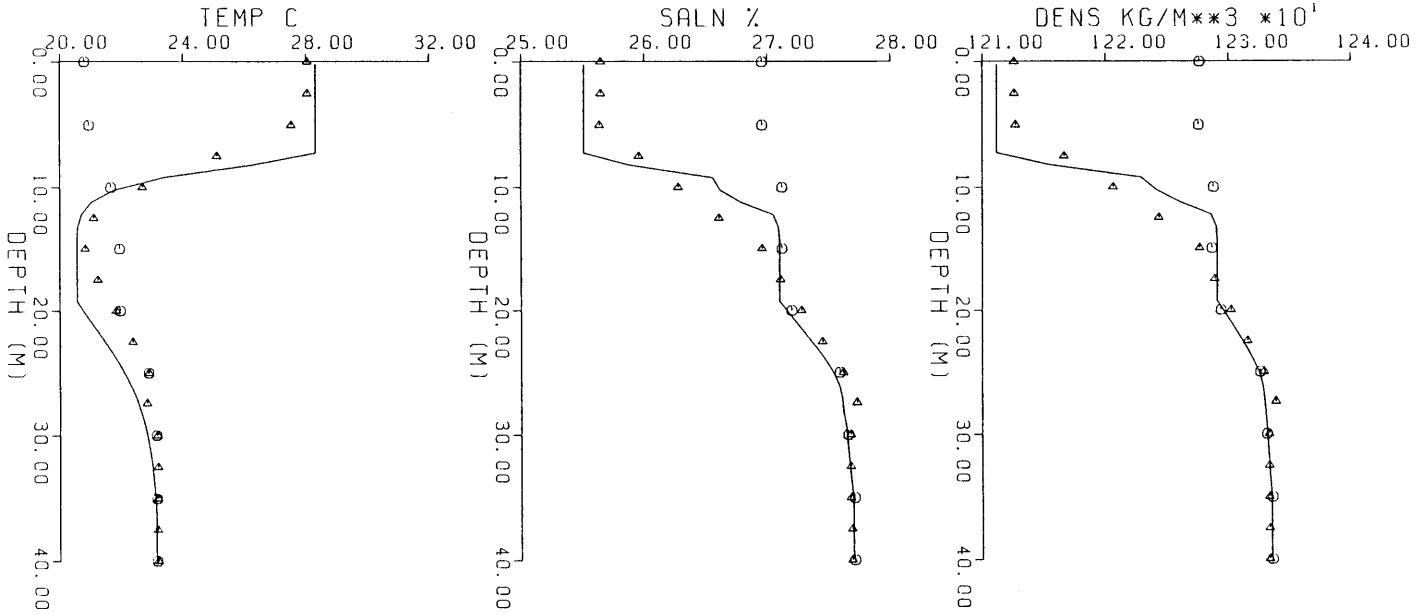

Fig. 9.2(g) Data and Model Results for the Period 19 December 1980 to 24 May 1981 with C_W = 3 and C_C = .1 and using Cube Root Mean Cube Wind Speed Values.

o Initial Data
Δ Final Data
— Model Result

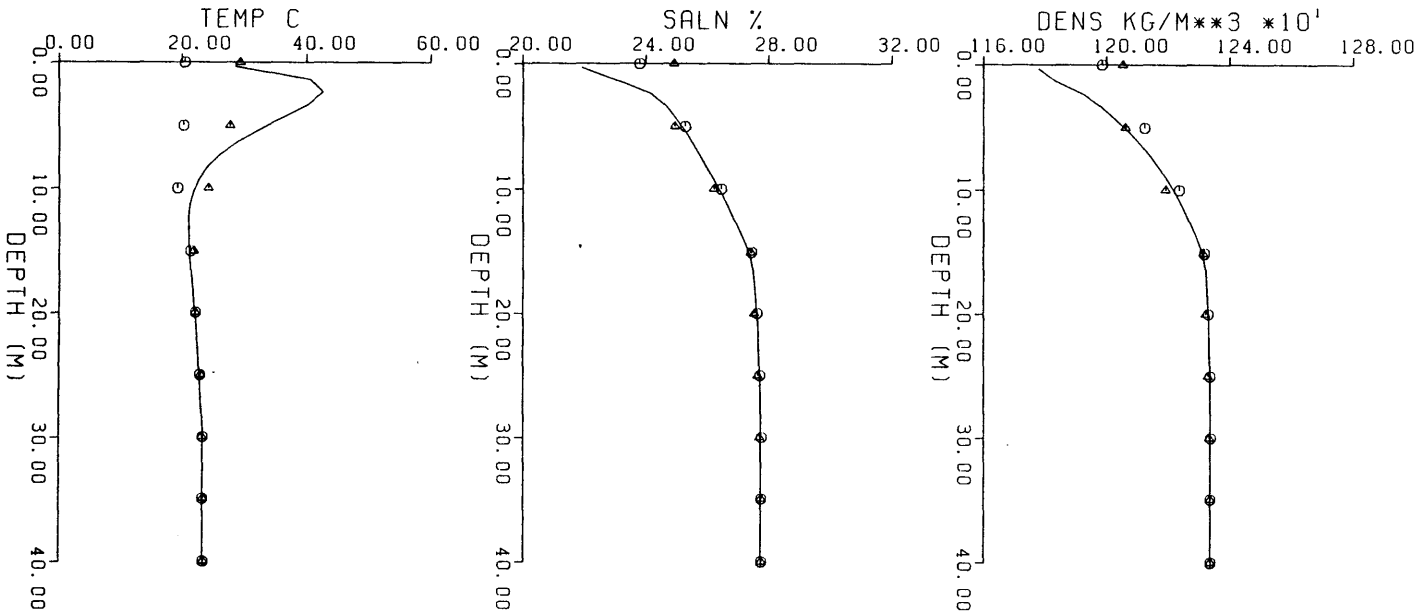

Fig. 9.3(a) Data and Model Results for the Period 12 March 1980 to 26 May 1980 with $C_w = 0$ and $C_c = 0.0$.

o Initial Data
Δ Final Data
— Model Result

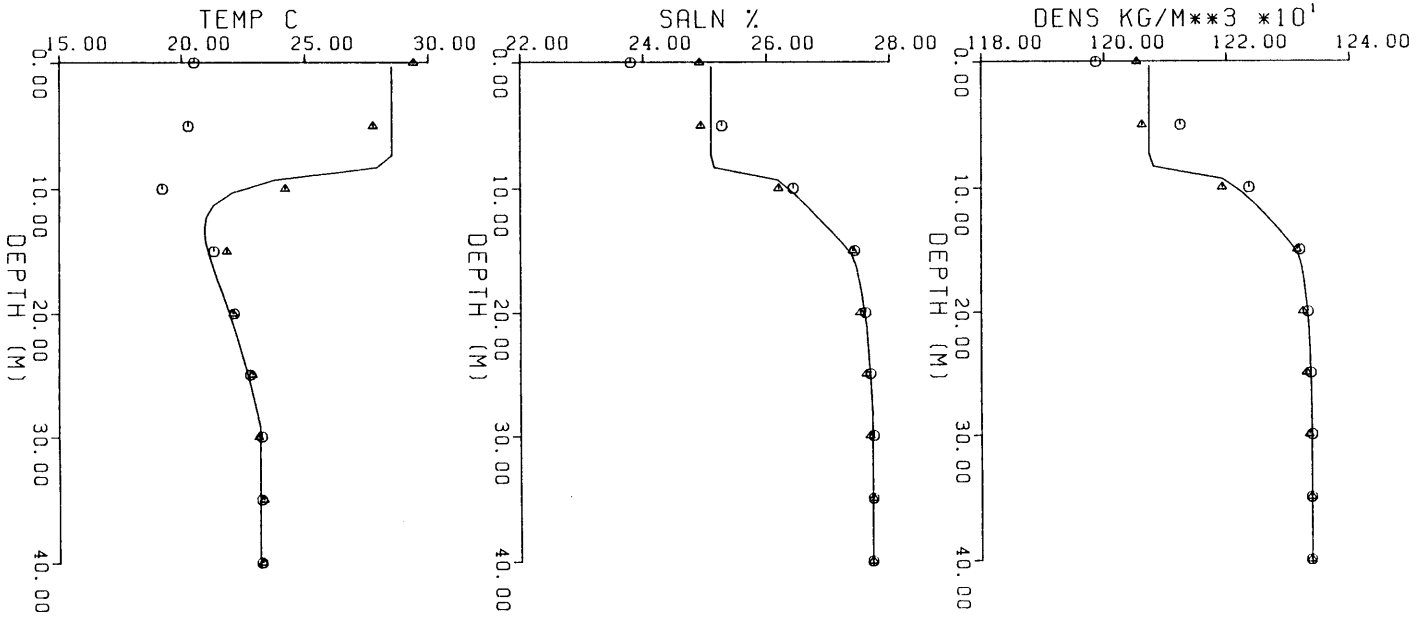

Fig. 9.3(b) Data and Model Results for The Period 12 March 1980 to 26 May 1980 with $C_W = 6$ and $C_c = 0.1$.

o Initial Data
Δ Final Data
— Model Result

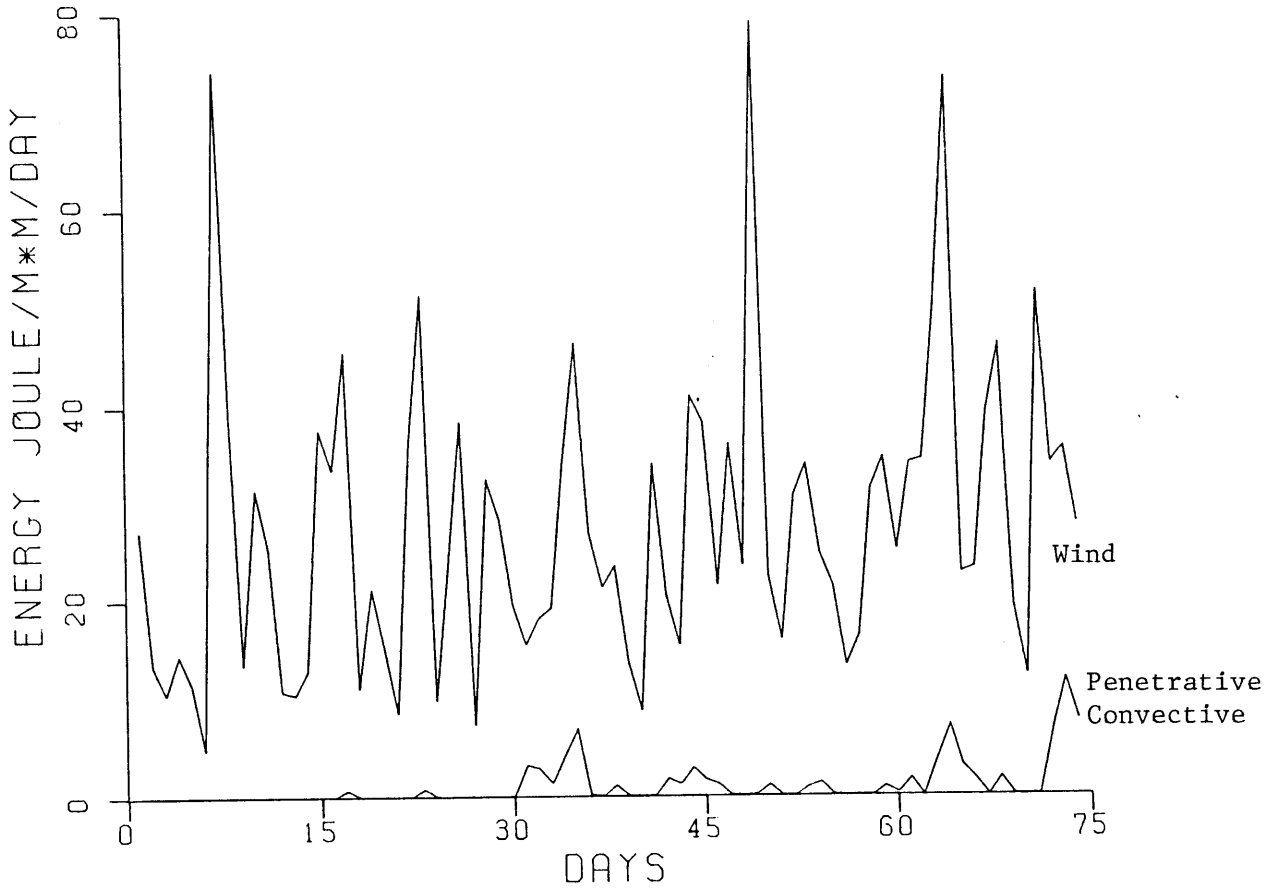

Fig. 9.3(c) Daily Input of Wind and Penetrative Convective Mixing Energy for the Period 19 March 1980 to 26 May 1980 with C_w = 6 and C_c = 0.1.

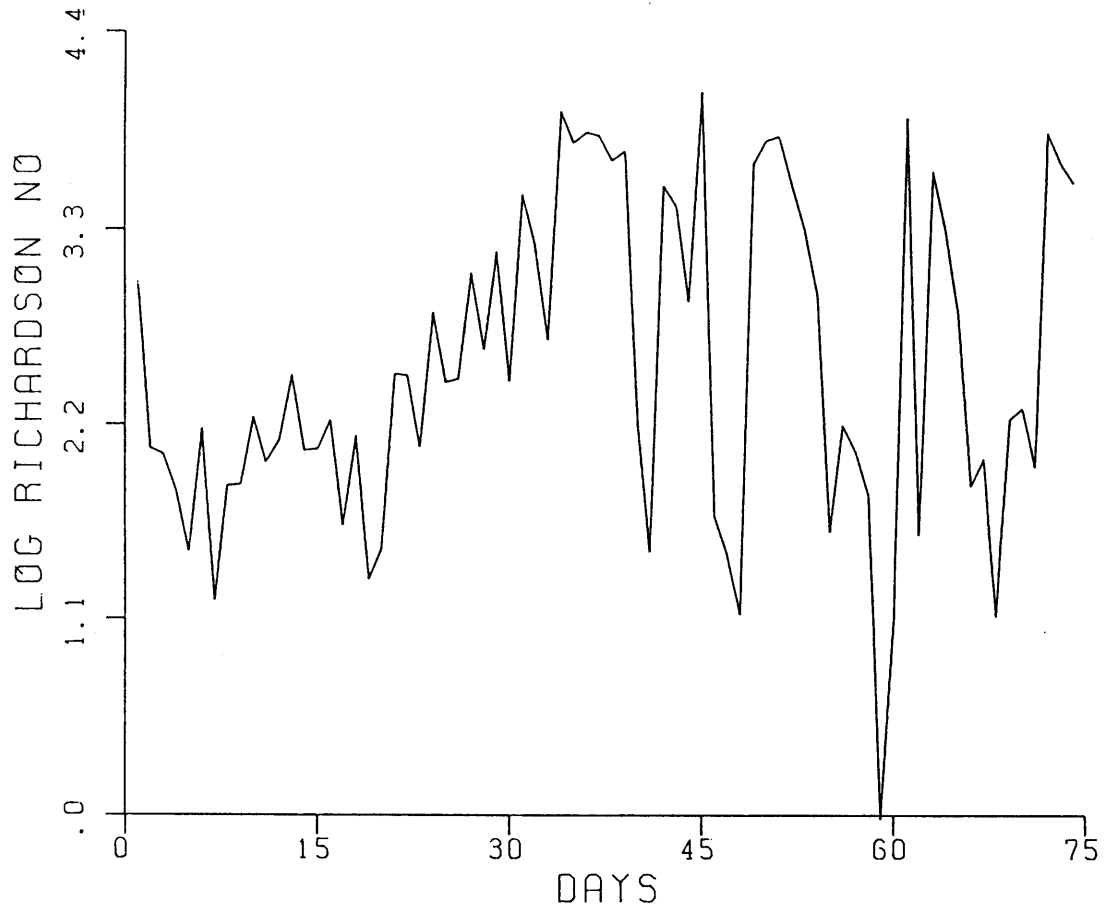

Fig. 9.3(d) Daily variation of Richardson Numbers for the Period 12 March 1980 to 26 May 1980 with C_w = 6 and C_c = .1.

value for this period is about 1700. Figure 9.3(e) and Table 9.3(b) show the daily and cumulative water balance for the lake. As mentioned before, this period is marked with an increase in the salt content necessitating a net inflow of about 200 mm saline water (Fig. 9.3(e)).

Fig 9.3(f) shows the model results with $C_w = 3$ and $C_c = 0.1$. As expected, the mixed layer is shallower than in the previous case, however the results are not as sensitive to wind mixing as in the two periods discussed in Section 9.2.2 and Section 9.2.3.

9.2.4 24 May to 20 July 1981

During this period the data indicates significant warming, concentration and deepening of the mixed layer by about 7 m. Note that the mixed layer is relatively shallow (compared with similar periods in the following years) due to large fresh water inflows during the 1980-81 winter. Results for a number of model runs are shown in Figs. 9.4 (a) to 9.4 (g) as well as in Table 9.4 (a) and Table 9.4 (b).

Fig 9.4 (a) shows a simulation with $C_w = C_c = 0$. Convective overturns maintain the mixed layer although no additional deepening is observed. Fig 9.4 (b) and Fig 9.4 (c) show the simulation results with two different combinations of C_w and C_c ($C_w = 3$, $C_c = 0.1$; $C_w = 6$, $C_c = 0.1$). Good comparison with data is obtained for both cases. Unlike the winter periods discussed in Section 9.2.1 and Section 9.2.2, results during this period are not very sensitive to values of C_w.

Fig 9.4 (d) shows the daily water balance for this period. Mean evaporation is of the order of 6.4 mm/day. Negative inflows are a direct consequence of errors in elevation either due to linear interpolation or

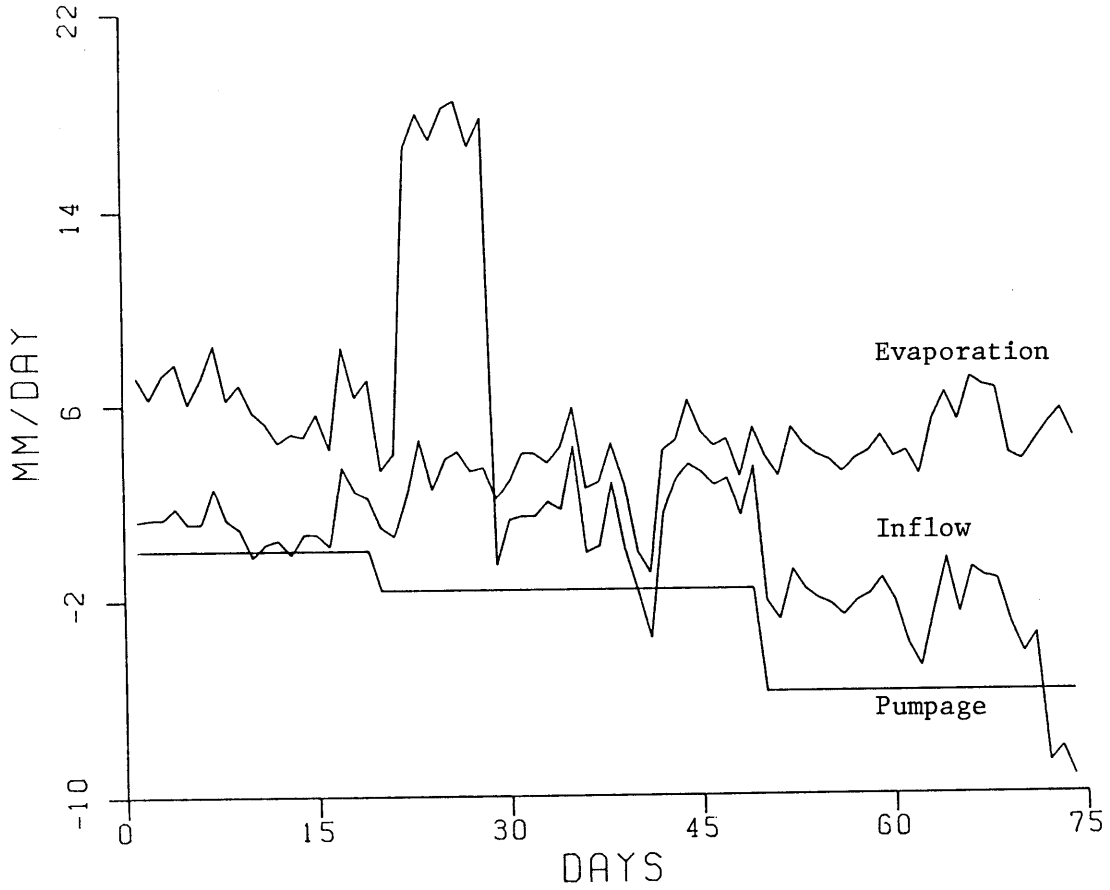

Fig. 9.3(e) Daily Water Balance for the Period 12 March 1980 to 26 May 1980 with C_w = 6 and C_c = .1

Table 9.3 (a)

Details of model run for the period 12 March 1980 - 26 May 1980

Calibration Coefficients			
C_w	0	3	6
C_c	0	0.1	0.1
Error Analysis Maximum Values			
Temperature °C	6.9	2.7	2.4
Salinity %	0.4	0.3	0.5
Density kg/m^2	5.3	3.5	6.0
Root Mean Square Values			
Temperature °C	1.8	1.0	1.0
Salinity %	0.2	0.1	0.1
Density kg/m^3	2.1	1.4	1.6
Mixing Parameters			
KE_w (J/m^2)	0	1034	2065
KE_c (J/m^2)	0	71	86
$\bar{u}_*$	.0034	.0034	.0034
$\bar{w}_*$	.0021	.0019	.0022
$\bar{R}_{i\sigma}$	3550	2160	1750
Change in Stability Index	2690	2690	2690
Error in Stability	-1990	430	760

Change → Final - initial

Error → Data - model

Table 9.3 (b)

Water and Heat Balance for the period 12 March 1980 - 26 May 1980

Calibration Coefficients			
C_w	0	3	6
C_c	0	0.1	0.1
Water Balance			
Evaporation (mm)	230	246	239
Pumpage (mm)	-200	-200	-200
Inflow (mm)	184	200	193
Net Inflow (mm)	154	154	154
Thermal Energy Balance			
Short Wave Radiation ($KCal/m^2/day$)	5060	5060	5060
Atmospheric radiation (")	7070	7070	7070
Back radiation (")	8970	9030	9010
Evaporative Flux (")	1830	1960	1890
Net Warming (")	1500	850	980
Meteorology			
Air Temperature (°C)	23.5		
Humidity (%)	55		
Wind Speed (m/s)	3.3		

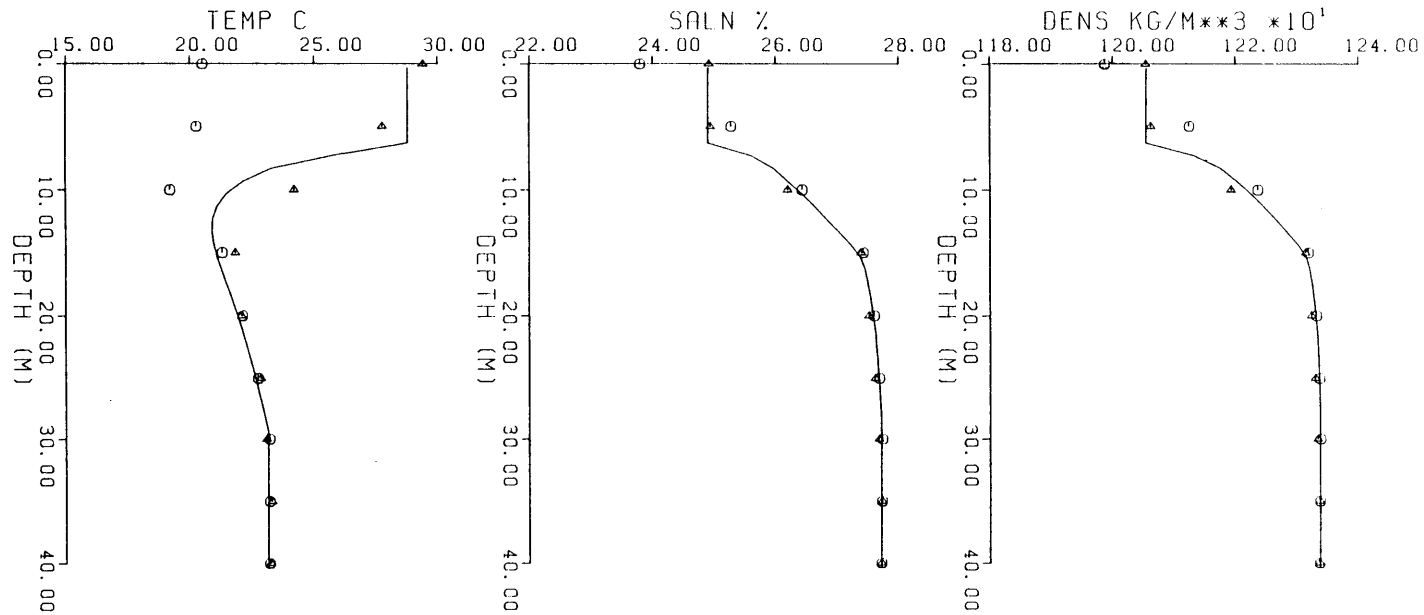

Fig. 9.3(f) Data and Model Results for the Period 12 March 1980 to 26 May 1980 with $C_w = 3$ and $C_c = 0.1$

o Initial Data
Δ Final Data
— Model Result

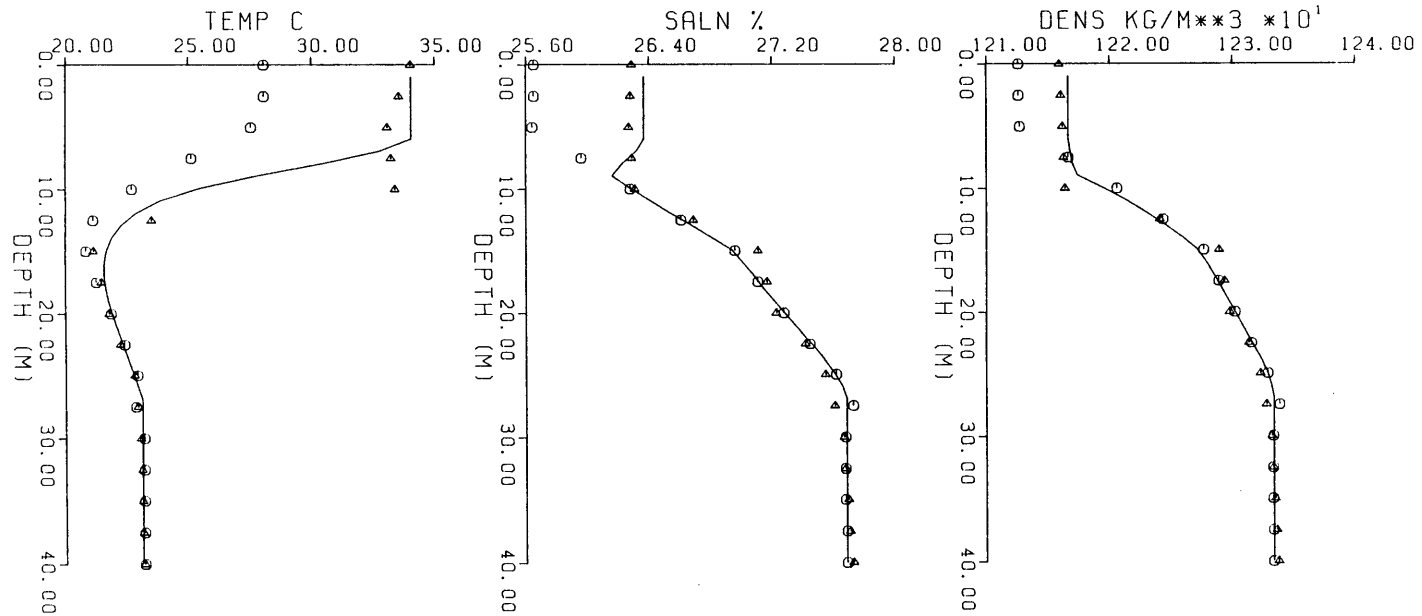

Fig. 9.4(a) Data and Model Results for the Period 24 May 1981 to 20 July 1981 with C_w = 0.0 and C_c = 0.0.

o Initial Data
Δ Final Data
— Model Result

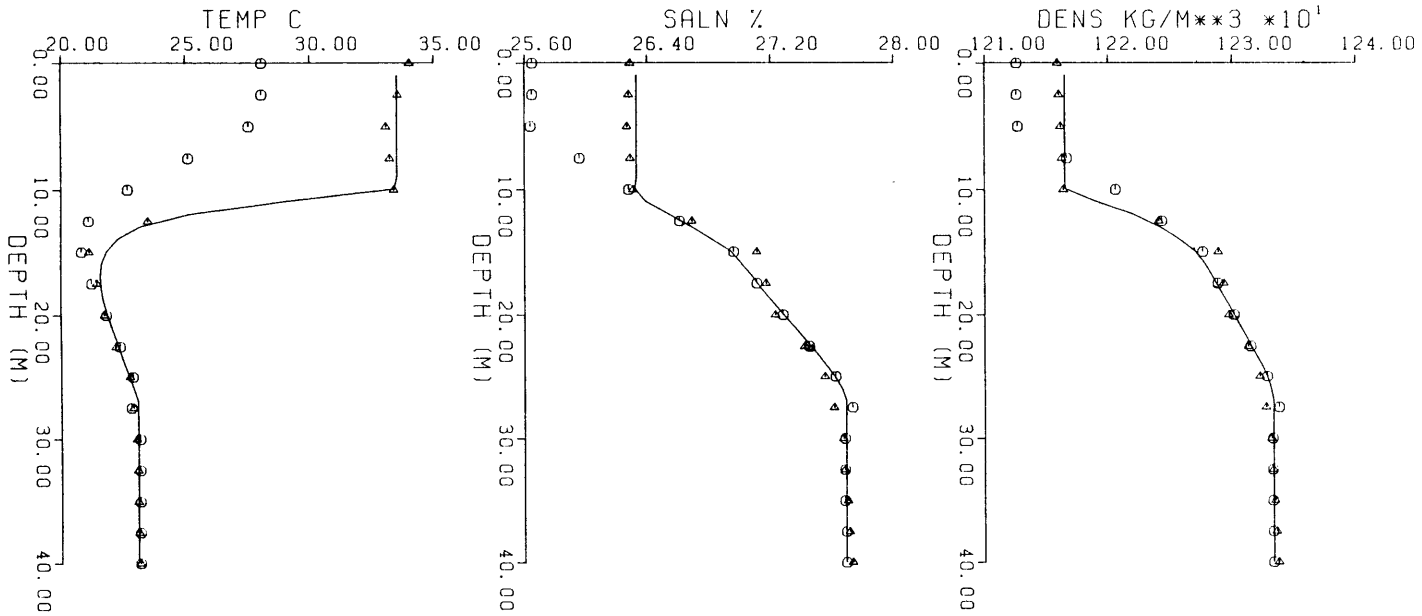

Fig. 9.4(c) Data and Model Results for the Period 24 May 1981 to 20 July 1981 with C_w = 3. and C_c = .1

o Initial Data
Δ Final Data
— Model Result

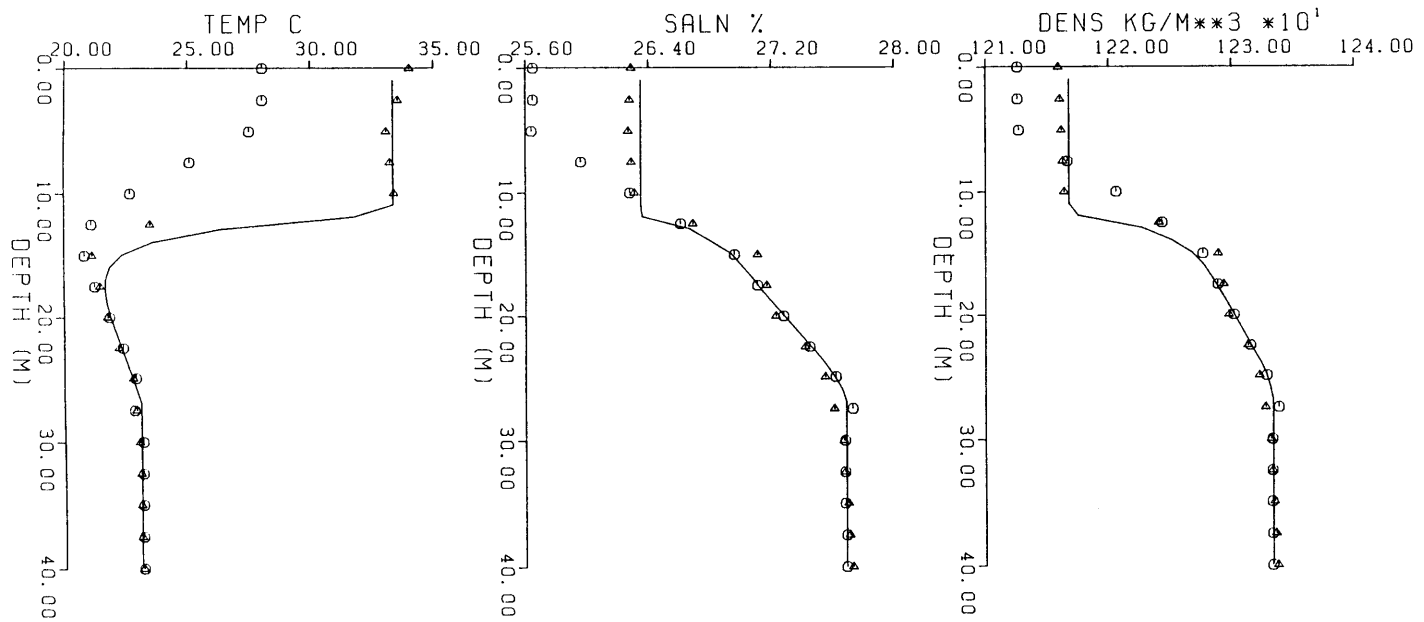

Fig. 9.4(b) Data and Model Results for the Period 24 May 1981 to 20 July 1981 with C_w = 6. and C_c = .1

o Initial Data
Δ Final Data
— Model Result

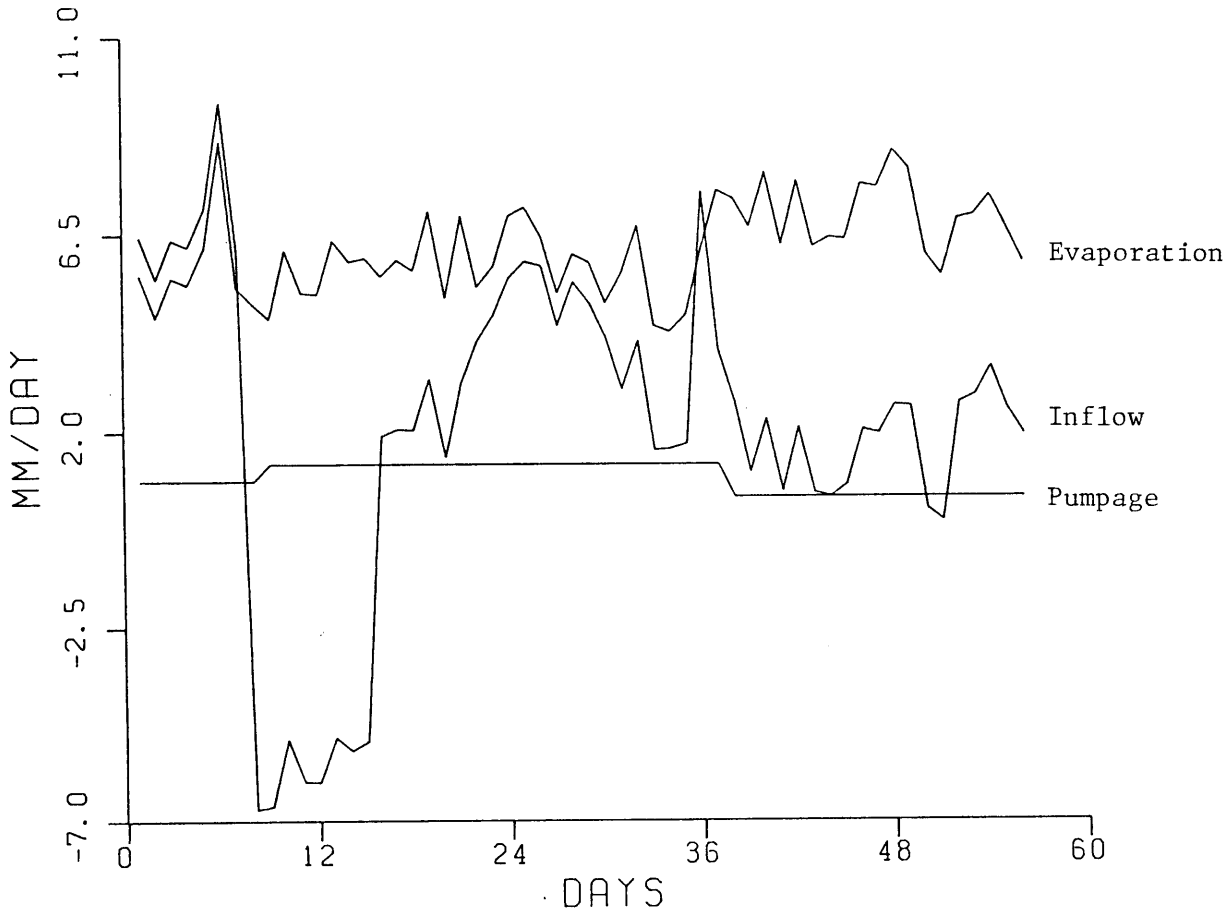

Fig. 9.4(d) Daily Water Balance for the Period 24 May 1981 to 20 July 1981 with C_w = 6 and C_c = .1

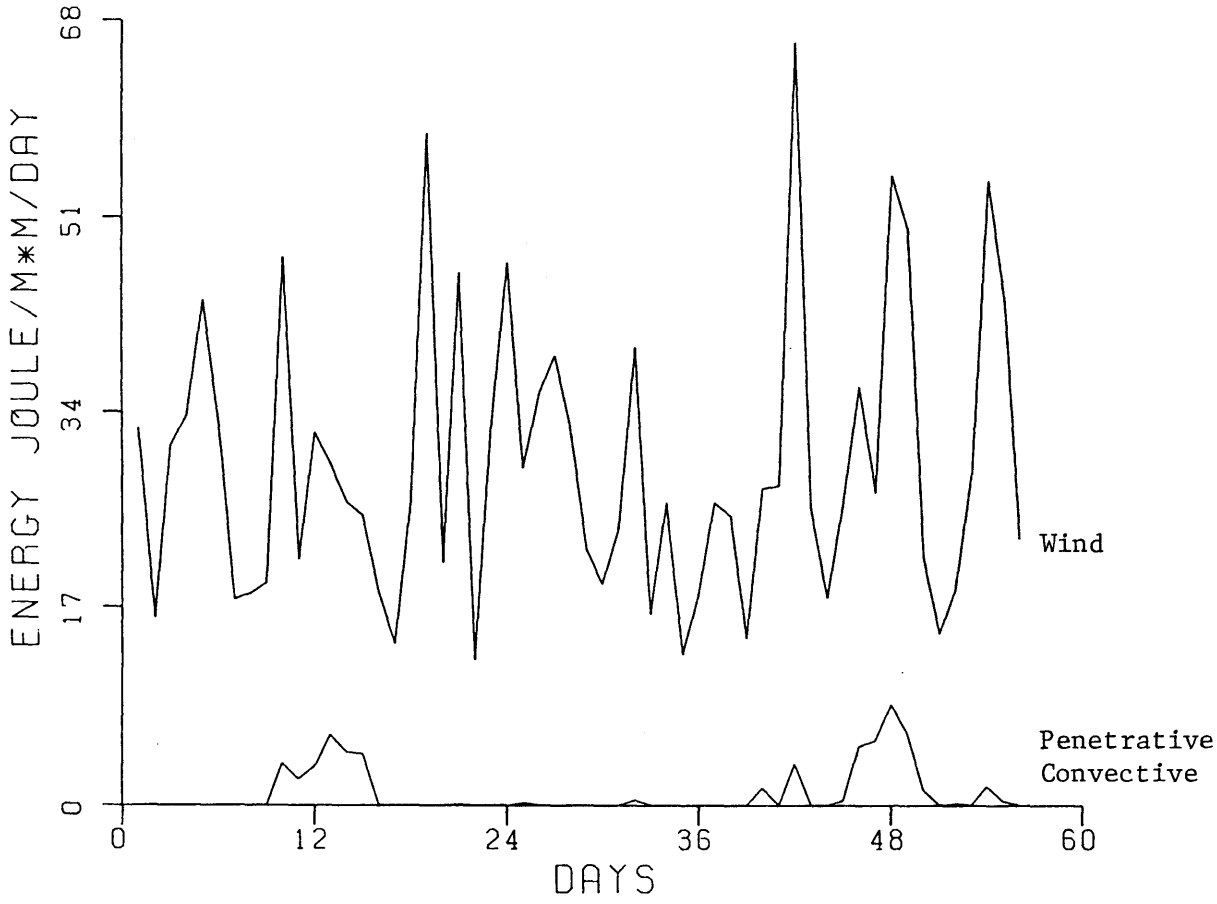

Fig. 9.4(e) Daily Input of Wind and Penetrative Convective Mixing energy for the Period 24 May 1981 to 20 July 1981 with C_w = 6 and C_c = .1.

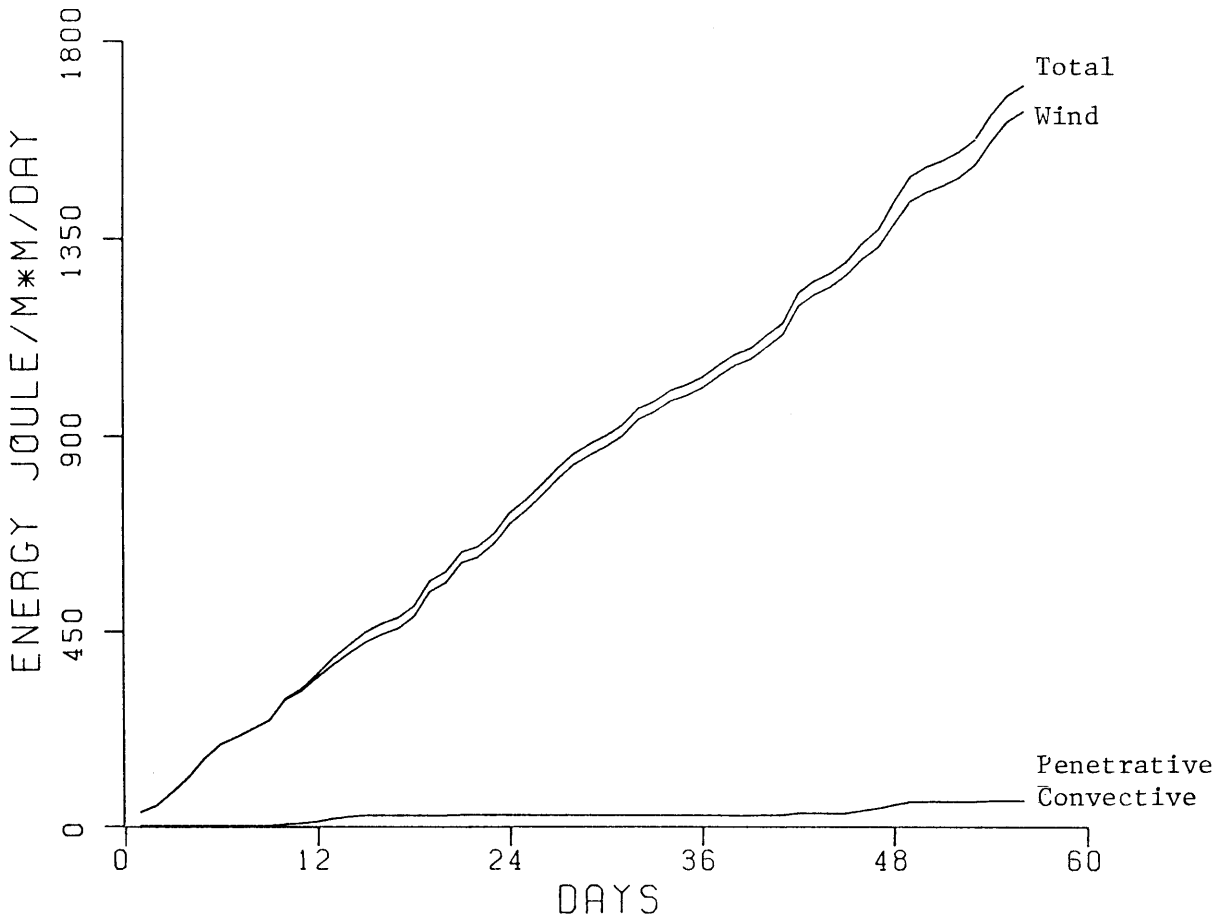

Fig. 9.4(f) Cumulative Wind and Penetrative Convective Mixing Energy for the Period 24 May 1981 to 20 July 1981 with $C_w = 6$ and $C_c = .1$

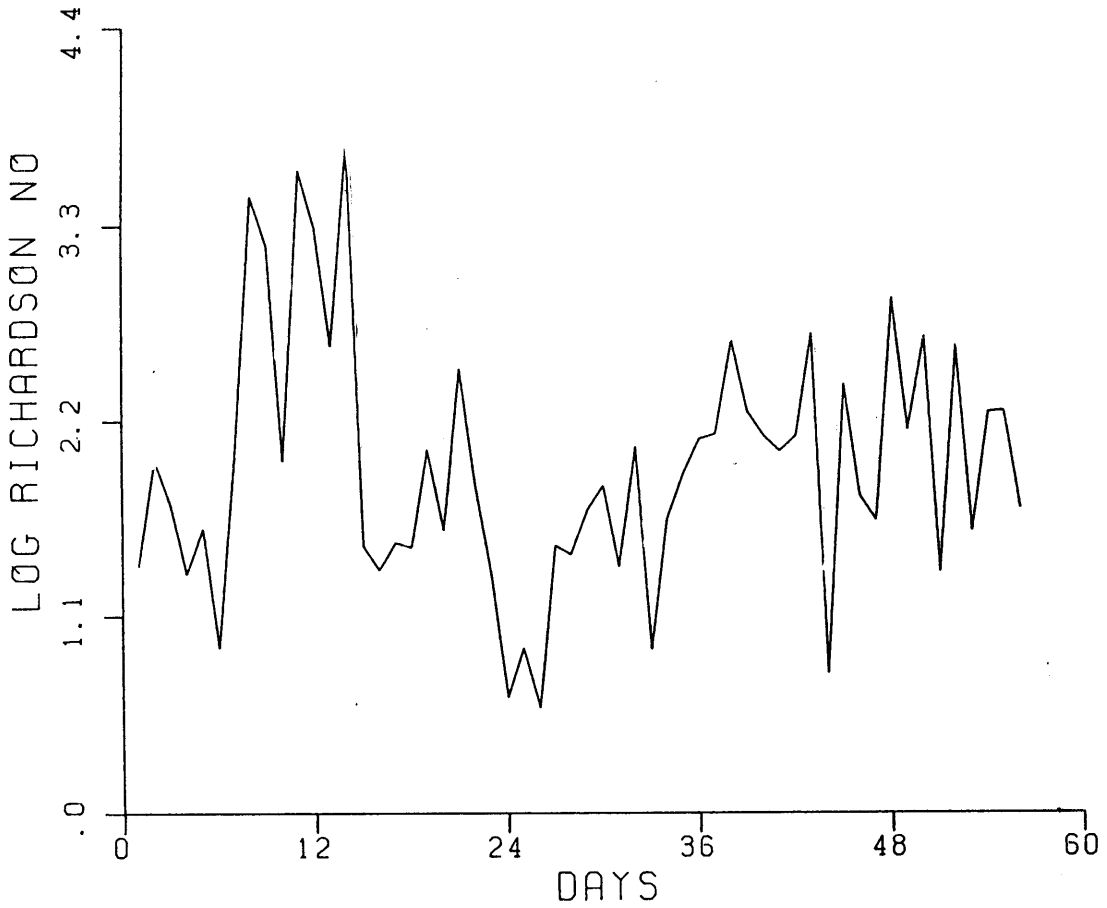

Fig. 9.4(g) Daily Variation of Richardson Number for the Period 24 May 1981 to 20 July 1981 with C_w = 6 and C_c = .1

Table 9.4 (a)

Details of model run for the period 24 May 1981 - 20 July 1981

Calibration Coefficients			
C_w	0	0	6
C_c	0	0.1	0.1
Error Analysis Maximum Values			
Temperature °C	8.0	.7	6.2
Salinity %	0.2	.2	0.3
Density kg/m^2	3.1	1.9	5.0
Root Mean Square Values			
Temperature °C	1.9	.2	1.3
Salinity %	0.1	.1	0.1
Density kg/m^3	0.8	.6	1.1
Mixing Parameters			
KE_w (J/m^2)	0	830	1660
KE_c (J/m^2)	0	60	59
$\bar{u}_*$	.00352	.00352	.00352
$\bar{w}_*$	.00200	.00200	.00188
$\bar{R}_{i\sigma}$	321	438	396
Change in Stability Index	-3103	-3103	-3103
Error in Stability	645	135	53

Change → Final - initial

Error → Data - model

Table 9.4 (b)

Water and Heat Balance for the period 24 May 1981 - 20 July 1981

Calibration Coefficients			
C_w	0	3	6
C_c	0	0.1	0.1
Water Balance			
Evaporation (mm)	387	365	352
Pumpage (mm)	53	53	53
Inflow (mm)	153	131	118
Net Inflow (mm)	-288	-287	-287
Thermal Energy Balance			
Short Wave Radiation ($KCal/m^2/day$)	6990	6990	6990
Atmospheric radiation (")	8130	8130	8130
Back radiation (")	9880	9820	9780
Evaporative Flux (")	3970	3750	3620
Net Warming (")	855	1211	1423
Meteorology			
Air Temperature (°C)	30.59		
Humidity (%)	43		
Wind Speed (m/s)	3.37		

actual measurement errors. Fig 9.4 (e) shows the daily input of mechanical energy due to wind and penetrative convective mixing. Clearly, wind mixing with cumulative input of 1660 Joule/m^2 is predominant compared with penetrative convective mixing of only 59 Joule/m^2. These cumulative values are shown in Fig 9.4 (f).

During this period the velocity scale associated with wind mixing $\bar{u}_{*,w}$ is about 1.7 times the velocity scale $\bar{w}_*$ associated with convective mixing. This is in sharp contrast to the situation during the fall periods charcterized by significant convective activity (Section 9.3) when $\bar{w}_*$ is greater than $\bar{u}_{*,w}$. Finally Fig 9.4 (g) is a plot of daily values of Richardson Number based on the velocity scale σ. The mean value is about 400.

Table 9.4 (b) shows the mass and thermal energy balance for this period. The short wave radiation is 15% more than the base case values.The effect of mechanical mixing on evaporation and back radiation is shown. Back radiation and evaporation are maximum for the case with no wind or penetrative convective mixing i.e. for the case where there is no mechanism to drive the thermal energy within the lake. Conversely, these thermal energy flux terms are minimum for the case of maximum mixing. The difference in the rate of evaporation for the case with zero mixing and 'maximum' mixing shown in Table 9.4(b) is about 10%.

Based on the analysis presented in Sections 9.2.1 to 9.2.4 the best estimate for $C_w = 6$.

9.3 Periods with Significant Convective Activity

During late summer and early winters the lake experiences rapid cooling as well as a high rate of evaporation. These two effects result in significant convective activity during this part of the year. Following are four such periods, corresponding to the dates on which profiles have been measured:

1. 21 September - 18 December 1981
2. 28 September - 1 November 1982
3. 25 August - 3 October 1983
4. 30 October - 10 November 1983

These four periods were used to estimate the value of C_c. Simulation results for the periods September to December 1981 and October to November 1983 are discussed below. During the first of these, both the salinity and the temperature profiles are stable. For the second period, the salinity profile is unstable and held up by the stable temperature profile. (Also see Appendix E)

9.3.1 21 September - 18 December, 1981

During this period the data indicates significant cooling and concentration both of which results in enhanced convective mixing. Fig. 9.5 (a), Fig. 9.5 (b) and Fig. 9.5 (c) show the initial and the final profile results for the case with $C_w = 6$ and $C_c = 0$; $C_w = 6$ and $C_c = 0.1$ and $C_w = 6$ and $C_c = 0.25$. As expected, the model indicates progressively deeper mixed layer depths as C_c is increased. Best results are obtained with $C_w = 6$ and $C_c = 0.1$ that has root mean square errors of .1°C. .04% and .3 kg/m^3 in temperature, salinity and density respectively (see also Table 9.5 (a)). Note that results with $C_c = 0$ also show good agreement with data.

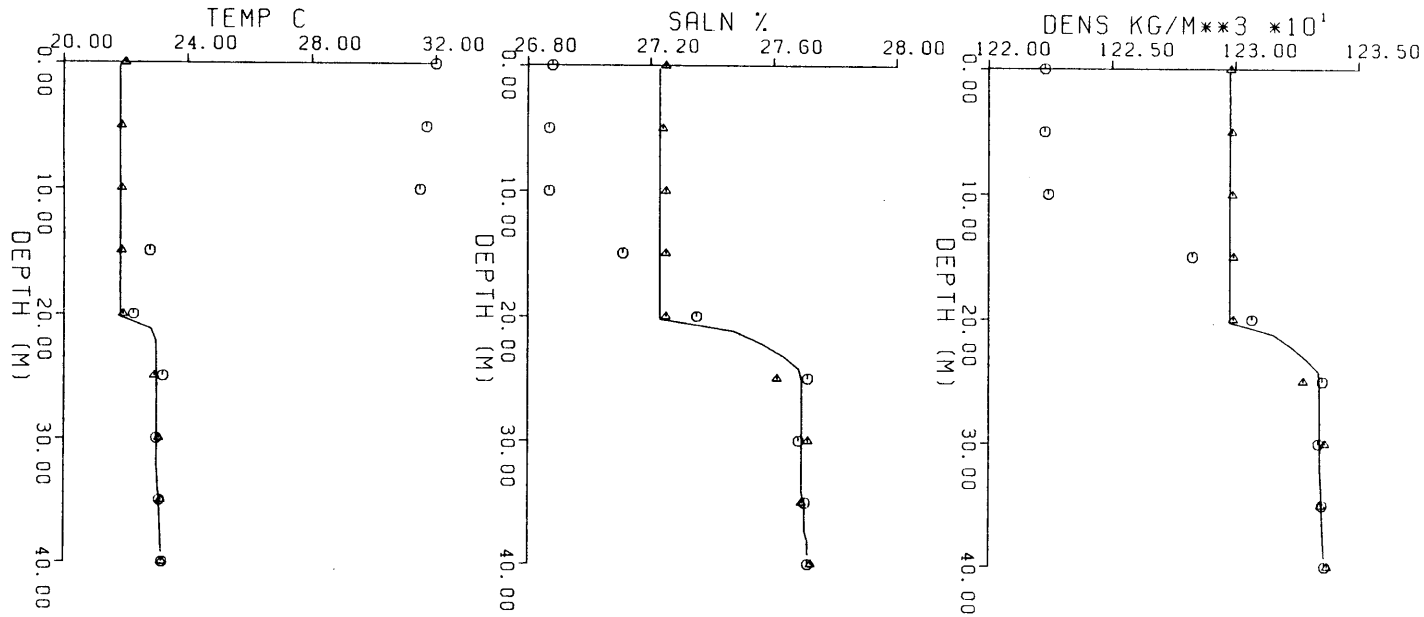

Fig. 9.5(a) Data and Model Results for the Period 21 September 1981 to 18 December 1981 with $C_w = 6$ and $C_c = 0.0$

○ Initial Data
Δ Final Data
— Model Result

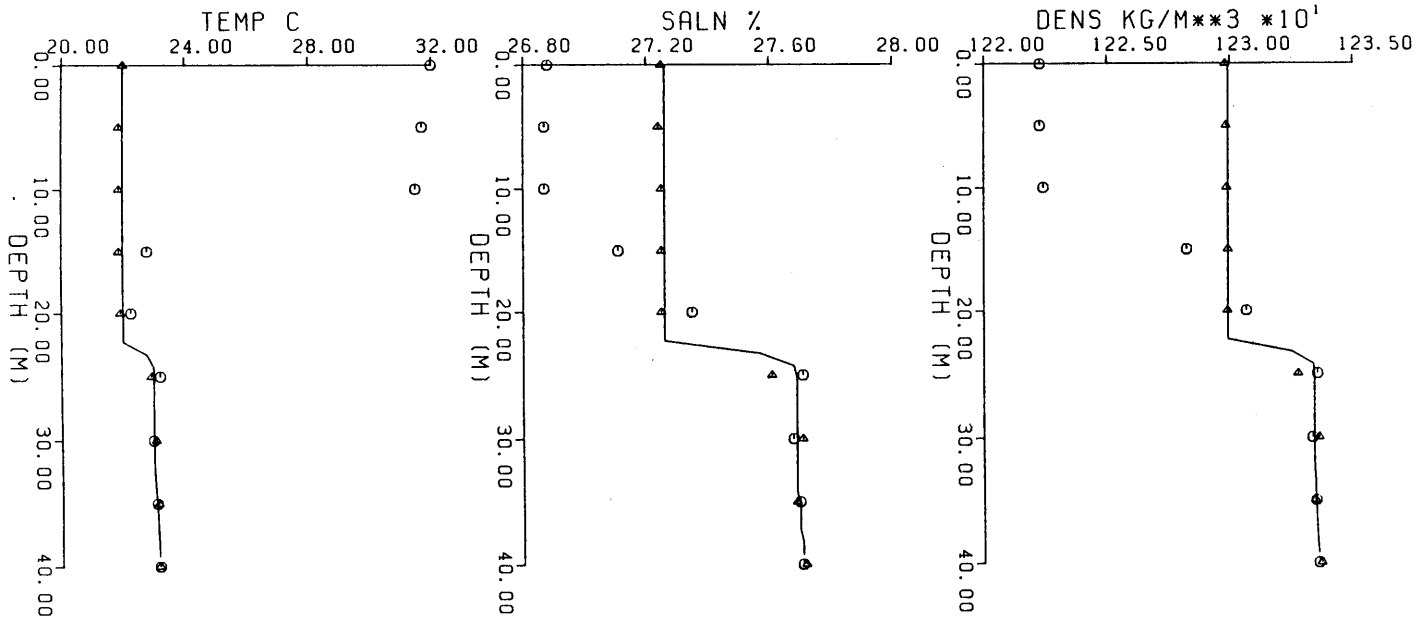

Fig. 9.5(b) Data and Model Results for the Period 21 September 1981 to 18 December 1981 with $C_w = 6$ and $C_c = .1$

o Initial Data
Δ Final Data
— Model Result

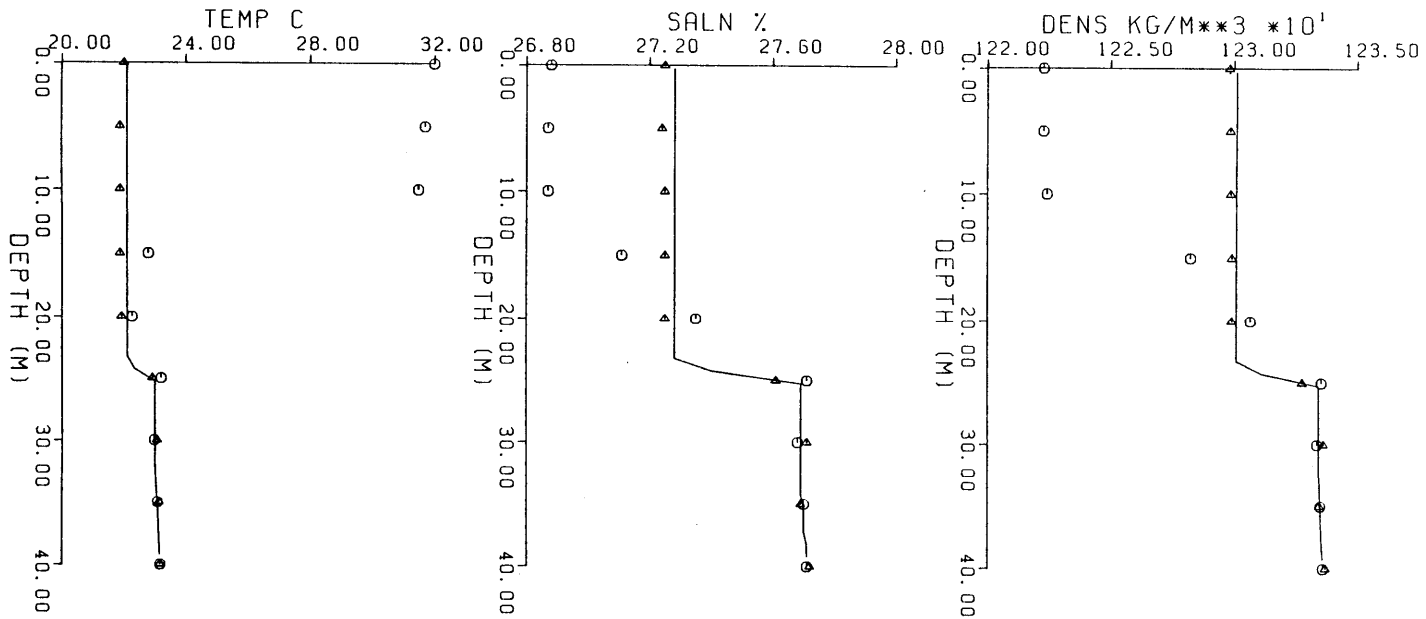

Fig. 9.5(c) Data and Model Results for the Period 21 September 1981 to 18 December 1981 with $C_w = 6$ and $C_c = .25$

o Initial Data
Δ Final Data
— Model Result

Table 9.5 (a)

Details of model run for the period 21 September 1980 - 18 December 1981

Calibration Coefficients		
C_w	6	6
C_c	0	.1
Error Analysis Maximum Values		
Temperature °C	.6	.5
Salinity %	.1	.2
Density kg/m^2	.7	1.2
Root Mean Square Values		
Temperature °C	.2	.1
Salinity %	.04	.04
Density kg/m^3	.3	.3
Mixing Parameters		
KE_w (J/m^2)	710	710
KE_c (J/m^2)	0	880
$\bar{u}_*$	.00280	.00280
$\bar{w}_*$	.00690	.00703
$\bar{R}_{i\sigma}$	1070	1790
Change in Stability Index	-3958	-3958
Error in Stability	-218	25

Change → Final - initial

Error → Data - model

Table 9.5 (b)

Water and Heat Balance for the period 21 September 1981 - 18 December 1981

Calibration Coefficients		
C_w	6	6
C_c	0	0.1
Water Balance		
Evaporation (mm)	410	410
Pumpage (mm)	158	158
Inflow (mm)	223	223
Net Inflow (mm)	-345	-345
Thermal Energy Balance		
Short Wave Radiation ($KCal/m^2/day$)	4630	4630
Atmospheric radiation (")	7080	7080
Back radiation (")	9430	9430
Evaporative Flux (")	2670	2670
Net Warming (")	-1330	-1320
Meteorology		
Air Temperature (°C)	22.58	
Humidity (%)	57	
Wind Speed (m/s)	2.79	

Table 9.5 (b) shows the cumulative water balance for this period. Mean evaporation rate is about 4.7 mm/day (Fig. 9.5 (d)). Fig. 9.5 and Fig. 9.5 (f) show the daily and cumulative input of wind and penetrative convective mixing energies for this period. The cumulative penetrative mixing energy of 876 Joule/m^2 is higher than the penetrative convective energy of 400 Joule/m^2. It is interesting to note that during this period of significant convective activity, $\bar{w}_*$ is larger than $\bar{u}_{*,w}$ by a factor of about 2.5. This is in sharp contrast to the May to July periods of low convective activity during which $\bar{u}_{*,w}$ is larger than $\bar{w}_*$. Finally, the Richardson Number during this period is significantly larger than during the early part of the year. Daily plot of Richardson Number is shown in Fig 9.5 (g).

9.3.2 3 October - 10 November 1983

This is the second period discussed in this section that is characterised by signficant convective activity as a result of the effects of cooling and concentration due to evaporation. During this period data indicates a deepening of the mixed layer by 5 m. Also the salinity profile is unstable and is held up by the stable temperature profile. As in the previous cases, three simulations were performed with C_w = 6 and C_c = 0; C_w = 6 and C_c = 0.1, and C_w = 6 and C_c = 0.25. A comparison of these simulation results with data are shown in Fig. 9.6 (a) to Fig. 9.6 (c). Further details of these runs are included in Table 9.6 (a) and Table 9.6 (b). Based on these, best fit value of C_c = 0.1 is selected.

The water balance for this period, shown in Table 9.6 (b) and Fig. 9.6 (d), indicates daily mean evaporation rate of 4.2 mm. Daily and

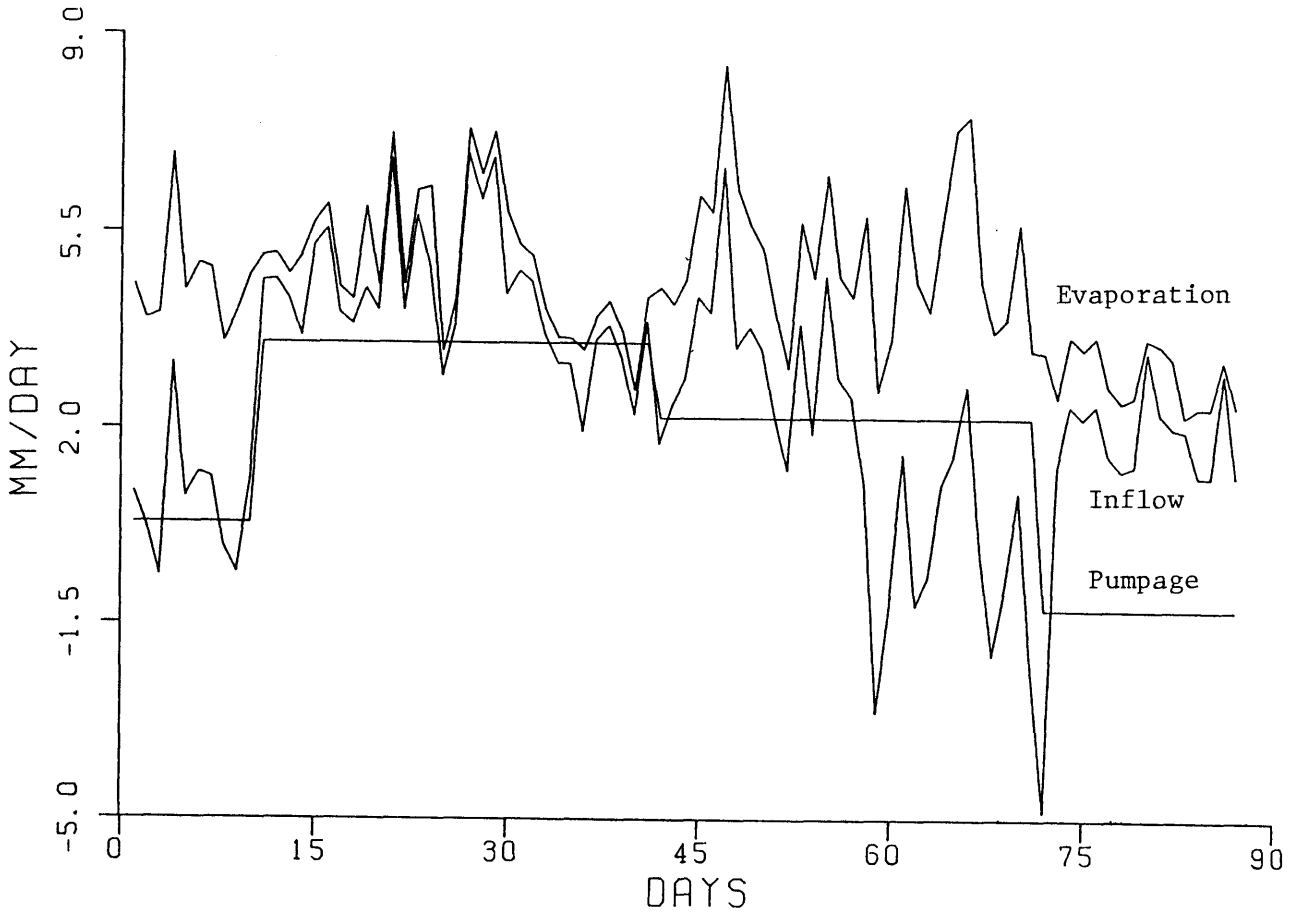

Fig. 9.5(d) Daily Water Balance for the Period 21 September 1981 to 18 December 1981 with C_w = 6 and C_c = .1

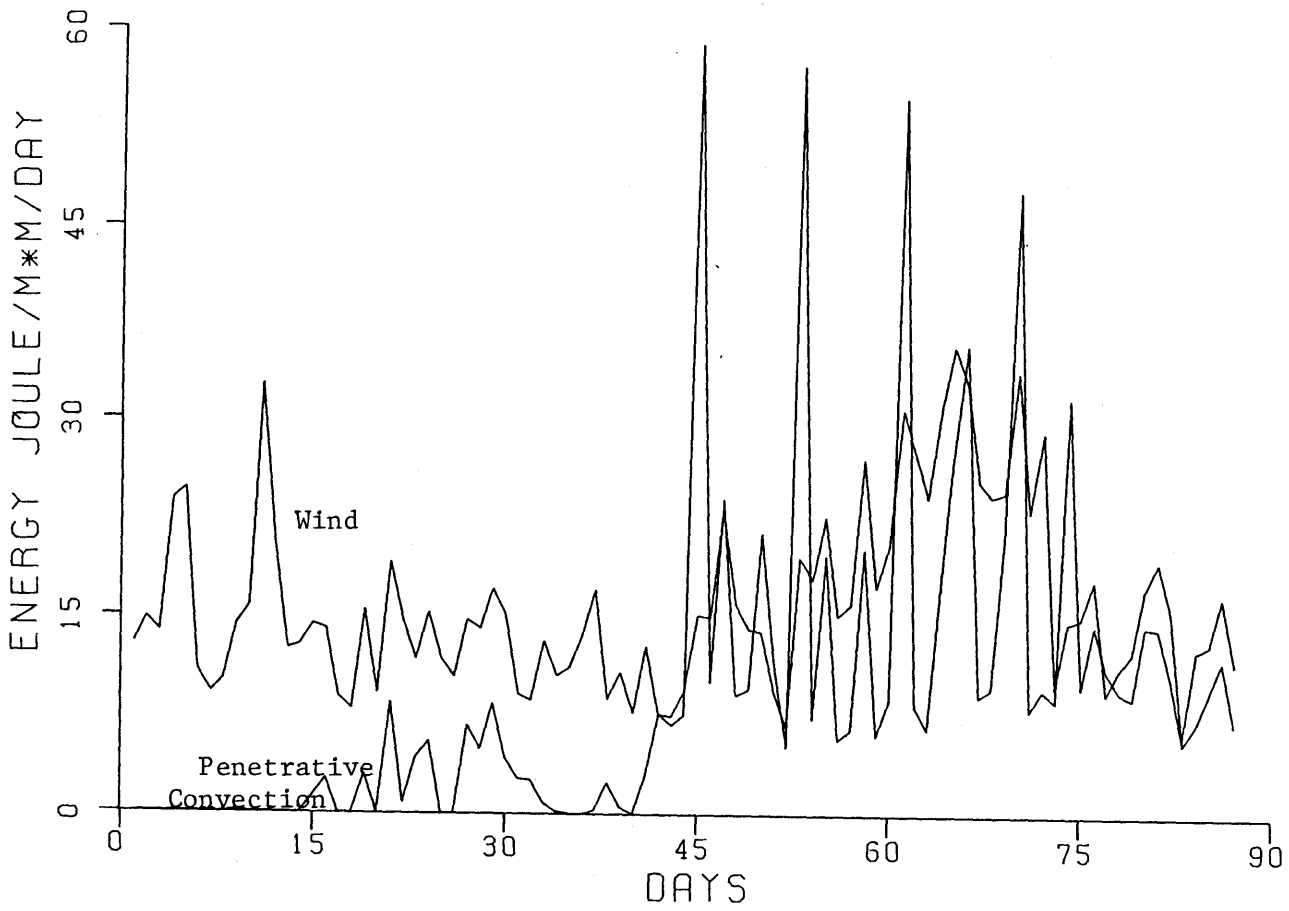

Fig. 9.5(e) Daily Wind and Penetrative Convective Mixing Energy for the Period 21 September 1981 to 18 December 1981 with $C_w = 6$ and $C_c = .1$

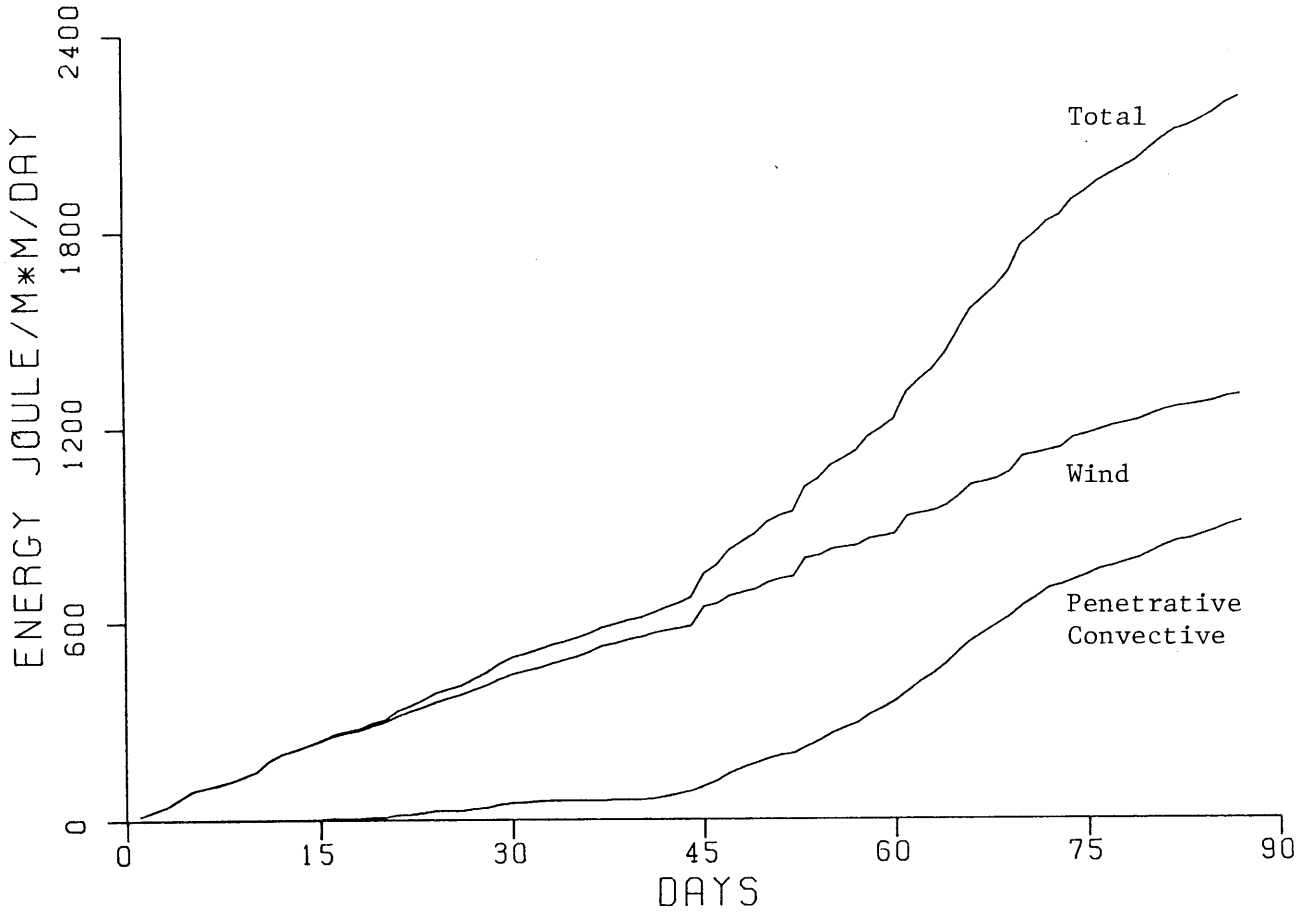

Fig. 9.5(f) Cummulative Wind and Penetrative Convective Mixing Energy for the Period 21 September 1981 to 18 ~~December~~ 1981 with $C_w = 5$ and $C_c = .1$

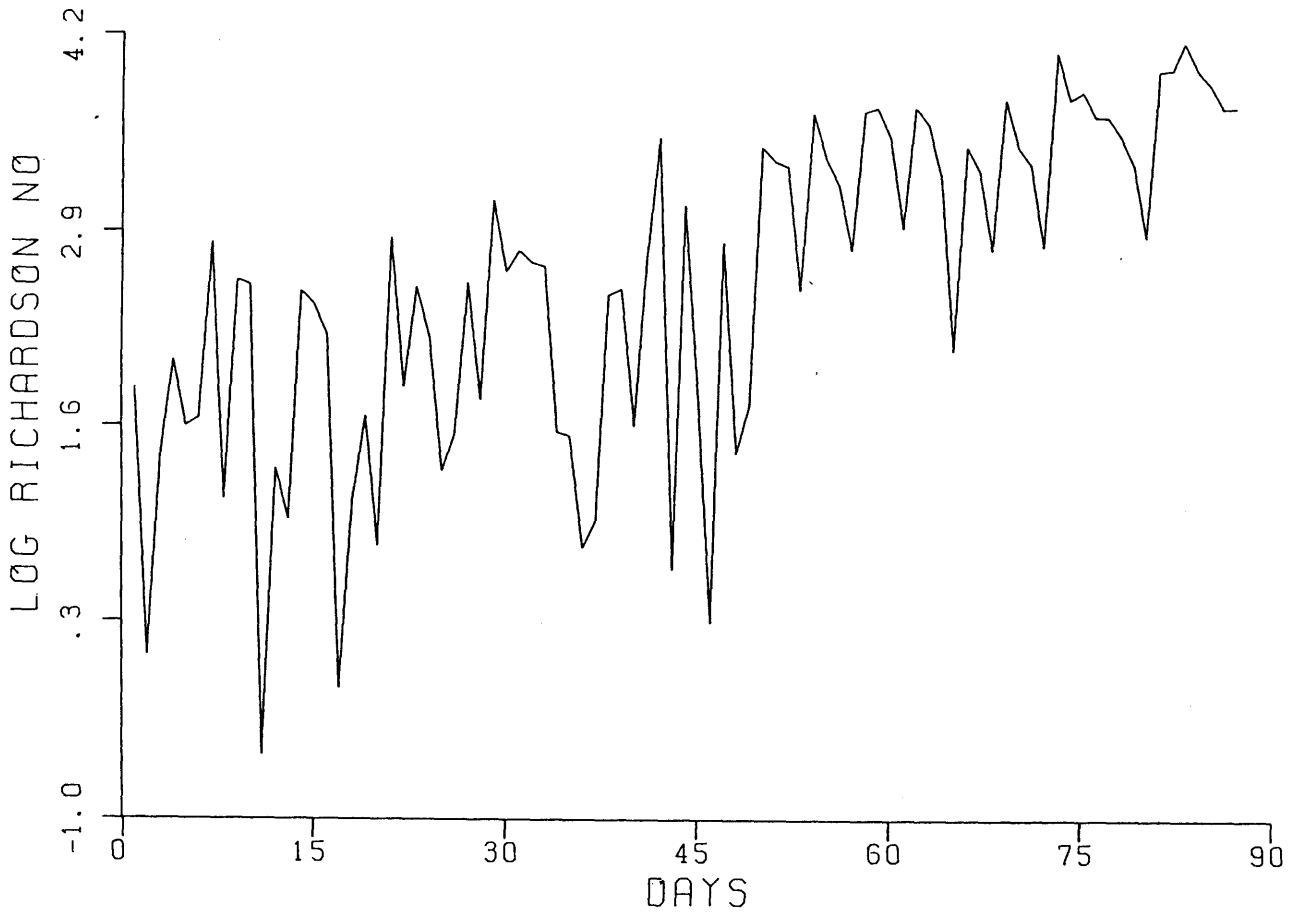

Fig. 9.5(g) Daily Variation of Richardson Number for the Period 21 September 1981 to 18 December 1981 with $C_w = 6$ and $C_c = .1$

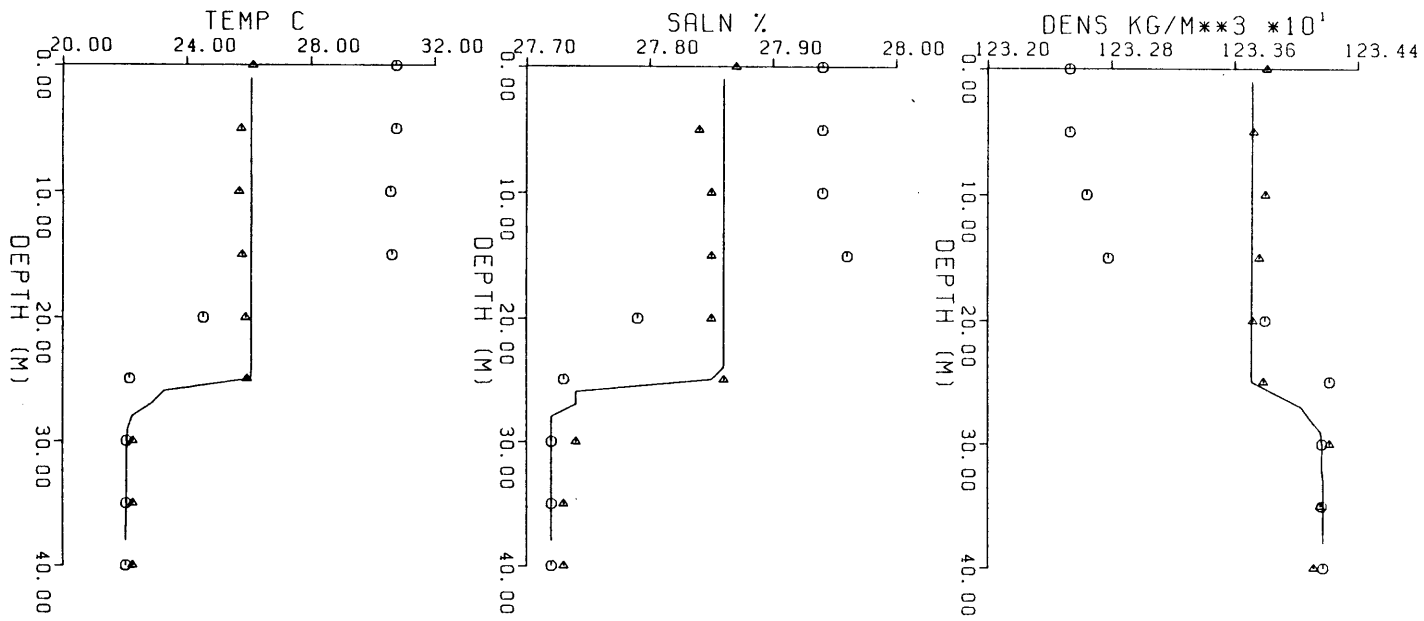

Fig. 9.6(a) Data and Model Results for the Period 3 October 1983 to 10 November 1983 with $C_w = 6$ and $C_c = 0.0$.

o Initial Data
Δ Final Data
— Model Result

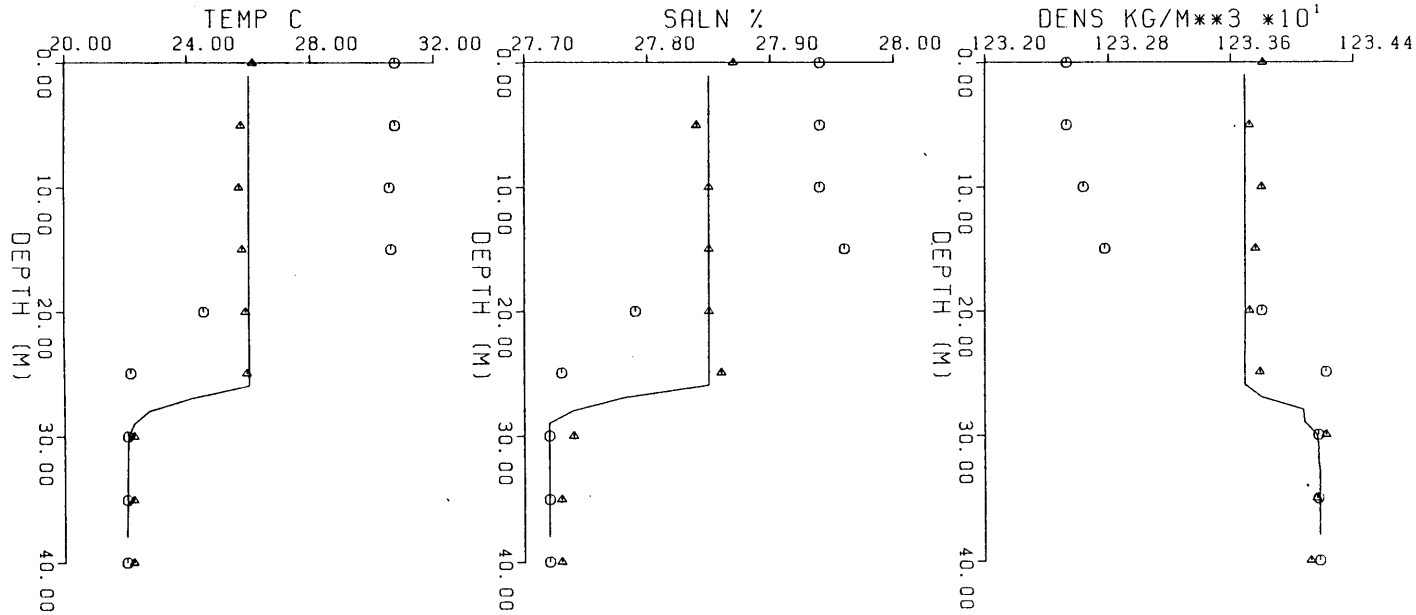

Fig. 9.6(b) Data and Model Results for the Period 3 October to 10 November 1983 with $C_w = 6$ and $C_c = .1$

o Initial Data
Δ Final Data
— Model Result

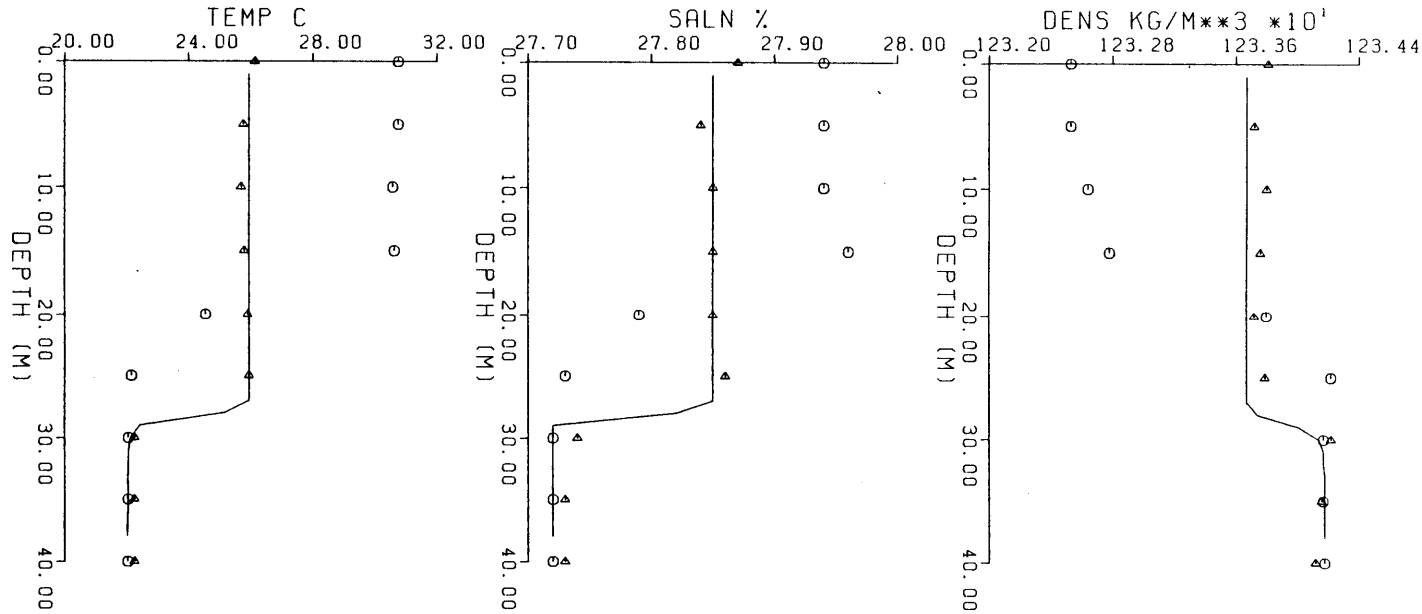

Fig. 9.6(c) Data and Model results for the Period 3 October 1983 to 10 November 1983 with $C_w = 6$ and $C_c = 0.25$

o Initial Data
Δ Final Data
— Model Result

Table 9.6 (a)

Details of model run for the period 3 October 1983 - 10 November 1983

Calibration Coefficients		
C_w	6	6
C_c	0.25	0.1
Error Analysis Maximum Values		
Temperature °C	3.0	2.3
Salinity %	0.1	0.07
Density kg/m^2	0.5	0.4
Root Mean Square Values		
Temperature °C	0.8	0.5
Salinity %	0.0	0.1
Density kg/m^3	0.2	0.1
Mixing Parameters		
KE_w (J/m^2)	5500	550
KE_c (J/m^2)	342	175
$\bar{u}_*$	.00264	.0026
$\bar{w}_*$	.00571	.0059
$\bar{R}_{i\sigma}$	636	500
Change in Stability Index	-1797	-1790
Error in Stability	0	-20

Change → Final - initial

Error → Data - model

Table 9.6 (b)

Water and Heat Balance for the period 3 October 1983 - 10 November 1983

Calibration Coefficients		
C_w	6	6
C_c	0.25	0.1
Water Balance		
Evaporation (mm)	154	156
Pumpage (mm)	239	239
Inflow (mm)	174	176
Net Inflow (mm)	-219	-219
Thermal Energy Balance		
Short Wave Radiation ($KCal/m^2/day$)	3080	3080
Atmospheric radiation (")	7780	7780
Back radiation (")	9290	9300
Evaporative Flux (")	2310	2340
Net Warming (")	-1020	1070
Meteorology		
Air Temperature (°C)	26.52	
Humidity (%)	44	
Wind Speed (m/s)	2.67	

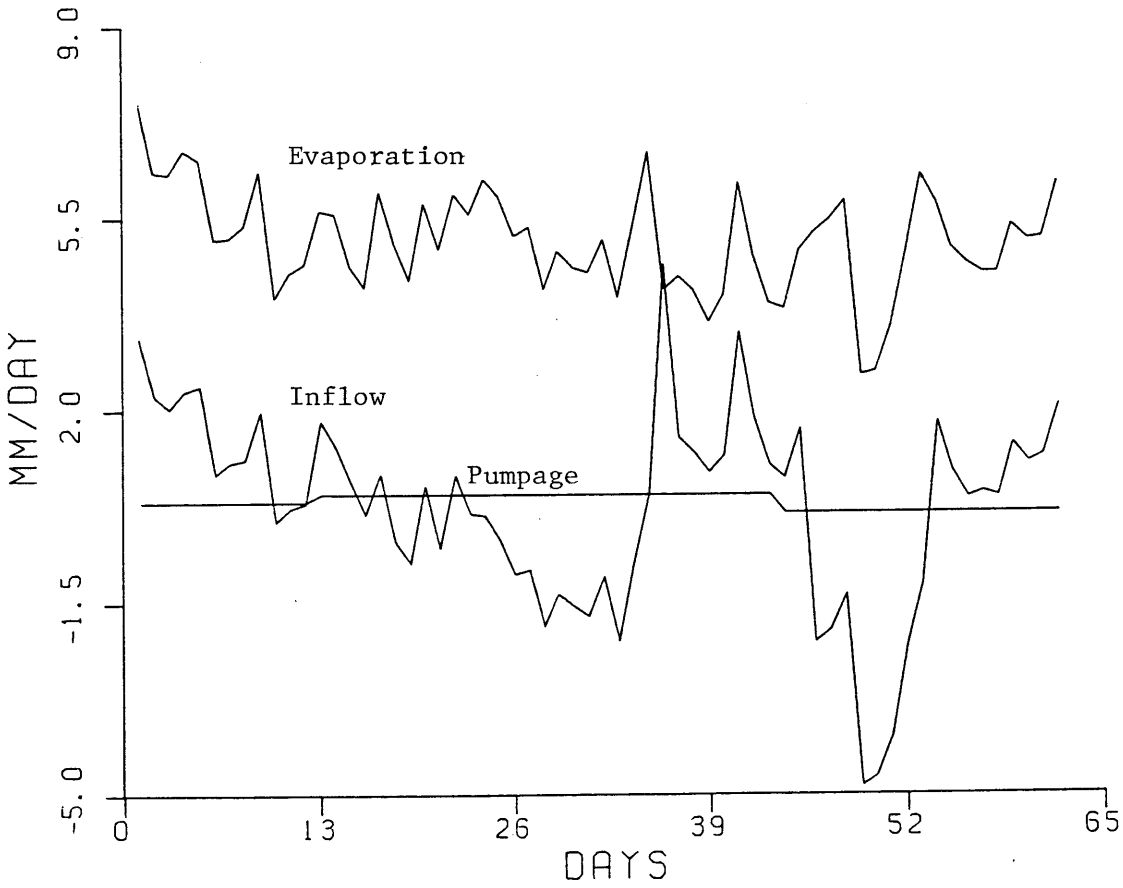

Fig. 9.6(d) Daily Water Balance for the Period 3 October 1983 to 10 November 1983 with $C_w = 6$ and $C_c = .1$

cumulative mixing energies are shown in Fig. 9.6 (e) and Fig 9.6 (f) that indicate total penetrative convective mixing energy of 177 Joule/m^2 and wind mixing energy of 275 Joule/m^2. The ratio of the velocity scale $\bar{w}_*$ to $\bar{u}_{*,w}$ is about 2.3, indicative of high convective activity. Finally, Fig. 9.6 (g) shows the daily variation of the Richardson number.

A number of important conclusions can be based on the results discussed in this section. During periods characterised by a high ratio of $\bar{w}_*$ to $\bar{u}_{*,w}$ convective activity in itself is sufficient to maintain the depth of the mixed layer. However, a combination of wind energy and penetration convective mixing energy is necessary to deepen the mixed layer as observed in the data. Best estimate of C_c is about 0.1.

9.4 Periods With both Wind and Convective Mixing

During the period May to September, both wind and convective mixing are important. A few simulations were performed to verify the best estimate of $C_w = 6$ and $C_c = 0.1$ obtained in the last two sections. As the summer progresses the rate of warming decreases and the evaporation rate stays constant or increases slightly as a result of these two effects convective activity increases. This is clear from the analysis of the following four periods:

1. 26 May - 6 October, 1980
2. 20 July - 21 September 1981
3. 25 July - 28 September, 1982
4. 6 July - 25 August, 1983

Of these four periods, two are discussed in the following sections.

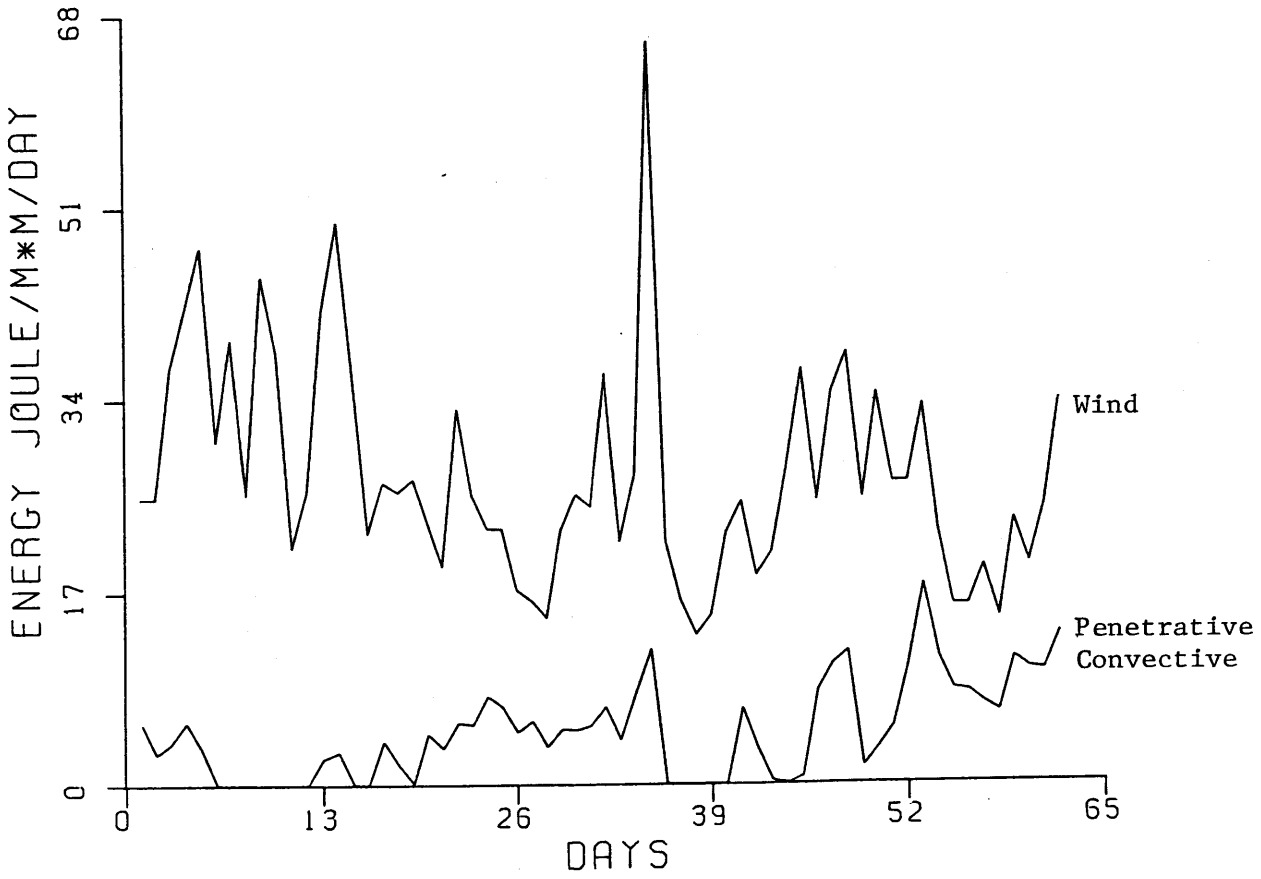

Fig. 9.6(e) Daily Input of Wind and Penetrative Convective Mixing Energy for the Period 3 October 1983 to 10 November 1983 with $C_w = 6$ and $C_c = .1$

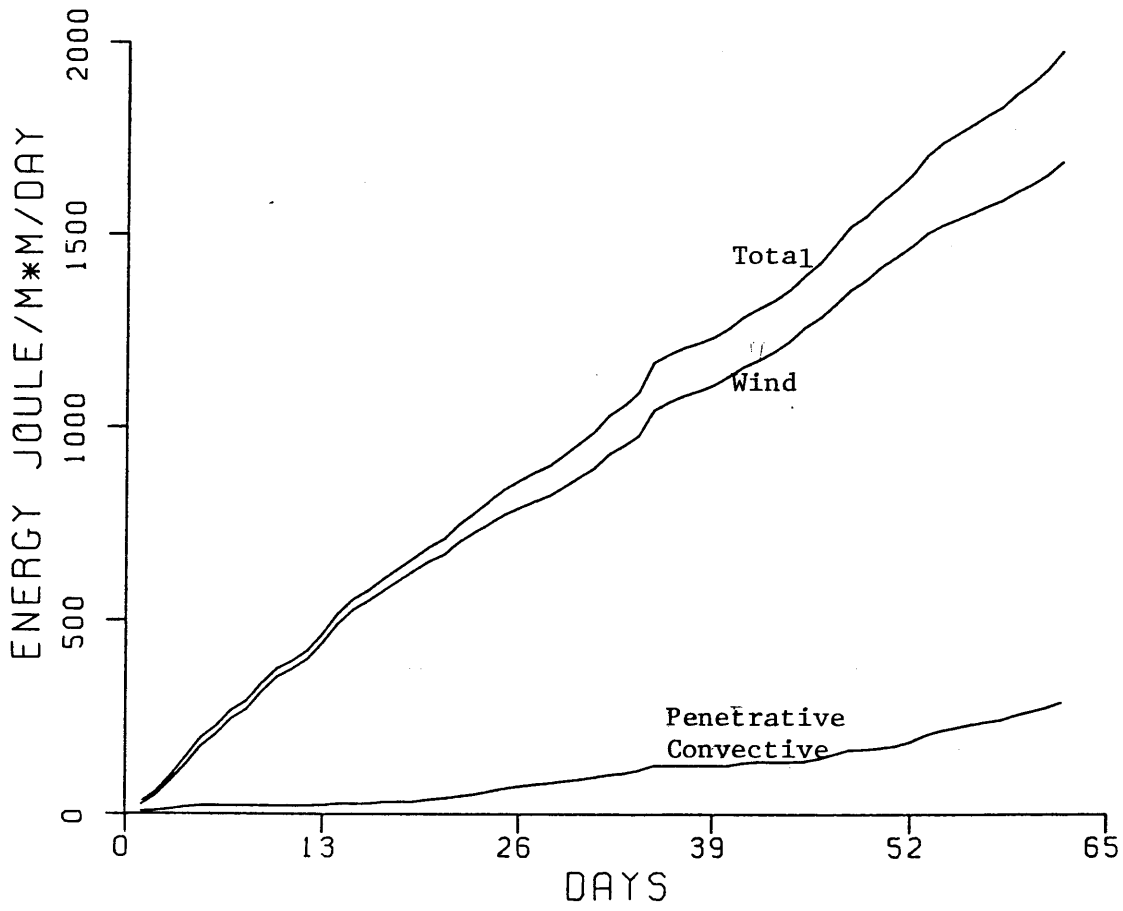

Fig. 9.6(f) Cummulative wind and Penetrative Convective Mixing Energy for the Period 3 October to 10 November 1983 with C_w = 6 and C_c = .1

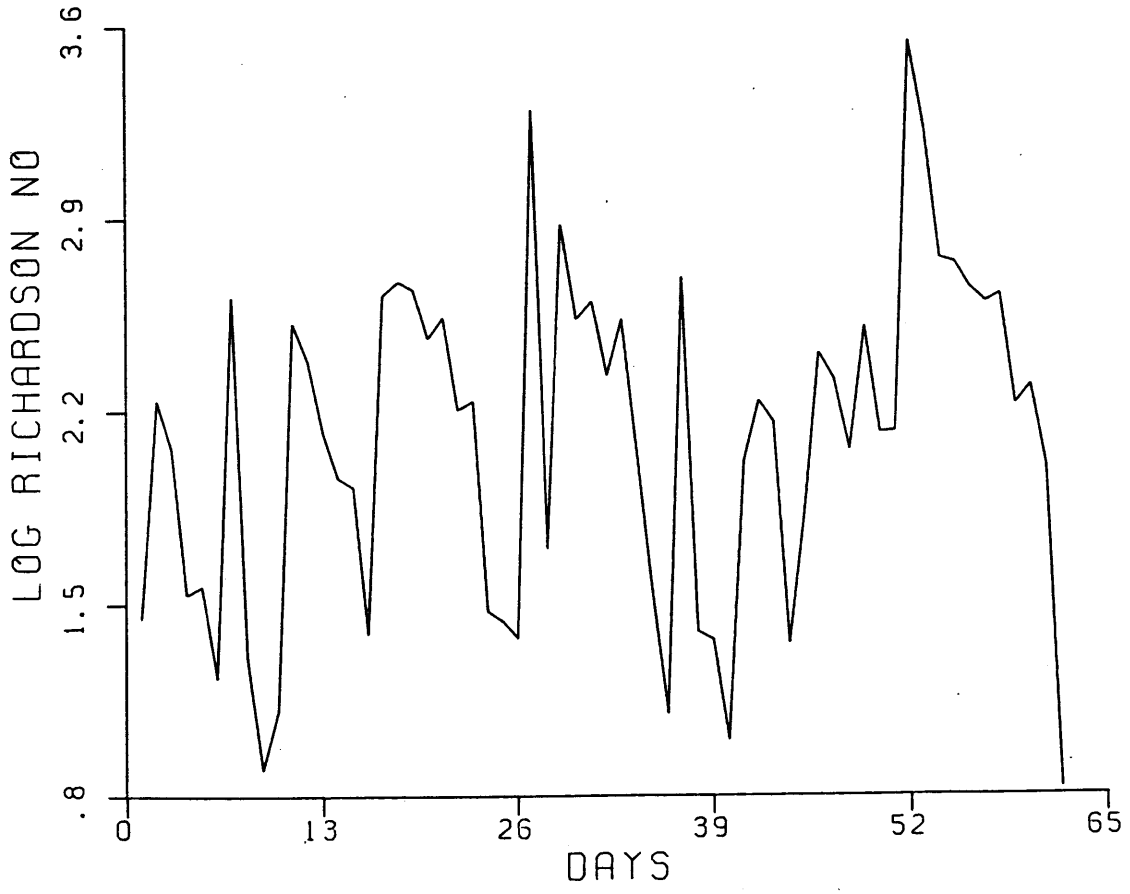

Fig. 9.6(g) Daily Variation of Richardson Number for the Period 3 October 1983 to 10 November 1983 with $C_w = 6$ and $C_c = .1$.

9.4.1 26 May - 6 October 1980

During this period the data (Fig 9.7 (a), shows slight warming, significant concentration and deepening of the upper mixed layer. Fig 9.7 (a) shows simulation results with $C_w = C_c = 0$. The results show reasonably good agreement with data indicating that convective overturns are a significant "mixing" mechanism during this period. The daily reduction in potential energy due to these overturns is shown in Fig 9.7 (b). As expected the magnitude of the convective activity increases as the summer progresses.

Fig 9.7 (c) shows the model results with $C_w = 6$ and $C_c = .1$. Comparison with the data is excellent. The daily input of mechanical energy due to wind and penetrative convective mixing is shown in Fig 9.7 (d). During the first three months of this period, penetrative convective mixing is very small compared with wind mixing. However, during the last two months, both the mixing mechanisms are important. Fig. 9.7 (e) compares the cumulative values of the mixing energies and shows that the input of energy due to wind mixing is much larger than penetrative convective mixing energy. Also, the ratio of $\bar{u}_{*,w}$ to $\bar{w}_*$ is about 0.7, which is lower than this ratio for the earlier part of the year and much larger for the latter part. Fig. 9.7 (f) shows the daily variation of the Richardson number that has a mean value of about 700 for this period.

The daily and the computed water balance for this period are shown in Table 9.7 (b) and Fig. 9.7 (g). Mean evaporation rate of about 6.5 mm/day is larger than the Jordan River inflows.

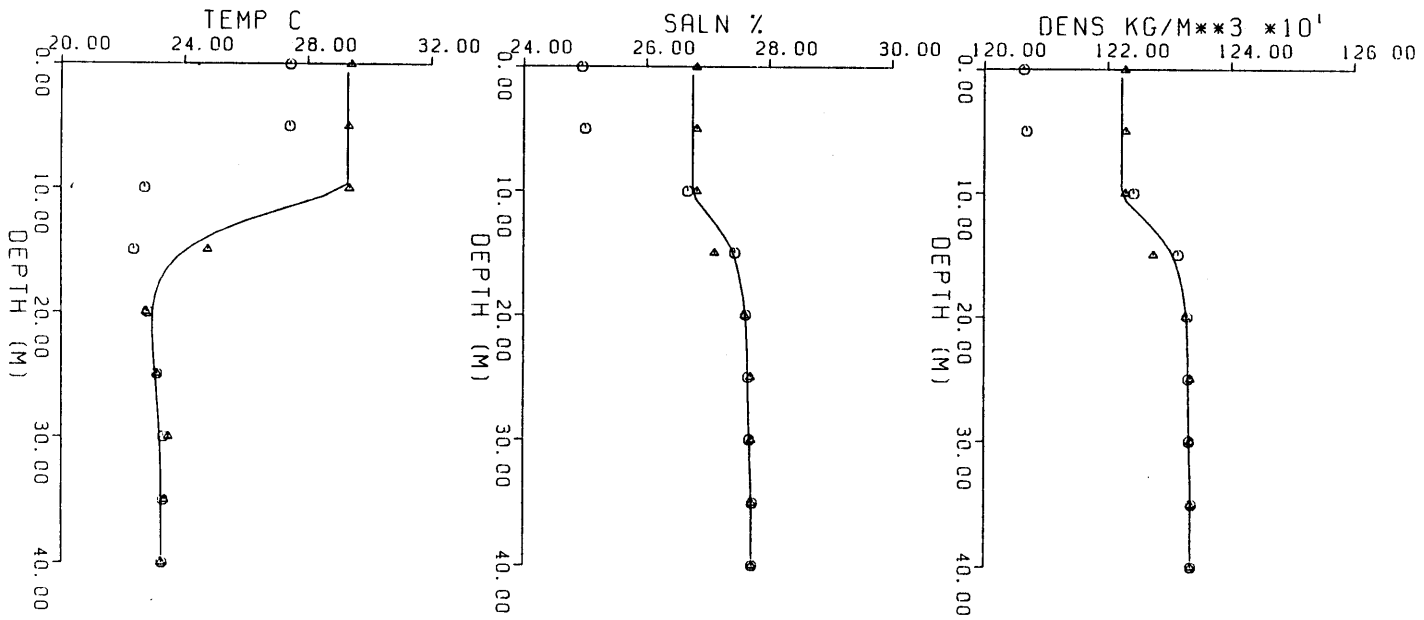

Fig. 9.7(a) Data and Model Results for the Period 26 May 1980 to 6 October 1980 with $C_w = 0$ and $C_c = .1$

o Initial Data
Δ Final Data
— Model Result

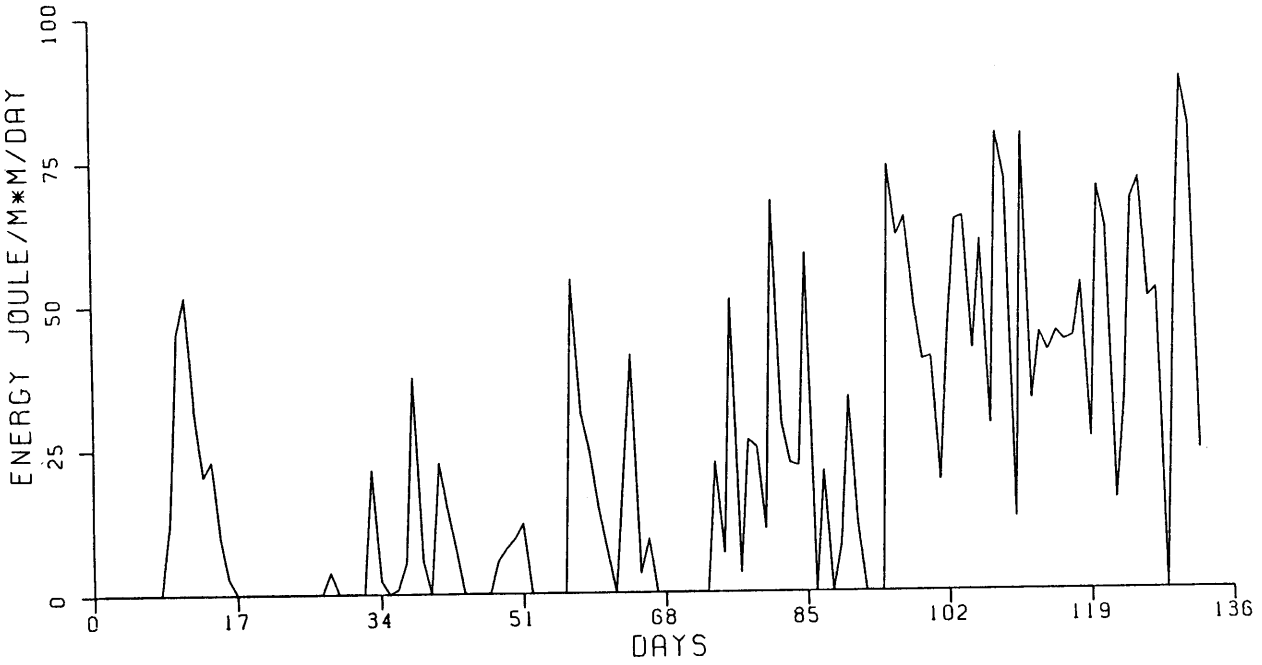

Fig. 9.7(b) Daily Reduction in Potential Energy due to Convective Overturns for the Period 26 May 1980 to 6 October 1980 with $C_w = 0$ and $C_c = .1$

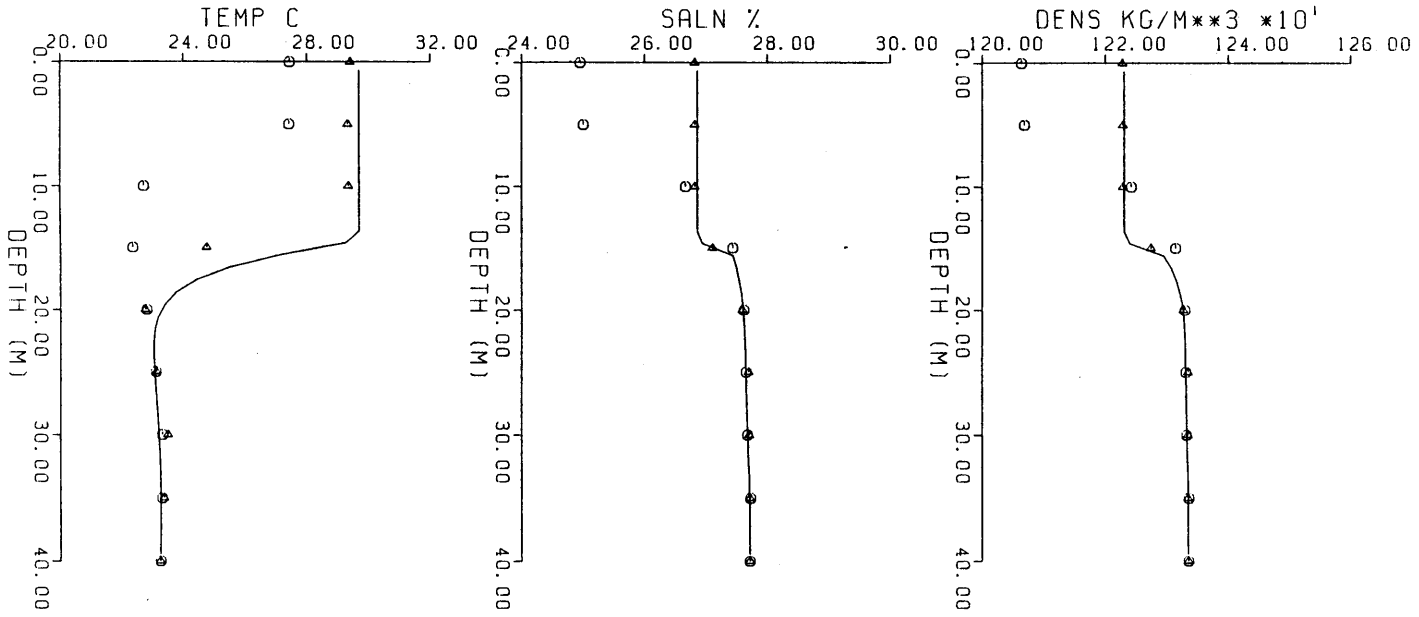

Fig. 9.7(c) Data and Model Results for the Period 26 May 1980 to 6 October 1980 with $C_w = 6$ and $C_c = .1$

o Initial Data
Δ Final Data
— Model Result

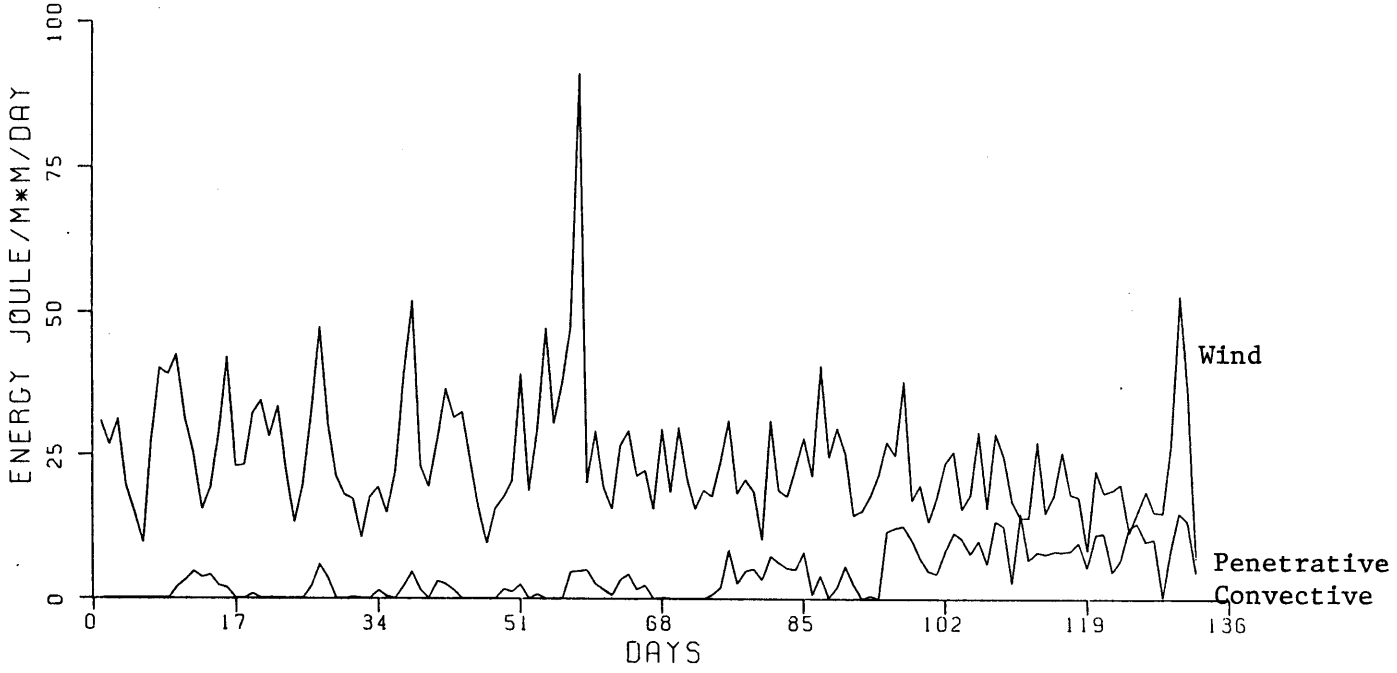

Fig. 9.7(d) Daily Input of Wind and Penetrative Convective Mixing Energy for the Period 26 May 1980 to 6 October 1980 with C_w = 6 and C_c = .1

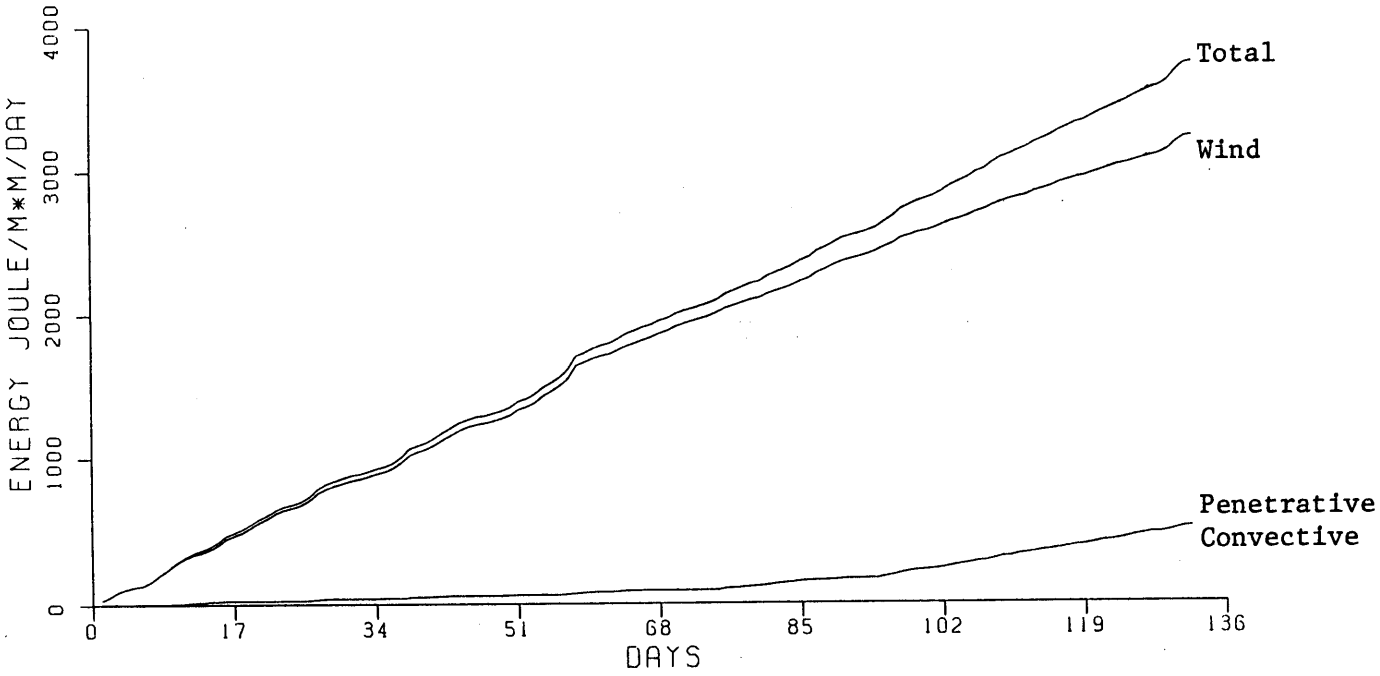

Fig. 9.7(e) Cumulative Wind and Penetrative Convective Mixing energy for the Period 26 May 1980 to 6 October 1980 with $C_w = 6$ and $C_c = .1$

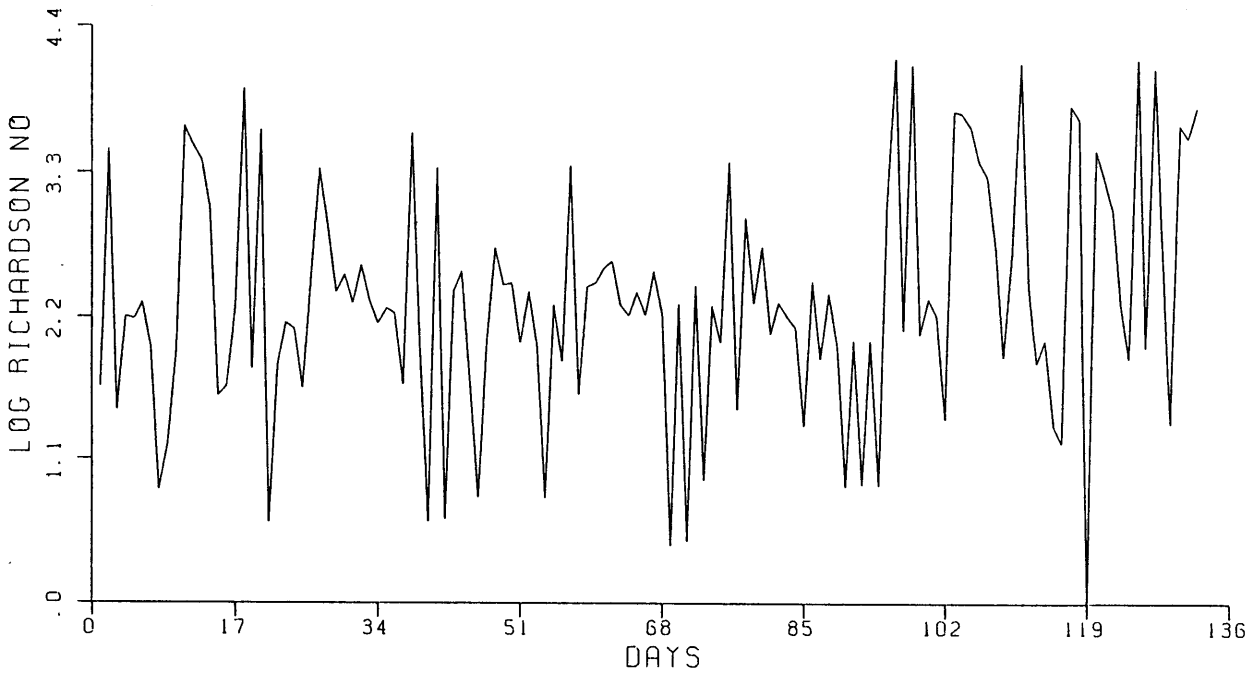

Fig. 9.7(f) Daily variation of Richardson Numbers for the Period 26 May 1980 to 6 OCtober 1980 with C_w = 6 and C_c = .1

Table 9.7 (a)

Details of model run for the period 26 May 1980 - 6 October 1980

Calibration Coefficients		
C_w	0	6
C_c	0	0.1
Error Analysis Maximum Values		
Temperature °C	.6	4.5
Salinity %	.3	0.2
Density kg/m^2	2.6	3.5
Root Mean Square Values		
Temperature °C	.2	1.2
Salinity %	.1	0.2
Density kg/m^3	.9	3.5
Mixing Parameters		
KE_w (J/m^2)	0	3260
KE_c (J/m^2)	0	520
$\bar{u}_*$	.00332	.00332
$\bar{w}_*$	.00410	.00462
$\bar{R}_{i\sigma}$	1020	1400
Change in Stability Index	-17540	-17540
Error in Stability	-289	-108

Change → Final - initial

Error → Data - model

Table 9.7 (b)

Details of Model run for the period 26 May 1980 - 6 October 1980

Calibration Coefficients		
C_w	0	6
C_c	0	0.1
Water Balance		
Evaporation (mm)	875	849
Pumpage (mm)	86	86
Inflow (mm)	224	248
Net Inflow (mm)	-687	-687
Thermal Energy Balance		
Short Wave Radiation ($KCal/m^2/day$)	6240	6240
Atmospheric radiation (")	8160	8160
Back radiation (")	9950	9920
Evaporative Flux (")	3810	3700
Net Warming (")	176	340
Meteorology		
Air Temperature (°C)	30.80	
Humidity (%)	45	
Wind Speed (m/s)	3.22	

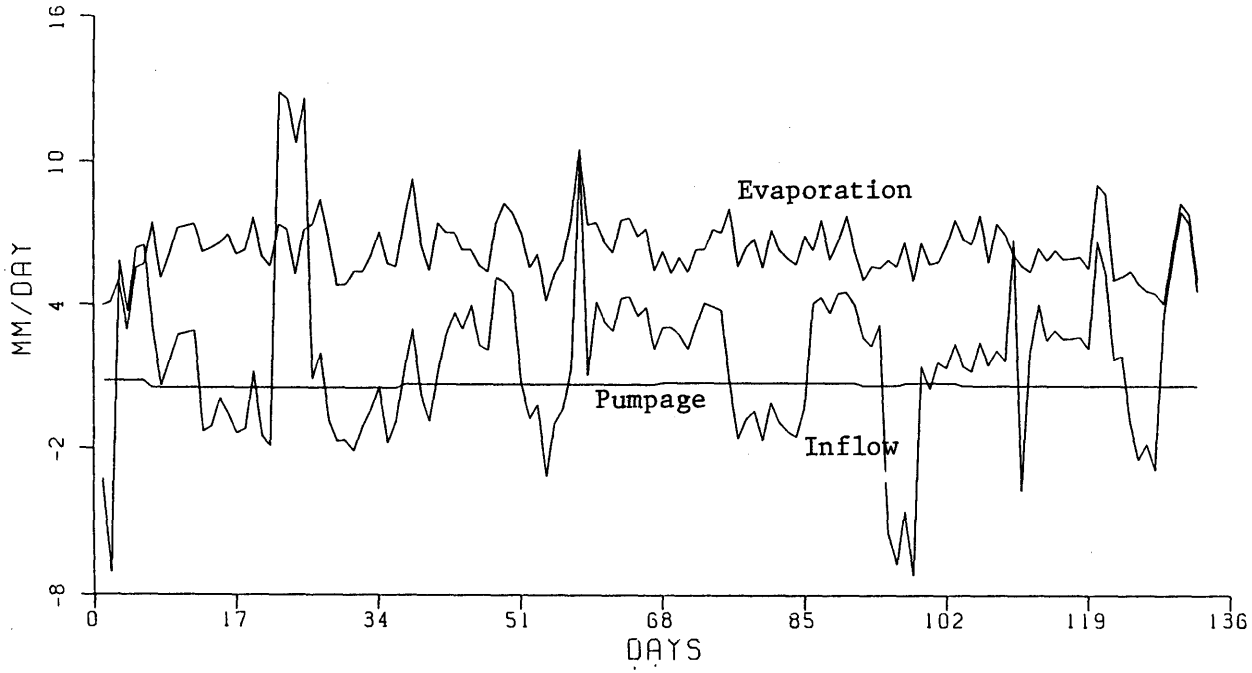

Fig. 9.7(g) Daily Water Balance for the Period 26 May to 6 October 1980 with C_w = 6 and C_c = .1

9.4.2 20 July - 21 September, 1981

During this period of sixty three days, the data Fig 9.8 (a), shows cooling and a slight concentration of the surface layer. No appreciable deepening of the mixed layer can be observed possibly due to lack of sufficient spatial resolution in the data. Results for two simulations are presented in this section.

Fig 9.8 (a) shows the results with $C_w = C_c = 0.0$. Convective overturns maintain the depth of the upper mixed layer. Fig. 9.8 (b) shows the reduction in the potential energy due convective overturns. Note that the convective activity increases with the passage of summer. This was also observed in the data analyzed in Section 9.4.1.

Fig 9.8 (c) shows the results for the case with $C_w = 6$ and $C_c = .1$. Agreement between the data and model result is good. Fig 9.8 (d) shows the daily water balance. Mean evaporation rate of 5.2 mm/day is larger than the Jordan River inflows resulting in a net concentration of the Dead Sea. Additional details of thermal energy balance and the water budget are shown in Table 9.8 (a) and Table 9.8 (b).

Fig. 9.8 (e) shows the daily input of wind and penetrative convective mixing energies. During most of this period, windmixing is larger than penetrative convective mixing. Also, the ratio of $\bar{u}_{*,w}$ to $\bar{w}_*$ of 0.6 which is comparable to a value of 0.7 for the previous year. Details of thermal energy balance and the water budget are shown in Table 9.8 (a) and Table 9.8 (b).

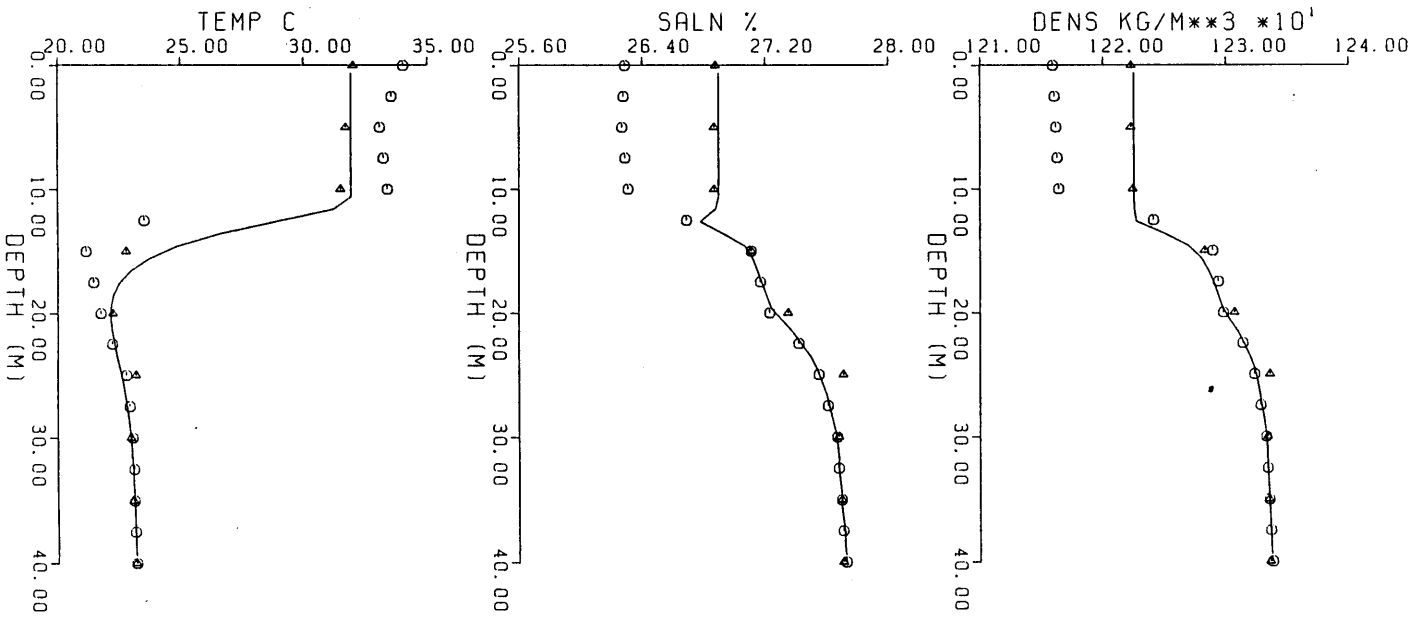

Fig. 9.8(a) Data and Model Results for the Period 20 July 1981 to 21 September 1981 with $C_w = 6$ and $C_c = 0.0$

o Initial Data
Δ Final Data
— Model Result

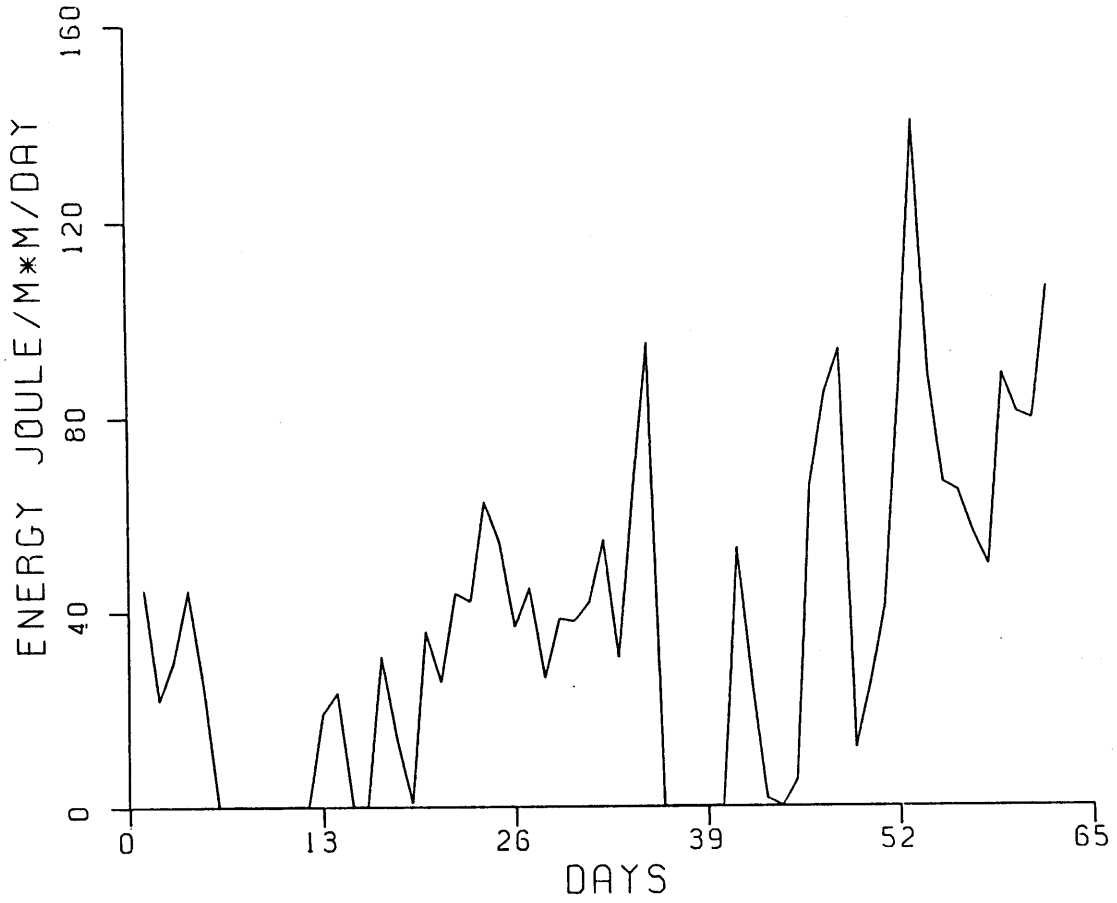

Fig. 9.8(b) Daily Reduction in Potential Energy due to Convective Overturns for the Period 20 July to 21 September 1981 with C_w = 0 and C_c = 0.0

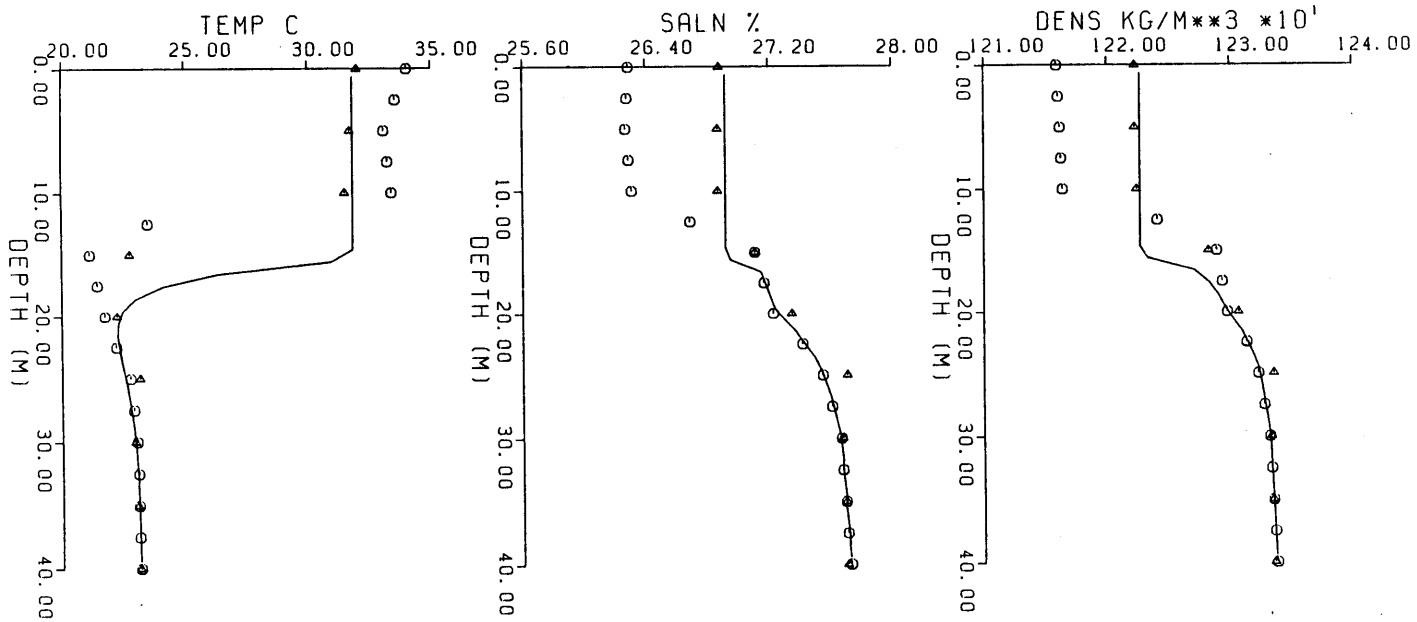

Fig. 9.8(c) Data and Model Results for the Period 20 July 1981 to 21 September 1981 with $C_w = 6$ and $C_c = .1$

o Initial Data
Δ Final Data
— Model Result

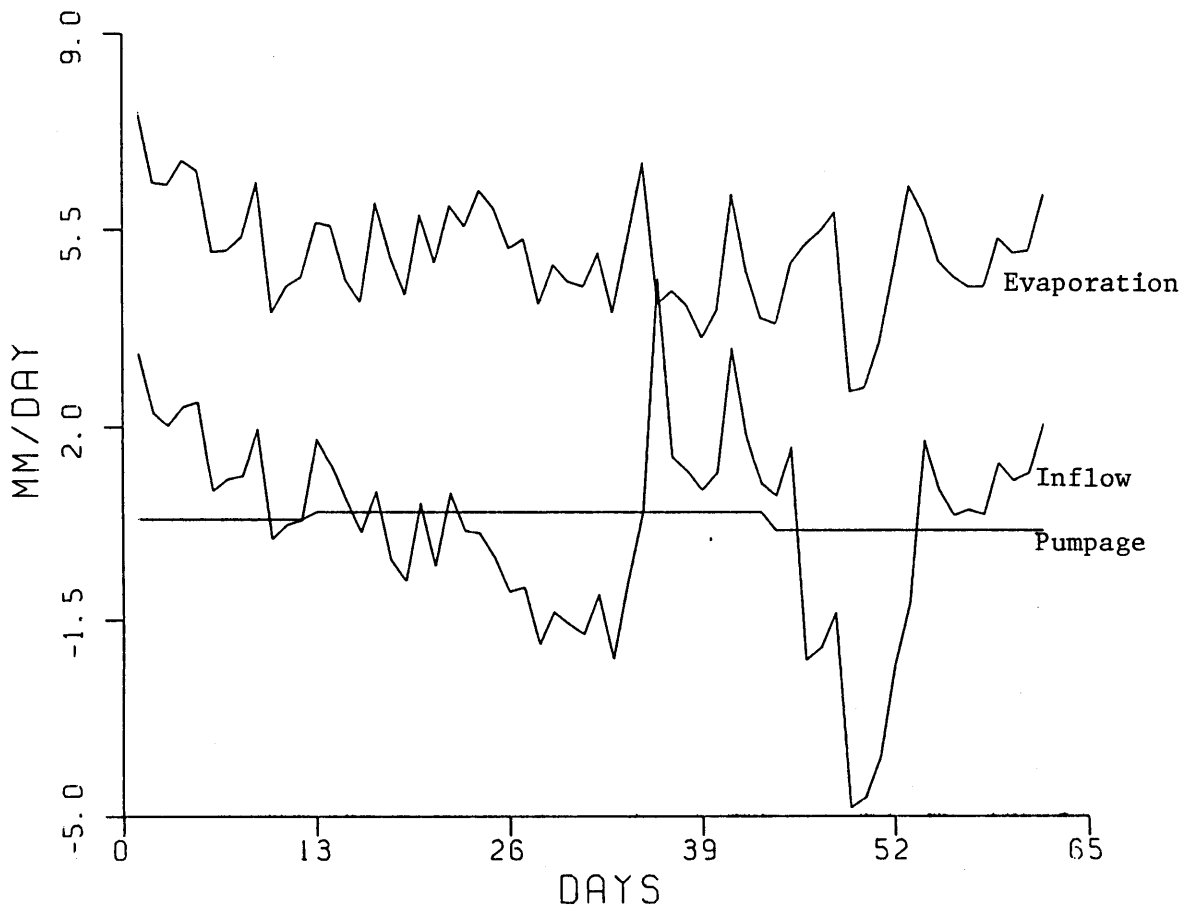

Fig. 9.8(d) Daily Water Balance for the Period 20 July 1981 to 21 September 1981 with $C_w = 6$ and $C_c = .1$

Table 9.8 (a)

Details of model run for the period 20 July - 21 September 1981

Calibration Coefficients		
C_w	0	6
C_c	0	0.1
Error Analysis Maximum Values		
Temperature °C	3.2	9.1
Salinity %	0.2	0.2
Density kg/m^2	3.2	5.6
Root Mean Square Values		
Temperature °C	0.9	2.6
Salinity %	0.1	0.1
Density kg/m^3	0.9	1.7
Mixing Parameters		
KE_w (J/m^2)	0	1700
KE_c (J/m^2)	0	300
$\bar{u}_*$	.00346	.00346
$\bar{w}_*$	.00577	.00563
$\bar{R}_{i\sigma}$	456	300
Change in Stability Index	-8821	-8821
Error in Stability	-14	-200

Change → Final - initial

Error → Data - model

Table 9.8 (b)

Water and Heat Balance for the Period 20 July - 21 September 1981

Calibration Coefficients		
C_w	0	6
C_c	0	.1
Water Balance		
Evaporation (mm)	346	320
Pumpage (mm)	21	21
Inflow (mm)	42	16
Net Inflow (mm)	-325	-325
Thermal Energy Balance		
Short Wave Radiation ($KCal/m^2/day$)	5320	5320
Atmospheric radiation (")	8310	8310
Back radiation (")	10040	9990
Evaporative Flux (")	3160	2920
Net Warming (")	-2	362
Meteorology		
Air Temperature (°C)	31.84	
Humidity (%)	52	
Wind Speed (m/s)	3.33	

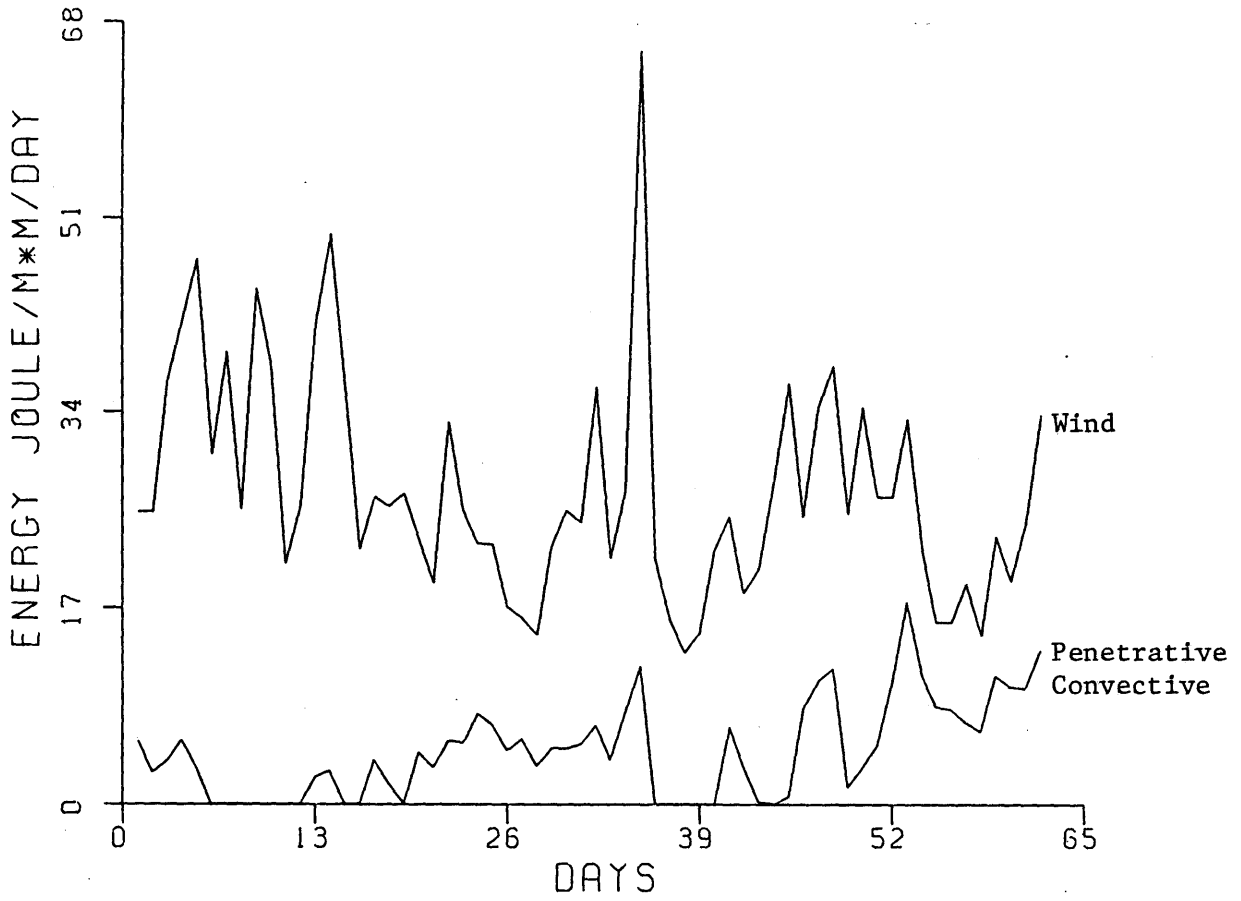

Fig. 9.8(e) Daily Input of Wind and Penetrative Convective Mixing Energy for the Period 20 July 1981 to 21 September 1981 with $C_w = 6$ and $C_c = 0.1$

9.6 Results of Continuous Simulation December 1979 to October 1981

9.6.1 Input Data

The results discussed in the previous sections are based on simulations extending over a period of one to three months. The input data for each of these short simulations was sequenced together to yield consolidated input data. This includes meteorological data, atmospheric long wave and short wave solar radiation as well as Jordan River inflows and pumpage by the salt works. Using this input sequence, a continuous simulation was performed with $C_w = 6$ and $C_c = 0.1$. A comparison of these results with the data gives an estimate of the accumulation of errors for long term simulations performed in a predictive mode (see Chapter 10) as well as information on the annual variability of important components of mass, salt, thermal energy and the mechanical energy budget.

Fig 9.9 (a) shows the meteorological input variables for the period 12 December 1979 to 21 September 1981. The annual variation in air temperature, humidity and wind speeds for the two years is very similar. Highest windspeeds as well as maximum variation in wind speeds occurs during the period December to March.

Fig 9.9 (b) shows the daily values of the Jordan River inflow for the two years. Note that this sequence was obtained by consolidating the inflows computed for a series of short simulations similar to those discussed in Section 9.2 to 9.5. The cumulative inflows for the periods 12 December 1979 to 6 October 1980 and 6 October 1980 to 21 September 1981 are 1.85 m and 1.54 m respectively. As mentioned before, maximum inflows occur during the winter months. Fig 9.9 (c) shows the daily pumpage (constant in each month) by the salt works. Recall that these values are obtained so as

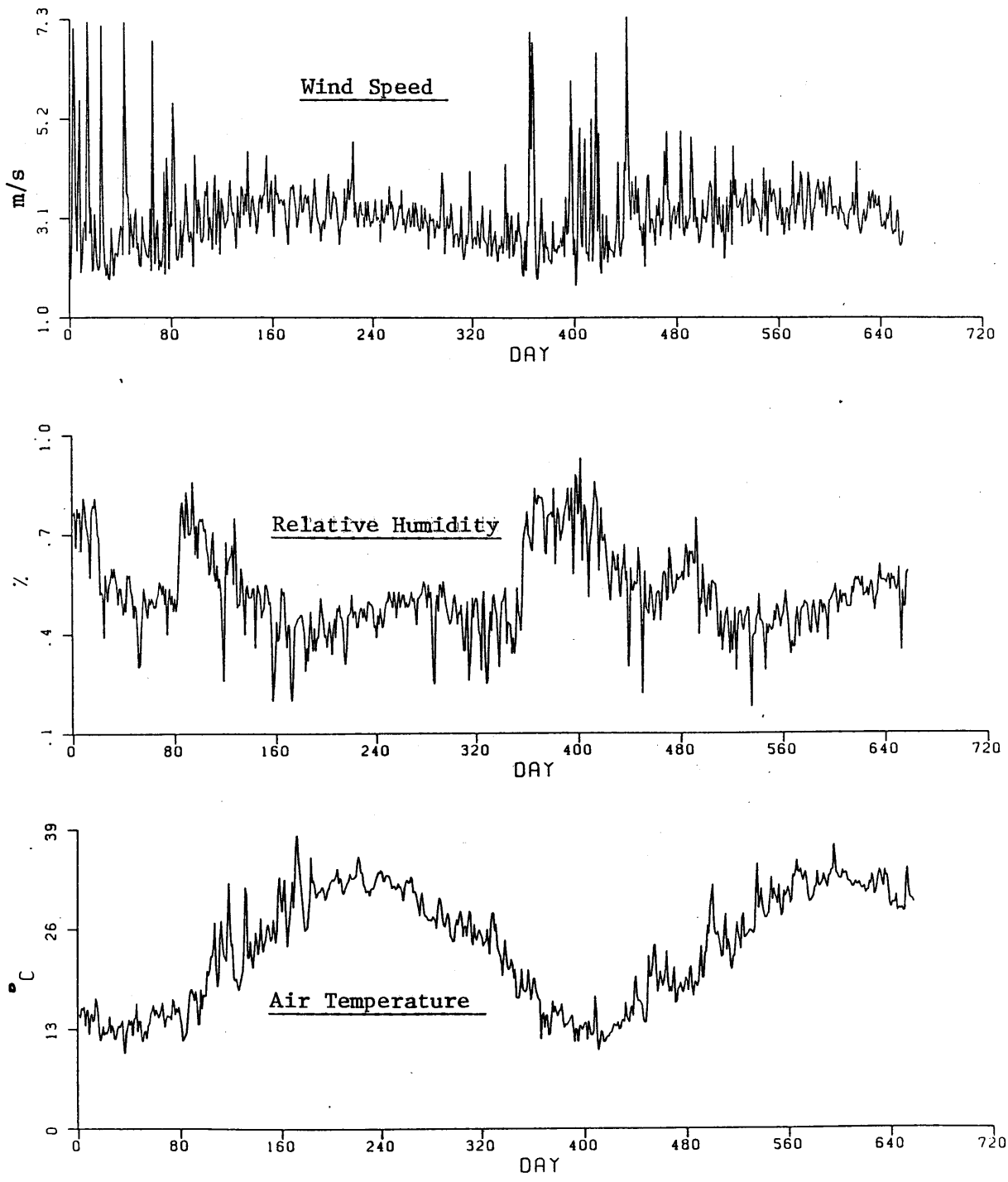

Fig. 9.9(a) Meteorological Variables for the Period 12 December 1979 to 21 September 1981

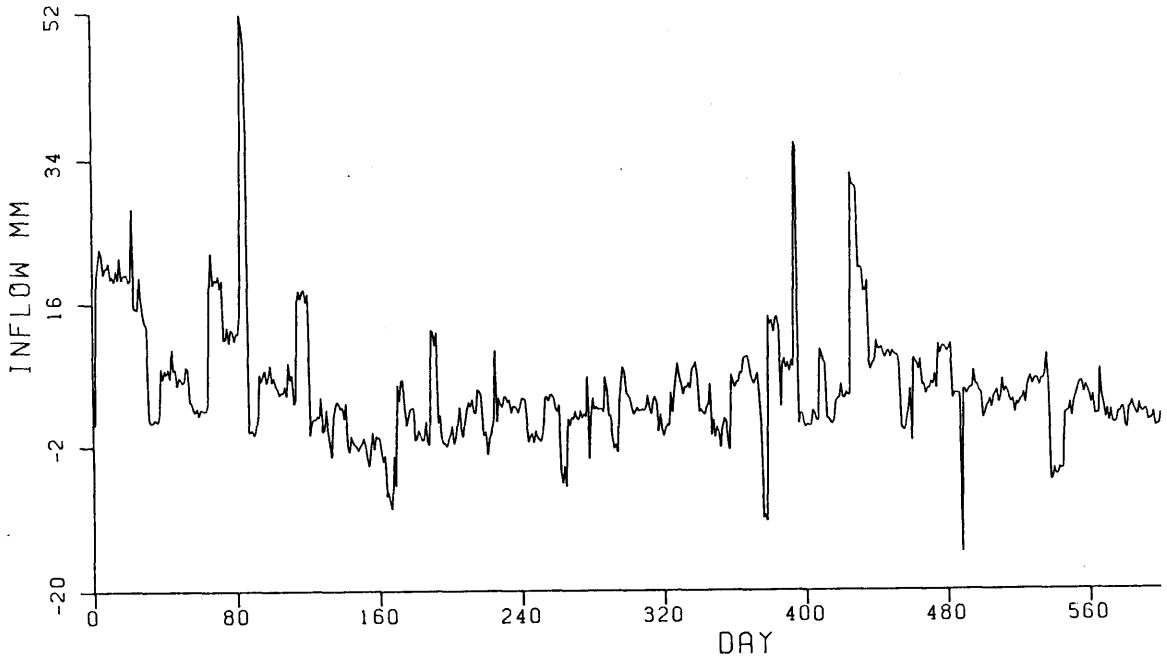

Fig. 9.9(b) Daily Values of Jordan River Inflows for the Period 12 December 1979 to 21 September 1981

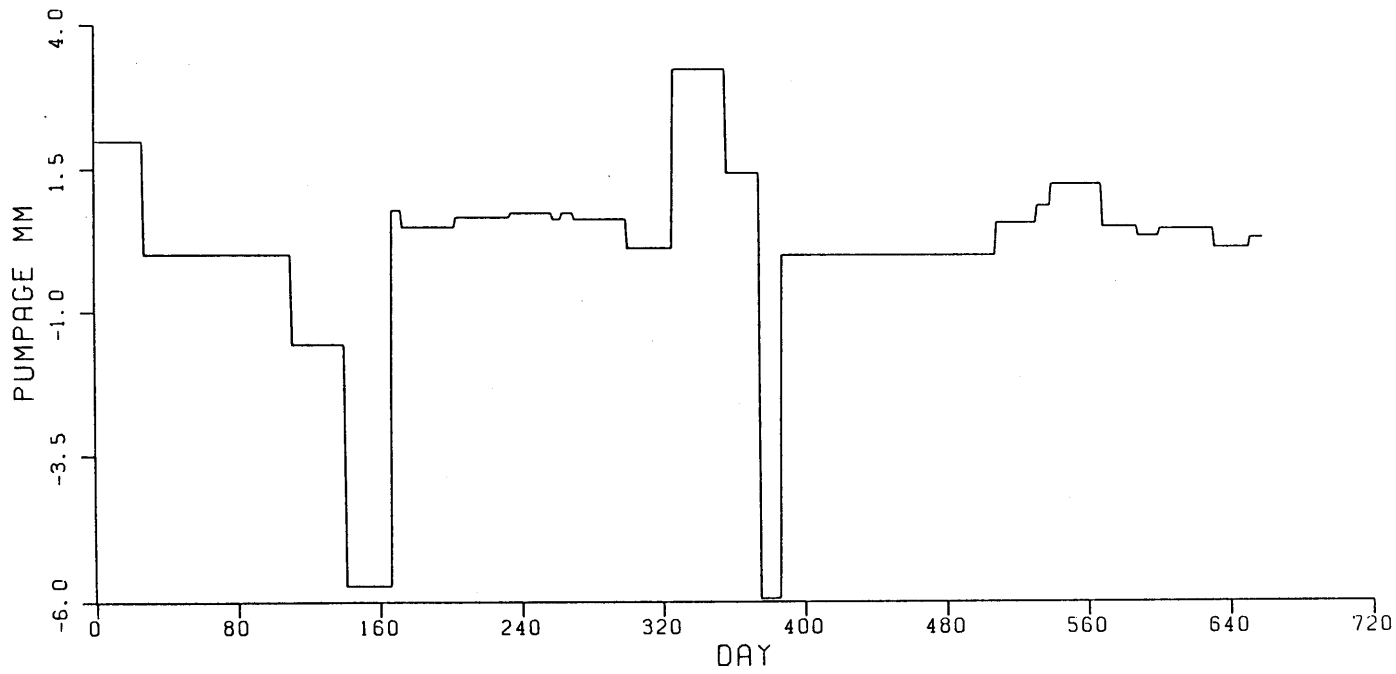

Fig. 9.9(c) Daily Values of Pumpage by the Salt Works for the Period 12 December 1979 to 21 September 1981

to effect good salt balance between the measured profiles. There is no pumpage during the winter, high fresh water inflow periods during which the Dead Sea surface salinities are lowest. Also, maximum Dead Sea brine is pumped during late summer. Cumulative pumpage for the entire period is about 28 cms approximately equally divided amongst the two water years.

9.6.2 Model Results

Fig 9.9 (d) to Fig 9.9 (g) compare the model results with measured profiles for a few days. Starting with an initial profile on 12 December 1979, the model results indicate excellent agreement with measured temperature and salinity profiles measured on 6 October 1980, i.e., 299 days after the start of simulation. These results are shown in Fig. 9.9 (d). Also, referring to Fig. 9.9 (e) to Fig. 9.9 (g) the results compare well (both in terms of surface temperature and salinity as well as the mixed layer depth) with profiles measured on 24 May 1981, and 20 July 1981 and the end of the period profile (21 September 1981).

Fig. 9.9(h) and Fig. 9.9 (i) show the temporal variation in surface temperature and salinity as predicted by the model. Also indicated on these figures are the surface temperature and surface salinities for the days on which profiles were measured. The data compare well with the model results. Fig. 9.9 (j) shows the variation of mixed layer depth for this period. The mixed layer depth is minimum during the fresh water inflow period (winter months) and is maximum in late summer. Note that since the data was measured at 5 m intervals, the mixed layer depth cannot be precisely estimated from the data.

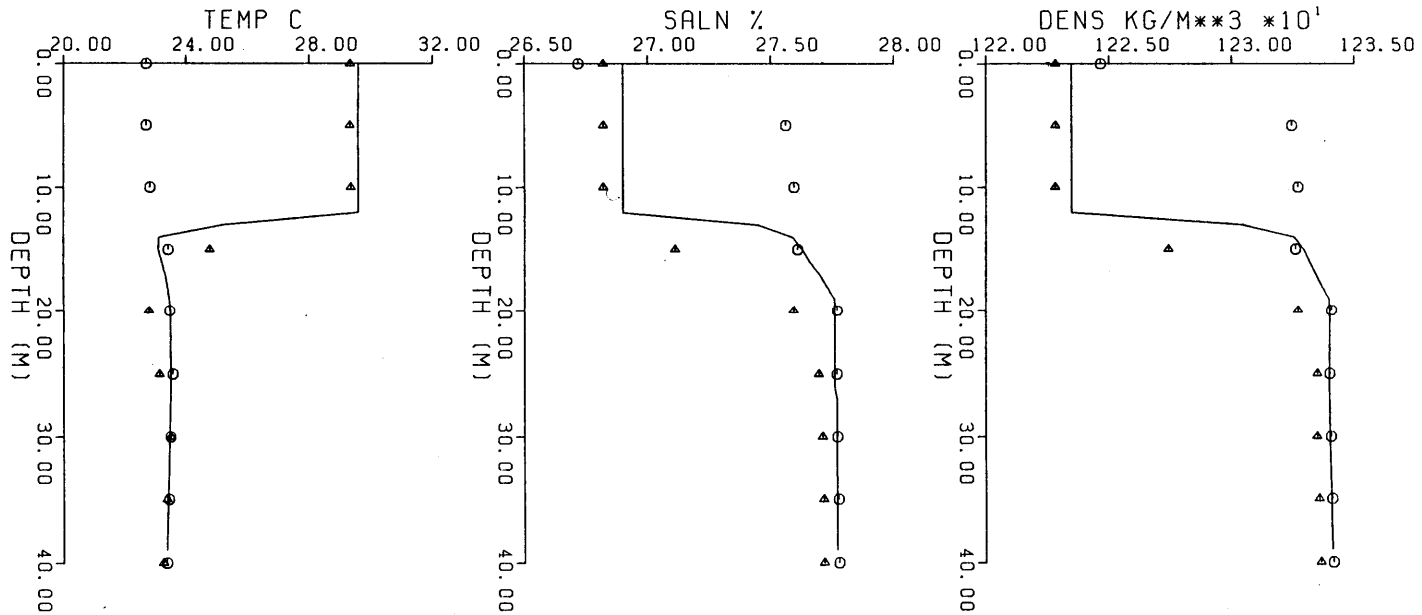

Fig. 9.9(d) Comparison of Data and Model Results for 6 October 1980 with C_c = 6 and C_c = .1 and Initial Conditions of 12 December 1979.

o Initial Data
Δ Final Data
— Model Result

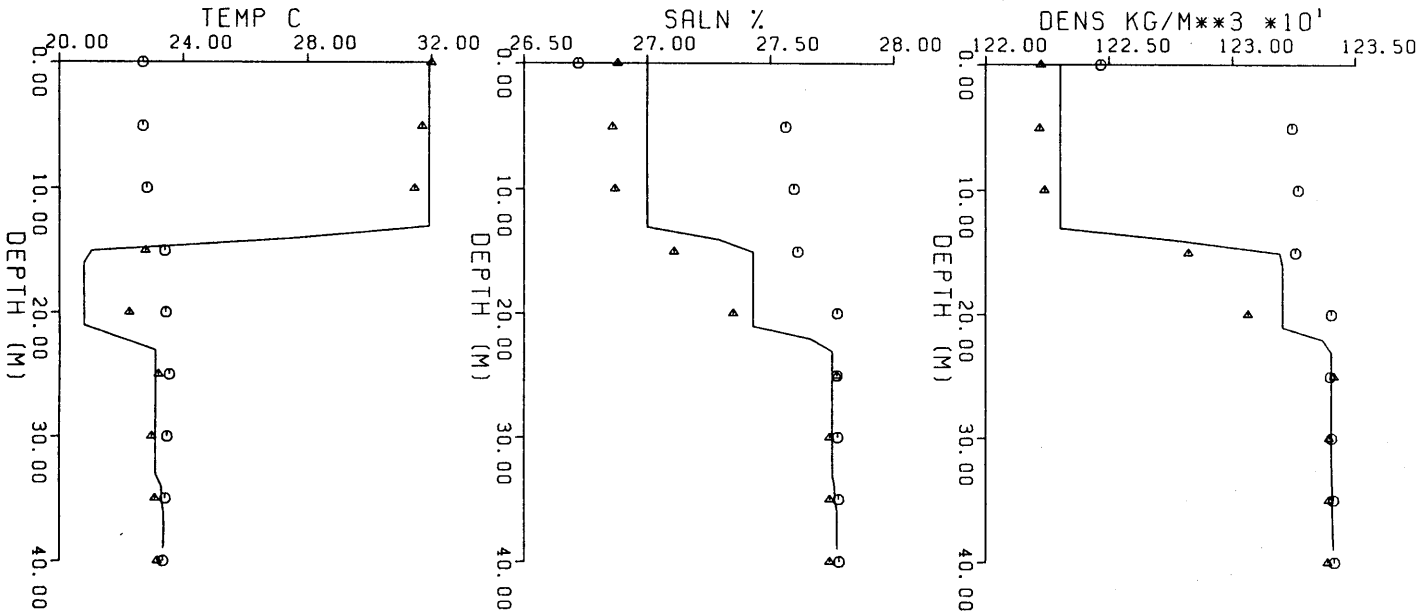

Fig. 9.9(e) Comparison of Data and Model Results for 24 May 1981 with C_c = 6 and C_c = .1 and Initial Conditions of 12 December 1979.

o Initial Data
Δ Final Data
— Model Result

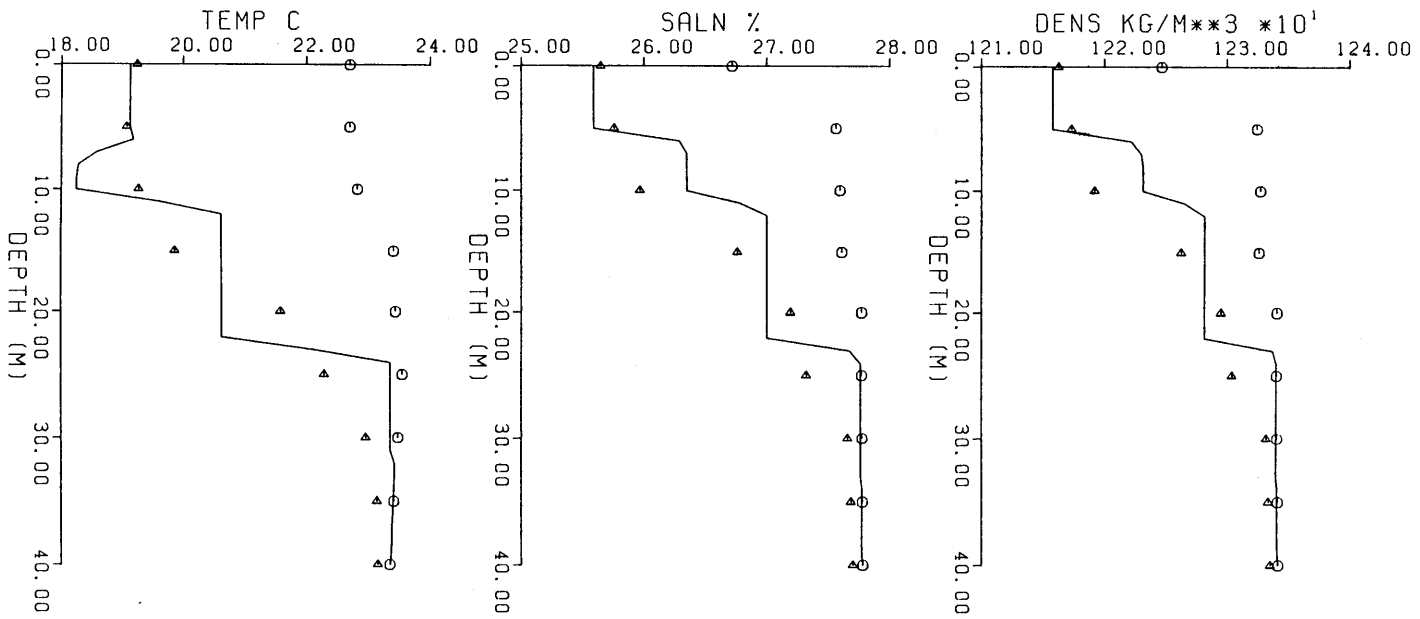

Fig. 9.9(f) Comparison of Data and Model Results for 20 July 1981 with C_w = 6 and C_c = .1 and Initial Conditions of 12 December 1979.

o Initial Data
Δ Final Data
— Model Result

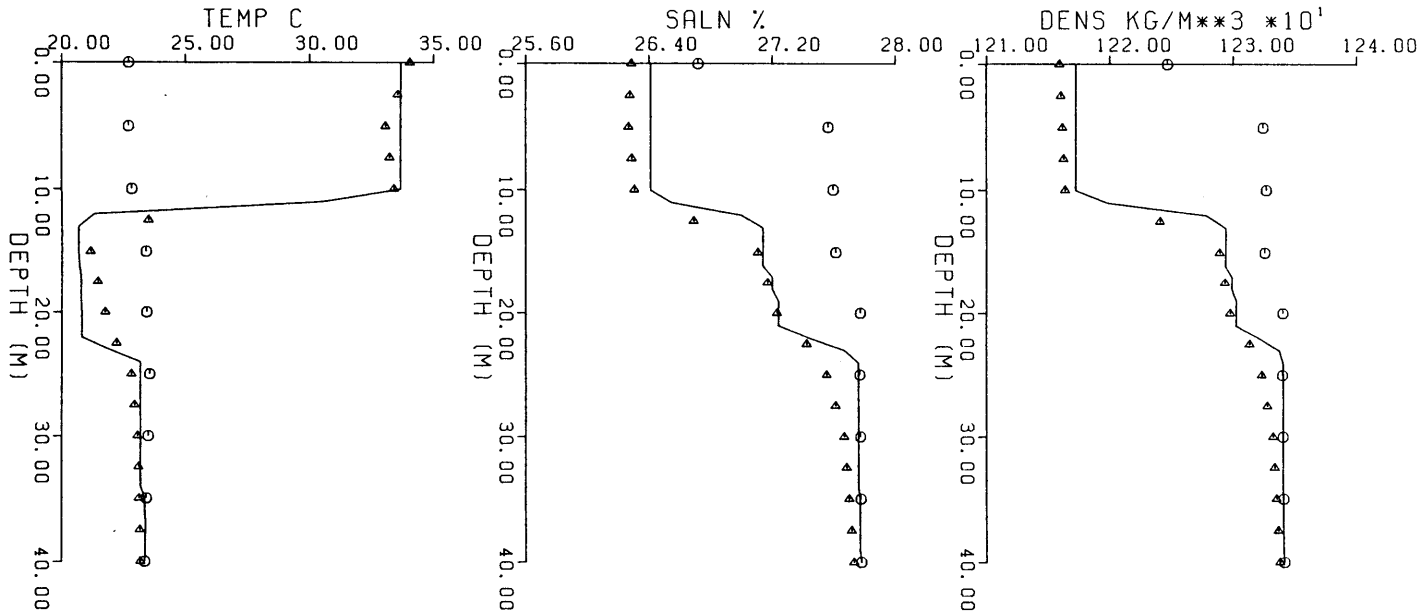

Fig. 9.9(g) Comparison of Data and Model Results for 21 September 1981 with C_w = 6 and C_c = .1 and Initial Conditions of 12 December 1979.

o Initial Data
Δ Final Data
— Model Result

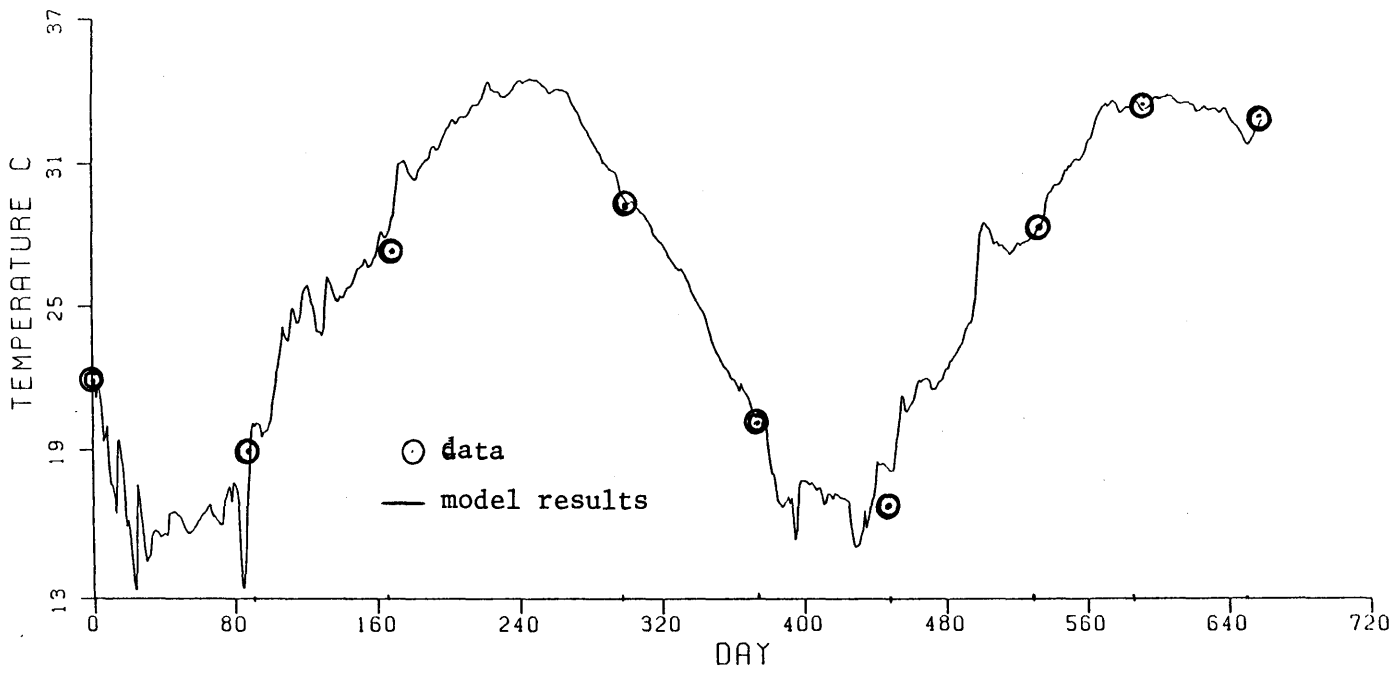

Fig. 9.9(h) Daily Variation of Surface Temperature (Data and Model Results) for the Period 12 December 1979 to 21 September 1981 with $C_w = 6$ and $C_c = .1$

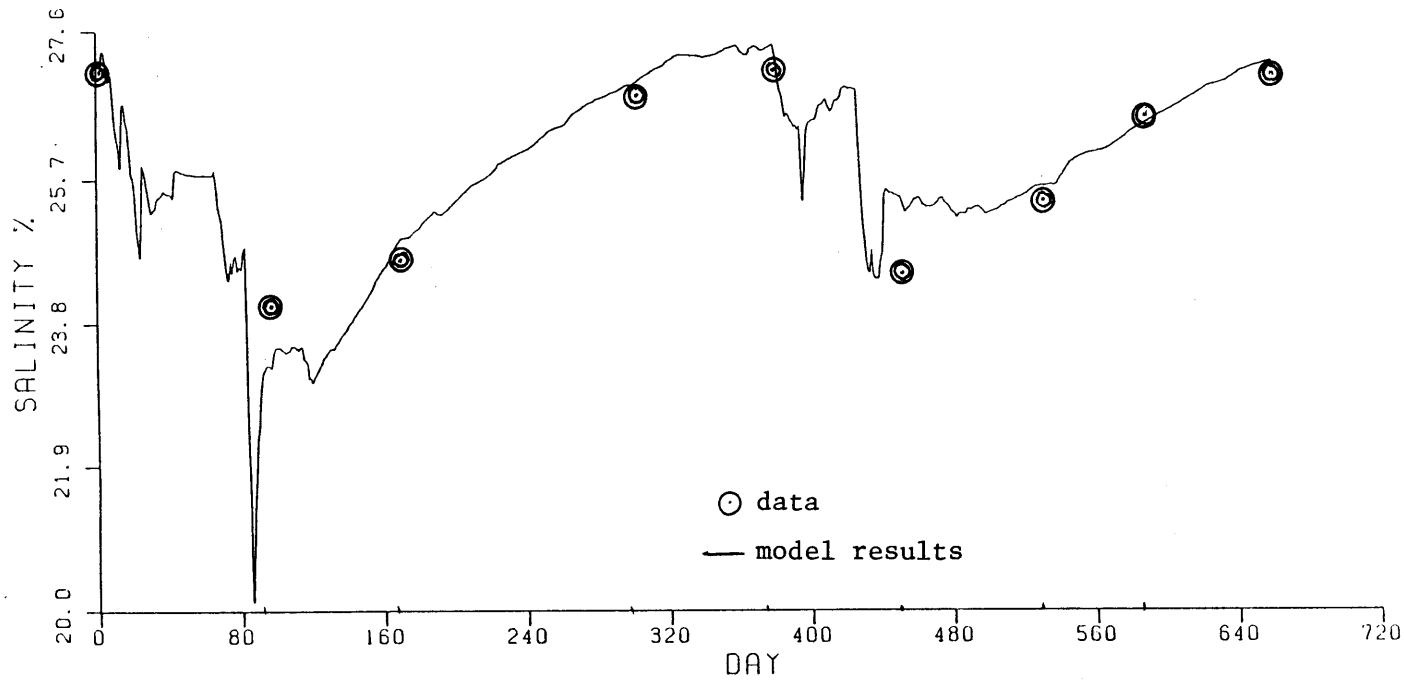

Fig. 9.9(i) Daily Variation of Surface Salinity (Data and Model Results) for the Period 12 December 1979 to 21 September 1981 with $C_w = 6$ and $C_c = .1$

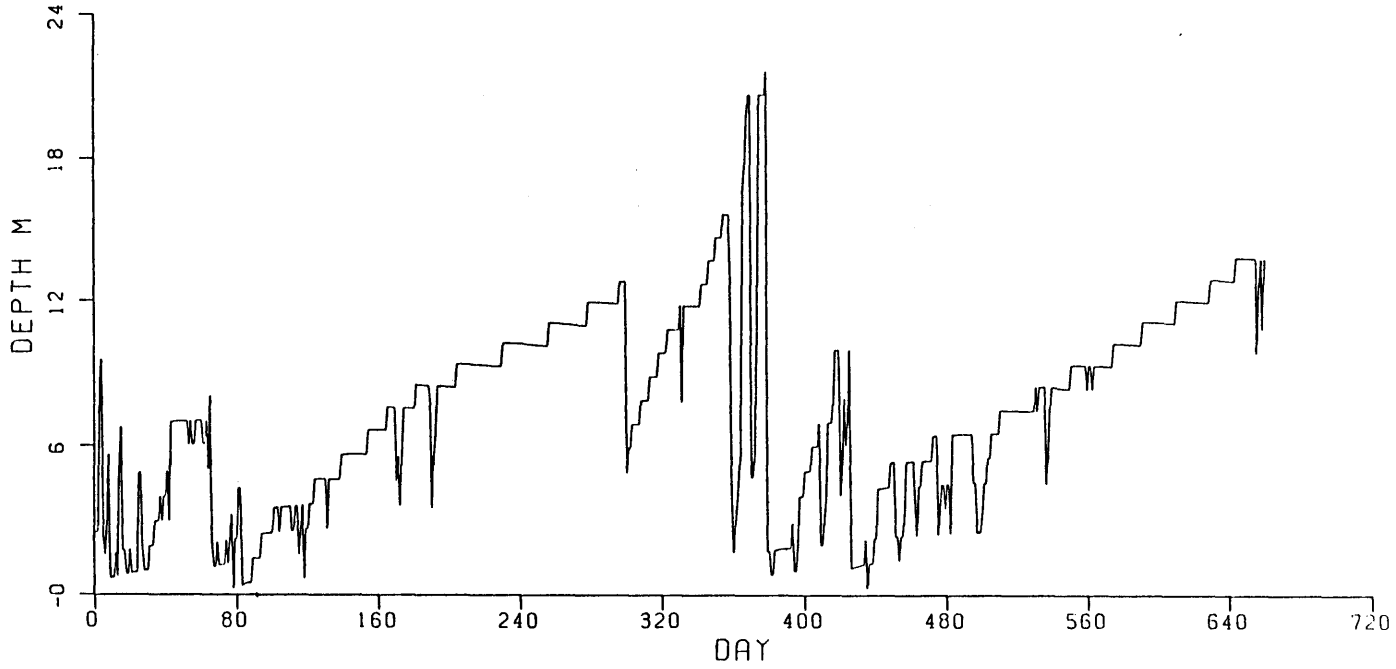

Fig. 9.9(j) Daily Variation of Mixed Layer Depth for the Period 12 December 1979 to 21 September 1981 with $C_w = 6$ and $C_c = .1$

Fig. 9.9 (k) shows the seasonal variations in the daily evaporation rate for this period. Cumulative evaporation for the periods 12 December 1979 to 6 October 1980 and 6 October 1980 to 21 September 1981 are 1.32 m and 1.44 m, respectively.

Fig. 9.9 (l) and Fig. 9.9 (m) show the daily and cumulative values of wind mixing energy for this period. Wind mixing ocurs throughout the year with maximum mixing energy occuring during the winter periods when the wind speeds are the highest. Fig. 9.9 (n) and Fig. 9.9 (o) show the daily and cumulative input value of penetrative convective mixing energy. Maximum convective activity occurs during late summer during September and October. Further, on an annual scale, energy due to penetrative convection is much smaller than wind energy, as shown in Table 9.9. Fig. 9.9 (p) shows the daily plot of Richardson number that has an overall mean value of about 1000.

Finally, Fig. 9.9 (q) shows the overall energy balance for the lake for the two periods. Since the water temperature is higher than the air temperature, (and the emissivity of water and air are about the same) back radiation is larger than atmospheric radiation.

9.7 Conclusions

A number of conclusions can be drawn from the discussions in this chapter. These are listed below.

1. The model has been adequately calibrated and verified. Estimated range for the parameters C_w is from 3 to 6 and for C_c from 0 to .25 with best estimates of $C_w = 6$ and $C_c = 0.1$. However, spatial and

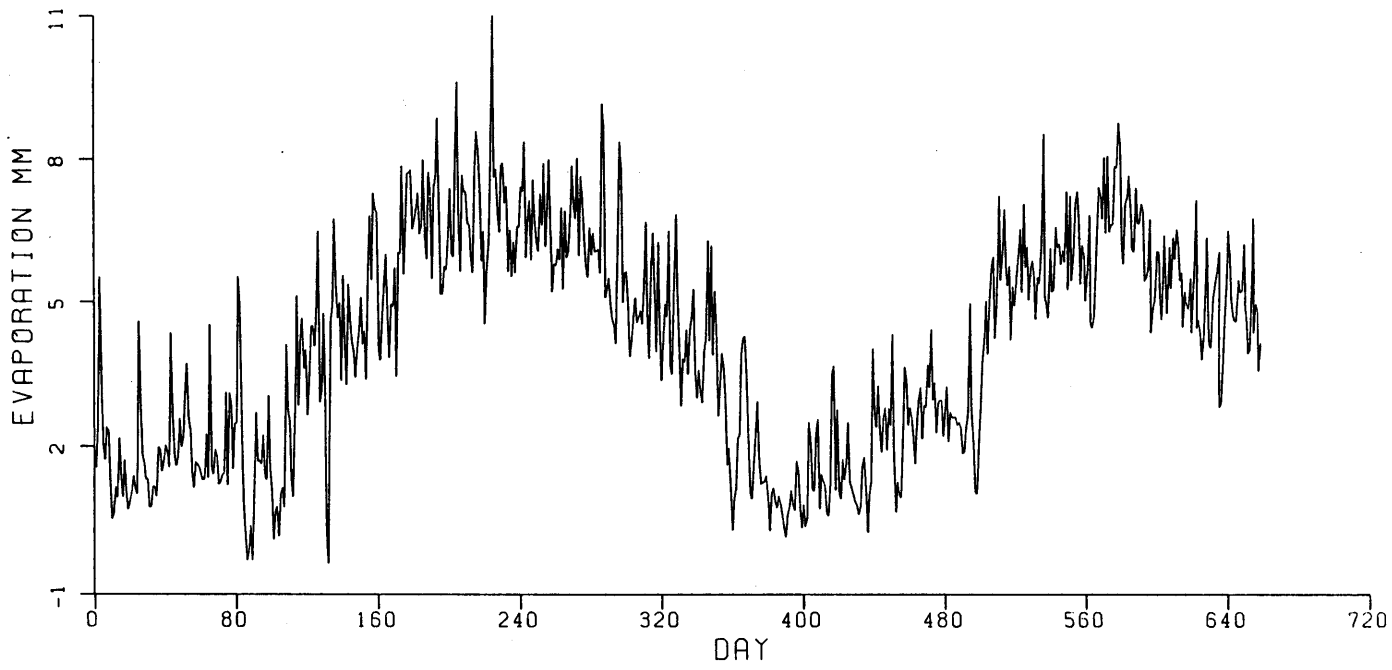

Fig. 9.9(k) Daily Variation of Evaporation for the Period 12 December 1979 to 21 September 1981 with C_w = 6 and C_c = .1.

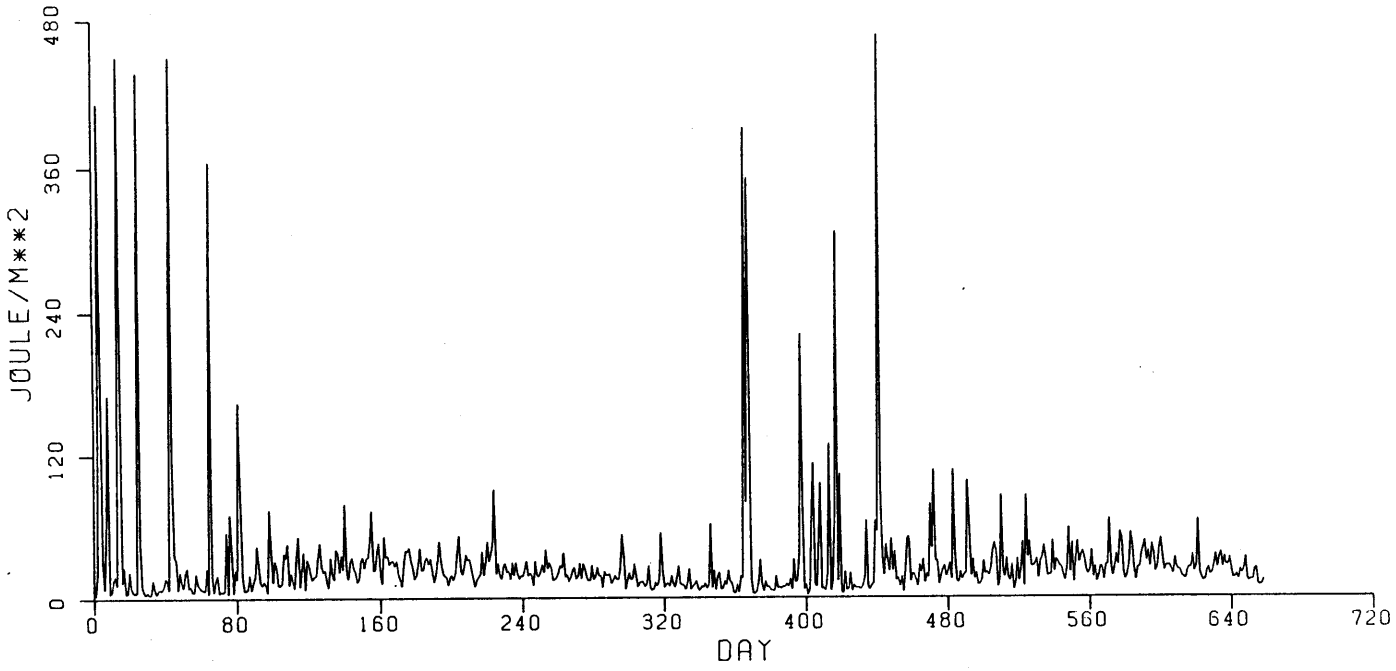

Fig. 9.9(1) Daily Input of Wind Mixing Energy for the Period 12 December 1979 to 21 September 1981 with $C_w = 6$ and $C_c = .1$

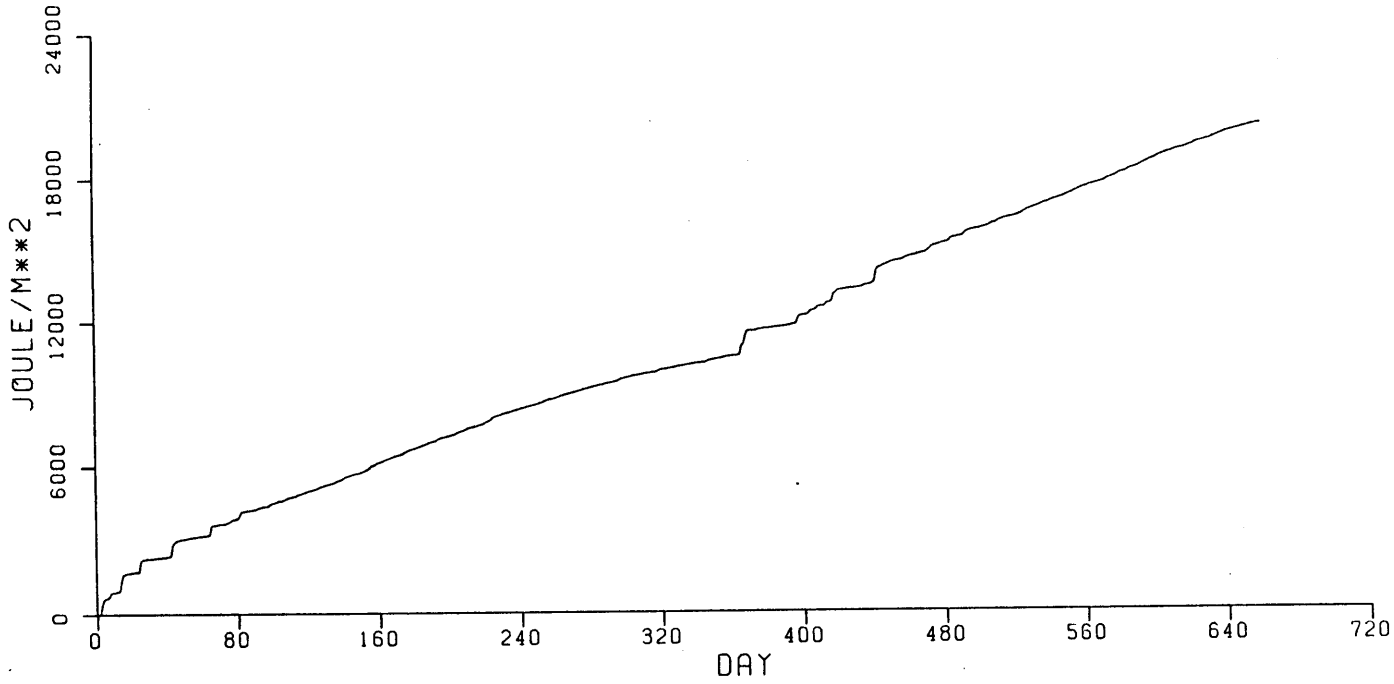

Fig. 9.9(m) Cummulative Input of Wind MIxing Energy for the Period 12 December 1979 to 21 September 1981 with $C_w = 6$ and $C_c = .1$

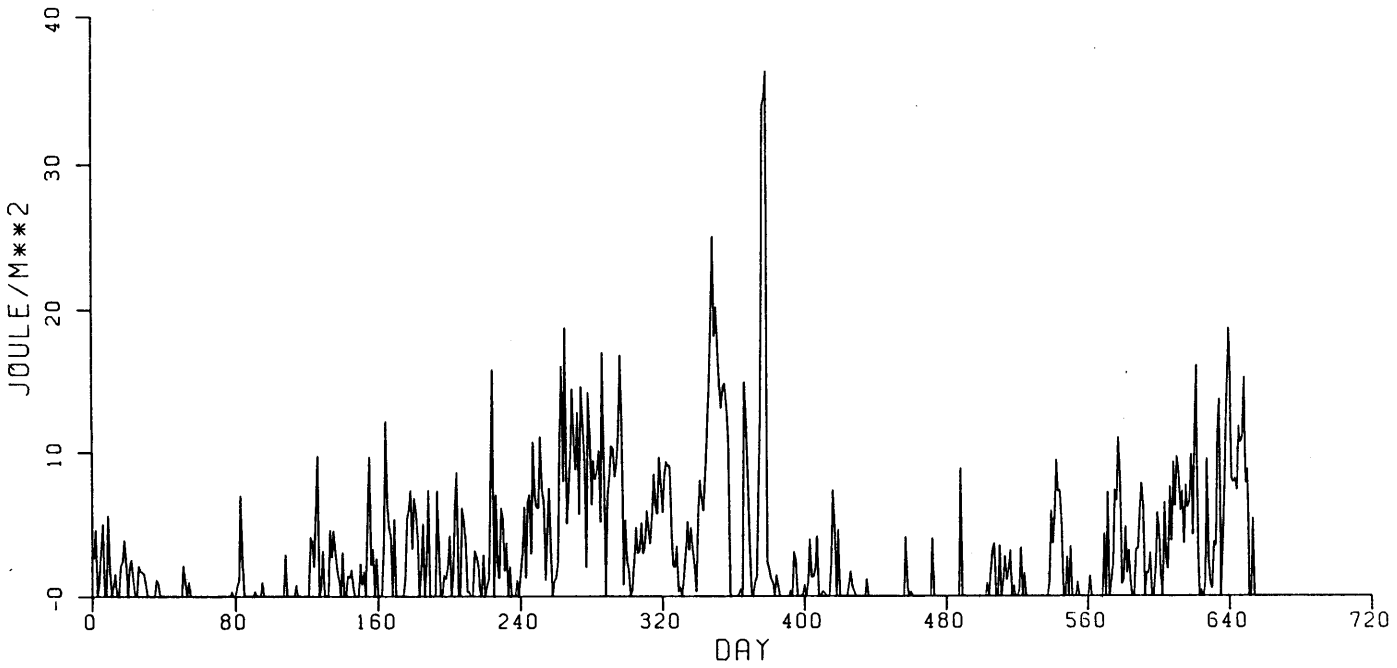

Fig. 9.9(n) Daily Values of Penetrative Convective Mixing Energy for the Period 12 December 1979 to 21 September 1981 with C_w = 6 and C_c = .1

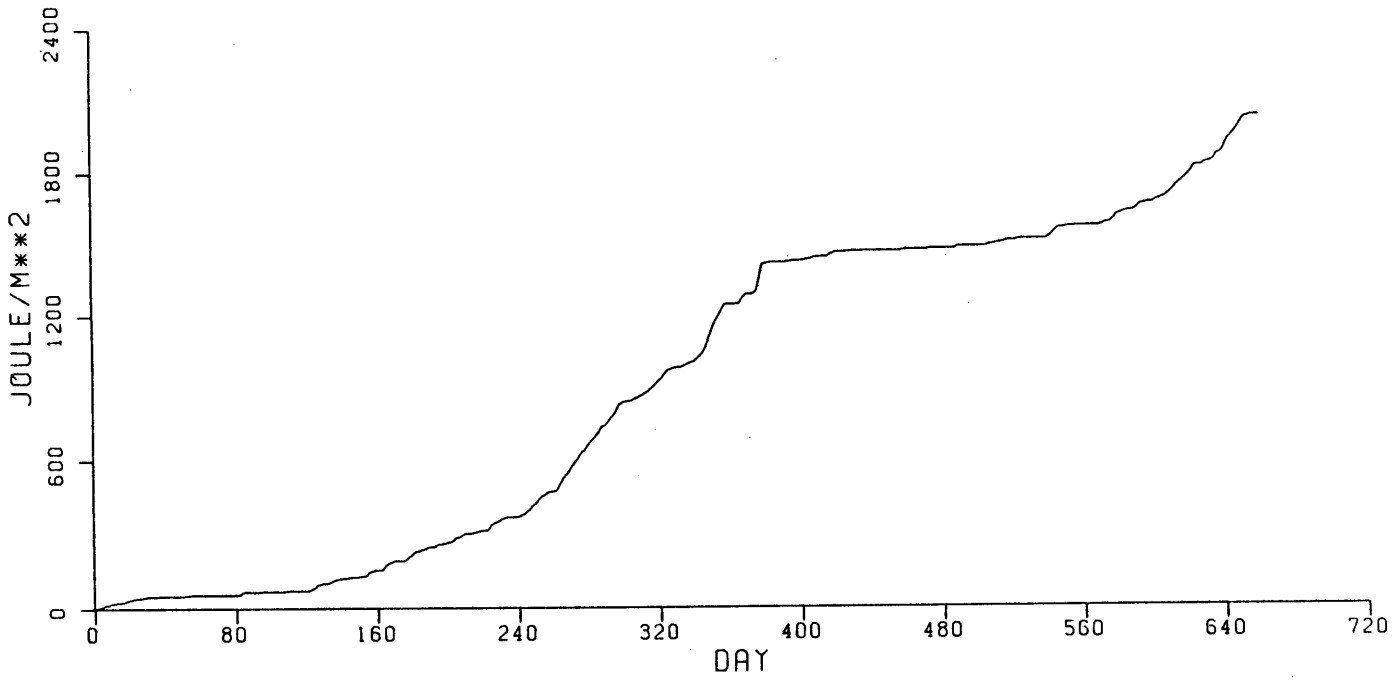

Fig.9.9(o) Cummulative Penetrative Convective Mixing Energy for the Period 12 December 1979 to 21 September 1981 with C_w = 6 and C_c = .1

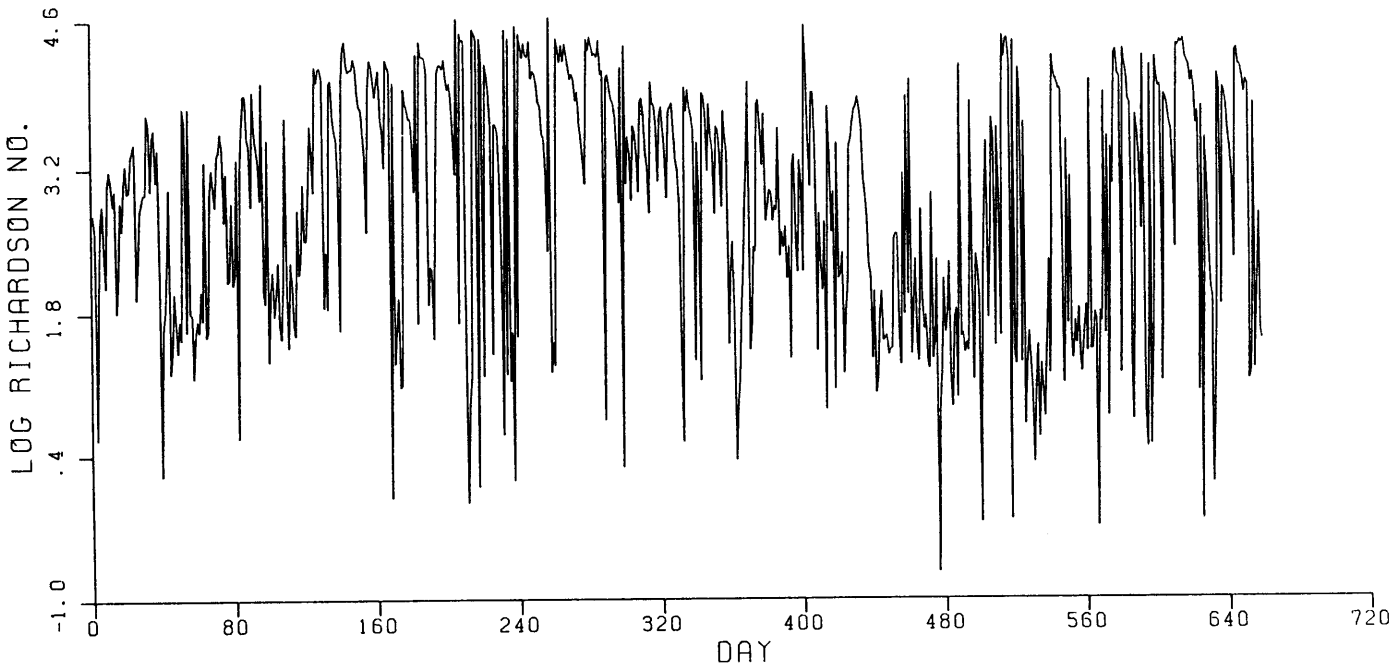

Fig. 9.9(p) Daily Variation of Richardson Numbers for the Period 12 December 1979 to 21 September 1981 with C_w = 6 and C_c = .1.

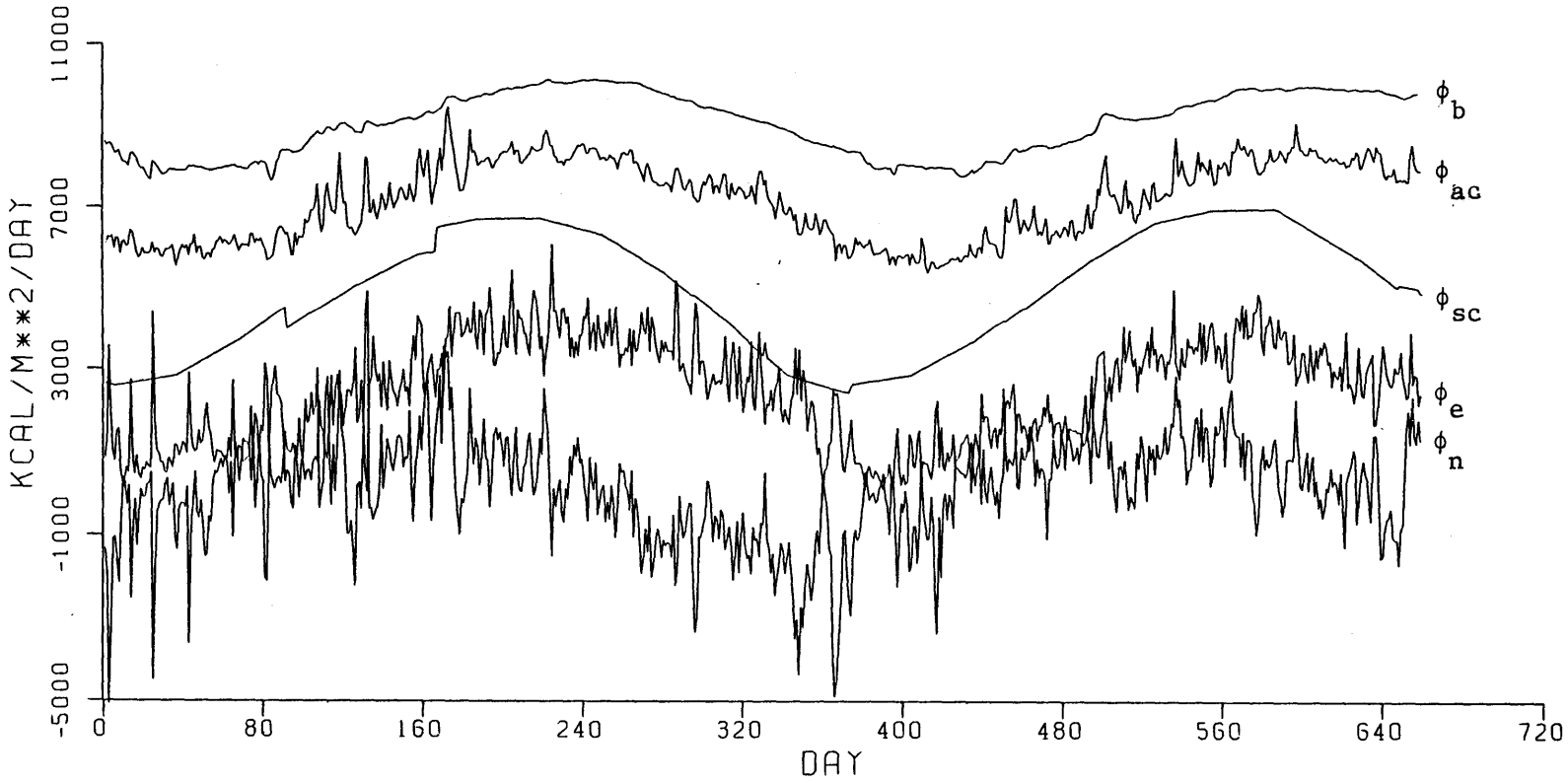

Fig. 9.9(q) Various Components of the Thermal Energy Balance for the Period 12 December 1979 to 21 September 1981.

Table 9.9

Annual Mixing Energies

Duration	12/10/79 - 10/6/80 299 days	10/6/80 - 9/21/81 359 days
C_w	6.0	6.0
C_c	0.1	0.1
KE_w J/m^2/day	32	30
KE_c J/m^2/day	1.7	2.9

temporal resolution of the data does not allow very precise values of C_w and C_c to be estimated.

2. Periods during which wind mixing and penetrative convective mixing are important have been identified. On an annual scale, the magnitude of wind mixing energy is much larger than penetrative convective mixing (Table 9.9).
3. For hypersaline lakes the surface temperature is generally higher than air temperature due to the effect of salinity on evaporation. This has two implications. First, the higher surface temperature tends to increase the rate of evaporation partially negating the reduction in evaporation due to salinity, the negative feedback effect. Second the back radiation term in the overall energy budget is larger than the atmospheric long wave radiation. (Fig 9.9 (e).
4. Annual evaporation from the Dead Sea is about 1.5 m. Inflows during the two wet winters 1979-80 and 1980-81 were of the order of 1.4 m and 1.1 m respectively. Annual pumpage by the saltworks during 1979-80 and 1980-81 amounted to about 14 cm/year.

Chapter 10

DEAD SEA WITH THE POWER PROJECT

10.1 Introduction

The model that has been described, calibrated and verified in the previous chapters is used here in a predictive mode to study the future evolution of the lake with the power project in operation. According to the proposed plan, the Mediterranean Dead Sea Project would convey about 1670 MCM/year (53 m^3/s) to the Dead Sea during the initial filling period of about 20 years until the lake reaches an elevation of about 390 mbsl. Following which the lake level would be maintained steady with a reduced inflow of 1250 MCM/year (39.6 m^3/s). The project is expected to generate 1850 $MKWh_e$/year during the filling period and 1450 $MKWh_e$/year during the steady state period with the station operating during peak hours only (about 48 hrs/week).

The water balance computations in the model were modified to compute daily lake elevations based on inflows from the power project, the Jordan River and outflows due to evaporation and pumpage. The input data used for these computations is discussed in Section 10.2. Important components of the heat, salt, and water budget and the lake stratification for the period of 30 years following the start of the project discharge are discussed in Section 10.3.

It is important to note that the model described in the previous chapters does not account for any near-field inflow mixing. This can be important in situations where the densimetric Froude number is high (Jirka et. al (1981), Ryan and Harleman (1973)). With the power project in

operation, the value of the densimetric Froude number would depend on the velocity at the outlet to the Dead Sea and the design of the discharge channel as expressed by:

$$F = \frac{U}{\left(\frac{g\Delta\rho\ell}{\rho}\right)^{1/2}} \qquad (10.1)$$

where, F = the densimetric Froude number, U = the discharge velocity, ℓ = the characteristic length scale of the inlet structure. Clearly, the value of U and hence F would also depend on whether the power plant is used for base load or for peaking purposes.

Experiments in two dimensional stratified flow, Elison and Turner (1959) and Price (1979) indicate that vertical turbulent entrainment or vertical inflow mixing ceases as $F \to 1$. For the case of Jordan River inflows only, F is significantly less than unity and this effect is not important. However, with the power project in operation, F may be larger than unity (depending on the discharge and design of the discharge channel) causing near field mixing to be important.

10.2 Input Data

Future simulations start with the lake elevation at 402.8 mbsl. This corresponds to lake level for October 1984. Also the initial temperature and salinity conditions for October 1984 have been used.

Inputs to the water budget consist of fresh water inflows from the Jordan River estimated at 530 MCM/year and a net pumpage by the salt works of 230 MCM/year. Note this value is about twice the pumpage for the year 1979-80 and 1980-81 and accounts for the installation and expansion of the

Arab Potash works. The above values have been recommended by Tahal (1982) and are based on a comprehensive study of future water use patterns in Israel. The annual variation of these quantities is assumed similar to those for the year 1979-82. Thus although the annual inflows and pumpage was invariant for the entire period of simulation, the day to day values varied with a frequency of three years.

The meteorological inputs used were the values representative of 1979-1982. Thus every third year in the long term simulation has identical inputs. This three year cycle is apparent in the model results discussed subsequently.

Fig 10.1, shows the activity coefficient of water in Dead Sea (β) for a range of salinities computed using eq. 6.18 with salinity as the measure of concentration. The values of β for sea water based on the data presented by Arons and Kientzler (1954) are also shown.

Intermediate values of β have been used for future simulations that reflect the changing salinity and ionic composition of the upper mixed layer with the project in operation.

10.3 Lake Elevation and Surface Salinities

Fig. 10.2 shows the lake elevations for a period of 30 years after the start of the power project. The first 22 years of this period constitute the filling period with continuous inflow at the rate of 53 m^3/s. This contributes an annual increase in lake level of about 2.2 m at the beginning of the first year and about 1.9 m towards the end of the thirty years. This reduction is due to an increase in the surface area of the Dead Sea by a factor of about 1.2. During the remaining eight years of the

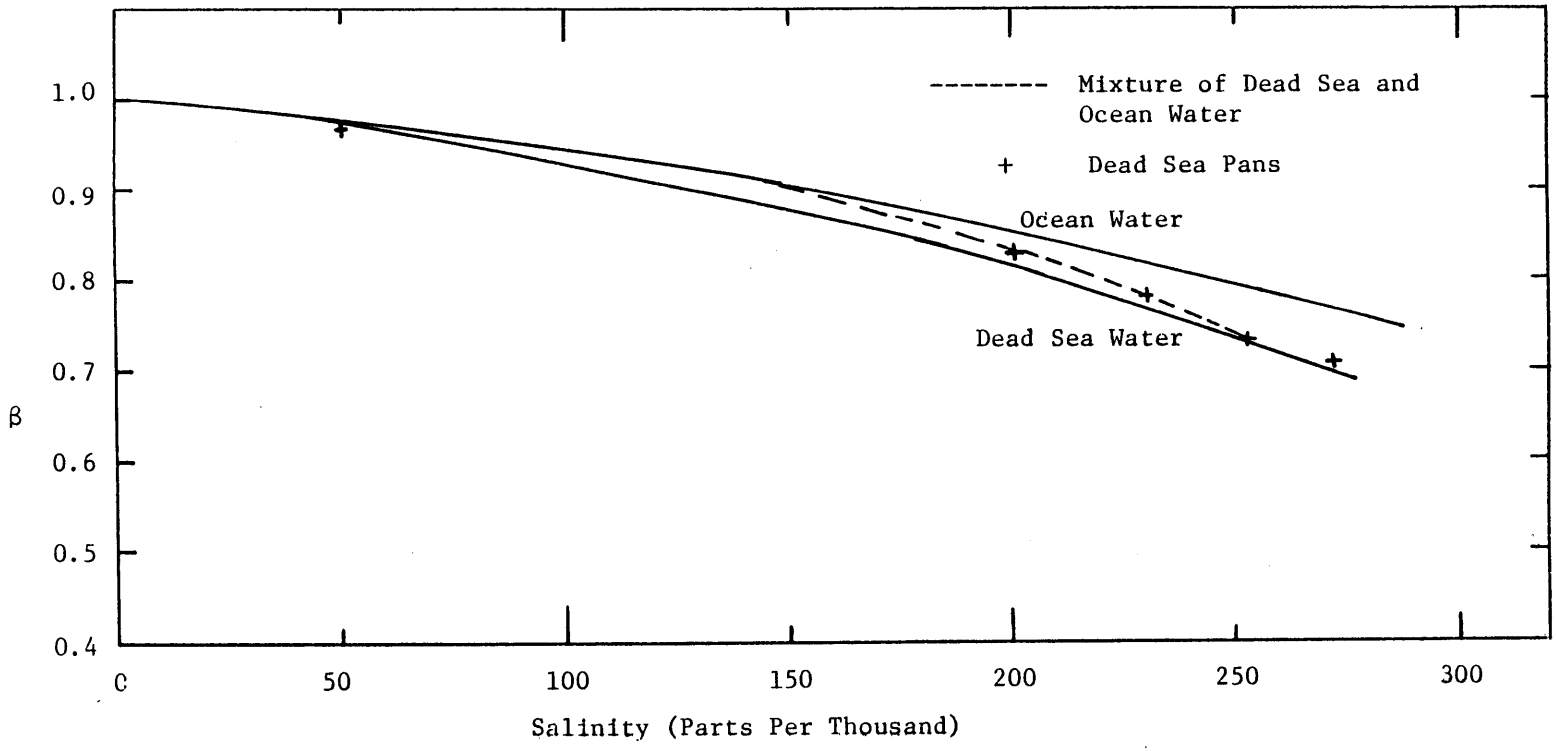

Fig. 10.1 The Activity Coefficient of Water in Ocean Water, Dead Sea Water and Mixtures

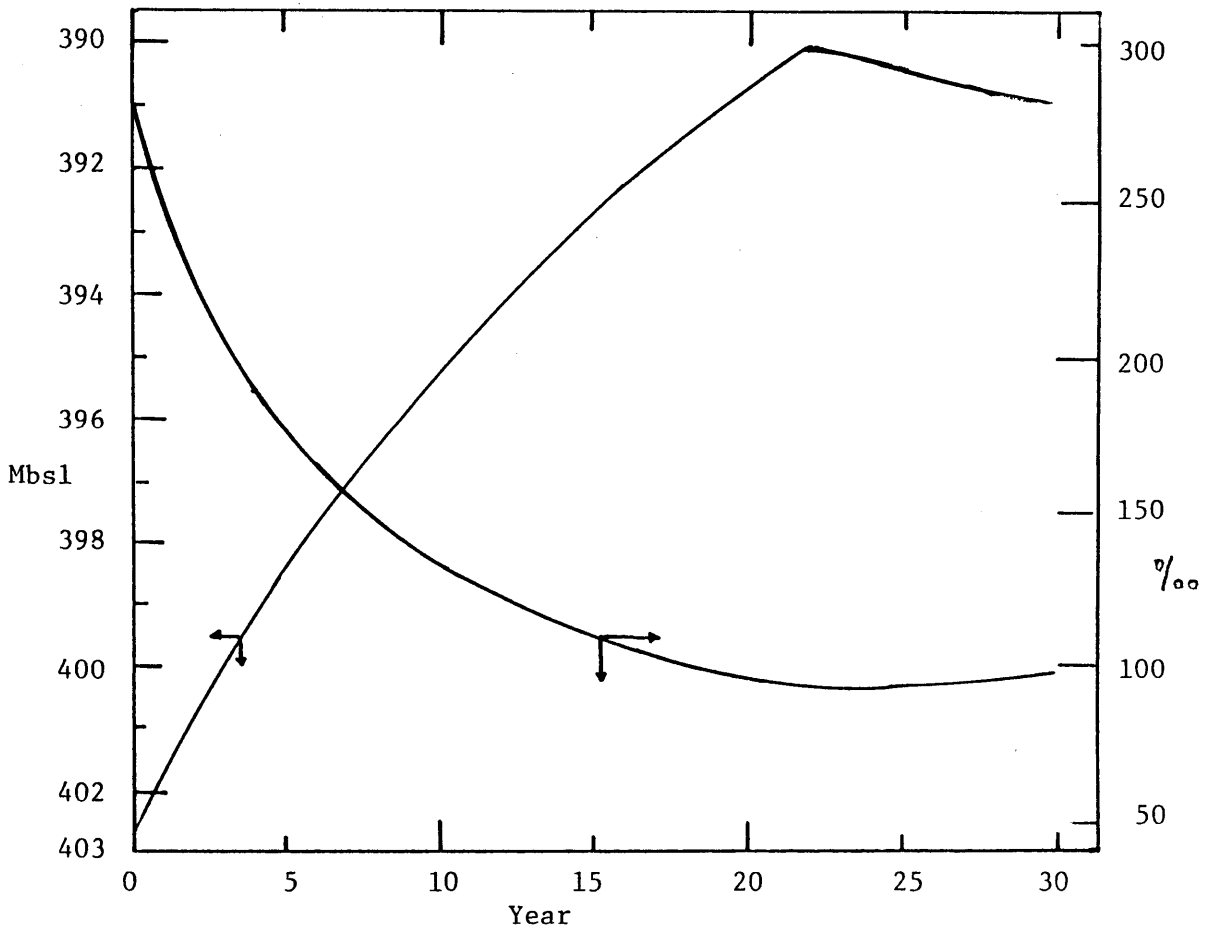

Fig. 10.2 Dead Sea Elevation and Surface Salinity with the Power Project in Operation

simulation, the project inflows were reduced to about 40 m^3/s. The effect of changing evaporation is discussed in Section 10.4.

With these inflows, the lake reaches an equilibrium level at about 391 mbsl. Inflows from the Jordan River contributes an annual increase in elevation of 0.7 m and 0.6 m in year 1 and year 30 respectively, while pumpage by the salt works reduces the elevation by about 0.3 m and 0.26 m respectively. As a result of net relatively fresh inflows, the lake experiences significant dilution. Fig. 10.2 also shows the surface salinities for the thirty years. Minimum surface salinity of 92.6°/oo is indicated at the end of the filling period. Thereafter the salinity shows a gradual increase to 93.6°/oo by the end of year 30 due to a slight drop in the lake level. Even at a steady lake elevation, the surface salinity is expected to increase since the project inflows continuously add salt to the lake.

10.4 Annual Evaporation and Temperature Feedback Effect

Fig. 10.3 shows the annual evaporation for the thirty year period. As expected, dilution of the surface increases evaporation, simultaneously reducing the surface temperature that is also shown in Fig. 10.3. Thus the increase in evaporation due to reduction in salinity is partially compensated by a decrease in evaporation due to a drop in temperature - the temperature feedback effect. These two effects can be quantified for any year as discussed previously in Section 6.3.5 for the case of pans.

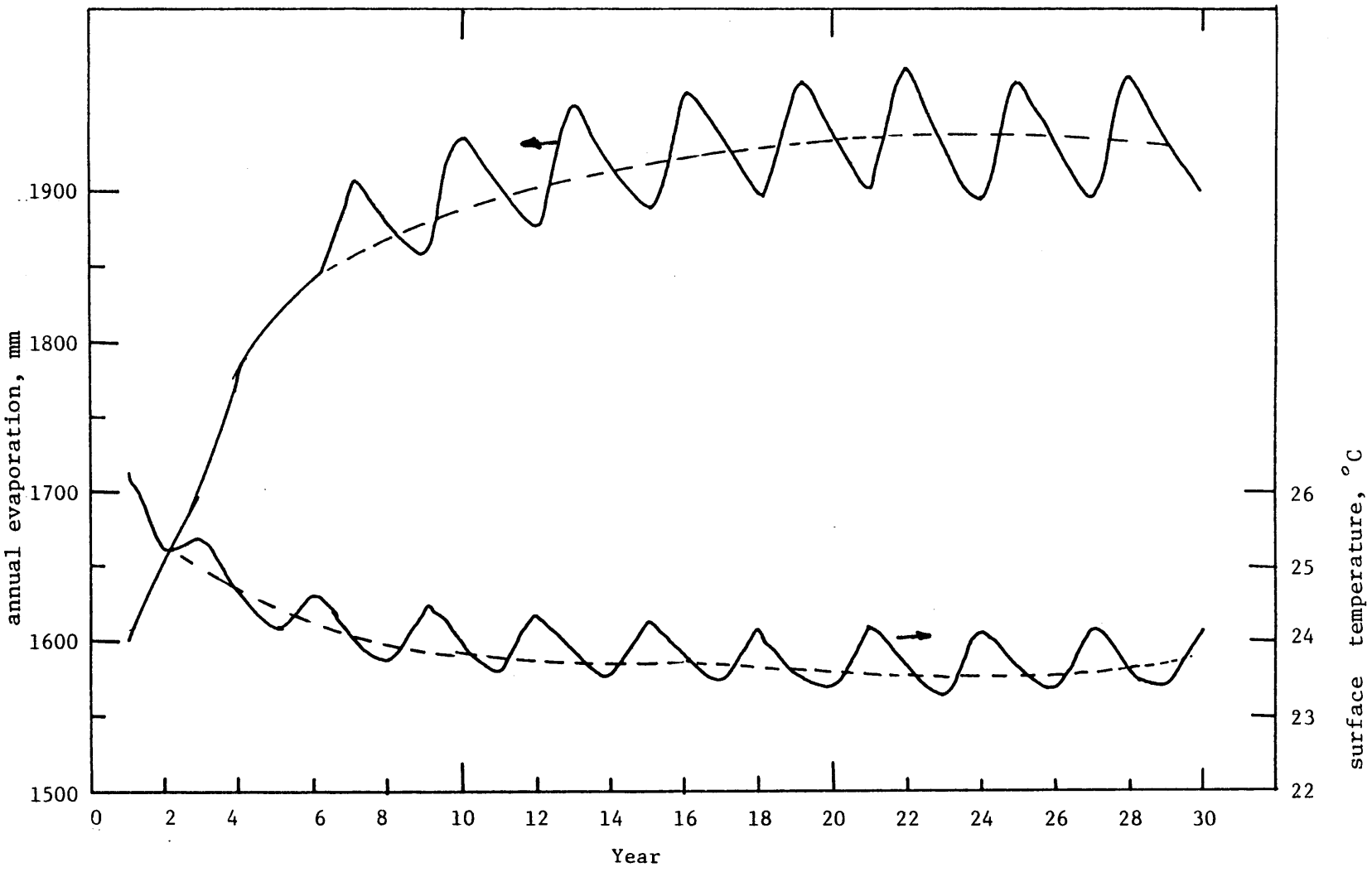

Fig. 10.3 Annual Evaporation and Surface Temperatures with The Project in Operation.

Comparing evaporation in year 1 with evaporation in year 22:

$$\alpha_L = \frac{E_1}{E_{22}} = \left[\frac{\gamma_1}{\gamma_{22}}\right] \left[\frac{e_{sat}(T_1) - \phi\, e_{sat}(T_a)}{e_{sat}(T_{22}) - \phi e_{sat}(T_a)}\right] \qquad (10.2)$$

Note α_L is defined as the ratio of lake evaporation for year 1 to lake evaporation for year 22.

In eq. 10.2, $\frac{E_1}{E_{22}} = 0.81$ and the value of the third-term (feedback effect) based on annual mean meteorology and computed annual mean surface temperature is 1.37. Thus $\gamma_1/\gamma_{22}=0.59$. This implies that the reduction in evaporation due to salinity effect alone is 41%. Simultaneously, there is an increase of 37% due to the temperature effect. The composite effect is a computed, modest decrease in evaporation of 19%.

It is interesting to compare these results for the lake with the pan data discussed in Chapter 6. Since there were no pans with a salinity corresponding to mean salinity for year 1 or year 22, the pan data were interpolated to obtain data for two hypothetical pans (Pan 12* and Pan 19*) that have the same salinity as year 22 and year 1 in the simulations. The ratio $\alpha_p = \frac{E_{19}^*}{E_{12}^*}$ (corresponding to $\alpha_L = .81$) is 0.69. This large difference in the observed evaporation rates for pan and lake is due to the difference in the temperature feedback effects as the two water bodies show very different surface temperatures (Table 10.1). The pans show much lower temperature since they were not insulated and loose thermal energy to the ground. This temperature dependence of α is further illustrated in Fig.

Table 10.1

Comparison of α and water temperature for experimental pans, simulation results and a pan and lake at equilibrium with Dead Sea meteorology.

Case	$T_s^* - T_a$	$T_{fresh}^{**} - T_a$	α	$\bar{T}_a$
Equilibrium Pan	2.9	0.4	.78	23.6
Equilibrium Lake	1.4	-1.1	.76	23.6
Experimental Pan	-1.1	-3.7	.69	23.3
Simulation Result	2.7	-0.1	.81	23.6

* salinity = 258 $^{o}/_{oo}$

** salinity = 92 $^{o}/_{oo}$

10.4 that shows the isopleths for α for a fixed mean meteorology and surface salinities representative of year 1 and year 22. The α value varies significantly depending on the surface temperature of the water body.

The difference in α_p and α_L has been explained by the fact that the Dead Sea pans were not insulated. A second explanation could be the difference in the windspeed functions for a pan and a large body of water. This effect is investigated below.

Table 10.2 shows the equilibrium temperatures and the α values computed for saline pan and lake. A pan coefficient of 0.7 has been assumed for computing the pan equilibrium temperatures. These results are also shown in Fig. 10.5. A number of interesting conclusions can be inferred.

First, α_p is always less than α_L, because lake temperatures are higher than pan temperatures. Second, the α value is very sensitive to meteorological conditions and in particular relative humidity values. This is obvious by comparing the humidity and α values for the months of December and June that have the highest and lowest relative humidity, respectively. Finally, Table 10.2 also shows the effect of using annual meteorology versus monthly meteorology to compute equilibrium temperatures and the α values. The equilibrium temperatures and the α values computed using annual mean meteorology is larger than the annual mean values based on monthly averaged values i.e.

$$\overline{T_E\,(T_a,\ \phi,\ W_z)} \ <\ T_E\,(\bar{T}_a,\ \bar{\phi},\ \bar{W}_z) \qquad (10.3)$$

10.5 Lake Stratification

The vertical salinity stratification within the Dead Sea is of interest to the operators of the salt works. The success of their operations

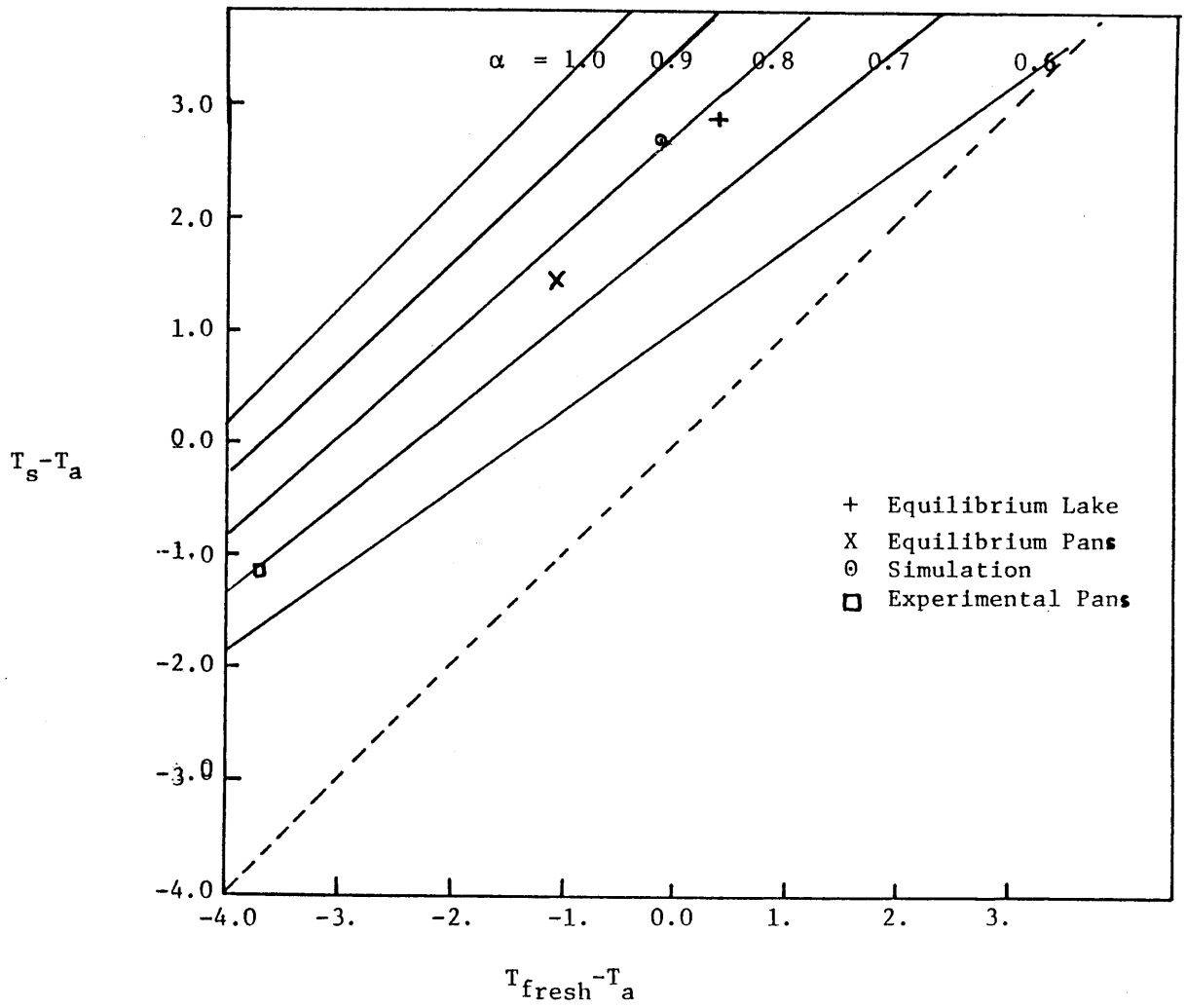

Fig. 10. 4 Variation of α for the Dead Sea Meteorology
(Also see Fig. 10.5)

Table 10.2 Monthly Meteorology, Equilibrium Temperatures and α values for a Pan and Lake

	METEOROLOGY			EQUILIBRIUM TEMPERATURE				ALPHA	
M	TA	W	H	SL	FL	SP	FP	L	P
JAN	13.14	2.91	55	14.34	12.68	13.57	11.84	.664	.645
FEB	14.58	2.82	48	16.83	15.03	15.63	13.78	.744	.728
MAR	17.49	3.12	69	21.91	19.74	20.73	18.51	.691	.653
APR	23.36	3.25	55	26.45	23.97	25.03	22.51	.771	.749
MAY	27.47	3.40	45	29.50	26.80	27.79	25.07	.820	.805
JUN	31.02	3.28	40	32.78	29.88	30.80	27.89	.846	.835
JLY	32.31	3.37	44	34.11	31.11	32.25	29.24	.840	.826
AUG	32.11	3.17	48	34.46	31.47	32.70	29.68	.827	.812
SEP	28.65	3.05	49	30.98	28.23	29.38	26.59	.807	.791
OCT	25.82	2.69	55	28.63	26.09	27.25	24.65	.770	.751
NOV	21.46	2.84	58	22.95	20.76	22.05	19.77	.689	.668
DEC	15.25	3.57	73	17.17	15.26	16.70	14.70	.450	.398
MEAN	23.56	3.13	53	25.81	23.42	24.49	22.02	.743	.722
USING MEAN ANNUAL METEOROLOGY									
	23.56	3.13	53	26.44	23.97	25.00	22.49	.776	.756

TA = AIR TEMPERATURE (C)
W = WIND SPEED (M/S)
H = RELATIVE HUMIDITY (%)

F FRESH
S SALINE
P PAN
L LAKE

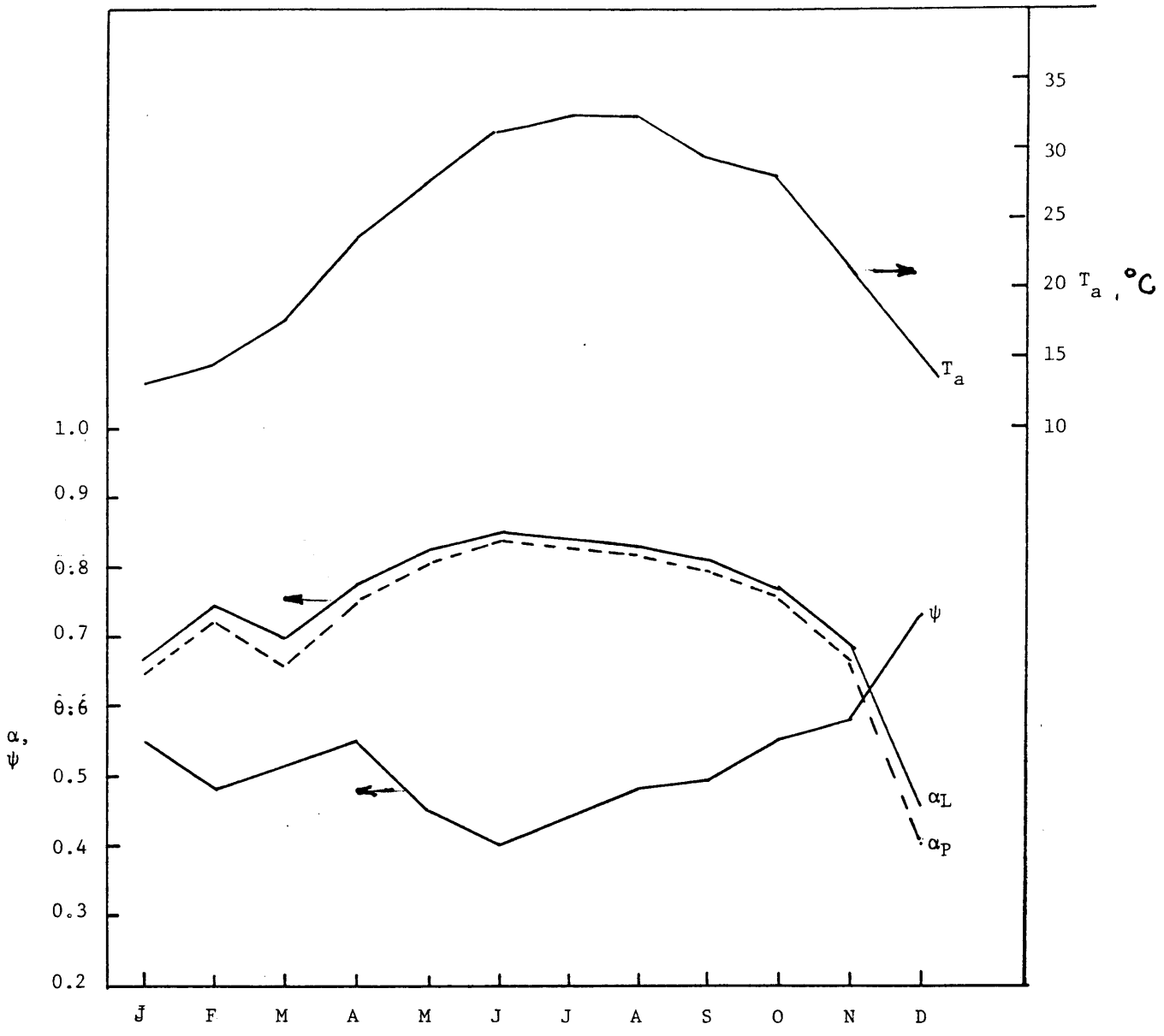

Fig. 10.5 Monthly Meteorology and α-values for a Pan and Lake at Equilibrium

depends on the availability of "pure" Dead Sea Water that is rich in magnesium, potassium and bromine salts. With the project inflows, the surface layers would consist of a mixture of Dead Sea and Mediterranean waters. It is of interest to estimate the mixed layer depth or the depth to which the Mediterranean sea water would penetrate. Operators of the salt works could then pump "pure" Dead Sea brines from below this depth.

Fig. 10.6 to Fig. 10.11 show the temperature salinity and density profiles for year 1, 2, 5, 10, 20 and 30 years since the start of the power project. For each year four profiles equally spaced (90 days apart) through the year are shown.

The salinity profiles indicate a progressive dilution of the upper mixed layer. Within the first few years, a sharp, permanent halocline develops at about 15 m below the surface. This insulates the lower part of the Dead Sea from any meteorological influence. This is also clear from the temperature profiles that indicate that the annual warming and cooling cycle is restricted to the top 10 m of the lake. Thus during summer the lake has warm water overlying cold water remaining from the previous winter.

Fig. 10.12 to Fig. 10.17 show details of salinity, temperature, and density isopleths for the top 15 m of the lake for years 1, 2, 5, 10, 20 and 30. These contours indicate the strong temperature stratification and a weak salinity stratification in the top 15 m of the lake. The stratification is destroyed in the fall due to surface cooling and significant convective activity when the mixed layer extends to a depth of about 15 m.

This stratification pattern implies that the Mediterranean Sea water mixes to a depth of about 15 to 20 m below the surface. It is recommended that

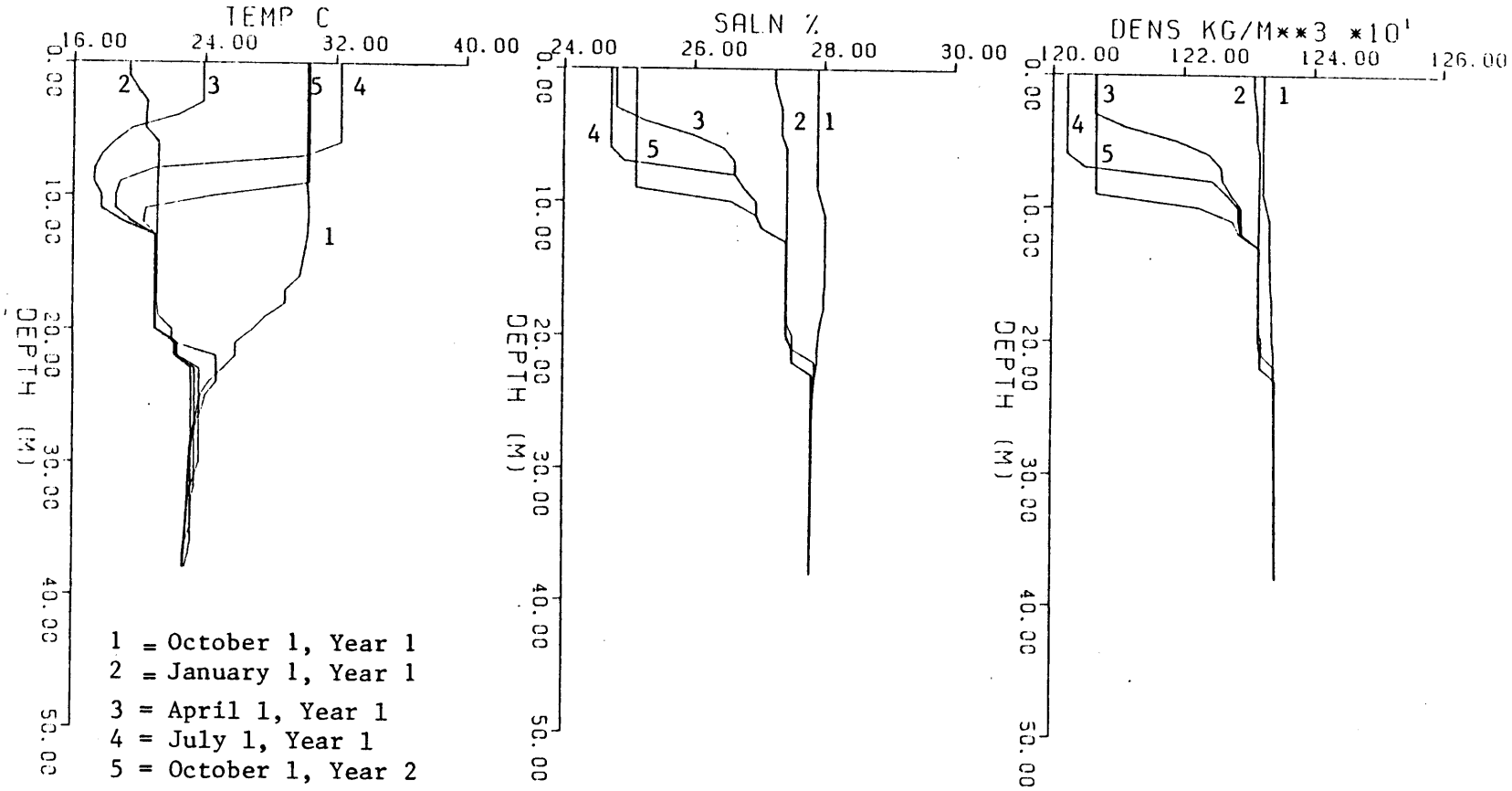

Fig. 10.6 Temperature, Salinity and Density Profiles for Year 1 with The Power Project in Operation

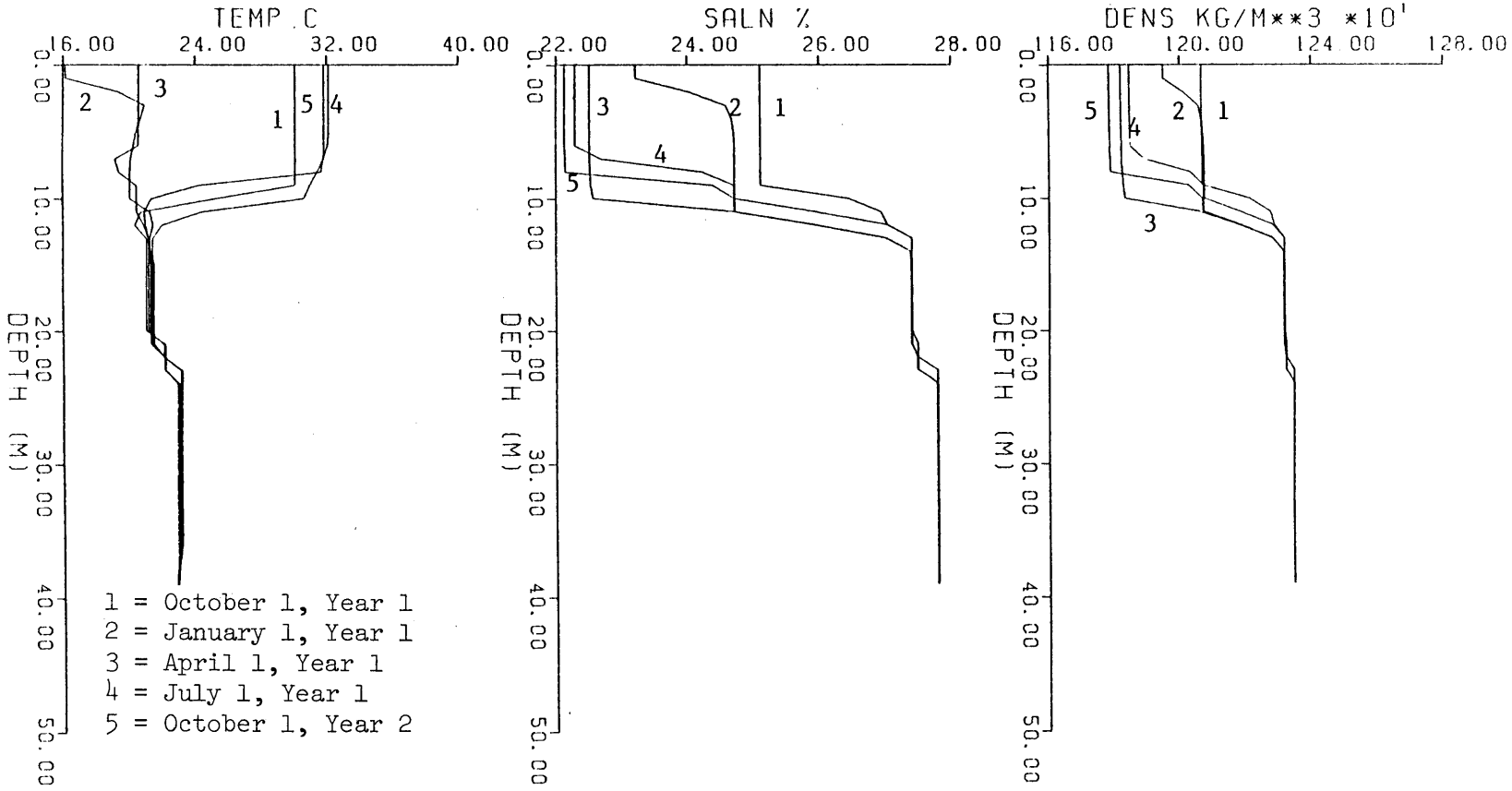

Fig. 10.7 Temperature, Salinity and Density Profile for Year 2 with The Power Project in Operation.

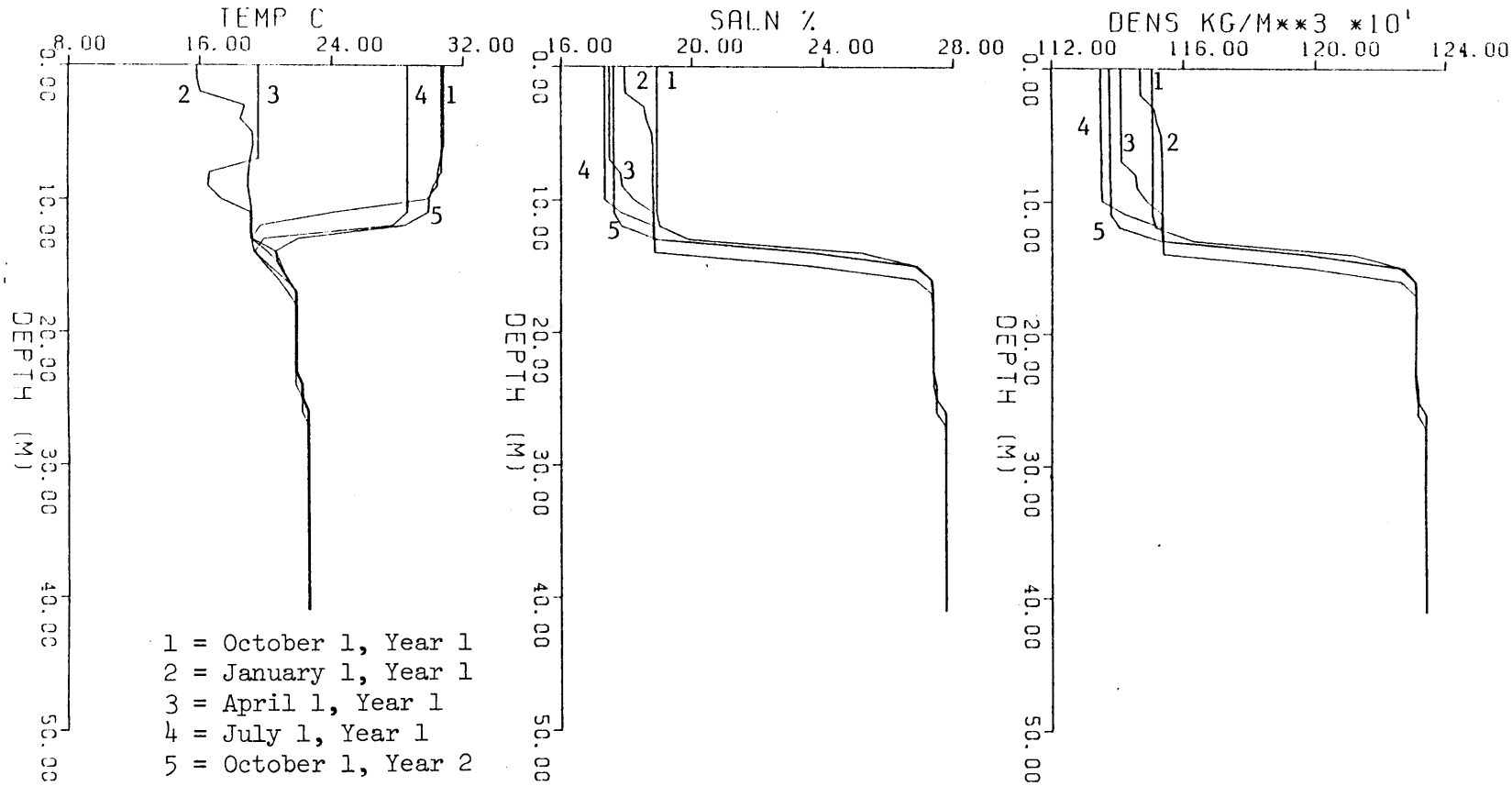

Fig. 10.8 Temperature, Salinity and Density Profiles for Year 5, with The Power Project in Operation.

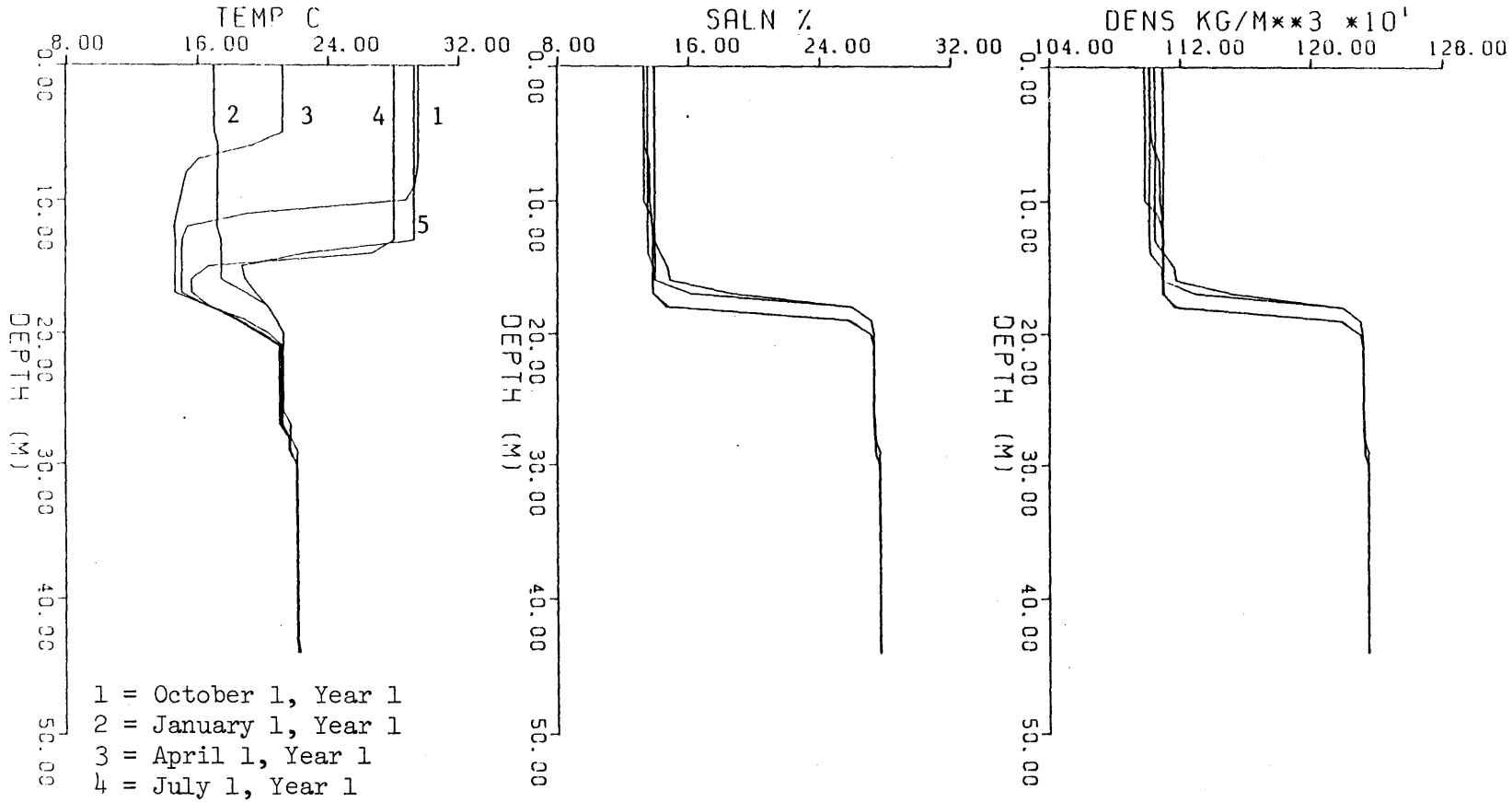

1 = October 1, Year 1
2 = January 1, Year 1
3 = April 1, Year 1
4 = July 1, Year 1
5 = October 1, Year 2

Fig. 10.9 Temperature, Salinity and Density Profiles for Year 10 with The Power Project in Operation.

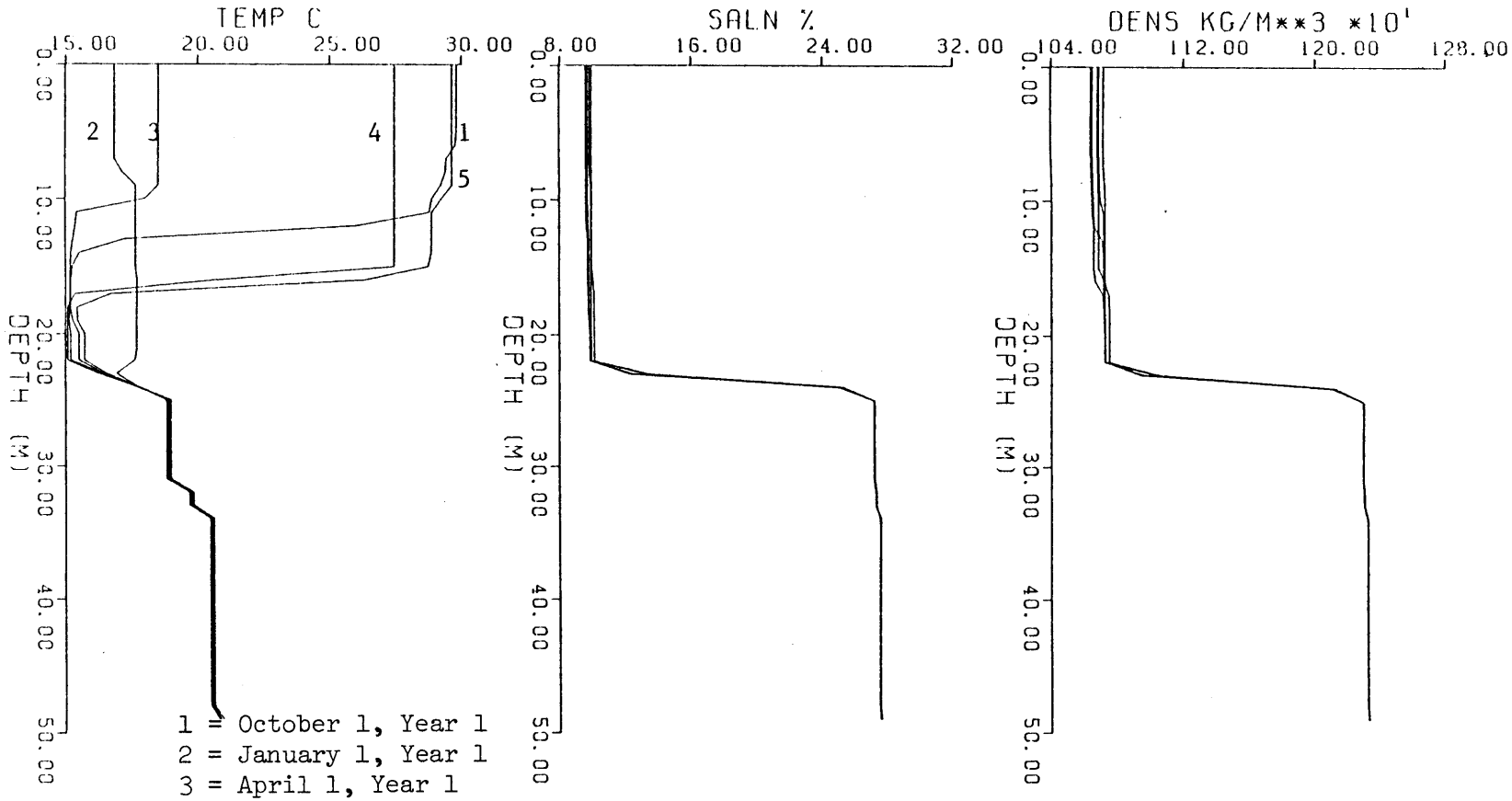

1 = October 1, Year 1
2 = January 1, Year 1
3 = April 1, Year 1
4 = July 1, Year 1
5 = October 1, Year 2

Fig. 10.10 Temperature, Salinity and Density Profiles for Year 20 with The Power Project in Operation.

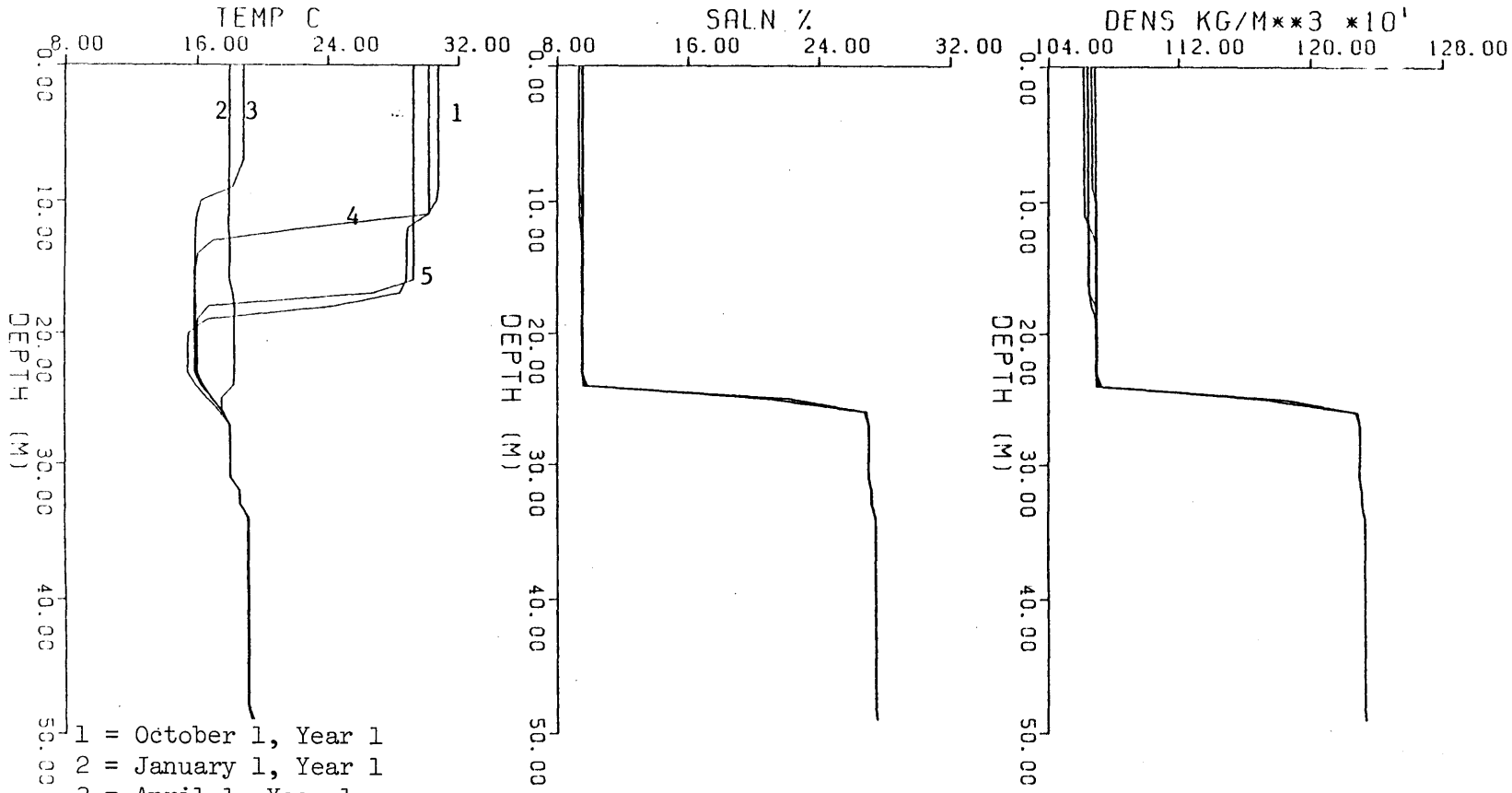

1 = October 1, Year 1
2 = January 1, Year 1
3 = April 1, Year 1
4 = July 1, Year 1
5 = October 2, Year 2

Fig. 10.11 Temperature, Salinity and Density Profiles for Year 30 with The Power Project in Operation.

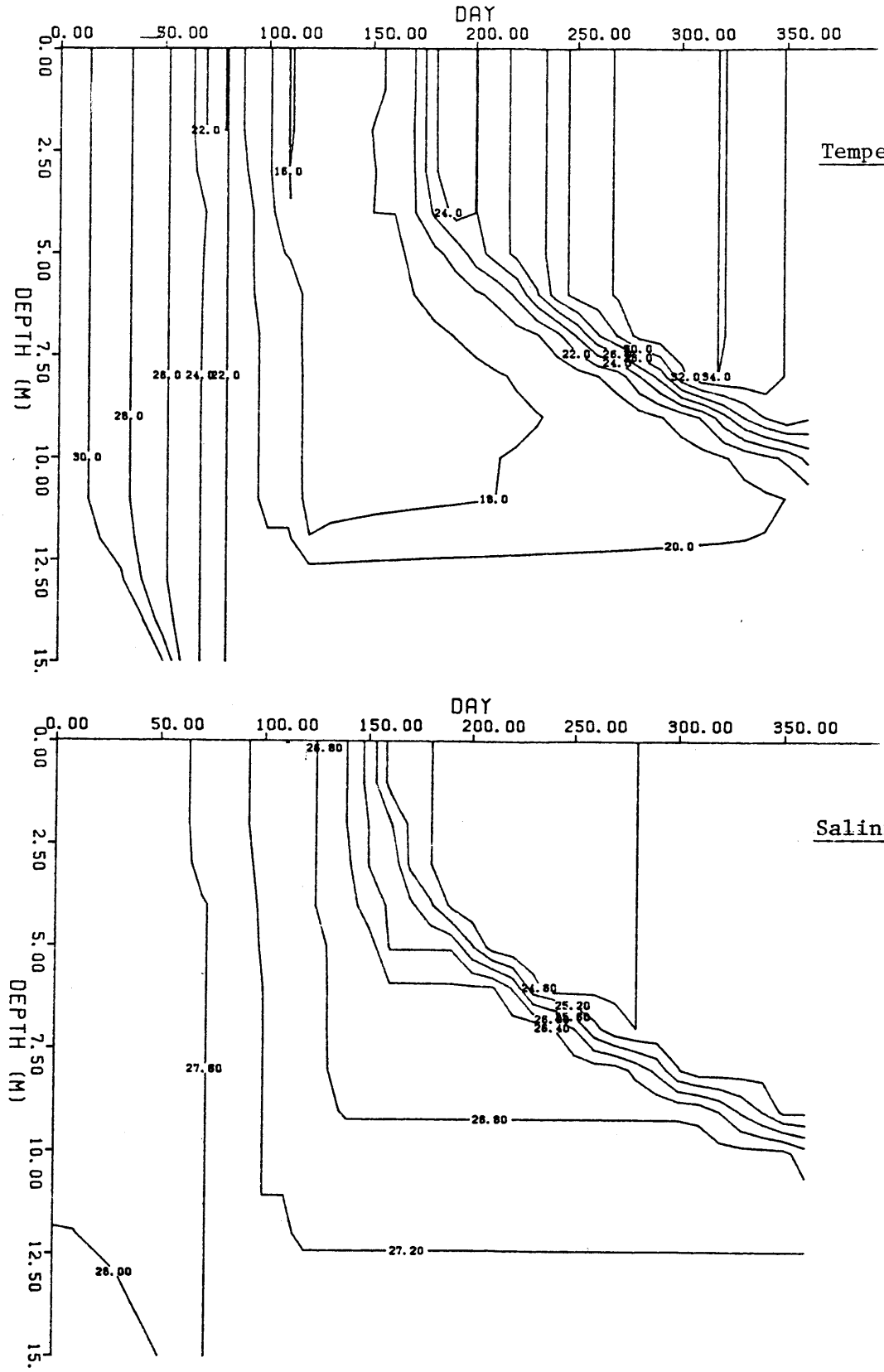

Fig. 10.12(a) Temperature and (b) Salinity Isopleths for Year 1 with The Power Project in Operation.

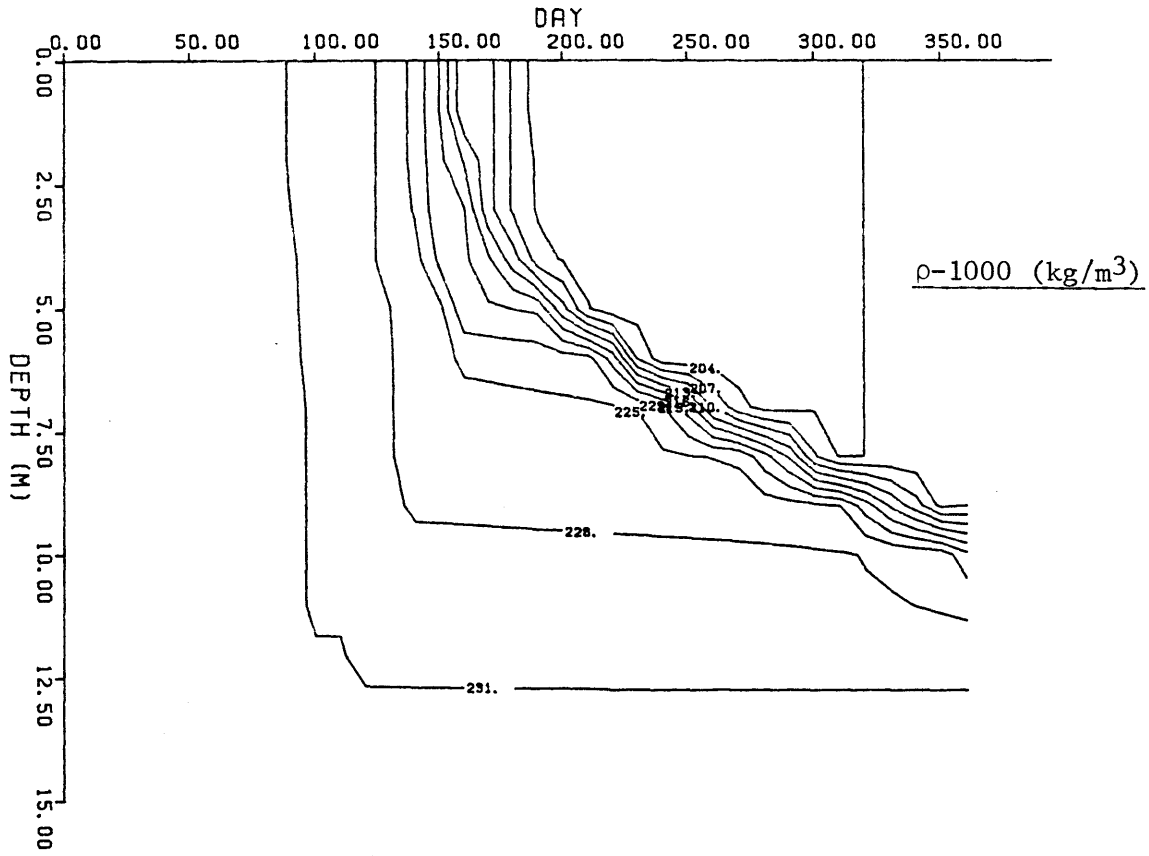

Fig. 10.12(c) Density Isopleths for Year 1 with The Power Project in Operation.

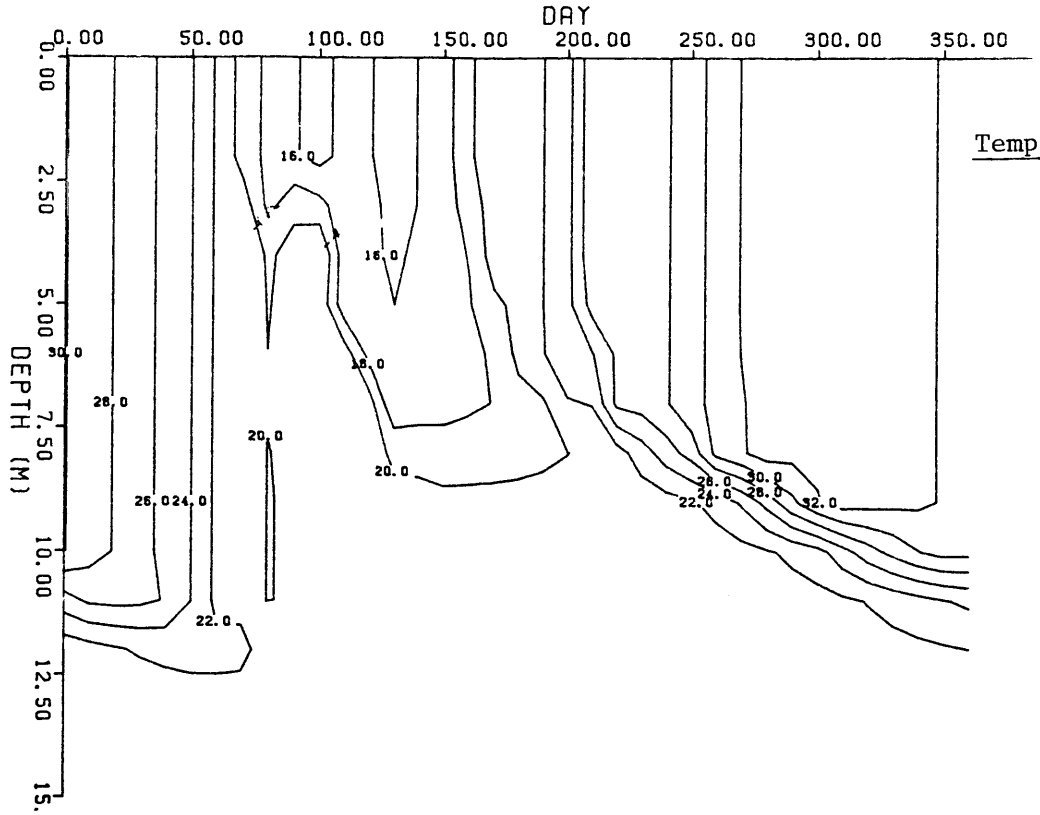

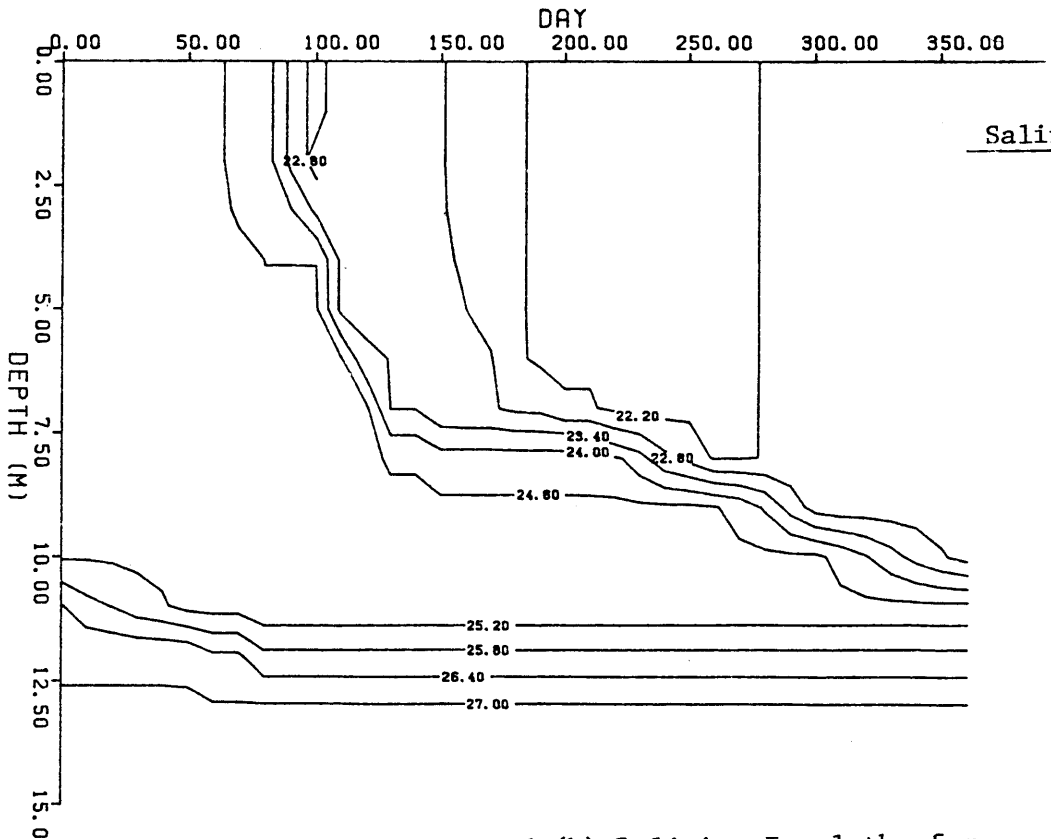

Fig. 10.13(a) Temperature and (b) Salinity Isopleths for Year 2 with The Power Project in Operation.

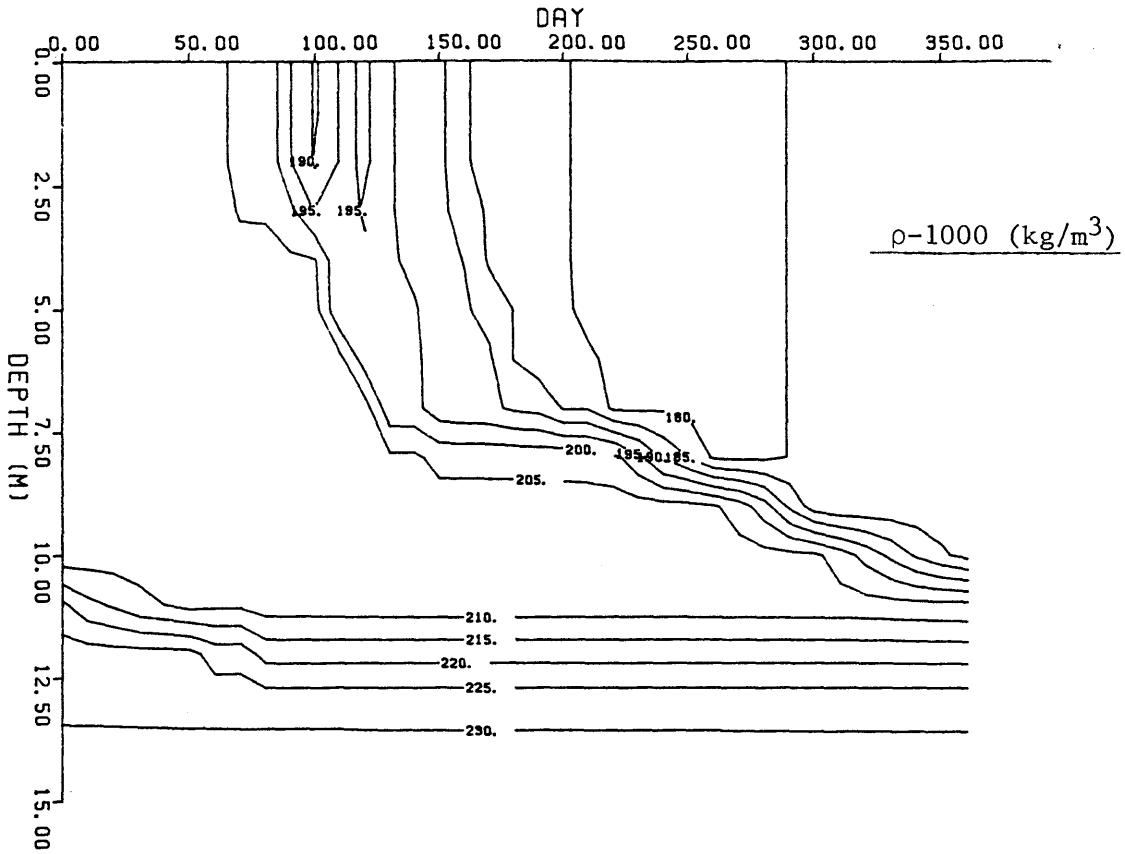

Fig. 10.13(c) Density Isopleths for Year 2 with The Power Project in Operation.

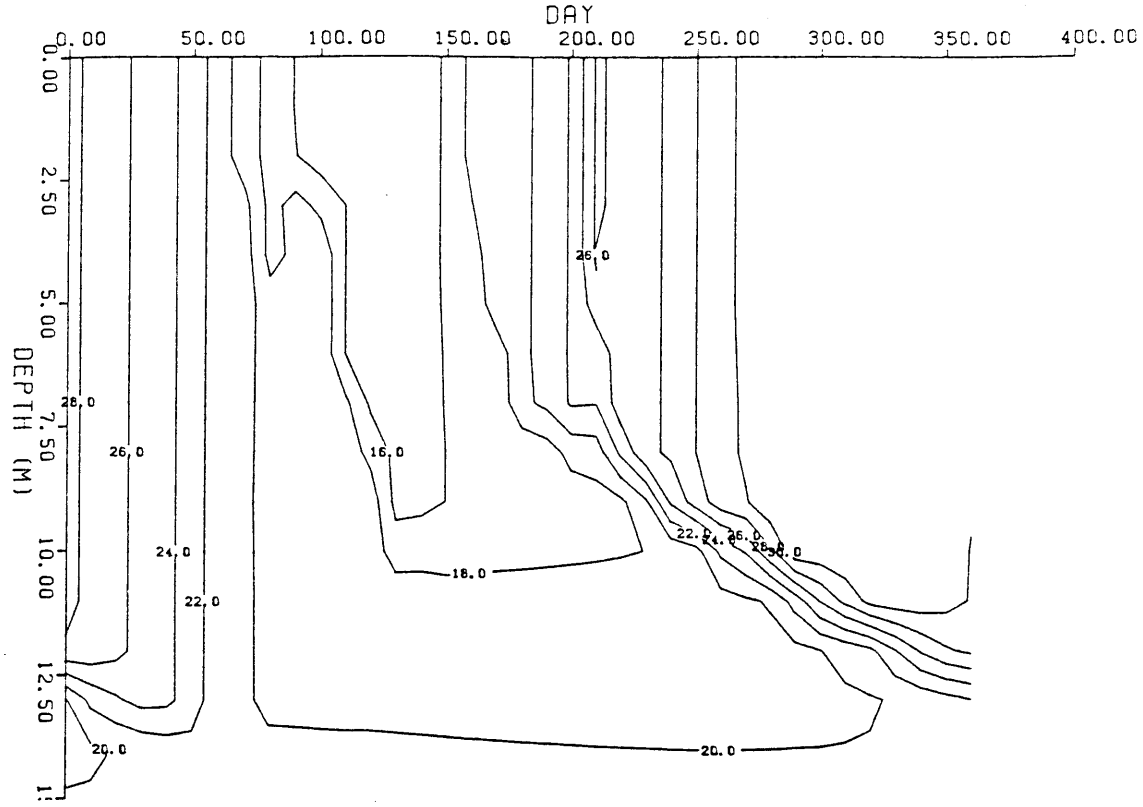

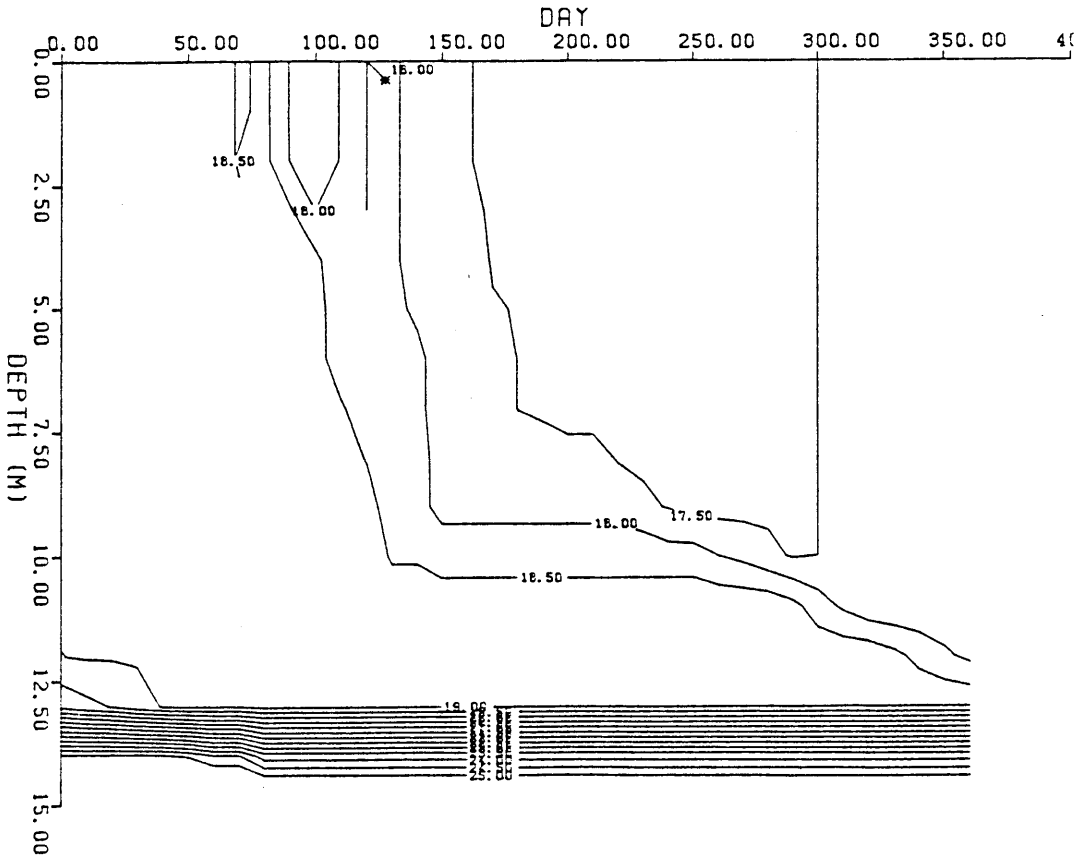

Fig. 10.14(a) Temperature and (b) Salinity Isopleths for YEar 5 with The Power Project in Operation.

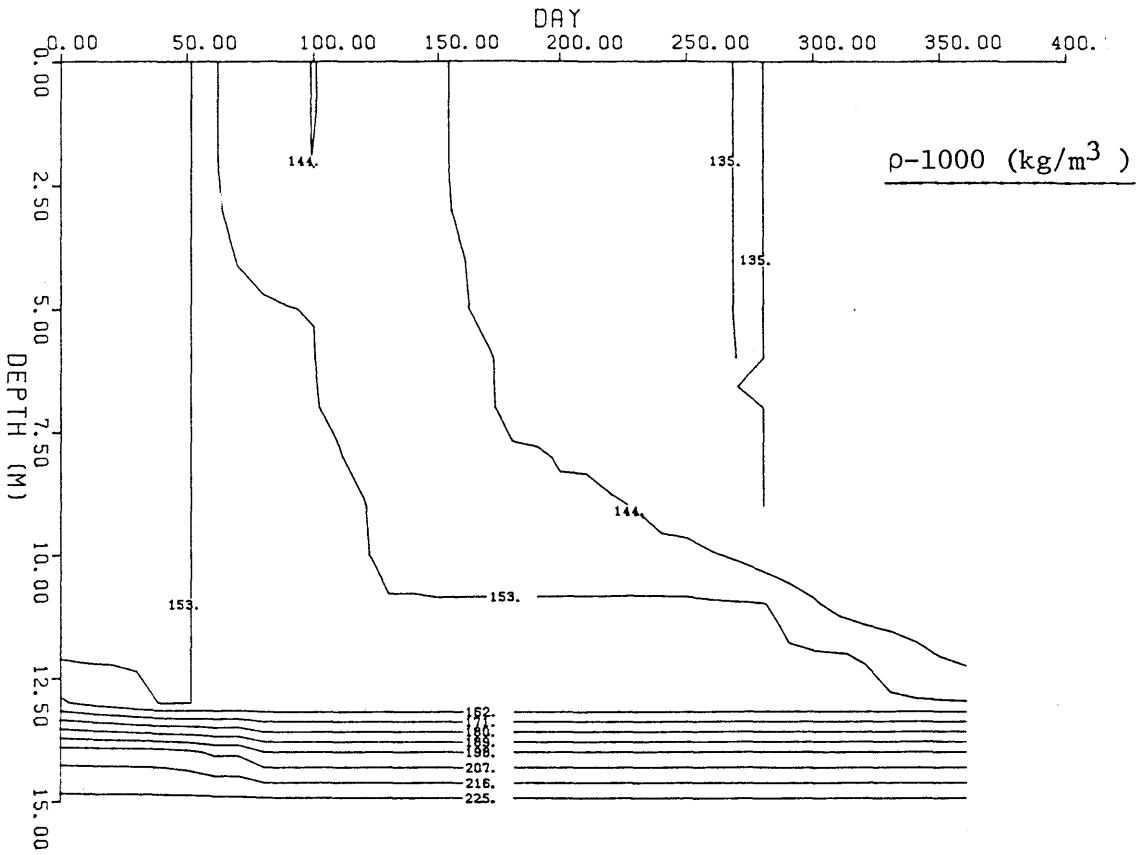

Fig. 10.14(c) Density Isopleths for Year 5 with The Power Project in Operation

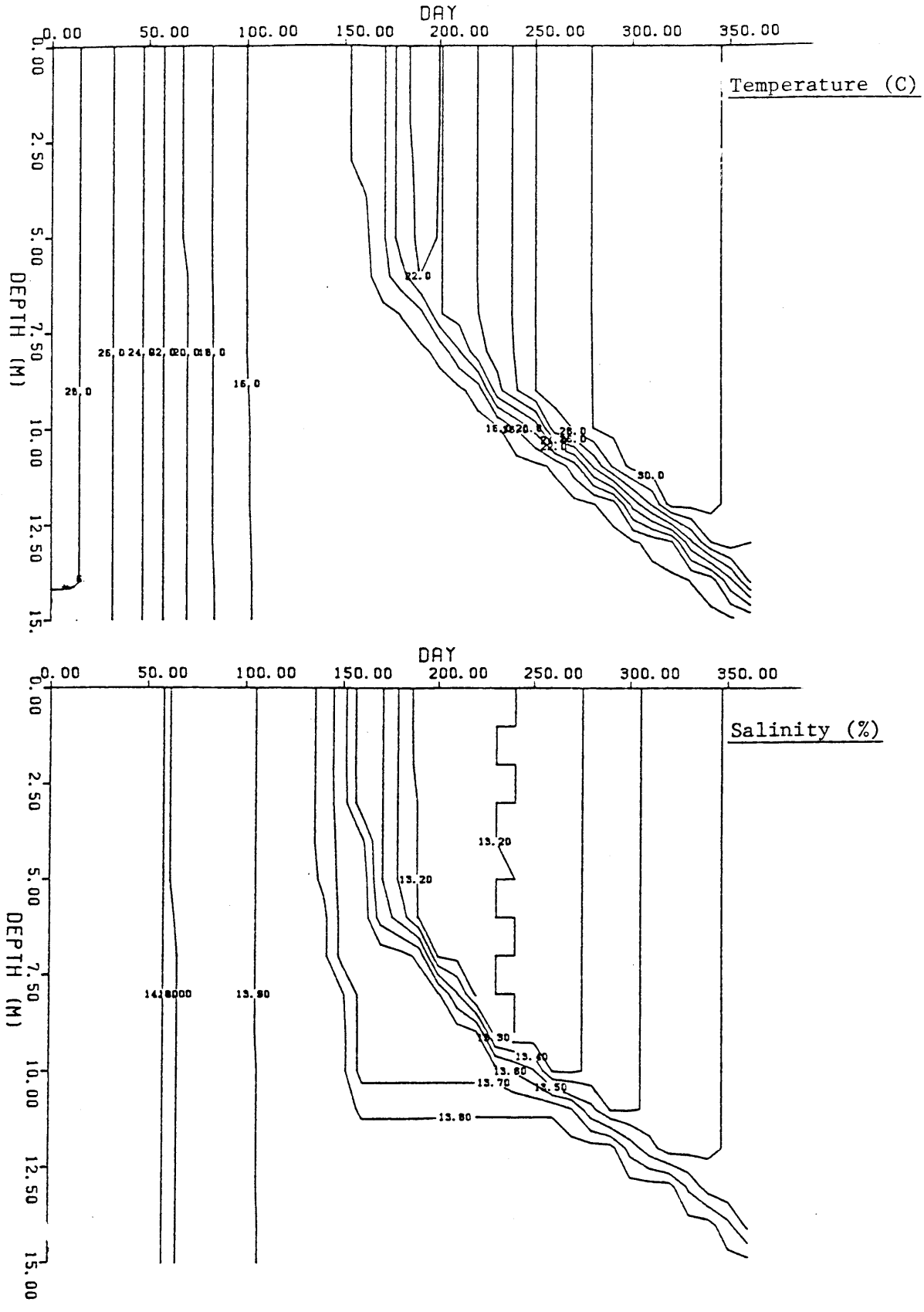

Fig. 10.15(a) Temperature and (b) Salinity Isopleths for Year 10 with The Power Project in Operation.

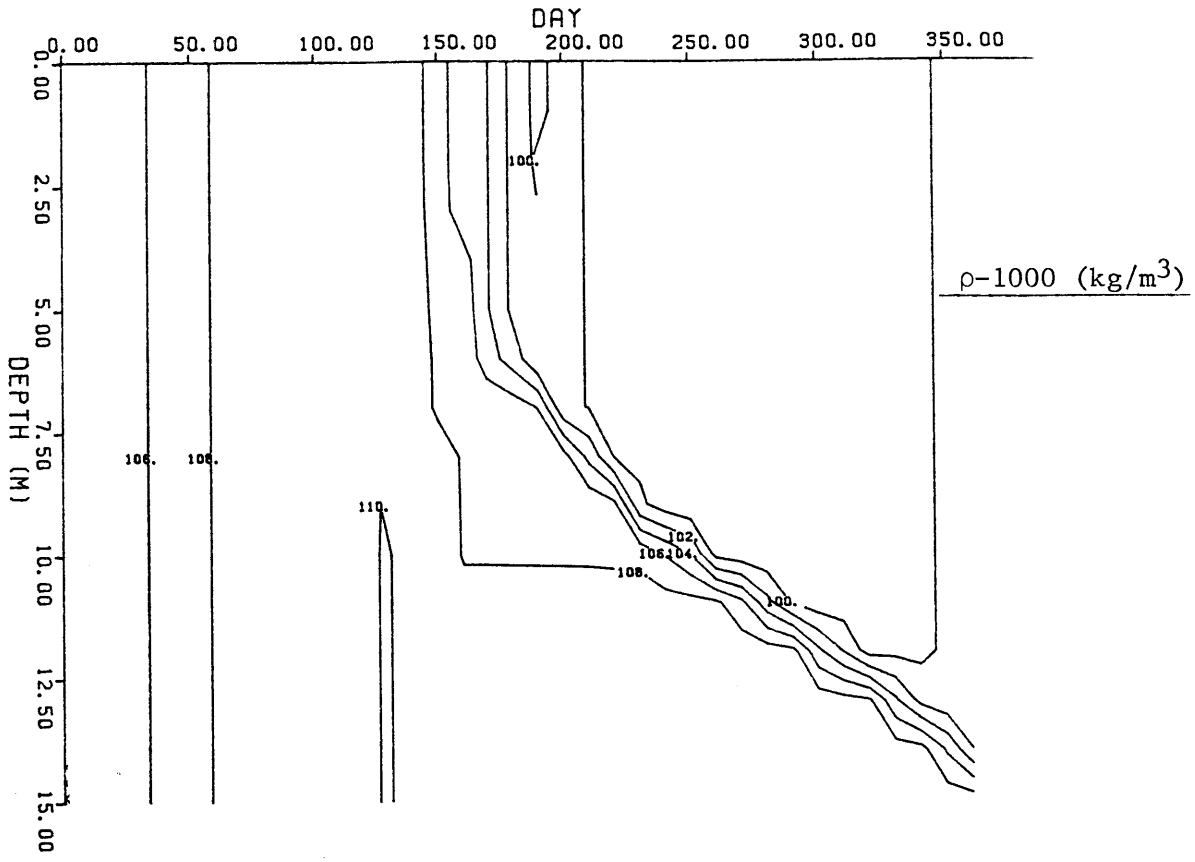

Fig. 10.15(c) Density Isopleths for Year 10 with the Power Project in Operation.

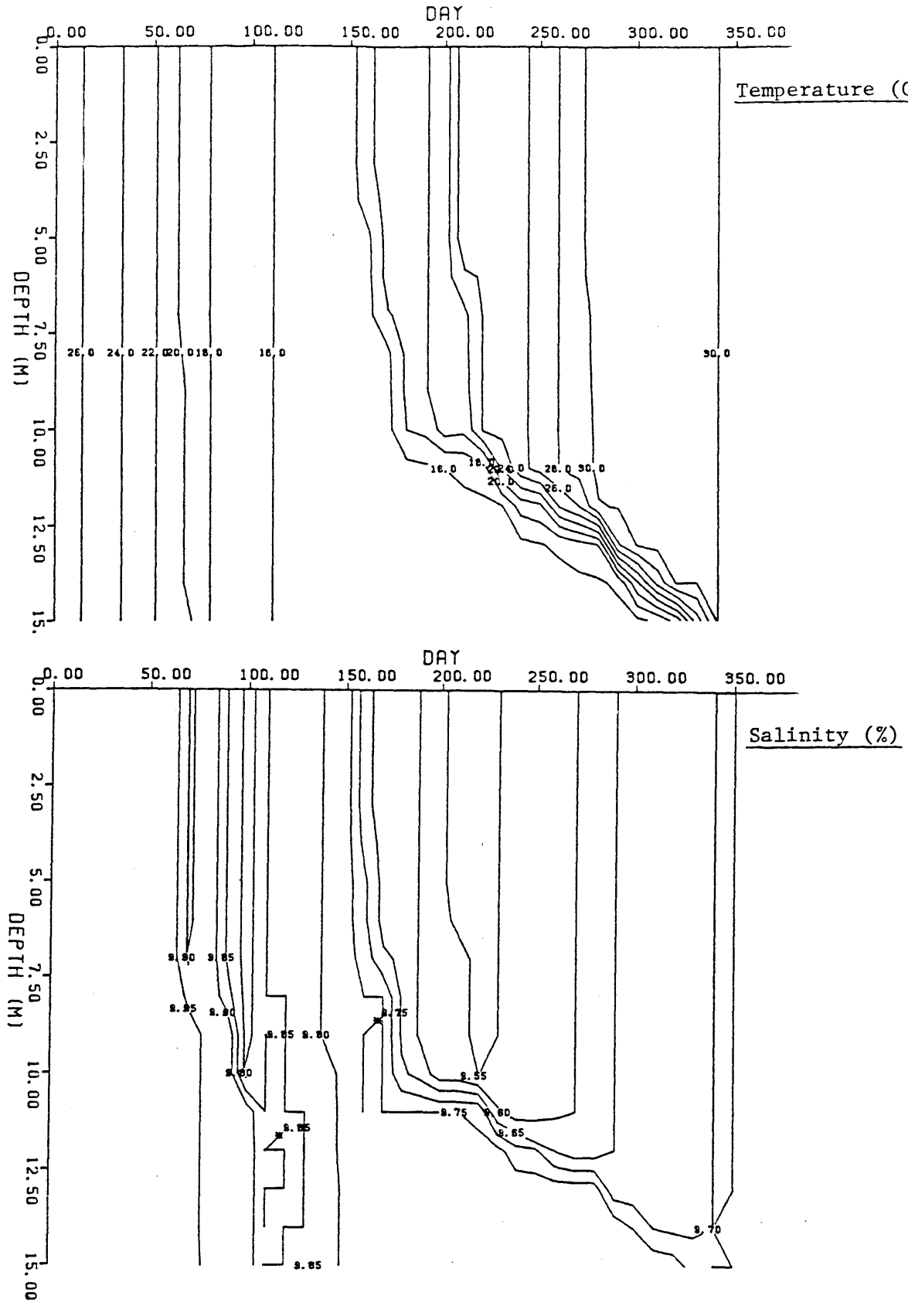

Fig. 10.16(a) Temperature and (b) Salinity Isopleths for Year 20 with The Power Project in Operation.

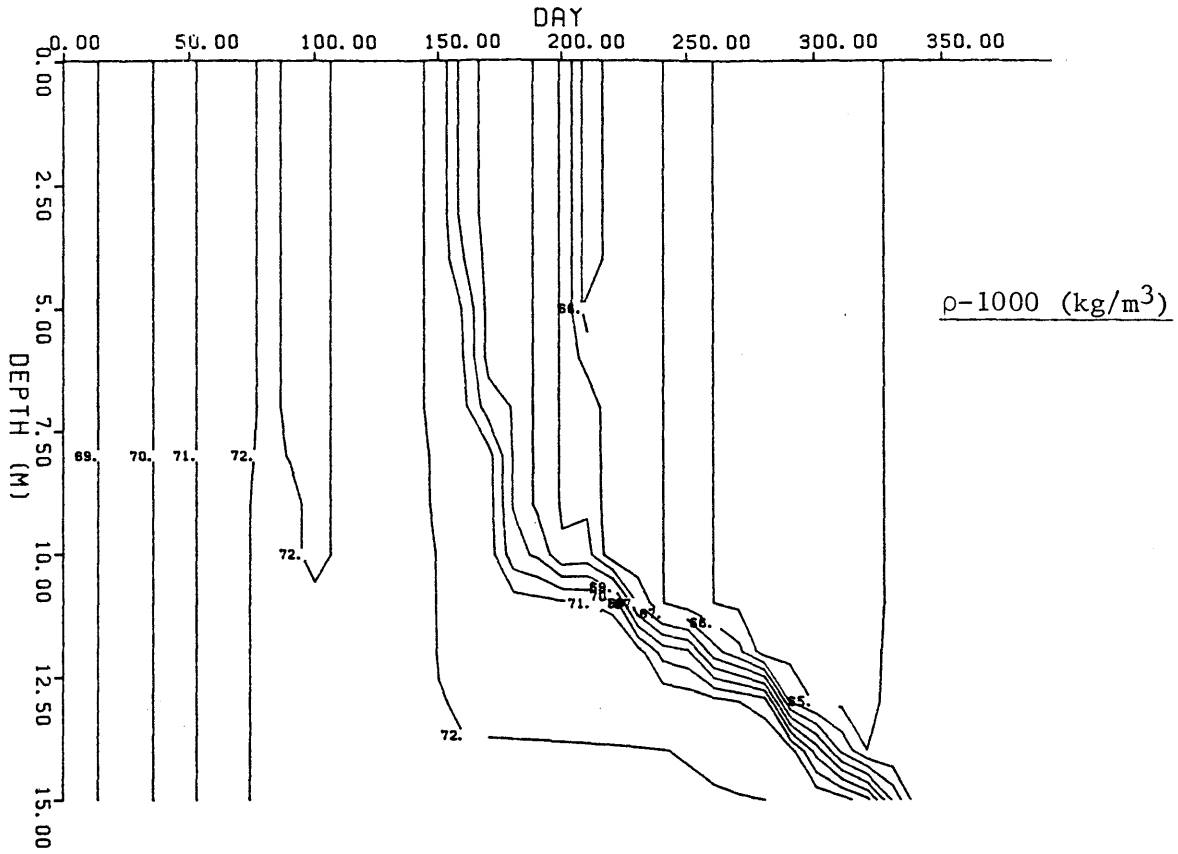

Fig. 10.16(c) Density Isopleths for Year 20 with The Power Project in Operation.

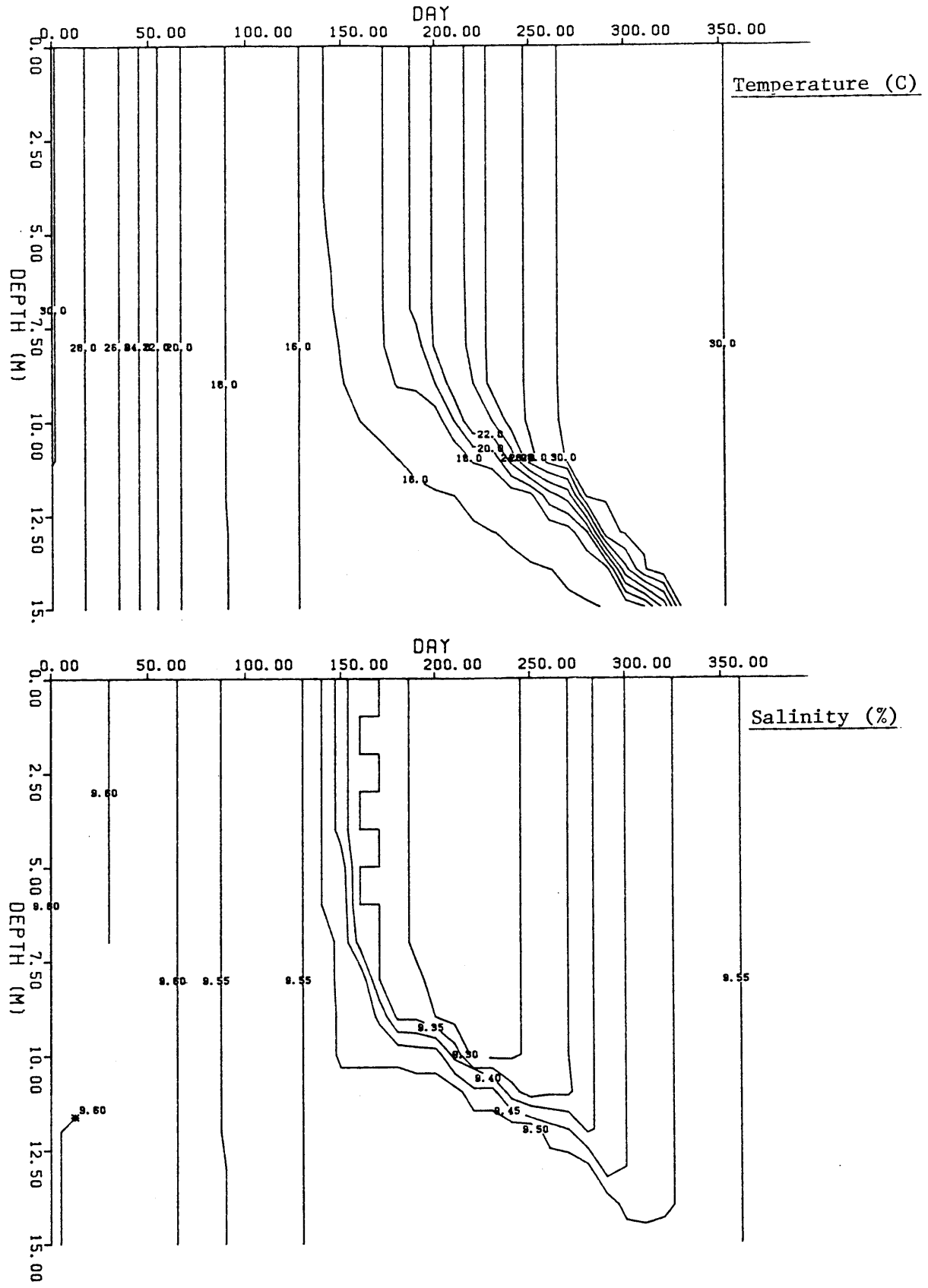

Fig. 10.17(a) Temperature and (b) Salinity Isopleths for Year 30 with The Power Project in Operation.

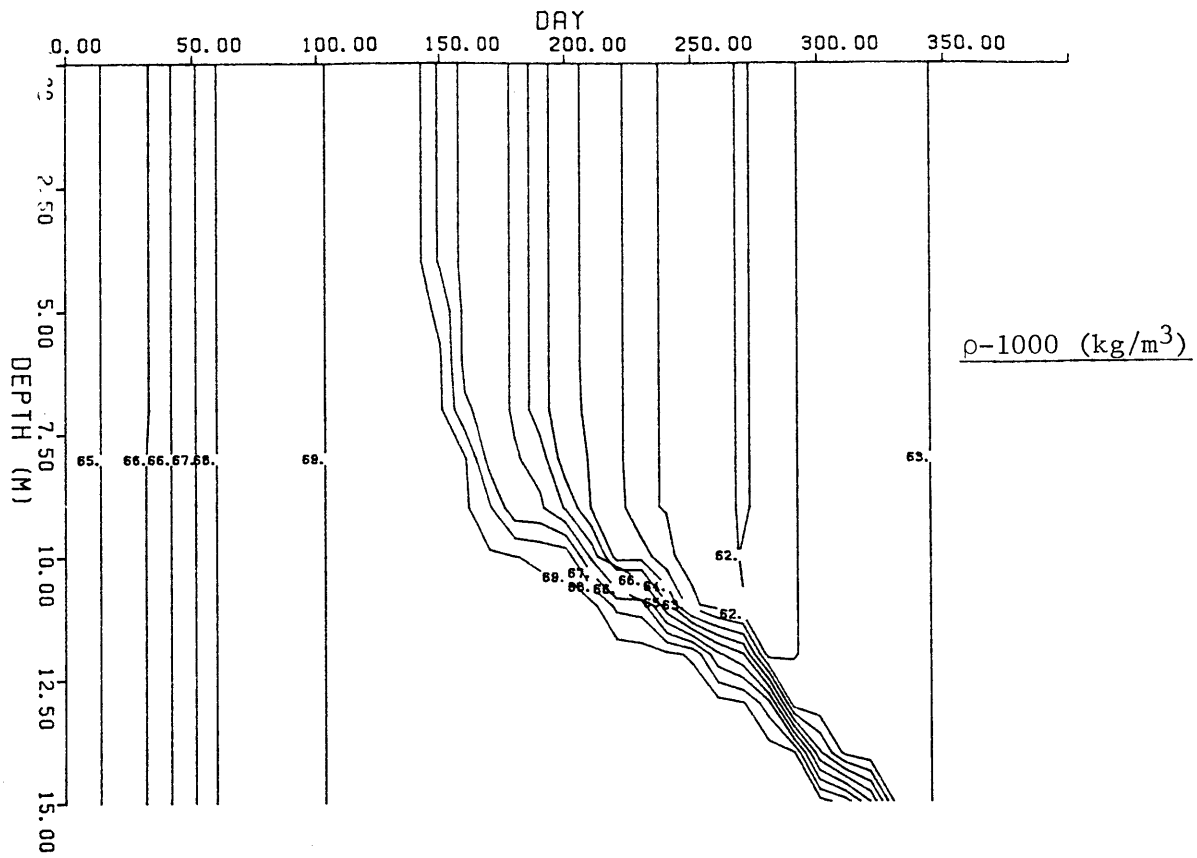

Fig. 10.17(c) Density Isopleths for Year 30 with The Power Project in OPeration.

the salt works pump brine from below this depth in order to extract "pure" Dead Sea water.

The annual mean Richardson number based on the velocity scale σ are of the order of 10^4. At such high Richardson numbers, the assumptions made in the development of the mixing algorithm, Chapter 7 are valid.

Finally, it is worth noting that the predicted stratification pattern is very similar to the stratification that existed prior to the 1979 historic overturn. Limited data available since the early part of this century (Steinhorn et. al. 1985) indicates the existence of a stable meromictic structure in the Northern Basin with a sharp pycnocline at about 40 m below the lake surface. As discussed in Chapter 2, this structure was destroyed by a reduction in fresh water inflows from the Jordan River. Thus, with the power project providing a continuous supply of relatively fresh water inflow, the Dead Sea would once again exhibit a stable meromictic structure.

Chapter 11

CONCLUSIONS

The general purpose of this research has been to study a few important physical processes that affect vertical stratification, surface heat and mass transfer in hypersaline lakes. In particular, the study was directed towards understanding the interesting stratification patterns observed in the Dead Sea since the historic overturn in 1979. Apart from the scientific interest that exists in explaining an observed natural phenomena, the study was also motivated by the fact that this knowledge would have some bearing on the design, operation and maintenance of existing and proposed facilities on the Dead Sea. Important conclusions of this study are itemized below:

(i) The effect of salinity and ionic composition on evaporation has been analysed in detail using data from evaporation pans located near the Dead Sea. The commonly used approach to account for the salinity effect based on the ratio of salt water to fresh water evaporation rates is difficult to use accurately since it is a function of salinity and chemical composition of the solution as well as the meteorology. A more accurate method that directly accounts for the effect of salinity on the saturation vapor pressure has been discussed. It has been shown that for solutions involving more than one salt this effect can be analytically computed based on weighted average of the effect of salinity for single solutions. Further, the negative feedback effect of temperature on evaporation from saline water has been quantified.

(ii) A number of commonly used long wave radiation formulae have been used to analyze the atmospheric long wave radiation data collected near the Dead Sea. Results indicate the site-specific nature of the coefficients contained in these formulae. A few formulae have been calibrated and verified using the Dead Sea data. Further, the importance of using cloud cover correction in calculating atmospheric radiation is shown.

(iii) A time-varying, one-dimensional (vertical) mathematical model was developed for a water body in which the density stratification is influenced by temperature and salinity gradients. This mixed-layer model consists of coupled heat, salt and water budgets as well as a mixing algorithm based on the turbulent kinetic energy budget. The mixing algorithm has only two calibration coefficients: one associated with wind mixing and the other with penetrative convection. These coefficients have been calibrated and verified using temperature and salinity data from the Dead Sea. Application of the model has indicated the dominance of these two mixing mechanisms at different periods in the year. On an annual level, wind mixing energy is significantly larger than the penetrative convective mixing energy.

(iv) The stability index budget approach to compute the magnitude of mixing energy directly from the measured profiles has been discussed. In this respect the importance of the sequence of physical processes in lake stratification has been indicated. Without knowing this sequence, the above method cannot be used to compute mixing energies and is hence of limited applicability.

(v) The model has been used to predict the Dead Sea surface elevation, annual evaporation and vertical stratification with the Mediterranean Dead Sea Project in operation. With the proposed inflows of 53 m^3/s for the first twenty two years of the project life, followed by reduced inflows of about 40 m^3/s, the Dead Sea is expected to reach a steady state level of 391 mbsl in about 30 years. This is based on projected estimates of fresh water inflows from the Jordan at 530 MCM and extractions by the salt works at 230 MCM, both of which significantly affect the lake elevation. The results indicate that the Mediterranean inflows would mix to a depth of about 15 m below the surface. The salt works can thus continue to pump "pure" Dead Sea brine rich in potassium and magnesium salts from below this depth, at a small additional pumping cost.

APPENDIX A

Description of Subroutines and Their Interactions

A.1 Introduction

The mathematical equations and the boundary conditions for the Dead Sea model have been discussed in Chapter 3. Chapter 5 and 6 gave further details of the boundary conditions while Chapter 7 discussed the mixing algorithm. This section gives further details and logic of the computer program. An effort was made to retain as close a similarity as possible to MITSOL (Ref. 20) that provided the general framework for this model.

A.2 Model Logic

At the beginning of any simulation input data is read by the main program (MDEAD). Data consists of values of calibration coefficients, bottom temperature and salinity, initial depth and number of vertical grids, grid size, initial and final temperature and salinity profiles (the latter for comparison with model results) as well as the length of simulation (days). Meteorological data including air temperature, wind speed and humidity as well as short wave radiation, cloud cover and albedo values are read in. Atmospheric long wave radiation may either be read in or computed using the meteorological data. For the case of model calibration and verification, lake elevations are read in, while for the case of future simulations, inflows constitute the input data. In both cases, the volume of daily pumpage for the salt works is an input. For situations when the input data has a lower spatial and temporal

resolution than the time and grid size of the model, subroutines VINT1 and VINT2 can be invoked for interpolation. The area of the lake at different elevations can either be read in or expressed in an analytical form. Having read all the data, the model enters the simulation loop.

Subroutine DRAG is called to compute the drag coefficient, the wind speed at two meters height and the surface shear stress.

Subroutine FLXOUT computes the various flux terms including the evaporative heat flux term using the β-method described in Chapter 6. Note these fluxes are based on the correct meteorological data but the previous days water surface temperature. These fluxes are corrected later in the simulation.

The value of the evaporative heat flux term is passed on to subroutine WTRB that computes the water balance for each time step. For the case of model simulation and verification, inflows to the lake are computed based on elevation, pumpage and computed evaporative mass influx. These inflows are then mixed with the surface layer/grid whose thickness can vary from 0.75 m to 1.25 m. The new value of the surface temperature and salinity are passed to the main program along with the thickness of the surface layer and any change in the number of grids.

For the case when the model is used for future simulations, inflows and pumpage are inputs. The lake elevation is then computed based on this data and evaporative flux calculated by FLXOUT.

Following this, MDEAD computes the new temperature and salinity profile based on the surface flux terms, the penetration of short wave radiation and molecular diffusion of heat and salt. The main program also computes the expansion/contraction due to changes in temperature and

salinity and adjusts the thickness of the surface layer and lake level accordingly. This effect is insignificant in the overall water balance of the lake, however, it is necessary for the accurate computation of the potential energies as discussed subsequently. The profile thus computed may be gravitationally unstable. This is checked by the subroutine AVER that performs gravitational mixing and results in a stable profile. This reduces the potential energy of the water column, (but preserves mass, salt and thermal energy), which is also recorded for use in subroutine MIX.

The profile is then subjected to the mixing algorithm by a call to subroutine MIX. This computes entrainment into the epilimnion based on the turbulent kinetic energy budget and results in a deepening of the epilimnion and a change in surface temperature and salinity. As such the surface flux terms, computed at the beginning of the simulation loop, would no longer be compatible with the new surface temperature and salinity values. This effect is corrected by including an iterative loop within each simulation. In this loop, the subroutines FLXOUT, AVER and MIX are called a number of times until the final surface temperature is within 0.01 °C of the value used to compute the surface flux terms. The final profile may now be printed, the elapsed time incremented by one step and the simulation loop repeated.

In addition to the above, the algorithm includes a number of "service" subroutines that are useful for diagnostic purposes as well as to output additional relevant information. For example, the subroutine POTEN can be called at any point in the program to write the current mass, salt, thermal energy, potential energy and stability index of the

profile. This subroutine was very useful in the initial development of the model when it was felt necessary to check that each of the subroutines conserved mass and salt. It is also used to compute the change in potential energy due to gravitational mixing and hence to compute the magnitude of penetrative convection.

The subroutine FMEAN keeps track of various variables and computes their mean values. These variables include surface temperature and salinity, meteorological variables, heat flux terms, water balance terms, mechanical energy values, depth of mixed layers as well as the value of the Richardson number. These variables at every time step can be written in an output file and plotted if necessary for detailed analysis of the simulation.

Finally, the subroutine FLAG can be used to output a set of specified variables at any point in the program. This subroutine is indispensable for any diagnostic analysis.

APPENDIX B

Functional Relationships for the Dead Sea

1) Equation of State (Ref. 123)

$$\rho(S,T) = 1.2318\ [1-3.4\cdot10^{-4}(T-25) + 7.4\cdot10^{-4}(S-276)]$$

where, ρ=density (kg/m^3), T=temperature (°C) and S=Salinity (°/oo)

$$\alpha_T = \frac{1}{\rho}\frac{\partial\rho}{\partial T} = -3.4\cdot10^{-4};\quad \beta_S = \frac{1}{\rho}\frac{\partial\rho}{\partial S} = 7.4\cdot10^{-4}$$

2) Thermal Heat Capacity (Ref. 144)

$$C_p = 1 - .00072 \times S$$

where, C_p = heat capacity (KCal/kg - °C)

3) Thermal Diffusion Coefficient (Ref. 144)

$$k_T = .0168 + .00002963 \times T$$

where, k_T = thermal diffusion coefficient (m^2/day)

4) Salt Diffusion Coefficient (Ref. 144)

$$k_S = .0001201 \times [1 + .029 \times (T - 20)]$$

where, k_S = salt diffusion coefficient (m^2/day)

5) Latent Heat of Vaporization L (Ref. 144)

$$L = 597.3 - 0.56 \times T$$

L = latent heat of vaporization (KCal/kg)

6) Elevation - Area Relationship (Northern Basin only) (Ref. 134)

$$A = 6.5967\ \exp[0.03592\ (500 + z)] + 514.9$$

where, A = Area (km^2) and z = elevation above mean sea level (m). Note z is negative.

APPENDIX C

The Turbulent Kinetic Energy Equation

C.1 Integration of the TKE Equation

The turbulent kinetic energy for a differential volume assuming horizontal homogeniety of mean quantities can be expressed as (eq. 7.6)

$$\frac{\partial \bar{q}}{\partial t} = -\frac{\partial}{\partial z}\overline{w'\left(\frac{p'}{\rho_o} + q\right)} - \overline{u'w'}\frac{\partial \bar{u}}{\partial z} - \frac{g\overline{\rho'w'}}{\rho_o} - \varepsilon \qquad (C.1)$$

where, the bar represents temporal averaging. u' and w' are turbulent fluctuations in the horizontal (x) and vertical (z) direction, $\bar{u}$ is a horizontal velocity scale associated with the mean flow of the hypolimnion, $\bar{q}$ is the turbulent kinetic energy per unit mass, p' and ρ' are turbulent fluctuations of pressure and density, ρ_o is a reference density and ε represents viscous dissipation within the control volume.

In eq. C.1, the first term represents the storage term, the second term the flux divergence term, the third term shear production term; the fourth term represents potential energy or work done during entrainment and the last term represents energy loss due to viscous dissipation. Eq. C.1 can be integrated over the mixed layer depth (extending from the surface z=0 to z=h), to obtain the bulk mechanical energy balance shown in Eq. 7.7. This integration is shown below.

Temporal Storage Term

$$\int_o^h \frac{\partial \bar{q}}{\partial t}\, dz = \frac{\partial}{\partial t} \bar{\bar{q}}\, h - \frac{\partial h}{\partial t}\, \bar{q}\Big|_{z=h} \qquad (C.2)$$

where, the second bar on q represents average over the mixed layer. The first term on the right hand side of eq. C.2 is zero assuming stationary conditions. The second term is expressed as Λ_T in eq. 7.7.

Flux Divergence Term

$$\int_o^h \frac{\partial}{\partial z} w'\left(\frac{p'}{\rho_o} + q\right) dz = w'\left(\frac{p'}{\rho_o} + q\right)\Big|_{h=z} - w'\left(\frac{p'}{\rho_o} + q\right)\Big|_{z=0} \qquad (C.3)$$

The first term in the right hand side of eq. C.3 represents the source of energy due to wind stirring and penetrative convection. The second term represents pressure fluctuations at the interface and the generation of internal waves. These waves propagate energy into the hypolimnion and hence reduce the energy available for entrainment. In eq. 7.7, these two terms are represented as Λ_K and Λ_L respectively. The parameterization of these terms is discussed in detail in Chapter 7.

The Mechanical Production Term

The parameterization of the mechanical production term is discussed in Section 7.3.3. In eq. 7. this term is expressed as Λ_S, i.e.,

$$\int_o^h \left(\overline{u'w'}\, \frac{\partial \bar{u}}{\partial z}\right) dz = \Lambda_S \qquad (C.4)$$

The Buoyancy Term

Integration of the buoyancy term, results in the change in potential energy due to entrainment represented by:

$$\int_o^h \frac{g\,\overline{\rho' w'}}{\rho}\,dz = \frac{d(PE)}{dt} \qquad (C.5)$$

The Viscous Dissipation Term

The viscous dissipation term, ε, following an energy cascade argument can be expressed as

$$\varepsilon \sim u^3/\ell \qquad (C.6)$$

where, u is a velocity scale and ℓ is a representative length scale of the turbulent eddies. Integration of this term yields a bulk measure of the energy dissipated in the hyplimnion due to viscous dissipation, i.e.,

$$\int_o^h \varepsilon\,dz = \Lambda_D \qquad (C.7)$$

Integral Mechanical Energy Equation

Combining eqs. C.2 to C.7, the integral mechanical energy budget for the upper mixed layer can be expressed (same as eq. 7.7):

$$\frac{d(PE)}{dt} = \Lambda_K + \Lambda_S - \Lambda_T - \Lambda_L - \Lambda_D \qquad (C.8)$$

C.2 Comparison of Energy Due to Shear Production and Wind Stirring

This section compares the energy available for entrainment due to wind stirring with the energy available due to shear production at the

interface. The energy available due to wind can be expressed as:

$$KE_w = C_w \rho u^3_{*,w} A \, dt \tag{C.9}$$

Similarly, the energy available due to shear production (eq. 7.24) is:

$$KE_S = C_s \rho \bar{u}^2 u_e A \tag{C.10}$$

An estimate of the entrainment velocity u_e can be obtained by equating the energy available due to wind stirring with the increase in potential energy due to entrainment:

$$\Delta PE = g \Delta \rho \, dh \frac{h}{2} A \tag{C.11}$$

or

$$u_e = \frac{C_w \rho u^3_{*,w}}{g \Delta \rho dh \frac{h}{2}} \tag{C.12}$$

Substituting eq. C.12 in eq. C.10 and taking the ratio of energy due to shear production with energy due to wind stirring,

$$\frac{KE_s}{KE_w} = \frac{C_s m^2}{R_i} \tag{C.13}$$

where, R_i = the Richardson number defined as $\frac{g \Delta \rho h}{u^2_{*,w}}$ and

$$m = \bar{u}/u_{*,w} \tag{C.14}$$

Using the value of m = 3.5 suggested by Csanady (1978), and with C_w of O(1)

$$\frac{KE_S}{KE_W} = \frac{O(10)}{R_i} \qquad (C.15)$$

Eq. C.15 implies that shear production is important with respect to wind stirring at low Richardson numbers only.

APPENDIX D

The Effect of Salt Water on the Dead Sea

D.1 The Dead Sea Potash Works (Israel)

The Dead Sea Potash Works (Israel), established in 1930, use the process of selective precipitation to harvest potash (potassium chloride), and more recently, bromine. During the period from March to November (until December during dry winters) Dead Sea brine is pumped and allowed to flow through a series of shallow, diked evaporation ponds in each of which different salts precipitate. Gypsum precipitates first followed by sodium chloride. These salts are of relatively less commercial value and are not harvested. Therefore, the dikes of these ponds need to be raised periodically to compensate for the rising bottom, approximately 0.28 m/year, due to salt precipitation. In the downstream evaporation ponds, carnallite ($KCl \cdot MgCl_2 \cdot 6H_2O$) together with some adhering sodium chloride precipitates when the brine density reaches 1330 kg/m^3. The carnallite is periodically slurried and pumped to the processing plant where it is broken down into its components to obtain potash of 97% purity. Small amounts are refined to 99.9%. After the precipitation of carnallite the brine is treated with chlorine to recover bromine. Finally, the remaining brine with a density of 1330 kg/m^3 is returned to the Dead Sea.

D.1.1 Brine Extraction

Table D.1 gives the monthly percentages and the annual volume of brine pumped from the Dead Sea for the years 1977 to 1982. This data was supplied by the Mediterranean Dead Sea Co. (1984). The volume of annual pumpage for the years 1970 to 1982 is plotted in Figure D.1. The data does not show any systematic trends. However, the Dead Sea Salt Works plan to increase their production in the future using dye in the ponds to enhance evaporation, which would clearly increase the annual pumpage.

Figure D.2 shows the monthly percentage extraction for the years 1979-1982. The monthly percentage is varied from year to year probably in response to meteorological conditions that affect evaporation and hence salt production. Generally towards the end of summer, (October and November) the rate of pumping is increased. This is to derive maximum benefit from the preceding high summer evaporation in the Dead Sea. Thus, at the beginning of the winter flood season, the evaporation ponds are filled with brine concentrated by the summer evaporation. No brine is pumped during the winter flood seasons (until March or April), i.e., during the period when the Dead Sea surface brines are least concentrated.

The return flows are estimated as 1/2.3 of the pumped volume and lagged by a period of one month. (Personal Communication, Mediterranean-Dead Sea Co., 1984) Thus, the volume of return flow in July, for example, is 1/2.3 the volume pumped from the Dead Sea in June. Note the density of the return flow is 1330 kg/m^3 while the density of the brine pumped from the surface layers of the Dead Sea is known from measurements

Table D.1

Dead Sea Water Pumped by Dead Sea Works (Israel)

Year	Total (MCM)	% of Total									
		Mar	Apr	May	June	July	Aug	Sept	Oct	Nov	Dec
1977	242.6	4.8	9.2	8.7	12.4	11.7	9.2	9.0	16.0	18.2	
1978	237.7		5.9	12.1	17.3	12.5	17.4	14.0	10.9	9.8	
1979	208.1	0.7	8.0	9.03	14.6	15.1	17.7	10.7	20.5	8.5	14.1
1980	245.6		2.5	10.4	10.1	12.2	14.0	13.1	6.2	17.3	14.1
1981	163.8			8.2	15.0	11.1	11.4	6.6	23.0	22.0	2.5
1982	214.5	1.5	14.3	11.9	16.8	11.6	13.0	9.5	6.2	7.6	6.2

Annual Pumping for 1970 to 1976

Year	1970	1971	1972	1973	1974	1975	1976
Total MCM	186.7	225.5	206.3	254.2	228.8	211.9	183.6

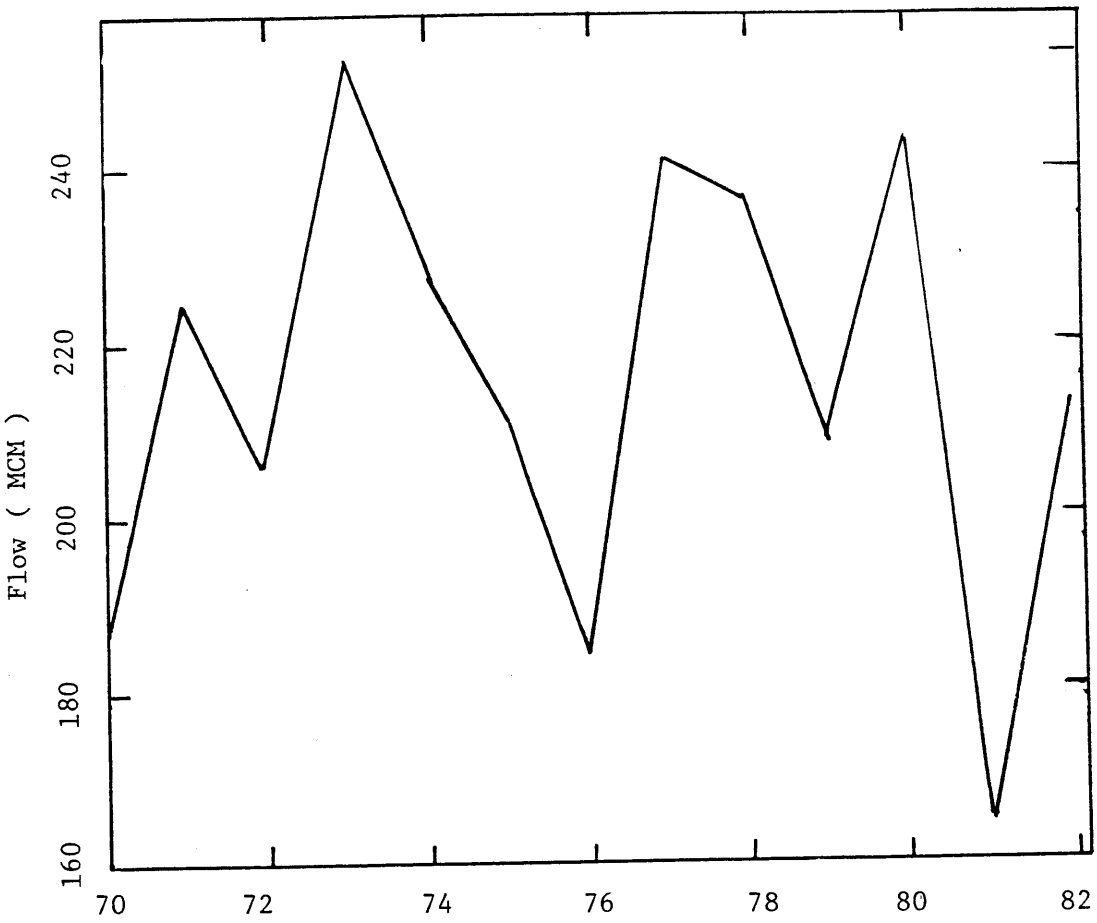

Fig. D.1 Annual Extraction (1970 to 1982) of Dead Sea Brine by the Dead Sea Works, ISrael

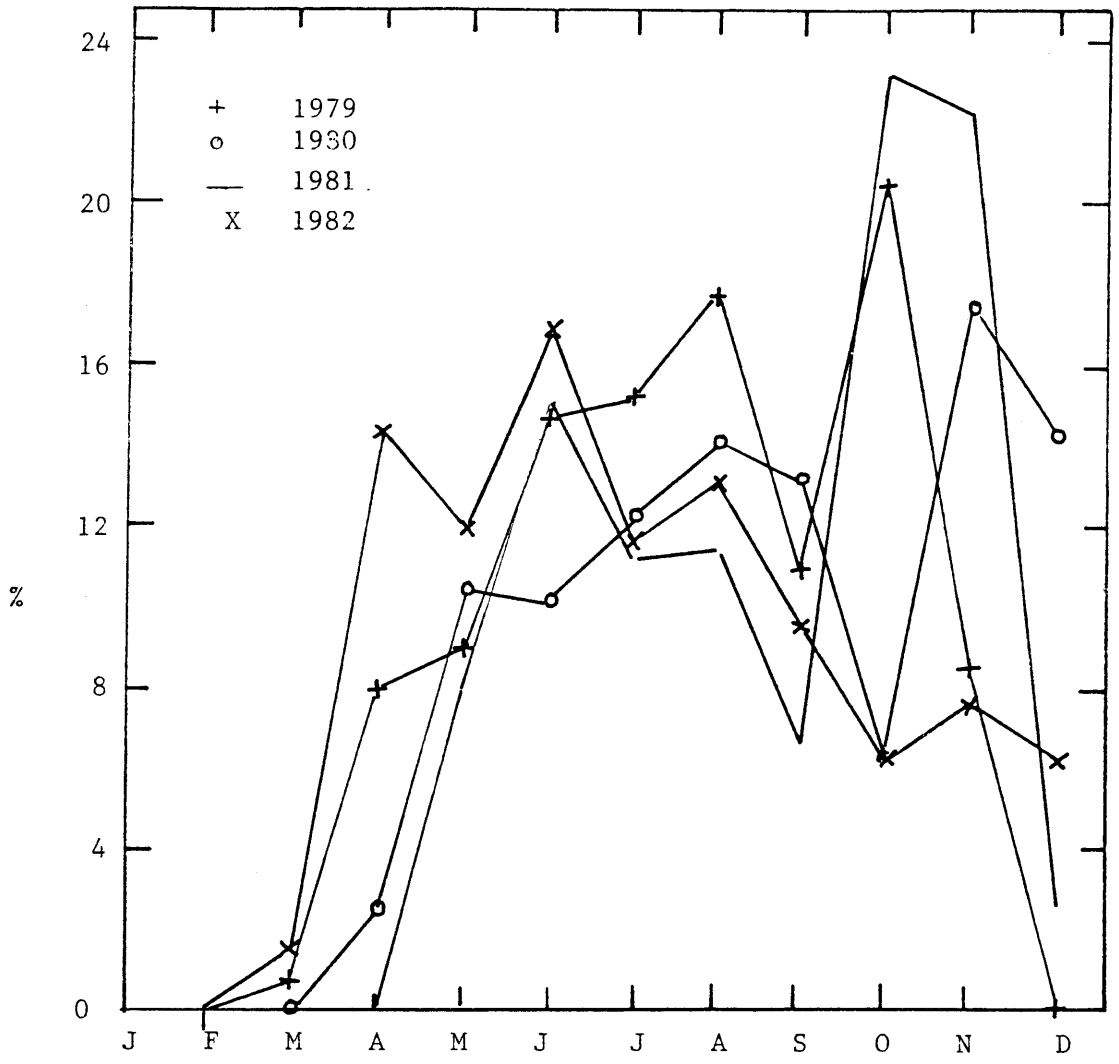

Fig. D.2 Monthly % Extraction of Dead Sea Brine by the Dead Sea Works, Israel

of the vertical profiles. Using the above information, Table D.2 has been derived to show the volume and weight of monthly pumpage and return flow.

Table D.3 shows the net volumetric (Q_N) extraction of brine. Using these values and knowing the mean surface area of the Dead Sea for each month, ($\bar{A}_s$) the change in the Dead Sea surface elevation (Δh) can be computed, i.e.,

$$Q_N = Q_P - Q_R \qquad (D.1)$$

$$\Delta h = \frac{Q_N}{\bar{A}_s} \times 100 \qquad (D.2)$$

where Q_p = volume of brine pumped from Dead Sea (MCM), Q_R = volume of return flow (MCM), and Δh is in cm; A_s in km^2. As shown in Table D.3, for the years 1979 to 1982, the annual drop in elevation due to the Dead Sea Salt Works varied from 10 cm in 1981 to a maxiumum of 20 cm in 1980.

D.1.2 Salt Extraction

Based on knowledge of the mass of brine pumped out of the Dead Sea (Table D.1) and its salinity, the total amount of salt pumped (St_P) from the Dead Sea is shown in Table D.4. Part of this salt precipitates in the evaporation ponds and the remainder (St_R), contained in the return flow, finds its way back to the lower mass of the Dead Sea. The salinity of the return flow was computed using the equation of state developed for the Dead Sea (see Appendix B) and assuming that the return flow has a temperature of 30° C. This yielded a value of 386°/oo. The

Table D.2

Volume and Weight of Monthly Pumpage and Return Flow

	1979				1980				1981				1982			
	Pumpage		Return Flow		Pumpage		Return Flow		Pumpage		Return Flow		Pumpage		Return Flow	
	Q_P*	W_P*	Q_R*	W_R*	Q_P	W_P	Q_R	W_R	Q_P	W_P	Q_R	W_R	Q_P	W_P	Q_R	W_R
JAN	-				-						15.1	20.1			1.8	2.4
FEB	-				-											
MAR	1.4	1.7			-								3.3	4.1		
APR	15.9	19.4	0.6	0.8	6.1	7.3							31.1	38.2	1.4	1.9
MAY	17.9	22.0	6.9	9.2	25.6	30.6	2.7	3.6	13.4	16.3			25.9	31.8	13.5	18.0
JUN	29.0	35.7	7.8	10.4	24.8	30.0	11.1	14.8	24.6	29.8	5.8	7.7	36.6	44.9	11.3	15.0
JUL	30.0	36.9	12.6	16.8	30.0	36.3	10.8	14.4	18.2	22.1	10.7	14.2	25.2	30.9	15.9	21.1
AUG	35.1	43.2	13.0	17.3	34.4	42.0	13.0	17.3	18.7	22.7	7.9	10.5	28.3	34.8	11.0	14.6
SEP	21.2	26.1	15.3	20.3	32.2	39.3	15.0	20.0	10.8	13.2	8.1	10.8	20.7	25.5	12.3	16.4
OCT	40.7	50.1	9.2	12.2	15.2	18.5	14.0	18.6	37.7	46.1	4.7	6.3	13.5	16.6	9.0	12.0
NOV	16.9	20.8	17.7	23.5	42.5	51.9	6.6	8.8	36.2	44.3	16.4	21.8	16.5	20.3	5.9	7.9
DEC	-		7.3	9.7	34.8	42.7	18.5	24.6	4.2	5.2	15.7	20.9	13.4	16.5	7.2	9.6
TOTAL	208.1	255.9	90.4	120.2	245.6	298.6	91.7	122.2	163.8	199.7	84.4	112.3	214.5	263.6	89.3	118.9

* Q_P, Q_R MCM

W_P, W_P 10^9 kg

Table D.3

Effect of the Dead Sea Work's Extraction on the Surface Elevation of the Dead Sea

	1979		1980		1981		1982	
	Q_N	Δh_{cm}	Q_N	Δh_{cm}	Q_N	Δh_{cm}	Q_N	Δh_{cm}
JAN					-15.1	-2.01	-1.8	-0.24
FEB								0
MAR	1.4	0.19					3.3	0.44
APR	15.3	2.04	6.1	0.81			29.7	3.96
MAY	11.0	1.47	22.9	3.02	13.4	1.77	12.4	1.66
JUN	21.2	2.83	13.7	1.81	18.8	2.48	25.3	3.38
JULY	17.4	2.32	19.2	2.54	7.5	0.99	9.3	1.24
AUG	22.1	2.96	21.4	2.84	10.8	1.43	17.3	2.32
SEPT	5.9	0.79	17.2	2.29	2.7	0.36	8.4	1.13
OCT	31.5	4.22	1.2	0.16	33.0	4.40	4.5	0.61
NOV	-0.8	-0.11	35.9	4.78	19.8	2.63	10.6	1.42
DEC	-7.3	-0.98	16.3	2.17	-11.5	-1.53	6.2	1.30
TOTAL	117.7	15.73	153.9	20.42	79.4	10.52	125.2	17.22

Table D.4

Loss of Salt from the Dead Sea Due to the Dead Sea Works

	1979			1980			1981			1982		
	St_p *	St_R	St_N	St_p	St_R	St_N	St_p	St_R	St_N	St_p	St_R	St_N
JAN								7.8	-7.8		0.9	-0.9
FEB												
MAR	0.5		0.5							1.1		1.1
APR	5.3	0.3	5.0	1.8		1.8				10.4	0.7	9.7
MAY	6.1	3.6	2.5	7.6	1.4	6.2	4.2		4.2	8.7	6.9	1.8
JUN	10.0	4.0	6.0	7.7	5.7	2.0	7.7	3.0	4.7	12.3	5.8	6.5
JUL	10.3	6.5	3.8	10.9	5.6	5.3	5.8	5.5	0.3	8.5	8.1	0.4
AUG	12.1	6.7	5.4	11.1	6.7	4.4	6.0	4.1	1.9	9.6	5.6	4.0
SEP	7.3	7.8	-0.5	10.4	7.7	2.7	3.5	4.2	-0.7	7.1	6.3	0.8
OCT	13.9	4.7	9.2	5.0	7.2	-2.2	12.4	2.4	10.0	4.6	4.6	0.0
NOV	5.8	9.1	-3.3	13.9	3.4	10.5	12.0	8.4	3.6	5.6	3.0	2.5
DEC		3.7	-3.7	11.4	9.5	1.9	1.4	8.1	-6.7	4.6	3.7	0.9
TOTAL	71.3	46.4	24.9	79.8	47.2	32.6	53.0	43.5	9.5	72.5	45.6	26.8

* 10^9 kg

latter could be in error because the equation of state developed for Dead Sea brine may differ significantly from that of the return flow due to differences in the salinity and chemical compositions. However, until further information is available this is the best approximation. The difference between St_p and St_R represents the loss of salt from the Dead Sea due to the salt works. Part of this salt is exported by the Potash Works and the remainder represents the gypsum and halite that is deposited in the pre-carnallite salt ponds, hence raising the bottom.

The total (gross) salt extracted from the upper water mass of the Dead Sea varies considerably. For the years 1979 to 1982, it varied from a minimum of 53.0×10^9 kg to 71.3×10^9 kg. The total for these four years amounts to 2.76×10^{11} kg that can be extrapolated to a value of 3.5×10^{11}kg for five years. Including the effect of the Arab Salt Works (discussed below) this value compares very well with 4×10^{11} kg estimated based on the vertical profiles (Section 8.3).

D.2 The Arab Potash Works (Jordan)

The Arab Potash Works, located directly opposite (East) of the Israeli Dead Sea Works, commenced salt production around the end of 1982. Information on the construction and operation of these are included in Khasawneh and Khoury (1983), Ballard and Brice (1984), Ashford and Boocock (1984) and a few documents issued by the United Nations. The following is reproduced from one of these reports (UN, 1983):

"The total production of potassium chloride (KCL) has now reached 600,000 tons per annum. The solar evaporation system consists of a 72 square kilometer salt pan which is considered to be the nucleus of all operations of salt precipitation leading to potassium chloride production. To this pan, Dead Sea brines of 1.225 specific gravity are pumped at a rate of 12 cubic metres per second. Sodium chloride is precipitated and the brines are concentrated to a specific gravity of 1.28 before they are transferred to the following stage.

In a second phase, the carnallite salts are harvested in a slurry form. The system includes two precarnallite pans, the areas of which are 11.35 sq. km and 2.50 sq. km and three carnallite pans. The role of precarnallite pans is to raise the specific gravity of the brine to reach 1.295 in the first one and 1.300 in the second. In the carnallite pans the evaporation process is finalized by the precipitation of the carnallite salt ($KCl \cdot MgCl_2 \cdot 6H_2O$). When specific gravity reaches 1.335, harvesting operations start and carnallite in a slurry form is pumped to the refinery. Carnallite pan No. 1 (41.5 sq. km) was ready for harvesting in 1982; carnallite pan No. 2 (5.09 sq. km) was ready in 1983; and carnallite pan No. 3 (6.68 sq. km) will be ready in 1984/85. In a third phase, mesh salts are refined until the final product, potassium chloride, is produced, with a projected output of 900,000 tons in 1985 and full production of 1.2 million tons in 1986.

The Jordanian Government is considering the expansion and doubling of potassium chloride production, after reaching the present goal of 1.2 million ton production from the Safi area in 1986, by constructing an

additional salt pan in the Lisan Peninsula. The Government is also considering the following potassium related projects: optimization of the current capacity, soda ash, magnesium oxide and refractory bricks; bromine and main derivatives, potassium sulphate, compound fertilizers and refined table salt. A contract for the construction of a plant with a production capacity of 30,000 tons of refined salt has been awarded and the work is expected to be completed by the end of 1985. While the feasibility studies concerning the other projects are almost complete, the government intends to update them in the light of recent price changes."

Based on the above information, Table D.5 gives details of the salt and mass balance for the Arab Potash Works. The density and salinity of the water pumped is assumed as 1230 kg/m^3 and 277°/$_{oo}$, respectively. The return flow is 1/2.3 of the volume pumped with a density and salinity of 1330 kg/m^3 and 386°/$_{oo}$, respectively.

D.3 The Combined Effect Of The Two Salt Works

A comparison of values reported in Table D.5 and Table D.3 indicates that the Arab Potash Works are as large as the Israeli Salt Works. The combined effect (after rounding off) of the two salt works on the Dead Sea salt and mass balance is indicated in Table D.6. On an annual level a drop in the Dead Sea elevation of about 0.4 m can be explained by net pumpage by the salt works. An approximate method of computing this effect is as follows:

Table D.5

Data for The Arab Potash Works (Jordan)

	12 month continuous operation	9 month operation
Q_p (MCM)	378.4	283.8
Q_r (MCM)	164.5	123.4
Q_N (MCM)	213.9	160.4
Δh (cm/year)	29.0	21.8
W_p (10^9 kg)	465.4	349.1
W_r (10^9 kg)	218.8	164.1
S_p (10^9 kg)	128.9	96.7
S_r (10^9 kg)	84.5	63.3
S_N (10^9 kg)	44.4	33.4

Table D.6

Annual Effect of the Two Salt Works on The Dead Sea

	Dead Sea Works *	Arab Potash Works 9 month operation	Total
Volume of brine pumped (MCM)	208	280	488
Volume of return Flow (MCM)	90	125	215
Net Consumption (MCM)	118	155	273
Weight of salt pumped (10^9 kg)	70	97	167
Weight of salt returned (10^9 kg)	46	63	109
Net salt consumption (10^9 kg)	24	34	58
Drop in Dead Sea Elevation (cm)	16.0	22	38

* Average of 1979 to 1982

Surface area of Dead Sea $\simeq$ 740 km^2

Surface area of evaporation ponds $\simeq$ 250 km^2

Total area available for evaporation = 990 km^2

Annual evaporation from the Dead Sea $\simeq$ 1.4 m

The water lost by evaporation in the evaporation ponds comes from the Dead Sea so that, equivalent depth of evaporation from Dead Sea

$$= 1.4 \times \frac{990}{740}$$

$$= 1.9 \text{ m}$$

Evaporation from evaporation ponds = (1.9 - 1.5)

$$= 0.4 \text{ m}$$

This estimate is close to 0.39 m obtained above.

APPENDIX E

Additional Model Calibration and Verification Runs

This section presents the results for a few additional model calibration and verification runs. The model results as well as the initial and final profiles are shown in the figures for each period while additional details are included in accompanying tables. The periods considered here are as follows:

Periods with Predominant Wind Mixing

24 May 1982 to 24 July 1982

16 May 1984 to 3 July 1984

Refer to Figs. E.1 (a) to E.2 (b) and Tables E.1 (a) to E.2 (b).

Periods When Penetrative Convective Mixing is Important

28 September 1982 to 1 November 1982

25 August 1983 to 3 October 1983

Refer to Figs. E.3 (a) to E.4 (b) and Tables E.3 (a) to E.4 (b).

An examination of these additional results further supports the conclusions of Chapter 9, i.e., a best fit value of $C_W = 6$ and $C_C = 0.1$. However, given the spatial resolution of the data it is difficult to assess the accuracy of these estimates.

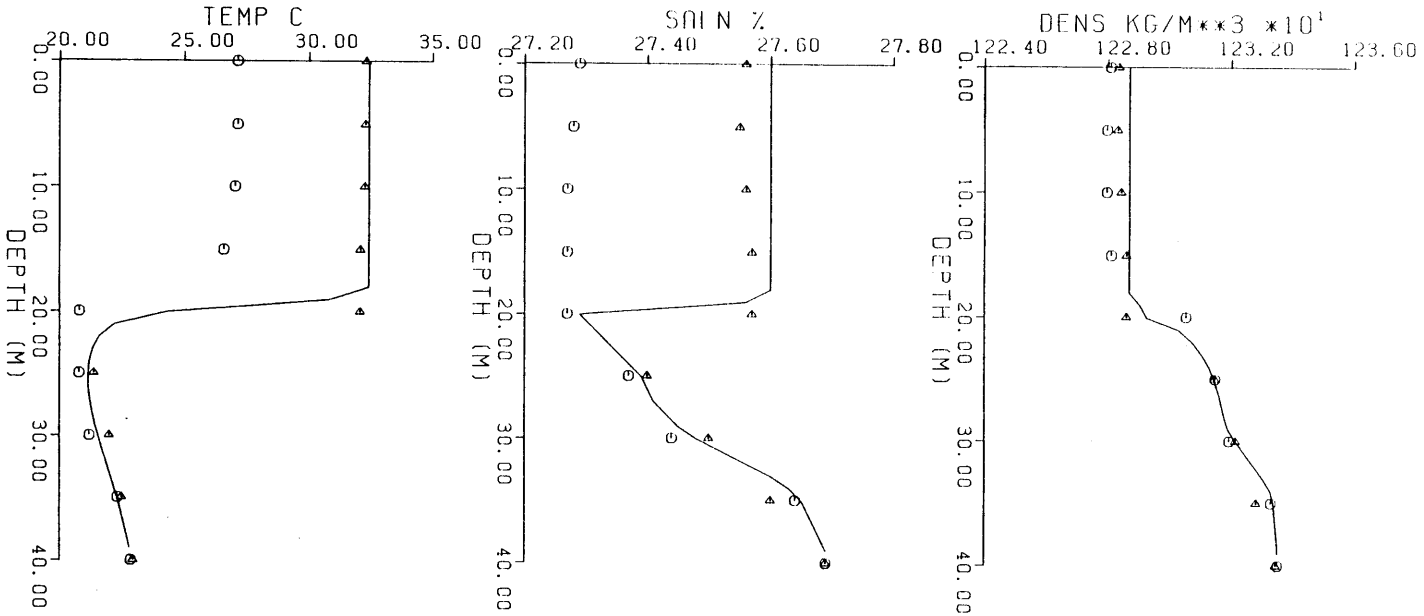

Fig. E.1 (a) Data and Model Results for the Period 24 May 1982 to 24 July 1982 with C_w = 3 and C_c = 0.1

o Initial Data
Δ Final Data
— Model Result

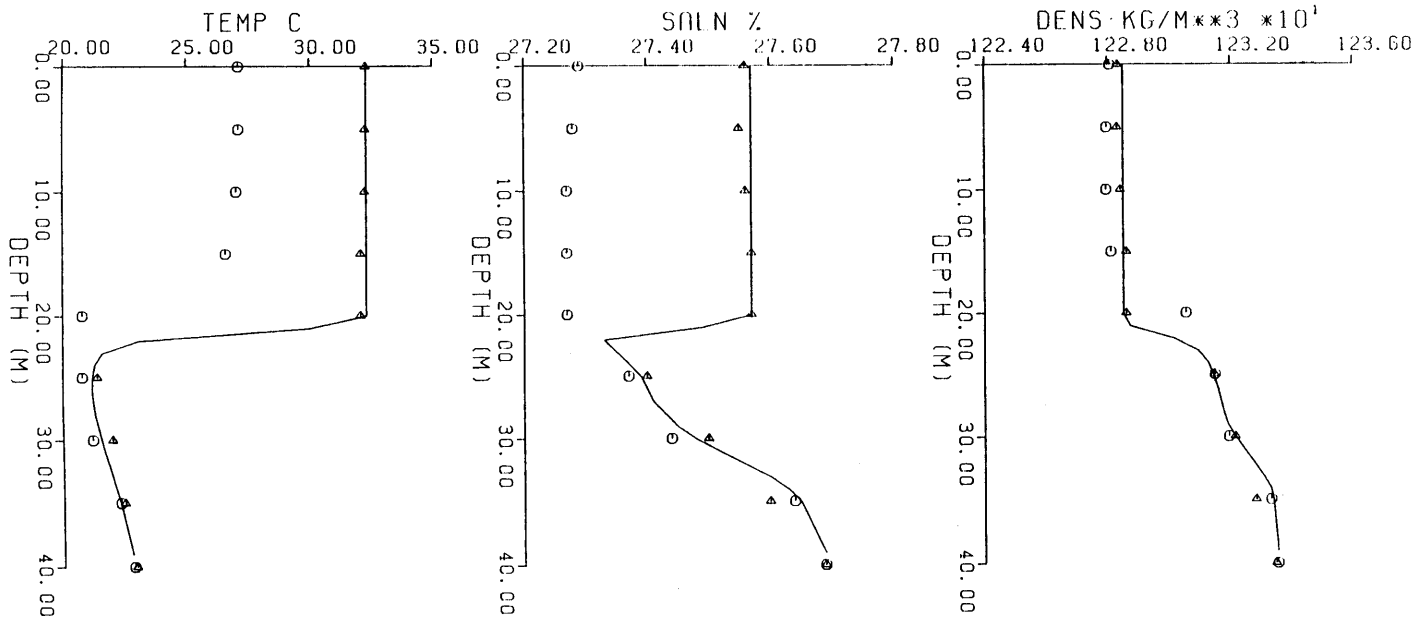

Fig. E.1 (b) Data and Model Results for the Period 24 May 1982 to 24 July 1982 with $C_w = 6$ and $C_c = .1$

o Initial Data
Δ Final Data
— Model Result

Table E.1 (a) Details of model run for the period 24 May 1982 to 24 July 1982

Calibration Coefficients		
C_W	3	6
C_C	0.1	0.1
Error Analysis Maximum Values		
Temperature °C	5.6	2.6
Salinity %	0.2	0.2
Density kg/m^2	0.5	1.0
Root Mean Square Values		
Temperature °C	1.4	0.8
Salinity %	0.1	0.03
Density kg/m^3	0.3	0.3
Mixing Parameters		
$KE_W(J/m^2)$	893	1787
$KE_C(J/m^2)$	94	90
$\overline{u_*}$	.0035	.0035
$\overline{w_*}$	.0028	.0027
$\overline{R_{I_\sigma}}$	300	250
Change in Stability Index	-859	-859
Error in Stability	230	22

Table E.1 (b) Water and heat balances for the period 24 May 1982 to 24 July 1982

Calibration Coefficients		
C_w	3	6
C_c	.1	.1
Water Balance		
Evaporation (mm)	305	291
Pumpage (mm)	23	23
Inflow	47	33
Net Inflow (mm)	-281	-281
Thermal Energy Balance		
Short Wave Radiation ($KCal/m^2/day$)	6280	6280
Atmospheric Radiation ($KCal/m^2/day$)	8370	8370
Back Radiation ($KCal/m^2/day$)	9800	9770
Evaporative Flux ($KCal/m^2/day$)	2890	2750
Net Warming ($KCal/m^2/day$)	1600	1820
Meteorology		
Air Temperature (°C)	30.37	
Humidity (%)	51	
Wind Speed (m/s)	34	

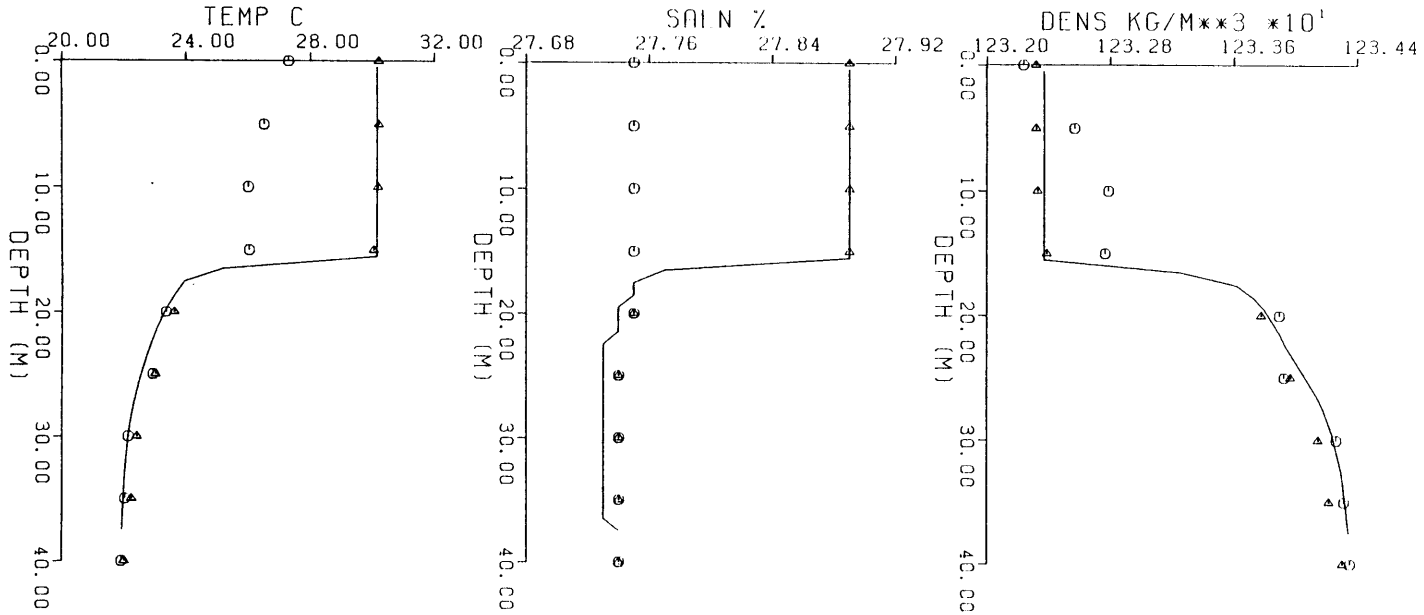

Fig. E.2(a) Data and Model Results for the Period 16 May 1984 to 3 July 1984 with C_w = 3 and C_c = 0.1

o Initial Data
Δ Final Data
— Model Result

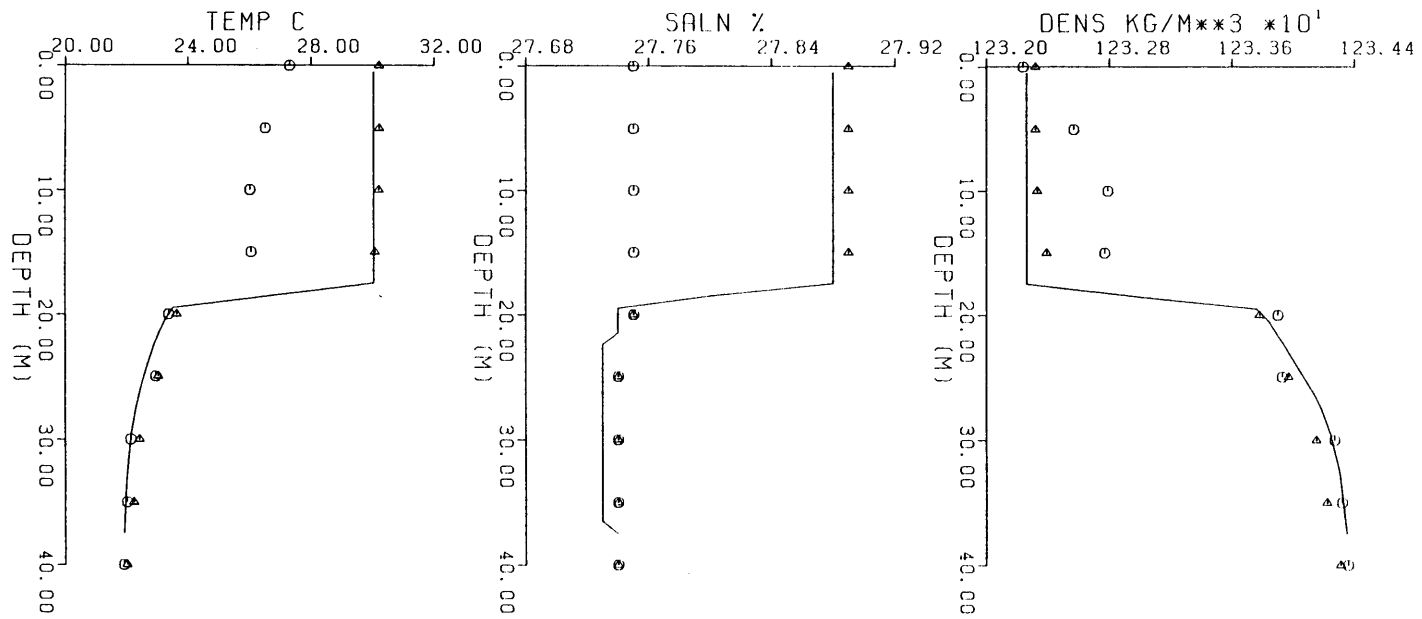

Fig. E.2(b) Data and Model Results for the PEriod 16 May 1984 to 3 July 1984 with $C_w = 6$ and $C_c = 0.1$

o Initial Data
Δ Final Data
— Model Result

Table E.2 (a) Details of model run for the period 16 May 1984 to 3 July 1984

Calibration Coefficients		
C_W	3	6
C_C	0.1	0.1
Error Analysis Maximum Values		
Temperature °C	4.0	6.4
Salinity %	0.1	0.1
Density kg/m^2	0.9	1.5
Root Mean Square Values		
Temperature °C	0.8	1.6
Salinity %	0.0	0.0
Density kg/m^3	0.2	0.4
Mixing Parameters		
$KE_w(J/m^2)$	561	1120
$KE_C(J/m^2)$	43	40
$\overline{u_*}$	.0031	.0031
$\overline{w_*}$	.0020	.0019
$\overline{R}_{I_\sigma}$	200	300
Change in Stability Index	310	310
Error in Stability	-70	-232

Table E.2 (b) Water and heat balance for the period 16 May 1984 to 3 July 1984

Calibration Coefficients		
C_w	3	6
C_c	0.1	0.1
Water Balance		
Evaporation (mm)	289	279
Pumpage (mm)	63	63
Inflow	192	182
Net Inflow (mm)	-160	-160
Thermal Energy Balance		
Short Wave Radiation ($KCal/m^2/day$)	6590	6590
Atmospheric Radiation ($KCal/m^2/day$)	7730	7730
Back Radiation ($KCal/m^2/day$)	9580	9540
Evaporative Flux ($KCal/m^2/day$)	3500	3390
Net Warming ($KCal/m^2/day$)	1150	1352
Meteorology		
Air Temperature (°C)	29.8	
Humidity (%)	36	
Wind Speed (m/s)	3.1	

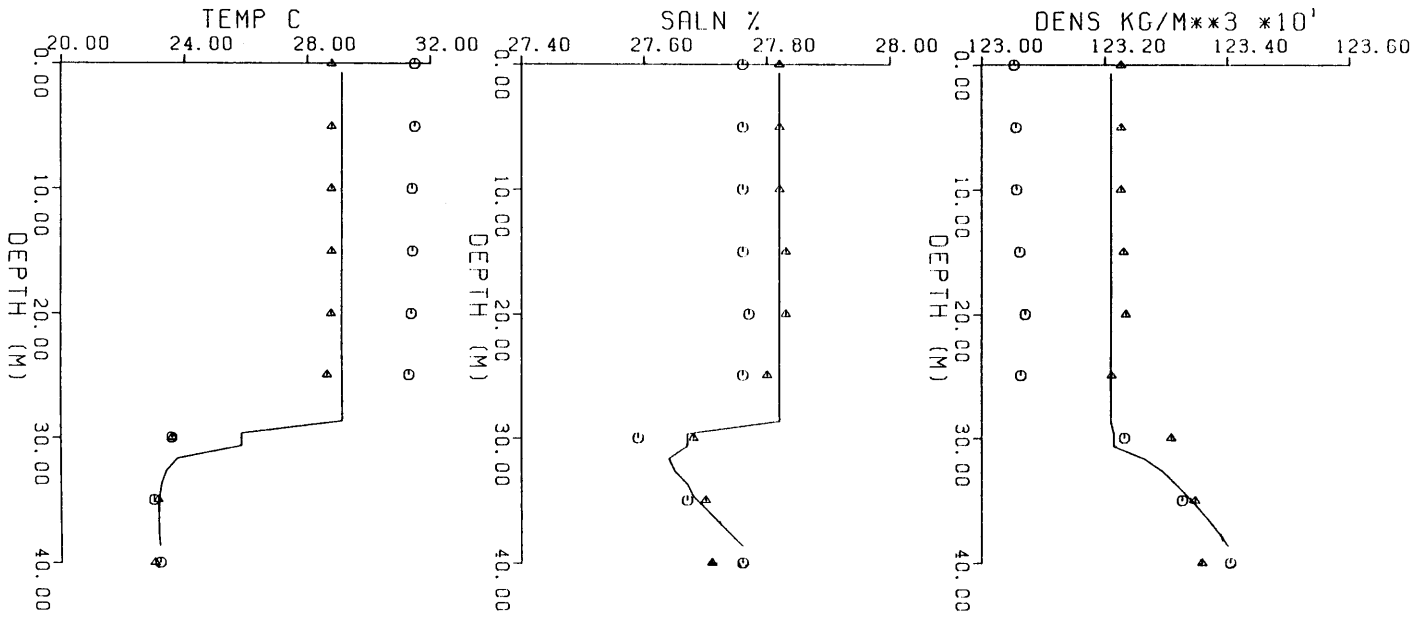

Fig. E.3(a) Data and Model Results for the PEriod 28 September 1982 to 1 November 1982 with $C_w = 6$ and $C_c = 0.0$

o Initial Data
Δ Final Data
— Model Result

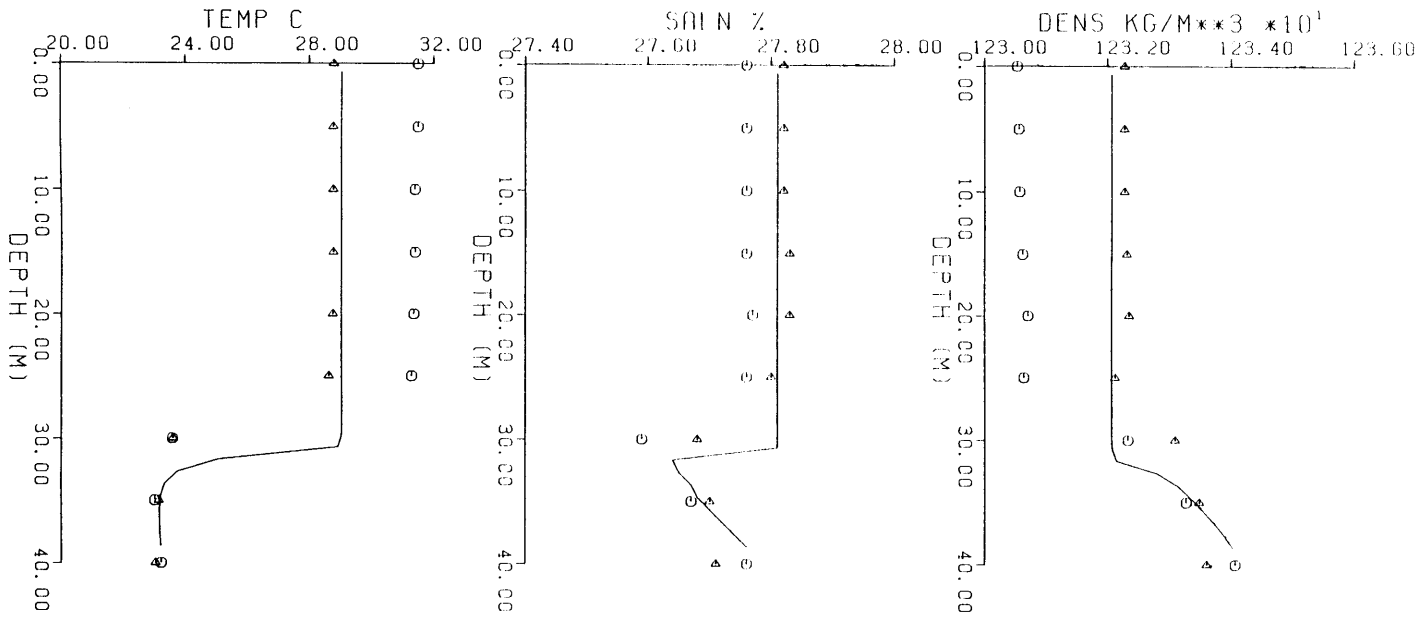

Fig. E.3(b) Data and Model Results for the Period 28 September 1982 to 1 November 1982 with $C_w = 6$ and $C_c = .1$

o Initial Data
Δ Final Data
— Model Result

Table E.3 (a) Details of model run for the period 28 September 1982 to 1 November 1982

Calibration Coefficients		
C_W	6	6
C_C	0	.1
Error Analysis Maximum Values		
Temperature °C	5.5	5.5
Salinity %	0.2	0.1
Density kg/m^2	1.2	1.3
Root Mean Square Values		
Temperature °C	1.9	2.1
Salinity %	0.0	0.1
Density kg/m^3	0.5	0.5
Mixing Parameters		
$KE_W(J/m^2)$	432	432
$KE_C(J/m^2)$	0	388
$\overline{u_*}$	.0027	.00268
$\overline{w_*}$	.0099	.0099
$\overline{R_{I_\sigma}}$	400	690
Change in Stability Index	-2040	-2040
Error in Stability	254	380

Table E.3 (b) Water and heat balance for the period 21 September 1982 to 1 November 1982

Calibration Coefficients		
C_w	6	6
C_c	0	.1
Water Balance		
Evaporation (mm)	166	164
Pumpage (mm)	14	14
Inflow	75	73
Net Inflow (mm)	-105	-106
Thermal Energy Balance		
Short Wave Radiation ($KCal/m^2/day$)	4360	4360
Atmospheric Radiation ($KCal/m^2/day$)	7670	7670
Back Radiation ($KCal/m^2/day$)	9660	9650
Evaporative Flux ($KCal/m^2/day$)	2800	2770
Net Warming ($KCal/m^2/day$)	-900	-860
Meteorology		
Air Temperature (°C)	27.4	
Humidity (%)	48	
Wind Speed (m/s)	2.7	

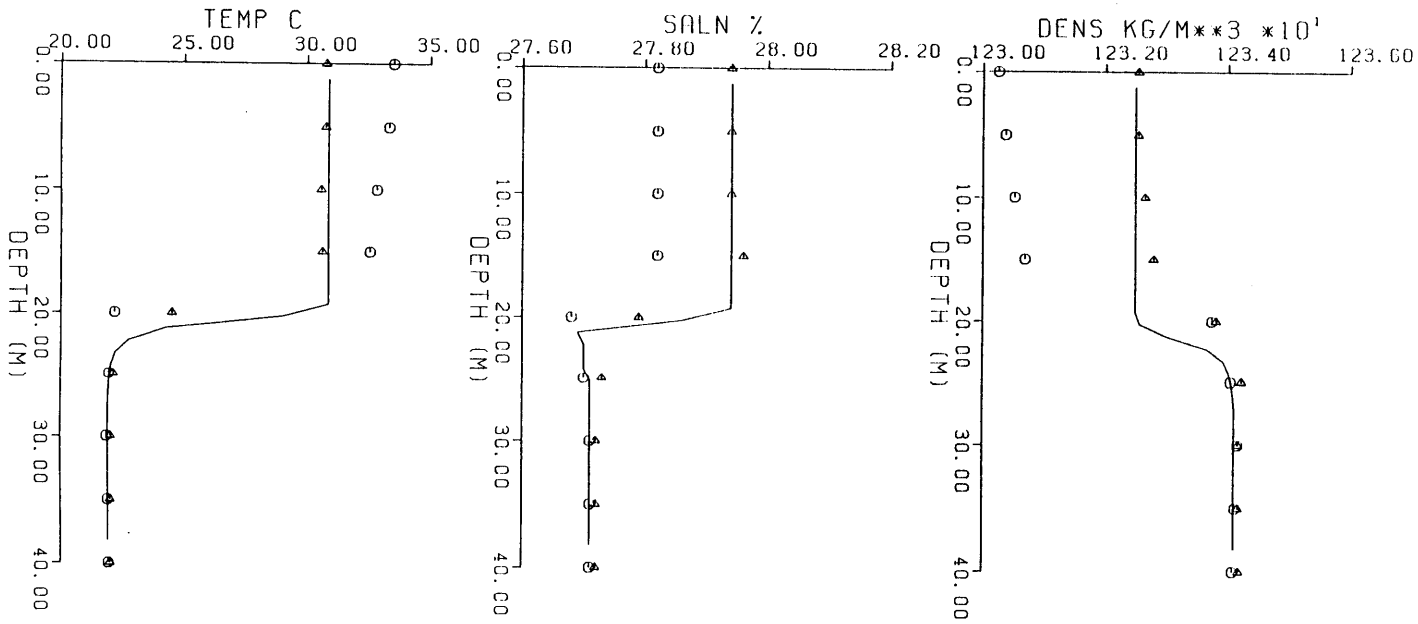

Fig. E.4(a) Data and Model Results for the Period 25 August 1983 to 3 OCtober 1983 with C_w = 6 and C_c = 0.0

o Initial Data
Δ Final Data
— Model Result

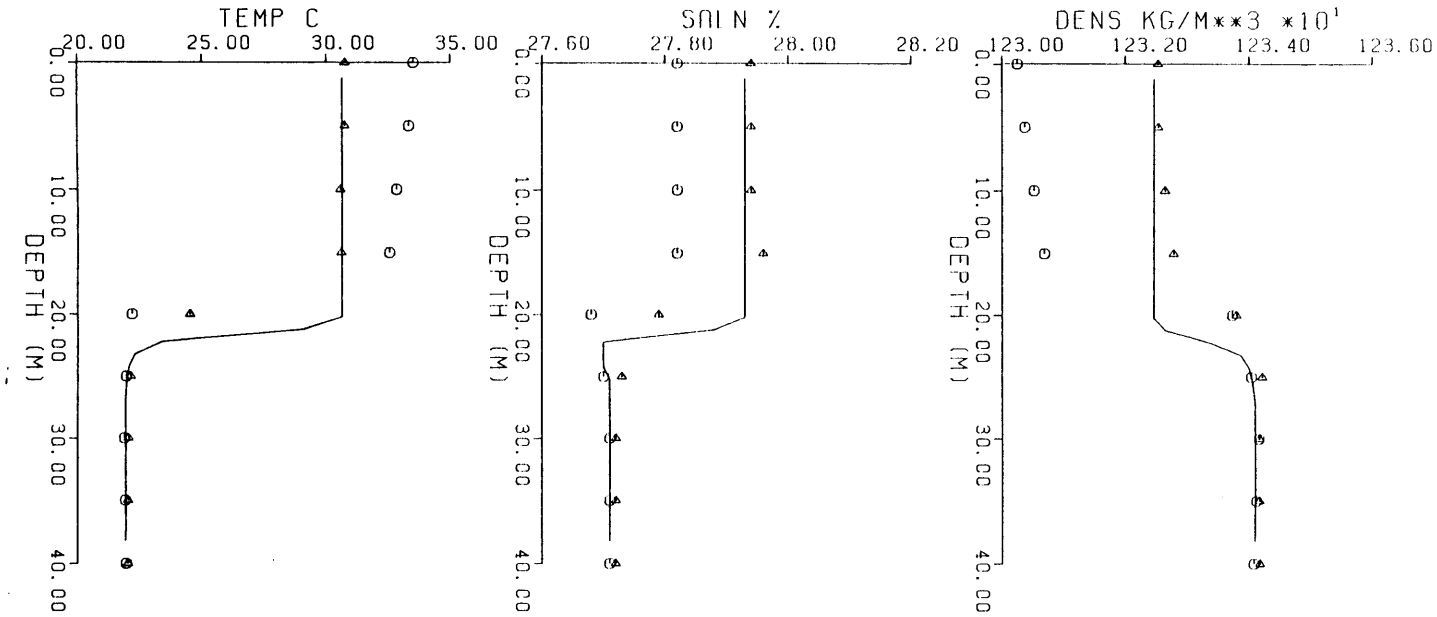

Fig. E.4(b) Data and Model Results for the Period 25 August 1983 to 3 October 1983 with $C_w = 6$ and $C_c = .1$

o Initial Data
Δ Final Data
— Model Result

Table E.4 (a) Details of model run for the period 25 August 1983 to 3 October 1983

Calibration Coefficients		
C_W	6	6
C_c	0.0	.1
Error Analysis Maximum Values		
Temperature °C	6.8	7.1
Salinity %	0.2	0.2
Density kg/m^2	1.4	1.5
Root Mean Square Values		
Temperature °C	2.1	2.4
Salinity %	0.0	0.1
Density kg/m^3	0.5	0.6
Mixing Parameters		
$KE_w(J/m^2)$	590	590
$KE_c(J/m^2)$	0	0
$\overline{u*}$	.0028	.0028
$\overline{w*}$	.0063	.0062
$\overline{R}_{I_\sigma}$	410	500
Change in Stability Index	-3145	-3145
Error in Stability	-37	-48

Table E.4 (b) Water and heat balance for the period 25 August 1983 to 3 October 1983

Calibration Coefficients		
C_w	6	6
C_c	0.0	.1
Water Balance		
Evaporation (mm)	230	227
Pumpage (mm)	45	45
Inflow	105	102
Net Inflow (mm)	-170	-170
Thermal Energy Balance		
Short Wave Radiation ($KCal/m^2/day$)	5280	5280
Atmospheric Radiation ($KCal/m^2/day$)	8310	8310
Back Radiation ($KCal/m^2/day$)	9860	9850
Evaporative Flux ($KCal/m^2/day$)	3380	3340
Net Warming ($KCal/m^2/day$)	91	148
Meteorology		
Air Temperature (°C)	31.1	
Humidity (%)	41	
Wind Speed (m/s)	2.8	

APPENDIX F

Measures used to Express Salt Concentration

This section reviews the various measures used to express the "concentration" of dissolved salts so that measurements expressed in different forms can be conveniently compared.

The term salinity usually connotes concentration by mass (or weight), i.e.,

$$S = \frac{\text{mass of salt}}{\text{mass of mixture of salt and solvent}} \qquad (F.1)$$

The advantage of this measure is that it is independent of density, and hence temperature or pressure. Oceanographers express salinity in parts per thousand ($^{\circ}/_{oo}$; equal to 1000S if S is defined as a fraction, as above) while those dealing with brine often refer to parts per hundred or, percent (%; equal to 100S). In these units the salinity of Mediterranean Sea water is about 39 $^{\circ}/_{oo}$ or 3.9 %, while that of the Dead Sea is in the range of 270-280 $^{\circ}/_{oo}$ or 27-28%.

Note that S refers to the concentration of all salts but analogous definitions could be used to express concentrations of specific ions such as the chloride ion. For oceans, the relative concentration of various ions remains nearly constant so that the concentration of specific ions can be accurately estimated from S. Conversely, the salinity, S can be estimated from concentration of specific ions. For example, oceanographers define CHLORINITY in grams per kilogram as the mass in grams of "atomic weight silver" just necessary to precipitate the

halogens in 0.3285233 kilogram of the seawater sample. (Sverdrup (1949))**. For sea water, the relationship between salinity (S) and Chlorinity (CL) is expressed as:

$$S = .03 + 1.805\ CL \qquad (F.2)$$

where S and Cl are expressed in $^{o}/_{oo}$

For concentrated brines such a relation cannot be derived since precipitation of the less soluble ions will alter the distribution.

Dissolved salts may also be expressed on a volume basis using species or partial densities, i.e.,

$$\rho_i = \frac{\text{mass of species i}}{\text{total volume of the solution at a given temperature}} \qquad (F.3)$$

expressed in units such as mg/l, g/l etc. This measure is commonly used to express the relative abundance of ions in solution. The densities of all ions combined is referred to as TOTAL DISSOLVED SOLIDS (TDS) and may be expressed as:

$$TDS = \sum_i \rho_i \qquad (F.4)$$

where, i = the number of ion species in the solution.

The SOLUTION DENSITY is defined as

$$\rho = \frac{\text{mass of solution}}{\text{volume at a temperature (T) and pressure (P)}} \qquad (F.5)$$

It may also be expressed as SPECIFIC GRAVITY (S.G.), i.e.,

$$S.G. = \frac{\text{mass of a given volume of solution}}{\text{mass of equal volume of water at a reference temperature}} \qquad (F.6)$$

Note, density can be expressed as a function of X, T and P i.e., $\rho(X,T,P)$ where X is a measure of the salt concentration in the solution. Generally, in environmental and water resource related issues, density of

a solution is expressed at atmospheric pressure and hence is considered a function of temperature and dissolved salt concentration only i.e., $\rho(X,T)$. For example, Appendix B includes such a relation (The EQUATION OF STATE) for the Dead Sea brines. Note that density, salinity and totaldissolved solids are related as

$$\rho = \frac{TDS}{S} \qquad (F.7)$$

where ρ and TDS are measured in the same units and S is expressed as a fraction. For example, the density of the Dead Sea based on TDS = 340 g/ℓ or S = 27.6% would be 1232 Kg/m^3 at 25°C. Also note that, for small concentrations where $\rho \simeq 1.0$ Kg/ℓ, the numerical values of TDS and S are nearly the same. For example, Mediterranean Sea water having salinity 39 $^{\circ}/_{oo}$ (39 g/Kg) would have total dissolved solids level of 40 g/ℓ.

Finally, the concentrations of salt in a solution can also be expressed in SIGMA-T units expressed as:

$$\sigma_{S,T,P} = (\rho(X,T,P) - 1)\ 1000 \qquad (F.8)$$

where, ρ is expressed in gm/cm^3. Thus, σ_{20} would refer to "density" of water at 20°C and atmospheric pressure. It is worth adding that IN-SITU DENSITY (i.e., evaluated at the temperature, salinity and pressure where measured) is often written as $\rho_{S,T,P}$ or $\sigma_{S,T,P}$.

---

* Sverdrup, H.U., Johnson, M.W. and Fleming, R.H. (1949) The Oceans: Their Physics, Chemistry and General Biology, Prentice Hall, New York

REFERENCES

1. Aase, J.K. and Idso S.B. (1978), "A comparison of two formula types for calculating long-wave radiation from the Atmosphere", Water Resour. Res. 14(4) pp. 623-625.

2. Adams, E.E., Salhotra, A.M. and D.R.F. Harleman (1983), "Mathematical Simulation of Evaporation, Salinity and Temperature for Two Hydrosolar Power Projects," Proc. of XXth IAHR Conference, Moscow, Vol. 3, pp. 96-103.

3. Adams, E.E., Harleman, D.R.F., Jirka, G.H., and Stolzenbach, K.D., "Heat Disposal in Water Environment," Ralph M. Parsons Laboratory, Department of Civil Engineering, M.I.T., Cambridge, MA 02139.

4. Aldama, A., Bowen, J.D. (1985), "Hypolimnetic Mixing in a Weakly Stratified Lake," Unpublished Paper, Ralph M. Parsons Laboratory, Department of Civil Engineering, M.I.T., Cambridge, MA 02139.

5. Anati, D.A. (1982/1983), "Two Years in the Lifetime of the Dead Sea"; "Dead Sea Summer 1982 Cruises Report"; "Dead Sea 1982 Overturn Cruise Report"; Solmat Systems Ltd., Jerusalem, Israel.

6. Anati, D.A., Stiller, M., Shasha, S. and Gat, J.R. (1985), "The Thermoholine Structure of the Dead Sea: 1979-1984," Unpublished Paper, Isotope Dept., Weizmann Institute of Science, Rehovot.

7. Anati, D.A. and Lerner, S., "Annual Report, Physical Processes in the Upper Dead Sea, 1982-1983", April 6, 1983.

8. Anati, D.A. and Lerner, S., "The 1983 - Overturn Preconditioning", July 19, 1983.

9. Anati, D.A. and Lerner, S., "Autumn Destratification", December 16, 1983.

10. Anati, D.A. and Lerner, S., "A Dry Winter", April 25, 1984.

11. Anati, D.A. and Doron, A., "The Dead Sea Thermoholine Structures in a Hypersaline Spring," August 7, 1984.

12. Anati, D.A. and Lerner, S., "Closing the Cycle," May 30, 1984, Solmat Systems Ltd., P.O.B. 3745, Jerusalem, Israel.

13. Anderson, E.R. (1954), "Energy budget studies, Water Loss Investigations: Lake Hefner Studies", Technical Report, U.S. Geol. Surv. Prof. Paper, 269, pp. 71-119.

14. Angstrom, A. (1918), "A Study of the Radiation of the Atmosphere", Smithson Misc. Collect., 65(3), 59 pp.

15. Angstrom, A. (1936), "Effective radiation during the second international polar year", Medd Statens Meteorol. Hydrogr. Anst., 6(8).

16. Arons, A.B. and Kientzler, C.F. (1954), "Vapor Pressure of Sea Salt Solutions," Trans. Am. Soc. Geophys. Union, Vol. 35, pp. 722-728.

17. Ashford, J.L. and Boocock, B.A. (1984), "Arab Potash Solar Evaporation System: Construction," Proc. Instit. Cov. Engrs. Part 1, Vol. 76, pp. 165-184.

18. Assaf, G. (1976), "The Dead Sea: A Scheme for a Solar Lake," Solar Energy, Vol. 18, pp. 293-299.

19. Assaf, G. (1980), "The Dead Sea-I, Energy Balance and Evaporation," Solmat Systems Ltd., Jerusalem, Israel.

20. Atkinson, J.F., Adams E.E., Salhotra, A.M. and Harleman, D.R.F. (1983), "User's Manual for Massachusetts Institute of Technology Solar Pond Program (MITSOL)," Ralph M. Parsons Laboratory, Department of Civil Engineering, M.I.T., Cambridge, MA 02139.

21. Atkinson, J.F. and D.R.F. Harleman (1983), "A Wind Mixed Layer Model for Solar Ponds," Solar Energy, Vol. 31, pp. 243-259.

22. Atkinson, J.F. and D.R. F. Harleman (1983), "Wind Mixing in Solar Ponds," Progress in Solar Energy, Vol. 6., ASES.

23. Atkinson et. al. (1984), "Entrainment in Diffusive Thermoholine Systems: Application to Salt Gradient Solar Ponds," Technical Report No. 300, Ralph M. Parsons Laboratory, Department of Civil Engineering, MIT, Cambridge, MA 02139.

24. Ballard, T.J.W., and Brice, G.J. (1984), Arab Potash Solar Evaporation System: Design," Proc. Instit. of Civ. Engrs. Part 1, Vol. 76, pp. 145-163.

25. Block, M.R., Ladislaus, F. and Spiegler, K.S. (1951), "Solar Evaporation of Brines," J. of Indus. and Engr. Chemistry, Vol. 43, No. 7, pp. 1544-1553.

26. Bloss, S. and Harleman, D.R.F. (1979), "Effect of Wind Mixing on the Thermocline Formation in Lakes and Reservoirs," Technical Report No. 249, Ralph M. Parsons Laboratory, Department of Civil Engineering, M.I.T., Cambridge, MA 02139.

27. Bonython, C.W. (1956), "The Influence of Salinity Upon the Rate of Natural Evaporation," Proc. Symposium Arid Zone, Res. 11, Climatol. Microclimatol., 65-71, UNESCO Canberra.

28. Bonython, C.W. (1966), "Factors Determining the Rate of Solar Evaporation in the Production of Salt," 2nd Northern Ohio Geological Society Symposium on Salt, 2, pp. 152-167.

29. Brunt, D. (1932), "Notes on R radiation in the atmosphere", Quart J. Roy. Meteorol. Soc., 58, pp. 389-418.

30. Brutsaert, W. (1975), "On a desirable formula for long-wave radiation from clear skies", Water Resour. Res., 11(S), pp. 742-744.

31. Brutsaert, W.H. (1982), "Evaporation into the Atmosphere - Theory, History and Applications," D. Reidel Publishing Co., Dordrecht, Holland.

32. Calder, R. and Neal, C. (1984), "Evaporation from Saline Lakes: A Combination Equation Approach," Journal of Hydrological Science, Vol. 29, No. 1, pp. 89-97.

33. Cengel, Y.A. and Ozisik, M.N. (1984), "Solar Radiation Absorption in Solar Ponds," Solar Energy, Vol. 33, No. 6, pp. 581-591.

34. Coantic, M.F. (1978), "Coupled Energy Transfer and Transformation Mechanisms across the Ocean Atmosphere Interface," Proc. 6th Int. Heat Transfer Conference, Vol. 6, Toronto, Canada.

35. Charnock, H. (1955), "Wind Stress on a Water Surface," Quart Journal Royal Met. Soc., 81, pp. 639.

36. Csanady, G.T. (1979), "A Developing Turbulent Surface Shear Layer Model," Journal of Geophysical Resources, Vol. 86, No. C8, pp. 4944-4948.

37. Dake, J.M.K. and Harleman, D.R.F. (1969), "Thermal Stratification in Lakes. Analytical and Laboratory Studies," Water Resour. Res., Vol. 5, No. 2.

38. Daniels, F. (1956), Experimental Physical Chemistry, McGraw-Hill Book Co., New York.

39. Deacon, E.L. (1970), "The derivation of Swinbank's long-wave radiation formula", Quart. J. Roy. Meteorol. Soc., 96, pp. 313-319.

40. Deardorf, J.W. (1970), "Convective Velocity and Temperature Scales for the Unstable Planetary Boundary Layer and the Rayleigh Convection," J. Atmos. Sci., 27, pp. 1211-1213.

41. DeCoster, M., and W. Schuepp (1957), "Measures de rayonnement effecting a' Leopoldville", Acad. Roy. Sci. Colon., Brussels Bull Sciences, 3, pp. 642-651.

42. Denman, K.L. and Miyake, M. (1973), "Upper-layer Modification at Ocean Station Paper: Observations and Simulation," Journal of Physical Oceanography, Vol. 3, pp. 185-195.

43. Denman, K.L. (1973), "A Time-Dependent Model of the Upper Ocean," Journal of Physical Oceanography, Vol. 3, pp. 173-183.

44. Dickson, D.R., Yepson, J.H., and Hales, J.V. (1965), "Saturated Vapor Pressure Over Great Salt Lake Brine", J. Geo. Phys. Res., Vol. 70, No. 2, pp. 500-503.

45. Dines, W.H. and Dines, L.H.G. (1927), "Monthly means of radiation from various parts of the sky at Benson, Oxfordshire," Mem. R. Meteor. Soc., 2, No. 11.

46. Fabuss, B.M., et al. (1965), "Thermodynamic Properties of Saline Water," Research and Development Progress Report No. 136, United States Department of the Interior.

47. Farmer, D.A. (1975), "Penetrative Convection in the Absence of Mean Shear," Quart. Journal of R. Met. Soc., Vol. 101, pp. 869-891.

48. Fischer, H.B. (1981), "Transport Models for Inland and Coastal Waters," Proc. of a Symposium on Predictive Ability, Dept. of Civil Eng., Univ. of California, Berkeley.

49. Fischer, Hugo B., E.J. List, R.C.Y. Koh, J. Imberger and N.H. Brooks (1979), "Mixing in Inland and Coastal Waters," Academic Press, London.

50. Gates, D.M. (1962), "Energy Exchange in the Biosphere", 151 pp., Marper and Row, New York.

51. Goody, R.M. (1964), "Atmospheric Radiation, 436 pp., Clarendon, Oxford.

52. Goss, J.R. and Brooks, F.A. (1956), "Constants for empirical expressions for downcoming atmospheric radiation under cloudless sky," J. Meteorol., 13, pp. 482-488.

53. Gratch, Eitan (1983), Personal Communication.

54. Guttman, Y. and Simon, A. (1984), (In Hebrew) "Hydrological Survey of the Western Shore of the Dead Sea, Stage A," TAHAL Consulting Engineers, Tel Aviv, Israel.

55. Halpern, D. (1974), "Observations of the Deepening of the Wind-Mixed Layer in the North East Pacific Ocean," Journal of Phy. Oceanography, Vol. 4, pp. 454-466.

56. Hamon, R.W., Weiss, L.L., Wilson, W.T. (1954), "Insolation as an Empirical Function of Daily Sunshine Duration," Monthly Weather Review, Vol. 82, No. 6.

57. Harbeck, Earl, Jr., Kohler, M.A., Koberg, G.E. and others (1958), "Water Loss Investigations, Lake Mead Study," USGS Professional Paper No. 298.

58. Harbeck, G.E., (1955), "The Effect of Salinity on Evaporation," USGS Professional Paper 272-A.

59. Helfrich, K.R. et al. (1982), "Evaluation of Models for Predicting Evaporative Water Loss in Cooling Impoundments," Report No. 1260-17, Electric Power Research Institute.

60. Higashi, K., Nakamura, K. and Hara, R. (1931), "The Specific Gravities and the Vapor Pressure of the Concentrated Sea Water at 0-175°C," J. Soc. Chem. Ind. Japan, Vol. 34, pp. 166-172.

61. Hill, M.N. (1962), The Sea - Vol. 1, Physical Oceanography, Interscience Publishers, New York and London.

62. Hughes, G.H. (1967), "Analysis of Techniques Used to Measure Evaporation from Salton Sea, California," USGS Professional Publication Paper No. 272-H.

63. Hull, J.R. (1980), "Computer Simulation of Solar Pond Thermal Behavior," Solar Energy, Vol. 25, pp. 33-40.

64. Hurley, O., Jirka, K.H. and Harleman, D.P.F. (1977), "Vertical Heat Transport Mechanisms in Lakes and Reservoirs," Technical Report No. 227, Ralph M. Parsons Laboratory, Department of Civil Engineering, MIT, Cambridge, MA 02139.

65. Idso, S.B., and Jackson R.D. (1969), "Thermal Radiation from the Atmosphere," J. Geophys. Res., 74(23), pp. 5397-5403.

66. Imberger, J. and Peterson, J. (1981), "A Dynamic Reservoir Simulation Model - DYRESM: 5, from Transport Models for Inland and Coastal Waters; Proceedings of a Symposium on Predictive Ability, ed. H.B. Fischer, Academic Press.

67. Janson, L. (1959), "Evaporation from Salt Water in Arid Zones," Bulletin No. 56 of the Division of Hydraulics at the Royal Institute of Technology, Stockholm, Sweden.

68. Jirka, G.H., Adams, E.E. and Stolzenbach, K.D. (1981), "Buoyant Surface Jets." Journal of Hyd. Div. ASCE, Vol. 107, No. HY11, Nov. 1981, pp. 1467-1487.

69. Jobson, H.E. (1972), "Effect of Using Averaged Data on the Computation of Evaporation," Water Resour. Res., 8, pp. 513-518.

70. Kantha, L.H. and R.R. Long (1980), "Turbulent mixing with stabilizing surface buoyancy flux." Phys. Fluid 23, pp. 2142-2143.

71. Kato, H. and Phillips, O.M. (1969), "On the Penetration of a turbulent layer into stratified fluid." J. Fluid Mech. 37, pp. 643-655.

72. Khasawneh and Khoury (1983), "Jordan: Arab Potash Company's First Step into the Potash Market," Phosphorus and Potassium, No. 125, May-June.

73. Kimbal, B.A. and Idso, S.A. (1982), "A model of thermal radiation from partly cloudy and overcast skies," Water Resour. Res., 18(4), pp. 931-936.

74. Kohler, M.A., (1954), "Lake and Pan Evaporation," in "Water Loss Investigations: Lake Hefner Studies," Technical Report, USGS Professional Paper 269, pp. 127-148.

75. Kraus, E.B. and J.S. Turner (1967), "A One-Dimensional Model of the Seasonal Thermocline, Pt. 2, The General Theory and Its Consequences," Tellus 19, 98-106.

76. Kreider (1980), "Solar Energy Handbook," McGraw Book Co., New York, Chapter 10 by Tabor, M. and Weinberger, Z.

77. Krumgalz, B.S. (1982), "Physico-Chemical Study of Dead Sea Waters," Marine Chemistry, pp. 477-492.

78. Levy, Y. (1980), "Seasonal Changes in Dead Sea Chemical Composition, 1979/80," Report MG/7/80/ Ministry of Energy and Infrastructure, Marine Geology Div., Geological Survey of Israel. Jerusalem, Sept. 1980.

79. Lewis, W.M., Jr. (1983), "Temperature, Heat, and Mixing in Lake Valencia, Venezuela," Limnological and Oceanography, Vol. 28, No. 2, pp. 273-286.

80. Madsen, O.S. (1976), "A Realistic Model of the Wind Induced Ekman Boundary Layer," J. of Physical Oceanography.

81. Marcus, Y. (1984), "The Vapor Pressures of Mixtures of Dead Sea Water with Mediterranean Water." Report submitted to the Mediterranean Dead Sea Co. Ltd., Dept. of Inorganic and Analytical Chemistry, The Hebrew University of Jerusalem, Jerusalem 91904 Israel.

82. McCutcheon, S.C. (1983), "Vertical Mixing in Models of Stratified Flow," Proc. of Conference on Frontiers in Hydraulic Engineering, ASCE, M.I.T., Cambridge.

83. Mediterranean Dead Sea Company, Personal communication with Eitan Gratch, (1982).

84. Mediterranean Dead Sea Company, Personal communication with Eitan Gratch, (1983).

85. Mediterranean Dead Sea Co., Ltd. (1983), "Mediterranean Dead Sea Project, Outline Design - Summary and Conclusions", Tel Aviv, Israel.

86. Mellor, G.L., Durbin, P.A. (1975), "The Structure and Dynamics of the Ocean Surface Layer," J. Physical Oceanography, Vol. 5, pp. 718-728.

87. Mermier, M. and Seguin, B. (1976), "Comment on 'On a desirable formula for long-wave radiation from clear skies' by W. Brutsaert" Water Resour. Res., 12(6), pp. 1327-1328.

88. Miller, J.R. (1976), "The Salinity Effect in a Mixed Layer Ocean Model," Journal of Physical Oceanography, Vol. 6.

89. Miller, D.H. (1981), "Energy at the Surface of the Earth - An Introduction to the Energetics of the Ecosystem," International Geophysics Series, Academic Press.

90. Munk, W.H. and Anderson, E.A. (1948), "Notes on the Theory of a Thermocline," J. Marine Res., Vol. 7, pp. 276-295.

91. National Research Council (1928), "International Critical Tables" New York, McGraw Hill, 1st Ed., Vol. 3.

92. Neev, D. and Emery, K.O. (1967), "The Dead Sea: Depositional Processes and Environments of Evaporites", Bulletin No. 41, Ministry of Development, Geological Survey, State of Israel, Jerusalem.

93. Neumann, J. (1958), "Tentative Energy and Water Balances for the Dead Sea," Bull. Res. Council of Israel, Vol. 76, pp. 137.

94. Niiler, P.P. (1975), "Deepening of the Wind Mixed Layer," J. Marine Res. 33, pp. 405-422.

95. Nimmo, W.H.R. (1964), "Measurement of Evaporation by Pans and Tanks," Australian Met. Mag., Vol. 46, pp. 17-53.

96. Nystrom, J.B. (1982), "Evaporation Measurement by the Floating Pan Method," Technical Report, Alden Research Laboratory, Worcester Polytechnic Institute, Holden, Massachusetts.

97. Omar, M.H. and El-Bakery, M.M. (1981), "Estimation of Evaporation from the Lake of the Aswan High Dam (Lake Nasser), Based on Measurements over the Lake," Agricultural Meteorology, 23, pp. 293-308.

98. Paily, P.P., Macagno, E.D. and Kennedy, J.F. (1974), "Winter Regime Surface Heat Loss from Heated Streams", IIHR Report No. 155, Instit. of Hyd. Res., University of Iowa, Iowa 52242.

99. Pedersen, F.B. (1980), "A Monograph on Turbulent Entrainment and Friction in Two-Layer Stratified Flow," Ins. of Hydrodynamics and Hydr. Eng., Technical University of Denmark, Ser. Paper No. 25, April 1980.

100. Penman, H.L. (1948), "Natural Evaporation from Openwater, Basic Soil and Grass," Proc. Roy. Soc. A, 193, pp. 120-145.

101. Penman, H.L. (1961), "Weather, Plant and Soil Factors in Hydrology," Weather, 16, pp. 207-219.

102. Picker, P., et. al (1974), "A High Precision Digital Readout Flow Sensimeter for Liquids," J. of Solution Chemistry, Vol. 3, No. 5, pp. 377-383.

103. Pritchard, D.W. (1960), "The Movement and Mixing of Contaminants in Tidal Estuaries," Proc. 1st Int. Conf. on Waste Disposal in the Marine Environment, Univ. of California, 1959, ed. E.A. Pierson, Pergamon Press.

104. Robinson, R.A. and Stokes, R.H. (1945), "A Thermodynamic Study of Bivalent Metal Halides in Aqueous Solutions. Part XV. Double Chlorides of Uni- and Bivalent Metals," Trans. Faraday Society, Vol. 41, pp. 752-755.

105. Robinson, R.A. and Bower, V.E. (1965), "An Additivity Rule for the Vapor Pressure Lowering of Aqueous Solutions," Journal of Research of the Nat. Bureau of Standards--A Phys. and Chem., Vol. 69A, No. 4, pp. 365-367.

106. Ryan, P.J. and Harleman, D.R.F. (1973), "An Analytical and Experimental Study of Transient Cooling Pond Behaviour." Technical Report No. 161, Ralph M. Parsons Laboratory, Department of Civil Engineering, MIT, Cambridge, MA 02139.

107. Salhotra, A.M., Adams, E.E. and Harleman, D.R.F. (1981), "Evaporation and Salinity Studies for the Qatara Depression Project," Progress Report, Technology Adaptation Program, M.I.T., Cambridge, MA 02139.

108. Salhotra, A.M., E.E., Adams and D.R.F. Harleman (1983), "Modelling Vertical Mixing in the Dead Sea," Progress Report No. 1, January 1983, Ralph M. Parsons Laboratory, M.I.T., Cambridge, MA 02139.

109. Salhotra, A.M., E.E., Adams and D.R.F. Harleman (1983), "Evaporation and Stratification Studies for the Dead Sea Progress Report No. 2," Ralph M. Parsons Laboratory, M.I.T., Cambridge, MA 02139.

110. Salhotra, A.M., E.E., Adams and D.R.F. Harleman (1984) "Effect of Salinity and Ionic Composition on the Rate of Evaporation. Analysis of Dead Sea Pan Evaporation Data," Progress Report No. 3, April 1984, Ralph M. Parsons Laboratory, M.I.T., Cambridge, MA 02139.

111. Salhotra, A.M., E.E., Adams and D.R.F. Harleman (1984), "Evaporation and Stratification Study for the Dead Sea," Proc. Fourth Congress APD-IAHR, Chiang Mai Thailand, pp. 1439-1457.

112. Salhotra, A.M., E.E., Adams and D.R.F. Harleman (1984), "Saturation Vapor Pressure of Mixtures of Dead Sea and Mediterranean Sea Water. Comparison of Direct Measurements by Y. Marcus with results from the Analysis of Evaporation Pan Data," Progress Report No. 4, Ralph M. Parsons Laboratory, M.I.T., Cambridge, MA 02139.

113. Salhotra, A.M., E.E., Adams and D.R.F. Harleman (1984), "A Review of Evaporation and Stratification Study of the Dead Sea," Ralph M. Parsons Laboratory, M.I.T., Cambridge, MA 02139.

114. Salhotra, A.M., E.E., Adams and D.R.F. Harleman (1985), "Comparison, Calibration and Verification of Atmospheric Long-Wave Radiation Formulae for the Dead Sea," Progress Report No. 5, Ralph M. Parsons Laboratory, M.I.T., Cambridge, MA 02139.

115. Salhotra, A.M., E.E., Adams and D.R.F. Harleman (1985) "The Effect of the Dead Sea Works (Israel) and the Arab Potash Works (Jordan) on the Water and Salt Balance of the Dead Sea," Progress Report No. 6, Ralph M. Parsons Laboratory, M.I.T., Cambridge, MA 02139.

116. Satterlund, D.R. (1979), "An Improved Equation for Estimating Long-Wave Radiation from the Atmosphere," Water Resour. Res., 15(6), pp. 1649-1650.

117. Sellers, W.D. (1965), "Physical Climatology", The University of Chicago Press, Chicago and London.

118. Sherman, F.S., Imberger, J. and Corcos, G.M. (1978), "Turbulence and Mixing in Stably Stratified Waters," Annual Review of Fluid Mechanics, Vol. 10.

119. Stanhill, G. (1980), "Evaporation from the Dead Sea, Report Nos. 1, 2 and 3," Division of Agricultural Meteorology, Agricultural Research Organization, Bet Dagan.

120. Stanhill, G. (1983), Personal communication.

121. Stefan, H. and D.E. Ford (1975), "Temperature Dynamics in Dimictic Lakes," J. Hydr. Div., ASCE, 101, pp. 97-114.

122. Steinhorn, I. and Gad Assaf, "The Physical Structure of the Dead Sea Water Column, 1975-1977," Ch. 12, Hypersaline Brines and Evaporatic Environments, Elsevier Scientific Publishing Co., Amsterdam.

123. Steinhorn, I. (1980), "The Density of Dead Sea Waters as a Function of Temperatures and Salt Concentration," Israel Journal of Earth Sciences, Vol. 29, pp. 191-196.

124. Steinhorn, I. and Gat, J.R. (1983), "The Dead Sea", Scientific American Vol. 249, No. 4, pp. 102-109.

125. Steinhorn, I. (1985), "The Disappearance of the Long-Term Meromictic Stratification of the Dead Sea," Limnology and Oceanography, pp. 451-471, Vol. 80, No. 3, May 1985.

126. Stoll, A.M. and Hardy, J.D. (1955), "Thermal Radiation Measurements in Summer and Winter Alaskan Climates," Eos Trans. AGU, 36, pp. 213-225.

127. Stommel, H., K. Saunders, W. Simmons and J. Cooper (1969), "Observations of the Diurnal Thermocline," Deep Sea Res. (suppl.), pp. 269-284.

128. Sturrok, Alex M., Jr. (1978), "Evaporation and Radiation Measurements at Salton Sea, California," Geological Survey Water Supply Paper 2053.

129. Sundaram, T.R. and R.A. Rehm (1973), "The Seasonal Thermal Structure of Deep Temperate Lakes," Tellus 25, pp. 157-167.

130. Svenson, U. (1978), "A Mathematical Model of the Seasonal Thermocline," Thesis Report No. 1002, Dept. of Water Resources Engr., Lund Inst. of Technology, Lund, Sweden.

131. Sverdrup, H.U., Johnson, M.W. and Fleming, R.H. (1942), "The Oceans," New York.

132. Swinbank, W.C. (1963), "Long-Wave Radiation from the Skies," Quart. J. Roy. Meteorol. Soc., 89, pp. 339-348.

133. Tahal Consulting Engineers, Ltd. (1982), "Hydrological and Limnological Investigations of the Dead Sea," Technical Report No. 3, Mediterranean Dead Sea Hydroelectric Project, Feasibility Study, August 1982.

134. Tahal Consulting Engineers, Ltd., "A Daily Simulation for Evaluation of Future Dead Sea Levels and Evaporation," Summary of reports by F. Mero, E. Simon and Y. Last, Tahal 04/82/06 (Hebrew) and Tahal 82 (draft).

135. Tennessee Valley Authority (April 1972), "Heat and Mass Transfer Between a Water Surface and the Atmosphere," Water Resources Research Lab. Report No. 14, Norris Tennessee.

136. Tucker, W.A. and Green, A.W. (1977), "A Time Dependent Model of the Lake Averaged Vertical Temperature Distribution of Lakes," Limnology and Oceanography, Vol. 22 (4), pp. 687-699.

137. Turk, L.T. (1970), "Evaporation of Brine: A Field Study on Bonneville Salt Flats, Utah," Water Resour. Res., Vol. 6, No. 4, pp. 1209-1215.

138. Turner, L.T. (1968), "The Influence of Molecular Diffusivity on Turbulent Entrainment across a Density Interface," J. Fluid Mech., 33, pp. 639-656.

139. Turner, L.T. (1969), "A Note on Wind Mixing at the Seasonal Thermocline," Deep Sea Research, Vol. 16, pp. 297-300.

140. Turner, J.S. (1973), "Buoyancy Effects in Fluids," Cambridge University Press, London.

141. United Nations (1982), "Israel's Decision to Build a Canal Linking the Mediterranean Sea to the Dead Sea," Report of the Secretary-General, Thirty-Seven Session Agenda Item 68. A/37/328.

142. United Nations (1983), "Israel's Decision to Build a Canal Linking the Mediterranean Sea to the Dead Sea," Report of the Secretary-General, Thirty-Eight Session Agenda Item 75. A/38/502.

143. United Nations (1984), "Israel's Decision to Build a Canal Linking the Mediterranean Sea to the Dead Sea," Report of the Secretary-General, Thirty-Ninth Session Agenda Item 77. A/39/142.

144. U.S. Office of Saline Waters (1971), "Technical Data Book," Prepared by M.M. Kellog and Co.

145. Vadasz, P. (1982), "A Halo-Thermal Simulation of the Dead Sea," M.S. Thesis, - Israel Institute of Technology. Technion.

146. Weast, R.C. (1981) (Ed.), Handbook of Chemistry and Physics, 62nd ed., CRC Press, Boca Raton, Fla.

147. Weiner, Dan (1980), "The Mediterranean Dead Sea Project," Journal of Solar Energy Engineering, Vol. 102, pp. 281-286.

148. The Weizmann Institute of Science, Israel, Dept. of Isotope Research, "Hydrographic Observation and Research of the Seasonal Changes in the Structure of the Dead Sea, Intermediate and Final Reports, 1979-1984".

149. Willis, G.E. and Deardorff, J.W. (1974), "A Laboratory Model of the Unstable Planetary Boundary Layer," J. Atmos. Sci., 31, pp. 1297-1307.

150. Wu, J. (1969), "Wind Stress and Surface Roughness at Air-Sea Interface," J. of Geophysical Res., Vol. 74, No. 2.

151. Wunderlich, W.O. (1972), "Heat and Mass Transfer Between a Water Surface and the Atmosphere," Laboratory Report No. 14, T.V.A. Engineering Laboratory, Norris, Tennessee.

152. Yamamoto, G. (1950), "On Nocturnal Radiation" Sci. Rep. Tohoku Univ. Ser., 5,2, pp. 27-43.

153. Zemen, O. and Lumley, J.L. (1977), "Buoyancy Effects in Entraining Turbulent Boundary Layers: A Second Order Closure Study," Proc. Turbulent Shear Flow Symposium, Penn. State Univ.

154. Zemen, O. and Temekes, H. (1977), "Parameterization of the Turbulent Energy Budget at the Top of the Daytime Atmospheric Boundary Layer," J. Atmos. Sci., 34, pp. 111-123.

155. Zilitinkevich, S.S., "Comments on 'A Model for the Dynamics of the Inversion Above a Convection Boundary Layer'", J. Atmos. Sci. 32, pp 991-992, 1975.